

UNIVERSITÉ LILLE 1 - UFR Sciences

**Ecole Doctorale**  
Science Pour l'Ingénieur (EDSPI)

# THÈSE

pour obtenir le titre de

**Docteur en Sciences**

de l'Université de Lille 1

**Discipline : Micro et nano technologies, acoustique et  
télécommunications**

présentée et soutenue par

Gabriel MUGNY

## **Simulation et modèles prédictifs pour les nanodispositifs avancés à canaux à base de matériaux alternatifs**

Thèse dirigée par Christophe DELERUE (directeur), Denis RIDEAU et François TRIOZON (co-encadrants) soutenue le 21 juin 2017 devant le jury composé de :

Dr. Philippe DOLLFUS	- Rapporteur
Pr. David ESSENI	- Rapporteur
Dr. Fabienne MICHELINI	- Examinatrice
Pr. Tibor GRASSER	- Examinateur
Dr. Evelyne LAMPIN	- Examinatrice
Dr. Christophe DELERUE	- Directeur
Dr. François TRIOZON	- Co-encadrant
Dr. Denis RIDEAU	- Co-encadrant

English title:

Simulation and predictive models for advanced nanodevices  
based on alternative channel materials

À mes grands-parents,  
Catherine et Paul Ricci  
tous deux nonangénaires.



## Abstract

Silicon has been *the* semiconductor material of choice in microelectronics industry since the commercialization of Metal Oxide Semiconductor Field Effect Transistors (MOSFETs), because it is a cheap, abundant material, with a native oxide of good quality and relatively good properties for both electron and hole transport. However, with the reduction in size of transistors, standard Si-based Complementary Metal Oxide Semiconductor (CMOS) architectures face growing challenges and new architectures and materials start to appear in the CMOS roadmap. Most recent nodes for Fully-Depleted Si-On-Insulator (FDSOI) or FinFET technology introduced SiGe material in the channel, to allow stress engineering and enhance hole transport in p-type MOS devices. III-V alloys such as InGaAs, are also considered as potential candidates for n-type MOS devices.

Facing this variety of materials and compositions, together with new device architectures and new physical phenomena appearing at the nanoscale (such as source-drain tunneling and quasi-ballistic transport), numerical models used in industry have to be adapted and refined in order to predict and assist the development of the technology. In this context, the qualitative comparison of the different MOSFET design architectures is not straightforward and there might be no unique universal solution.

This PhD work aims at contributing to the development of numerical tools for advanced device simulation including alternative materials. It is a collaboration between the industry (STMicroelectronics-Crolles) and research institutes (CEA-Grenoble and IEMN-Lille). The modeling of advanced low-power MOSFET devices is investigated with predictive, but efficient tools, that can be compatible with an industrial Technology Computed Aided Design (TCAD) framework. In the first part of this document, a review of numerical tools based on different approaches is given, as well as the challenges for the simulation of MOSFET devices made with InGaAs or SiGe channels. In the second part, the results of this thesis work are presented. The electronic properties of bulk materials and nanostructures are investigated in the first Chapter with tools ranging from atomistic tight-binding and empirical pseudo-potential to effective mass model. The electrostatic properties of III-V Ultra-Thin Body and bulk capacitance are then investigated in the second Chapter, including a description of the traps response. The transport properties (low-field mobility and saturation velocity) of thin films and nanowires are investigated in the third Chapter. Finally, the transport in linear and saturation regime of a template FDSOI device is investigated in the fourth Chapter, based on two codes developed at CEA/IEMN and STM: TB\_SIM and UTOX respectively. The first one includes a full quantum transport solver, based on the Non-Equilibrium Green Function (NEGF) formalism, while the second one includes a semi-classical Quantum-corrected Drift Diffusion (QDD) solver, based on the resolution of closed- or open-boundary Schrödinger equation, including a Kubo-Greenwood solver for the mobility.

This work makes use of a broad variety of approaches, models and techniques. Physical-based tools are developed, allowing to improve in the predictive power of TCAD models for devices with short-channel length and alternative channel materials.

**Keywords:** MOSFET, FDSOI, numerical models, quantum transport, InGaAs, SiGe.



## Résumé en français

Le silicium (Si) a été *le* matériau semiconducteur de choix dans l'industrie microélectronique depuis son commencement et l'invention du transistor MOS, car c'est un matériau bon marché, abondant, qui possède une bonne interface avec son oxyde natif et de relativement bonnes propriétés de transport d'électron et de trou. Cependant, alors que la miniaturisation des composants se poursuit, les architectures CMOS (de l'acronyme anglais: "Complementary Metal-Oxide-Semiconductor") conventionnelles à base de Si font face à des défis de plus en plus grands et de nouvelles architectures, ainsi que de nouveaux matériaux, commencent à apparaître dans la feuille de route CMOS. Les nœuds les plus récents pour les technologies FDSOI (pour "Fully-Depleted Si-On-Insulator") ou FinFET ("Fin Field-Effect-Transistor") introduisent du SiGe dans le canal, afin d'améliorer le transport des trous dans les dispositifs MOS de type p. Des alliages III-V, tels que l'InAs ou le GaAs, sont également considérés comme des candidats potentiels pour les dispositifs MOS de type n.

Face à cette diversité de matériaux et de compositions, ainsi que d'architectures de dispositifs et de phénomènes physiques qui apparaissent à l'échelle nanoscopique (tels que l'effet tunnel entre la source et le drain et le transport quasi-balistique), les modèles numériques utilisés en industrie doivent être adaptés et raffinés, afin de pouvoir prédire les performances et aider le développement de ces technologies. Dans ce contexte, la comparaison qualitative de différentes architectures n'est pas évidente et il peut ne pas y avoir de solution universelle unique.

Ce travail de thèse a pour but de contribuer au développement d'outils numériques pour la simulation de dispositifs avancés à base de matériaux alternatifs au Si. C'est un travail de collaboration entre l'industrie (STMicroelectronics à Crolles) et des instituts de recherche (le CEA à Grenoble et l'IEMN à Lille). Le but de ce travail est l'investigation et la modélisation de dispositifs MOSFET avancés pour des applications de basse puissance, grâce à des outils prédictifs, mais efficaces et peu coûteux numériquement, qui peuvent être compatibles avec un environnement de TCAD ("Technological Computer-Assisted Design") industriel. Dans la première partie de ce document, une revue des outils numériques est donnée, mettant le doigt sur les défis inhérents à la simulation de dispositifs MOSFET nanoscopiques à base de canaux InGaAs ou SiGe. Dans la deuxième partie de ce document, les résultats de ce travail de thèse sont présentés. Les propriétés électroniques des matériaux massifs et des nanostructures sont étudiées dans le premier Chapitre, avec des outils allant de la méthode atomistique des liaisons fortes et des pseudo-potentiels empiriques, au modèle de masse effective. Les propriétés électrostatiques des capacités III-V massives et des films ultra-minces sont étudiées dans le deuxième Chapitre, comprenant une description de la réponse des pièges d'interfaces. Les propriétés de transport (mobilité effective à faible champ et vitesse de saturation) dans les films minces et nanofils sont étudiées dans le troisième Chapitre. Finalement, le transport en régime linéaire et saturé de dispositifs-modèles pour la technologie FDSOI est étudié dans le quatrième Chapitre, à l'aide de deux codes développés au CEA/IEMN et à STM: TB\_Sim et U20XPP respectivement. Le premier code inclut un modèle de transport entièrement quantique, basé sur les fonctions de Green hors équilibre (NEGF, pour l'acronyme de l'anglais:

“Non-Equilibrium Green’s Function”). Le second code inclut un modèle semi-classique de dérive diffusion quantique (QDD, pour l’acronyme de l’anglais: “Quantum-corrected Drift-Diffusion”), basé sur la résolution de l’équation de Schrödinger avec conditions aux limites ouvertes ou fermées, ainsi qu’un modèle “Kubo-Greenwood” pour les calculs de mobilité.

Ce travail fait usage d’une large variété d’approches et de modèles différents. Des outils basés sur une approche physique sont développés, permettant d’améliorer la capacité prédictive des modèles TCAD conventionnels, pour la modélisation des dispositifs nanoscopiques à faible longueur de grille et à base de matériaux SiGe ou InGaAs.

**Mots-clés:** MOSFET, FDSOI, modèles numériques, transport quantique, InGaAs, SiGe.

## Remerciements

Cette thèse n'aurait *officiellement* pas été possible sans le soutien de plusieurs personnes et d'entités (STMicroelectronics, le CEA et l'IEMN) que je remercie ici. Elle n'aurait également pas été possible *personnellement* sans l'appui, l'aide précieuse et la stimulation intellectuelle d'un grand nombre de personnes.

Je tiens tout d'abord à remercier très chaleureusement mes trois encadrants qui se sont chacun impliqués fortement dans la thèse, auprès desquels j'ai beaucoup appris et avec qui j'ai eu un grand plaisir à travailler et à lier des liens d'amitiés. Merci François pour ton soutien infaillible dans les moments difficiles (les dernières corrections avant soumission d'articles, préparation de la soutenance et collecte de fonds pour le coiffeur), ta patience, ta pédagogie, ta générosité et les discussions passionnantes sur la physique, les physiciens, leur nationalité et autres anecdotes. Merci Denis pour ton engagement sans retenues, tes nouvelles idées stimulantes, les discussions passionnées sur le code, les équations et les résultats obtenus, les heures passées parfois jusqu'à tard à comprendre un problème de physique ou d'implémentation, ta ténacité et ta générosité. Et, last but not least, merci Christophe pour ton regard avisé de chercheur et ton aide précieuse pendant chaque étape de la thèse, ton accueil chaleureux lors de mes séjours à Lille, ta disponibilité, ton ouverture et toutes les discussions extrêmement enrichissantes sur la physique (et la politique). Merci également à Yann-Michel d'avoir enrichi nombreuses de nos discussions par tes conseils.

Il faudrait ensuite écrire un chapitre entier pour pouvoir remercier comme il se doit tout le monde qui a contribué, de près ou de loin, à cette thèse. Pendant ces trois ans (et quelques poussières), ma route a croisé celle d'un grand nombre de thésards, chercheurs, ingénieurs, physiciens, amis, collègues, qui y ont tous contribué d'une manière ou d'une autre et auprès desquels j'ai beaucoup appris et grandi. Par souci de place sur le papier, je me contenterai ici de donner une liste pêle-mêle, non exhaustive.

Pour la team *UTOX*, un grand merci à Fabio Goncalves Pereira et Davide Garetto (et bien sûr Denis Rideau), mais aussi à Christian Kriso, Omar Saket, Adrian Camiolo et Yassine Oussaiti. Un merci particulier à Gaspard Hiblot également, qui fait partie de la team, mais aussi des collègues des III-V. Pour continuer du côté de ST, je remercie les collègues de TCAD: Sébastien G.G., Floria Blanchet, Frédéric Monsieur, Giacomo Garegnani, Olivier Nier, Sylvain Lioni, Assawer Soussou, Maurin Douix, Komi Ewuame, Yvan Denis, Clément Sart, Aurélie Juncker, Alizée Costard, Vincent Fiori, Guillaume Marchand, Clément Tavernier, Roberto Gonella. Les arrivées plus récentes: Nicolas Guitard, Christelle Buj, Thomas Cabout, Benjamin Vianne, Axel Pic, Idir Raid. Mais également les amis d'autres équipes: Matteo Causo, Benjamin Cabanes, Arthur Arnaud, Jihane Boughaleb, Loic Gaben, Alexia Valery, Segolene Gourat, Loic et Carole Martel, Benoit Legoux, Tuan, Krishna, Evan, Charly, ...

Pour la team *TB\_Sim*, un grand merci à Jing Li, Yann-Michel Niquet, ZaiPing Zeng et Léo Bourdet (et bien sûr François Triozon et Christophe Delerue). Un merci particulier à Jing Li qui fait partie de l'équipe, mais aussi des amis de l'évent team. Pour continuer du côté du CEA, je remercie les collègues du LSM: Benoît Sklénard, Philippe Blaise, Anthony Payet, Anouar Idrissi, Alberto Dragoni, Eamon McDermott, Kevin Morot, Hélène

Jacquinet, Sébastien Martinie, Sébastien Guarnay, Jean-Charles Barbé, Marie-Anne Jaud, Joris Lacord, Pierrette (bonne retraite), Pascal Scheiblin, Olga Cueto. Une pensée pour François de Crécy et Gilles Lecarval, qui nous ont quittés pendant cette thèse. Merci à la team “III-V”: Mathilde Billaud, Blend Mohamad, Julien Duvernay, Zdenek Chalupa, Hervé Boultry, Mickaël Cassé, Charles Leroux, Felipe Costantini, Maxime Bizouerne, Philippe Ferrandis, Gautier. Merci également aux amis d’autres équipes: Andréina Liendos, Matthias Alemany, Ivan Duchemin, l’*event team* du C5.

Merci aux collègues de l’AnR *noodles*: Marc Bescond, Quentin Rafhay, Marco Pala, Alessandro Cresti, Evelyne Lampin, Nicolas Cavassilas. Ainsi qu’aux collègues de Lille: Didier Stievenard, Isabelle Lefebvre, Bruno Grandidier, Kodjo, Sergio.

Un grand merci aux amis grenoblois qui ne rentrent pas dans les cases plus hauts: André Fonteles et Lya Sudario, Nicole Silva, Sayo et Mopelola Loto, Alva et Elsa Bruun, HongCam Hoang, Laura Barboza, Germercy Paredes et Julien Armando, ZhiHua Fang, Yu Fu, JiaYin Guan, Maya et Antonio Gasperini, Victoria Tovpeko, Howard Diehl, Abror Karimov, Johannes Stroebel, Emma Reavley, Ruben Lopez, le *small group* (dont Simona Preiksaite, Aurélien et Elizabeth Gabriele, Jessica Selim, Livi Fogas, Paola Gjekushi, Kolade, Dorothy Kim), ICG, les volleyeurs du parc Mistral.

Je prends le temps d’inclure les amis du LAAS dans ces remerciements: Fuccio Cristiano, Richard Monflier et Richard Daubriac, que j’ai eu la chance de connaître lors d’un post-doc éclair, en début de préparation de la soutenance.

Je consacrerai finalement le dernier paragraphe aux amis plus anciens, collègues de master et bachelor, qui ont toujours été présents sur la route et continuent à l’être. Les amis de Nice, qui n’ont pas cessé de m’ouvrir l’esprit vers la beauté de la physique: François Gustave, Martin Monloubou, Bruno Garbin, Amandine Cossetini, Hugo Thomas, Manu ShenRyuLaw, Imane Meziane Tani, Ana Magaly Sanchez Palencia. Les collègues du LMSC à l’EPFL, qui m’ont transmis la passion des III-V et du monde des nanofils: Anna Fontcuberta i Morral, Carlo Colombo, Eleonora Russo-Averchi, YY, Julien, Anna Dalmau, Daniel Rüffer, Martin Heiss. Les collègues de l’EPFL: Eugène Mikheev, Yannick Fontana, RuiNing Wang, Raphaël Meyer. Les amis de l’ULCO: Momo ElRohm, Manu, Christian, Kevin, YaoChen. Sans oublier les amis suisses et d’ailleurs: Jayjay et Nath, OLo et Lucie, Vince et Blandine, Timo et Anne, Jo’, WaiTeng Luen, Diana Duong. Un merci à la famille genevoise, niçoise et argentine. Merci encore à tous ceux que je n’ai pas eu le temps de nommer ici.

Un énorme merci finalement à ma famille pour le soutien dans les moments difficiles. Merci à ma soeur Aline, ma tante Sylvie, et mes grands-parents. Un merci particulier à ma maman qui m’a toujours soutenu et pour le trajet jusqu’à Lille pour la soutenance!

书山有路勤为径，  
学海无涯苦作舟。<sup>1</sup>  
韩愈

“As a man who has devoted his whole life to the most clear-headed science, to the study of matter, I can tell you as a result of my research about the atoms this much: there is no matter as such! [...]”  
Max Planck

---

<sup>1</sup>Partial translation: there is no royal road for learning [379], diligence is the path to the mountain of knowledge [378].



# Contents

Abstract . . . . .	ii
Résumé en français . . . . .	iv
Remerciements . . . . .	vi
List of acronyms and abbreviations . . . . .	xiii
<b>Context of the thesis</b>	<b>1</b>
III-V MOSFETs . . . . .	2
Simulation tools . . . . .	2
Objectives . . . . .	6
<b>1 Band structure</b>	<b>7</b>
1.1 Band structure in bulk materials . . . . .	9
1.1.1 Resolution of the stationary Schrödinger equation . . . . .	10
1.1.2 <i>Ab initio</i> methods . . . . .	10
1.1.3 Empirical pseudo-potential method (EPM) . . . . .	11
1.1.4 Tight-binding (TB) . . . . .	13
1.1.5 $\mathbf{k} \cdot \mathbf{p}$ theory (KP) . . . . .	14
1.1.6 Si and Ge band structure . . . . .	17
1.1.7 GaAs and InAs band structure . . . . .	19
1.1.8 Alloys: random supercell versus virtual crystal approximation . . . . .	26
1.1.9 Stress influence on band structure . . . . .	31
1.2 Band structure in nanostructures . . . . .	35
1.2.1 Confinement effect on band structure . . . . .	35
1.2.2 GaAs and InAs thin films . . . . .	41
1.2.3 III-As and SiGe nanowires . . . . .	46
1.3 Conclusion of the Chapter . . . . .	49
<b>2 Electrostatics and trap dynamics</b>	<b>50</b>
2.1 Capacitance of ideal MOS devices . . . . .	50
2.1.1 Modeling strategy . . . . .	50
2.1.2 Quantum and non-parabolic effects on $C(V)$ . . . . .	54
2.1.3 Bulk MOSCAPs . . . . .	55
2.1.4 Ultra-Thin Body and BOX (UTBB) MOSCAPs . . . . .	59
2.2 Capacitance with defects . . . . .	63
2.2.1 Point defects in III-As/oxide structures . . . . .	64

2.2.2	Influence of traps on electrostatics and capacitance . . . . .	67
2.2.3	Model . . . . .	70
2.2.4	Comparison with experiment . . . . .	74
2.3	Conclusion of the Chapter . . . . .	78
<b>3</b>	<b>Semi-classical transport</b>	<b>79</b>
3.1	Low-field mobility . . . . .	80
3.1.1	Linearization of Boltzmann transport equation . . . . .	81
3.1.2	Scattering rates within KP models . . . . .	85
3.1.3	Mobility in planar thin films . . . . .	94
3.1.4	Scattering rates within TB models . . . . .	101
3.1.5	Mobility in nanowires . . . . .	103
3.2	Saturation velocity . . . . .	108
3.2.1	Methodology: resolution of Boltzmann transport equation (BTE) . .	109
3.2.2	Si nanowires . . . . .	110
3.2.3	SiGe nanowires . . . . .	114
3.3	Conclusion of the Chapter . . . . .	116
<b>4</b>	<b>Device simulation and quantum transport</b>	<b>117</b>
4.1	Devices solvers . . . . .	117
4.1.1	Overview of models . . . . .	117
4.1.2	Quantum-drift diffusion (QDD) . . . . .	120
4.1.3	Non-equilibrium Green function (NEGF) . . . . .	126
4.2	Poisson-Schrödinger-based QDD: linear regime . . . . .	131
4.2.1	Device considered: FDSOI PMOS architecture . . . . .	131
4.2.2	Charge confinement: Poisson-Schrödinger vs Density-Gradient . . .	132
4.2.3	Mobility: empirical models vs Kubo-Greenwood . . . . .	134
4.3	NEGF vs QDD: saturation regime . . . . .	138
4.3.1	Extraction of parameters from NEGF . . . . .	139
4.3.2	Saturation mechanisms . . . . .	142
4.3.3	QDD model: mobility extraction at high-field . . . . .	144
4.3.4	Ballistic effects: quantum resistance and injection velocity . . . . .	147
4.4	Conclusion of the Chapter . . . . .	150
<b>5</b>	<b>General conclusion of the thesis</b>	<b>152</b>
5.1	Summary . . . . .	152
5.2	Contributions . . . . .	154
5.3	Perspectives . . . . .	154
<b>A</b>	<b>Parameters for band structures models</b>	<b>157</b>
A.1	<b><math>\mathbf{k} \cdot \mathbf{p}</math> models</b> . . . . .	<b>157</b>
A.1.1	<i>Low order</i> models . . . . .	157
A.1.2	<i>High order</i> models . . . . .	162
A.2	NL-EPM model . . . . .	166
A.3	TB models . . . . .	167

<b>B Non-radiative multiphonon theory</b>	168
B.1 Vibrational overlap . . . . .	169
B.2 Electronic overlap . . . . .	171
B.3 Derivation of MPA model: resolution of electronic overlaps . . . . .	172
<b>C Derivation of the POP momentum relaxation time expression</b>	174
<b>D Intervalley transitions in III-V: deformation potential</b>	177
<b>Bibliography</b>	181

## List of acronyms and abbreviations

MOS	Metal Oxide Semiconductor
FET	Field Effect Transistor
FDSOI	Fully Depleted Silicon-On-Insulator
UTBB	Ultra-Thin Body and BOX
TFET	Tunnel Field Effect Transistor
MOSCAP	Metal Oxide Semiconductor Capacitance
CMOS	Complementary Metal Oxide Semiconductor
TCAD	Technology Computer Aided Design
NW	Nanowires
SC	Semiconductor
BZ	First Brillouin zone
DFT	Density Functional Theory
EPM	Empirical Pseudopotential Method
NL-EPM	Non-Local Empirical Pseudopotential Method
LCBB	Linear Combination of Bulk Bands
LCAO	Linear Combination of Atomic Orbitals
TB	Tight Binding
KP	$\mathbf{k} \cdot \mathbf{p}$ method
EMA	Effective-Mass Approximation
NP-EMA	Non-Parabolic Effective-Mass Approximation
VCA	Virtual Crystal Approximation
DOS	Density-Of-States
CBE	Conduction-Band Edge
MPA	Multi-Phonon Approximation
WFP	Wave-Function Penetration
EOT	Equivalent Oxide Thickness
BTE	Boltzmann Transport Equation
RTA	Relaxation Time Approximation
KG	Kubo-Greenwood formula
PS	Poisson-Schrödinger
DG	Density-Gradient
QDD	Quantum Drift Diffusion
QTBM	Quantum Transmission Boundary Matrix
NEGF	Non-Equilibrium Green's Function
MS	Modespace
MSMC	Multi-Subband Monte Carlo
VFF	Valence-Force Field
POP	Polar-Optical Phonon
PH	Phonon
SR	Surface Roughness
LC	Local Coulomb
RC	Remote Coulomb
AD	Alloy Disorder
SDT	Source-Drain Tunneling

# Context of the thesis

As the miniaturization of conventional low-power Complementary Metal Oxide Semiconductor (CMOS) devices has recently been slowing down, numerous alternatives have been introduced in order to continue to gain in performances. These alternatives include Fully-Depleted Si-On-Insulator (FDSOI) and FinFET architectures, high- $\kappa$  gate oxide and SiGe source and drain regions.

However, regardless of these innovations, the physical size of the transistor will soon face a limit, as seen in the last International Technology Roadmap for Semiconductors (ITRS) report in 2015, that predicted the end of the scaling in 2021, with a gate length of 10 nm [60, 140]. Moreover, the unit cost of the transistor has already plateaued since the 28 nm node and with the introduction of FinFET architecture in the roadmap [262].

Fortunately for research, a number of challenges/unknowns remain and these innovations bring new physical phenomena that require advanced fundamental studies. One main challenge is the heat evacuation and, in a more general picture, the power consumption. The reduction of the power consumption is particularly interesting for new applications in area such as Internet of Thing, but also for the sake of power efficiency and lower ecological impact. The main target for the reduction of the power consumption is the reduction of the supply voltage  $V_{dd}$ . Therefore, potential candidates, including Tunnel Field Effect Transistors (TFET) architecture and Ge and III-V channels materials, are intensively studied for the future technological nodes.

One way to reduce the  $V_{dd}$  is to reduce the subthreshold swing (SS), theoretically limited by thermionic effects to a minimum value of 60 mV/dec in conventional architectures. TFET architecture, based on quantum tunneling effect, can potentially reach lower SS values, but faces numerous challenges and is not ready for mass production. Another way to decrease the  $V_{dd}$  is to increase the ON-current, through the use of boosters and high-mobility materials. In this view, InGaAs and SiGe materials are potential candidates to replace Si as channel materials, due to their higher electron and hole mobility, respectively.

At the beginning of this PhD, SiGe materials were considered as potential candidates for channel materials for p-type MOSFETs, in order to increase the ON-current through stress engineering (in addition to source/drain stressors), and also to adjust the threshold voltage. At the time of writing this document, while 14 nm FinFET remains with Si channel, 22 nm FDSOI devices with SiGe channels are being introduced in the market by GlobalFoundries [377] and SiGe channels are considered as viable solution for FinFET at the 10 nm node [122].

---

## III-V MOSFETs

For n-type MOSFETs, III-V materials (particularly InGaAs alloys) were also considered as potential candidates for low-power logic in future nodes, and were expected for a long time to enter the market [380, 376]. Working InAs transistors can be found in the literature from as early as in 1966 [40] and GaAs integrated circuits have been commercialized in the 1980's [131, 77]. More recently, InGaAs MOSFETs with good performances have been reported in 2008 [394], followed briefly by the demonstration of III-V nanoscale devices close to the state-of-the-art by Intel in 2009 [293], 2010 [295] and 2011 [294].

At the beginning of this PhD, a broad variety of architectures and solutions for III-V MOSFETs were presented at the IEDM conference in 2013, going from planar devices [185, 5] to Trigate [139, 169, 170] and 3D nanowires arrays [355, 405]. At the time of writing this document, InGaAs MOSFETs are still considered as potential candidates and numerous papers continue to be published in this topic. However, as stated by del Alamo in Ref. [66], “progress in recent times has been brisk, but much work remains to be done before III-V CMOS can become a reality”. Indeed, while the progress of the process technologies resolved some issues, some major problems remain, such as: i) their interfaces with oxide, ii) the high contact resistance, iii) the co-integration of III-V nMOSFETs on 300 mm CMOS production line, iv) their cost, v) the high variability and vi) contamination issues.

Aside from these process issues, intrinsic limitations can also occur in nanoscale devices and it is thus not clear whether ideal InGaAs MOSFETs can outperform Si MOSFETs in the architectures of the 14, 10 or 7 nm nodes. On the one hand, InGaAs MOSFETs should operate close to the ballistic limit, where their high injection velocity would be a good advantage. On the other hand, their low density-of-states and degraded electrostatic integrity (due to their high dielectric constant) would require multi-gate architectures. The increased tunneling probability due to their low effective mass would also limit the minimum gate length.

In light of these uncertainties and the broad range of solutions and architectures, simulation studies are necessary to help define the roadmap and to predict the performances of III-V MOSFETs in future nodes. In the last few years, several numerical studies aimed at comparing InGaAs with strained-Si and Ge technologies for the 10 and 7 nm nodes, using a broad variety of different approaches, such as quantum transport with [199] or without scattering [271, 167], Monte Carlo approaches [191, 87], quantum-corrected drift-diffusion [150, 317] and compact modeling [18, 134].

These numerous studies show the difficulty to model nanoscale transistors in a predictive manner, considering different channel materials and device architectures. In the following section, we briefly introduce the different simulation tools available and numerical challenges to simulate nanoscale devices.

## Simulation tools

In a broad overview, devices simulation tools can be divided on the basis of two factors: the accuracy of their description of the electronic structure, and the models used to describe the transport and scattering interactions.

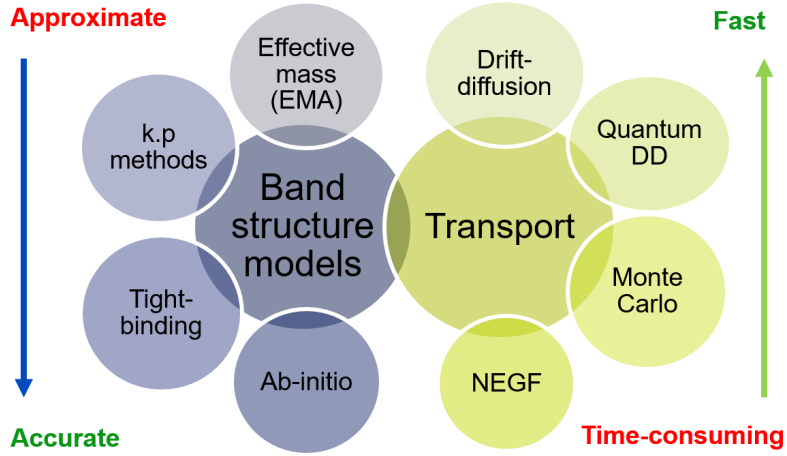


Figure 1. Schematic of the two types of descriptions needed in a device solver and examples of models. When going from up to down, both the accuracy and the computation cost tend to increase.

On the first aspect, the band structure description may vary from accurate and time-consuming *ab initio* codes to approximate and efficient effective-mass or classical solvers, as sketched in Fig. 1. The accuracy of the semi-empirical approaches depends on the set of fitting parameters used, that need to be extracted from *ab initio* simulations or from experimental data. These parameters are usually provided by reference papers in the literature for most common semiconductors, as detailed in Sec. 1.1.7 of Chapter 1.

On the second aspect, the transport description may go from full-quantum solvers based on the Non-Equilibrium Green Function (NEGF) formalism, to classical Drift-Diffusion (DD) solvers based on the moments of the Boltzmann transport equation (BTE).

Although many groups are working on numerical models and it would be vain to provide a complete and exhaustive list of existing codes, some groups are particularly active in the microelectronics domain and their codes can be considered as references. Commercial tools used in Technology Computer Aided Design (TCAD) framework are usually based on “fast” methods such as Drift-Diffusion. These tools include: **Sentaurus Device** suite by Synopsys [213] and **Minimos-NT** from GlobalTCAD solutions [112] (recently acquired by Sylvaco Group [323]).

More accurate codes are available in academic groups, usually requiring heavier computational resources (super computers in many cases). These state-of-the-art solvers include quantum solvers based on the NEGF formalism and Multi-Subband Monte Carlo (MSMC) solvers. For the NEGF codes, one can name: **NEMO5** [243] and **NanoMOS** [241] from G.Klimeck’s and M.Lundstrom’s group at Purdue University, **OMEN** from G.Klimeck’s group at Purdue and M.Luisier’s group at ETHZ of Zürich [261], the code of M.Pala at IMEP-LaHC in Grenoble [61] and **TB\_Sim** from Y.M.Niquet and F.Trioizon at CEA-LETI and C.Delerue at IEMN-Lille [381]. For the MSMC codes, one can name the code of D.Esseni, P.Palestri and L.Selmi at the University of Udine [365] and the code of F.Gamiz’

---

group at the University of Granada [364]. Moreover, particle or ensemble Monte Carlo codes are also used, such as **MONACO** from A.Bournel and P.Dollfus at IEF-Paris [230], **GARAND** from Gold Standard Simulations (GSS) and A.Asenov’s group at the University of Glasgow [104] and **Archimedes GNU** from J.M.Sellier at Purdue [12]. Finally, “bulk” Monte Carlo codes, used to derive transport properties of bulk material, include: **Damocles** developed by M.Fischetti and S.E.Laux at IBM/Stanford [63] and **Sparta** from F.Bufler at Synopsys/ETHZ [333].

These advanced solvers are very often needed to model nanoscale MOSFET transistors in a predictive manner, as conventional TCAD solvers used in industry are based on too simplified models and face several issues [280]. However, their high computational cost makes advanced solvers difficult to use in an industrial framework, without access to a super-computer. Therefore, compromises need to be investigated to improve the physical models and accuracy of TCAD solvers, while keeping their computational cost low, in order to remain compatible with an industrial framework.

Among physical phenomena emerging in nanoscale transistors that need to be accounted for in simulation tools, one can quote:

- Quantum confinement effects, along the MOS structure (leading to dark-space, sub-bands creation and increase of the band gap);
- Quantum tunneling through the gate oxide, inducing gate leakage;
- Quantum tunneling along the transport direction (source-drain tunneling and band-to-band-tunneling), hindering the OFF-current;
- Quasi-ballistic current, as a percentage of carriers flow across the device without any scattering.

Moreover, to simulate channels made of alternative materials (InGaAs and SiGe), additional effects need to be accounted for, such as:

- The multivalley character of the conduction band structure of III-As and Ge materials, as well as the non-parabolic dispersion of the lowest valley at the  $\Gamma$  point;
- The low density-of-states of the conduction band and the high traps densities at the interfaces, influencing the electrical response (creation of inversion charge) as well as the transport (additional scattering);
- The new scattering mechanisms, intrinsic to these materials, such as alloy disorder and polar-optical-phonons.

Since standard models in TCAD tools usually rely on a classical density-of-states expression based on a single isotropic effective-mass (drift-diffusion model), several “empirical” corrections must be included to account for the effects listed above (in particular the satellite valleys population and non-parabolicity of InGaAs materials). To avoid empirical models and to improve the predictive power of TCAD tools, physical-based models can be included instead [112], closing the gap between academic advanced solvers and conventional TCAD solvers. The predictive tools that will be discussed in this work include the resolution of the Schrödinger equation, coupled with physical models to derive the transport parameters, such as the low-field effective mobility.

---

## Tools used in this work

In this work, two existing codes were used: `UTOX`, developed at STMicroelectronics by D.Rideau and `TB_Sim` developed at CEA by Y.M.Niquet and F.Triozon and at IEMN by C.Delerue.

`UTOX` is a code developed at STMicroelectronics in two different versions. Its Matlab version includes the resolution of the Schrödinger equation in bulk materials and thin films in the KP, TB and EPM approaches, together with valence force field models for phonons. This version is used to model the materials properties in the bulk or in nanostructures (such as the optical response and density-of-states). Another version, written in C/C++, includes 1D (`UTOXPP`) and 2D (`U2OXPP`) Poisson-Schrödinger solvers, both linked to a Graphic User Interface coded with the Qt-designer package. This version is used to model the characteristics of planar devices (e.g., electrostatics, effective mobility and electrical current). The `U2OXPP` package includes a Quantum-corrected Drift-Diffusion solver, that can be used to model the current flowing in a MOSFET device. A schematic of a 2D simulation is shown in Fig. 2.

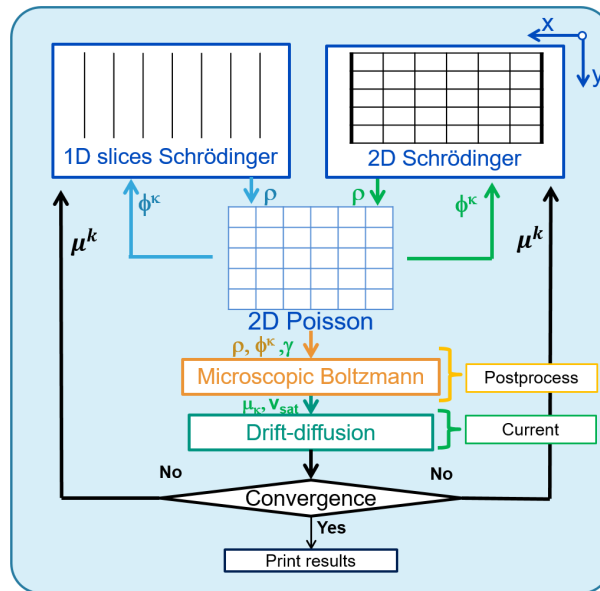


Figure 2. Schematic of self-consistent loops in the `U2OXPP` solver.

`TB_Sim` is a code developed at CEA and IEMN in Fortran 90, including different modules that can be used as tool boxes to build advanced codes. These modules include sparse matrix format, efficient numerical algorithms for the resolution of linear systems and eigenvalues equations, 1D, 2D and 3D Poisson and Schrödinger solvers within the KP and TB approaches, energy relaxation within valence force field models, as well as tools for the calculation of optical properties and resolution of the Boltzmann transport equation. It also includes a geometrical NEGF solver that can be used to model the current in 3D devices with an accurate description. Its cutting-edge parallel performances allow heavy

---

simulations to run on super computers with good efficiency.

These two codes are often complementary and the cross-comparison of the results with both codes allows benchmarking and validation of the numerical implementations, as well as physical approximations.

During this PhD, new models have been implemented in these two codes. These models include for `UTOXPP`: non-parabolic EMA, 8-band and extension of the full-band KP models, polar-optical phonon scattering, resolution of 2D Schrödinger equation with open and close boundary conditions and inclusion of phonon in a mode-space approach (see Sec. 5.2 and the dedicated Chapters for more details about the models). For `TB_Sim`, they include: non-parabolic EMA, polar-optical scattering in KP, atomistic alloy disorder scattering in TB, generalized VFF model for phonons and resolution of BTE at high-field.

## Objectives

The objective of this PhD is twofold: on the one hand, to investigate the physical properties of alternative materials and to compare different approaches for the band structure calculation; on the other hand, to participate in the development of an industrial simulation framework for advanced FDSOI architectures, and to propose solutions for the improvement of the prediction power of the conventional TCAD tools.

In this view, the strategy of the PhD was to build new codes and methodologies to account for the effects mentioned above in a “light” approach, compatible with an industrial TCAD framework. A variety of different approaches and models for the band structure is used and compared, giving an overview of numerical models. The manuscript is organized as follows.

In the first Chapter (1), the band structures of  $\text{In}_x\text{Ga}_{1-x}\text{As}$  (hereafter InGaAs) and  $\text{Si}_{1-x}\text{Ge}_x$  (hereafter SiGe) materials are first investigated, by means of commonly used empirical approaches, including EPM, TB, full-band KP and NP-EMA. The relevant parameters such as satellite valley position, effective masses and non-parabolic dispersion are extracted and discussed. The band structures and the confinement effects in InGaAs and SiGe thin films and nanowires are also discussed.

In the second Chapter (2), the capacitance of InGaAs bulk and UTBB MOSCAP devices is simulated with NP-EMA and TB models and the results with the different solvers are compared, for ideal devices without traps. The effects of non-parabolicity and satellite valleys are discussed in particular. In the second part of the Chapter, the knowledge of the traps distribution close to the interface with oxide is discussed, as well as the different models that are able to treat them.

In the third Chapter (3), the effective mobilities of InGaAs and SiGe bulk and thin films are investigated with KP models and the linearized Boltzmann transport equation. The effective mobility and high-field drift velocity of SiGe nanowires are also investigated with TB models.

Finally, in the fourth and last Chapter (4), two Quantum Drift-Diffusion (QDD) approaches are presented, and used to model the characteristics of a template Si FDSOI device. The results are also compared with full-quantum solver (NEGF).

# Chapter 1

## Band structure

The knowledge of the electronic band structure is the first brick which numerical models are built on. As opposed to Si, the conduction band of Ge and many III-V materials presents local minima (so-called *valleys*) at different symmetry points in the Brillouin zone that can potentially contribute to the electronic transport, as depicted in Figure 1.1. The accurate knowledge of the position of the satellite valleys and their effective mass is thus relevant to transport, as well as their dependence on stress and confinement. Moreover, the band structure of III-V materials close to the conduction band minimum at the  $\Gamma$  point is generally non-parabolic, which makes the simple parabolic effective mass approach fail at moderate inversion.

For these reasons, a first part of this work is devoted to the study of bulk band structure and the extraction of relevant parameters through different physical models, such as the Empirical Pseudo-potential Method (EPM), the Tight-Binding (TB) method and the full-band  $\mathbf{k} \cdot \mathbf{p}$  (KP) models. Although these models rely on empirical parameters fitted to match the bulk experimental and/or first-principle band structure and effective masses, they make use of different physical description and can be used in nanostructures to describe the variation of the band structure with confinement, stress or alloy composition.

In this Chapter, we study the band structure of InGaAs and SiGe materials based on these empirical models. We first present the models and the associated physical approximations. For a more complete description of these models, further information is found in reference books about solid-state physics such as [13, 398, 83, 151] as well as more specific references in the following sections. In-house existing codes are used to compute the band structure with EPM, TB and KP models, with parameters taken from the literature and eventually adapted. In particular, parameters for full-band KP models are extracted for InAs and GaAs. Quantities such as effective mass, band gaps and density-of-states are deduced from these studies and compared with recent papers based on *ab initio* techniques. The treatment of disordered alloys and the description of stress are finally discussed.

In the second part, we apply these models to confined nanostructures, such as thin films and nanowires and study the influence of confinement on the band structure and electronic properties. The Effective-Mass Approximation (EMA) and 8-band KP models are discussed and compared to atomistic TB. In particular, the different models to include non-parabolic corrections in EMA (NP-EMA) are studied. These models are used in the

other Chapters to compute the carrier mobility and transport in devices.

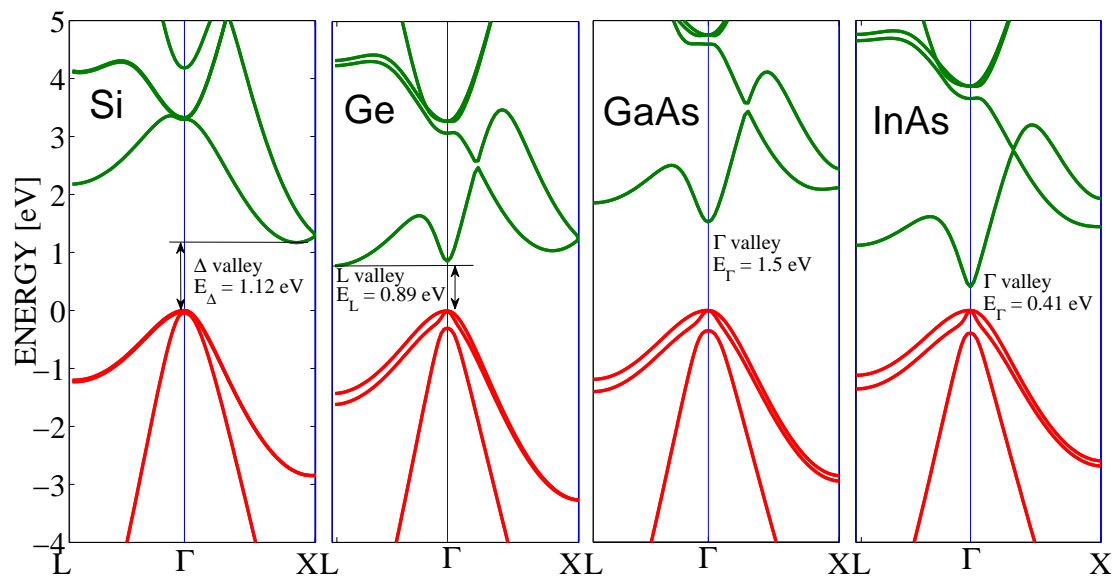


Figure 1.1. Band structures of materials studied in this work: Si, Ge, GaAs and InAs, obtained with NL-EPM model in UTOX with parameters from Ref. [51] (see text in Sec. 1.1.7) reproducing experimental gaps and masses. Conduction bands are shown in green, while valence bands are in red.

## 1.1 Band structure in bulk materials

Let us first introduce the concept of “band structure” in a bulk material. In perfect crystals, atoms are ordered periodically without defects and the wavefunction has the form of Bloch waves [13, 398]:

$$\psi_{n\mathbf{k}}(\mathbf{r}) = \frac{1}{\sqrt{\Omega}} u_{n\mathbf{k}}(\mathbf{r}) e^{i\mathbf{k}\mathbf{r}} \quad (1.1)$$

where  $u_{n\mathbf{k}}(\mathbf{r}) = u_{n\mathbf{k}}(\mathbf{r} + \mathbf{R})$  is a periodic function rapidly oscillating with the period of the crystal ( $\mathbf{R}$  is a Bravais lattice vector,  $\mathbf{r}$  is a real space vector,  $n$  is a quantum number indexing the eigenstates and  $\mathbf{k}$  is the wavevector of the state). In reciprocal space, the periodicity of the crystal is depicted by a primitive cell that can be repeated in all directions, namely the First Brillouin Zone (BZ).

In the case of Diamond and Zinc-Blende structures (the most stable crystalline structure of Si and bulk III-As respectively), the crystal is composed of two face-center cubic lattices imbricated together. The Wigner-Seitz cell (which is the smallest pattern from which the infinite crystal can be reconstructed) depicted in Fig. 1.2(left) is composed of two atoms. The bulk BZ in this case is shown in Fig. 1.2(right), together with high symmetry points of the  $O_h$  point group (see, e.g., Ref. [13]).

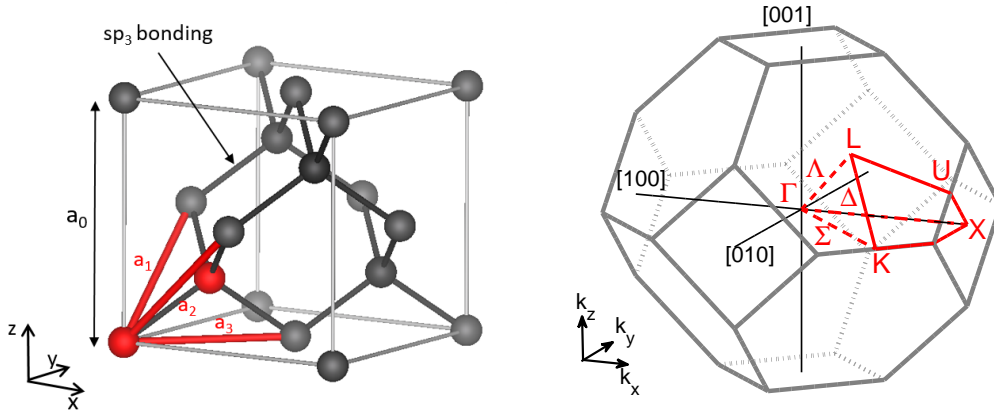


Figure 1.2. Left: Cubic cell of Silicon (Diamond structure). Atoms forming the Wigner-Seitz cell are highlighted in red, while Bravais vectors are noted  $a_1$ ,  $a_2$  and  $a_3$ .  $a_0$  denotes the lattice constant. Right: First Brillouin Zone of Diamond and Zinc-Blende crystallographic structures.

The energy dispersion of the system plotted on the BZ is called hereafter “band structure” and describes the available energy levels for each wavevectors  $\mathbf{k}$  (in other words, the eigenvalues of the crystal Hamiltonian). It can be computed from the resolution of the Schrödinger equation, following some approximations that will be described in this Chapter.

### 1.1.1 Resolution of the stationary Schrödinger equation

All properties of solids are in principle described by the many-body Schrödinger equation:

$$\{H_e + H_L + H_{eL}\} \psi = E\psi \quad (1.2)$$

where  $\psi$  is the many-body wavefunction and the Hamiltonian operators account for electron  $H_e$ , ion  $H_L$  and electron-ion  $H_{eL}$  contributions. This equation is unsolvable without further approximations.

First, as lattice ions have a mass of several orders of magnitude higher than electrons ( $\sim 10^{-27}$  versus  $10^{-30}$  kg), we can consider the electrons moving very fast compared to ions. This is the so-called Born-Oppenheimer (or “adiabatic”) approximation. In this approximation, Equation (1.2) is separated into two equations:

$$(T_e + V_{ee} + V_{eL})\phi = E_e\phi \quad (1.3)$$

$$(T_L + V_L + E_e)\chi = E\chi \quad (1.4)$$

where  $\psi \equiv \phi\chi$ ,  $T_e$  and  $T_L$  are the kinetic energy of electrons and lattice ions, respectively;  $V_{ee}$ ,  $V_{eL}$  and  $V_L$  are the potential energy stemming from electron-electron, electron-ion interaction and ionic potential, respectively. The first equation describes the electronic part of the problem, which needs to be solved to obtain the band structure. We will discuss different approaches to treat electron-ion interactions in more details in Chapters 2 and 3, for the calculation of the lattice relaxation effects during capture and emission of carriers on point defects (so-called multiphonon models) and electron-phonon scattering mechanisms in transport.

Second, while many-body Hamiltonian can be used to compute the electron-electron interactions [211, 219, 68], the problem is very soon intractable even for a few electrons. For this reason, electrons are usually considered as independent, leading to a single particle problem. The interactions of a single electron with the others is then treated in a mean-field approximation, through a potential term  $V_s$ . The single-particle Hamiltonian thus becomes:

$$H = \frac{\hat{p}^2}{2m_0} + V_s(\mathbf{r}) \quad (1.5)$$

where the first term is the kinetic energy of free electrons with mass  $m_0$  and momentum  $p$  and  $V_s(\mathbf{r})$  is the screened potential energy of the crystal (accounting for interactions with lattice ions, core and valence electrons).

However, even after these important approximations, the problem of solving electronic band structure from the Schrödinger equation remains very heavy without further *a priori* hypothesis on the wavefunctions and atomic potential of the system. The different hypotheses of the main models used in solid state physics will be introduced briefly in the following subsections.

### 1.1.2 *Ab initio* methods

As their name indicates, *ab initio* (or equivalently first principle) methods allow the computation of the fundamental electronic states with no fitting parameters. Popular *ab initio* codes are based on the Density-Functional Theory (DFT) leading to the Kohn-Sham

Hamiltonian, describing non-interacting electrons in an effective potential (or mean-field) that includes the external potential and Coulomb interaction between electrons. In these models, the total energy of the system, including the exchange-correlation energy, is written as a *functional* of the electronic density  $E[\rho]$ . The density itself can be expressed as a function of the Kohn-Sham wavefunctions. Different functionals of the density can be used to describe the many-body exchange and correlation terms in a tractable way. The choice of the functional can influence the result. Moreover, the band gaps of semiconductors and insulators are usually underestimated by DFT. However, corrections can be applied through the Green function formalism (GW) or through newly developed Hybrid Functionals (e.g., HSE), that are able to reproduce experimental band gaps. To improve the efficiency of the calculation, core electrons are very often not included, but they are recast into a pseudo-potential.

As these methods are not developed, nor used intensively during this work, we will not go into further details. They, however, are very useful tools to obtain physical quantities hard to measure experimentally. We will thus compare our results with those from *ab initio* studies found in the literature whenever possible.

### 1.1.3 Empirical pseudo-potential method (EPM)

The theory of pseudo-potential is widely used in DFT to limit the number of electrons in the self-consistent calculations. It consists in replacing the strongly oscillating potential in the core region of the atom by a smooth pseudo-potential, associated with a pseudo-wavefunction. The pseudo-potential is chosen so that the pseudo-wavefunction matches the one of all electrons calculation far from the ions (at  $r > r_0$ ). The Empirical Pseudo-potential Method (EPM), on the contrary, aims at describing valence electrons. It resembles to *ab initio* pseudo-potentials, but only describes Fourier coefficients of pseudo-potential as empirical parameters whose values are fitted in order to reproduce the bulk band structure. It has been first developed in solids in the early 1960's and has been used in 1976 by Chelikowsky and Cohen [50, 51] to compute the band structure of several group IV and III-V semiconductors. This method describes the wavefunctions with a plane-waves basis, evolving in a periodic potential described by a few empirical parameters in the reciprocal space:

$$V_s(\mathbf{r}) = \sum_{\mathbf{G}} V(\mathbf{G})e^{i\mathbf{G}\cdot\mathbf{r}}$$

where  $\mathbf{G}$  is a reciprocal lattice vector and  $\mathbf{r}$  is a real space vector. The periodic part of Bloch function in Equation (1.1) is also expanded in plane waves:

$$u_{\mathbf{k}}(\mathbf{r}) = \sum_{\mathbf{G}'} A_{\mathbf{k}}(\mathbf{G}')e^{i\mathbf{G}'\cdot\mathbf{r}}$$

The Schrödinger equation becomes:

$$\frac{\hbar^2}{2m_0} A_{\mathbf{k}}(\mathbf{G})(\mathbf{k} + \mathbf{G})^2 + \sum_{\mathbf{G}'} V_{\mathbf{G}-\mathbf{G}'} A_{\mathbf{k}}(\mathbf{G}') = E_{\mathbf{k}} A_{\mathbf{k}}(\mathbf{G}) \quad (1.6)$$

where  $V_{\mathbf{G}-\mathbf{G}'}$  is given by:

$$V_{\mathbf{G}-\mathbf{G}'} = \frac{1}{\Omega} \int_{\Omega} d^3\mathbf{r} e^{-i\mathbf{G}\cdot\mathbf{r}} V_s(\mathbf{r}) e^{i\mathbf{G}'\cdot\mathbf{r}}$$

In the case of Zinc-Blende structure, the symmetry of the crystal helps to simplify this term, which can be expressed as a function of symmetric ( $V_s$ ) and anti-symmetric ( $V_a$ ) form factors, depending only on the norm  $G$  [398]:

$$V_G = V_s(G) \cos(G \cdot R) - iV_a(G) \sin(G \cdot R)$$

In this local model, only six local form factors at particular  $G$  are sufficient to describe the whole band structure when stress is not included (undeformed crystal). However the wavefunctions need to be expanded on a significant number of plane waves (typically  $\sim 200$  planes waves), leading to a relatively high numerical cost compared to other semi-empirical models. In addition, the approximation of local form factors is sometimes too restrictive to capture the electronic structure and a “non-local” EPM model has been introduced later [51], where the pseudo-potential are not only position dependent (through  $G$ ), but also energy-dependent (through the angular momentum  $l$ ). This correction allows a more accurate description of the band structure, but also adds a significant computational cost. Finally, spin-orbit interactions can be introduced using additional terms in the Hamiltonian, following the expression given in Potz and Vogl (1981) [289].

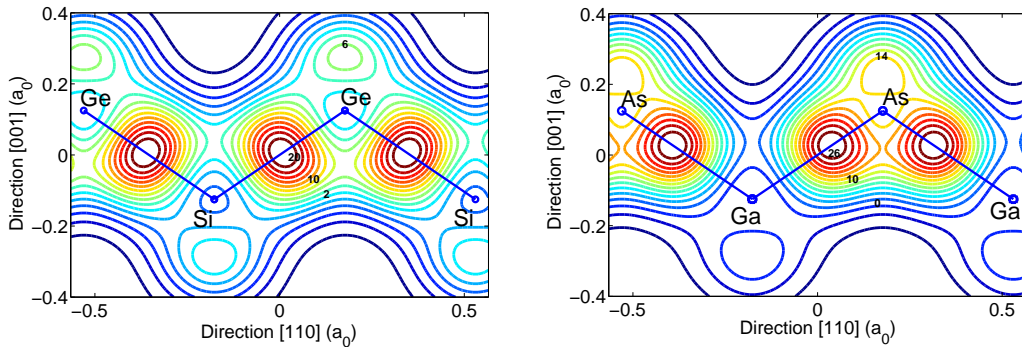


Figure 1.3. Charge density from  $3s^2$  and  $3p^2$  valence electrons in  $\text{Si}_{0.5}\text{Ge}_{0.5}$  (left) and  $\text{GaAs}$  (right) bulk crystals, obtained with local EPM model in the UTOX package and parameters from Refs. [50] and [54] respectively (see text in Sec. 1.1.7).

Although this method is expensive numerically when the size of the system increases, it is very efficient and accurate in bulk and small systems and gives a correct description of the band structure at high energy. For example, the band structure of Si, Ge, GaAs and InAs materials shown in Figure 1.1 were obtained with this method including “non-local” corrections, using the *in house* solver UTOX.

It is interesting to mention here that both the local atomic potential and the charge density of valence electrons can be recomposed in real space from this method. Figure 1.3

shows an isocontour plot of the charge density of  $3s^2$  and  $3p^2$  valence electrons in  $\text{Si}_{0.5}\text{Ge}_{0.5}$  ordered crystal and GaAs in the  $[1\bar{1}0]$  plane of the cubic crystal. We can observe that the valence charge is mainly located at the center of the  $sp^3$  bonds in SiGe and no ionic polarization is induced, while As atoms in GaAs attracts more valence charge, due to the electronegativity difference between the two atomic elements. This is the signature of a non-negligible ionic nature of the covalent bonding in III-As materials, which induces an ionic polarization and is responsible for the polar-optical phonon scattering that will be discussed in Chapter 3.

#### 1.1.4 Tight-binding (TB)

The empirical Tight-Binding (TB) theory comes from the idea that atomic orbitals can form a set of basis states on which crystal Bloch wavefunctions can be expressed. J.C.Slater and G.F.Koster popularized this method in 1954 named Linear Combination of Atomic Orbitals (LCAO) [327].

While the EPM projects the wavefunctions on plane waves, the TB method considers the problem from the opposite viewpoint, writing the wavefunctions as a LCAO. In this model, the crystal potential is written as:

$$V_s(\mathbf{r}) = V_{at}(\mathbf{r}) + \Delta V(\mathbf{r})$$

where  $V_{at}(\mathbf{r})$  is the potential of an isolated atom at  $\mathbf{R} = 0$ , and  $\Delta V(\mathbf{r}) = \sum_{\mathbf{R} \neq 0} V_{at}(\mathbf{r} - \mathbf{R})$  is the contribution of all other atoms ( $\mathbf{R}$  denoting the position of an atom in the lattice). The Bloch wavefunctions are written as:

$$\psi_{n\mathbf{k}}(\mathbf{r}) = \sum_{\beta, \eta} c_{\beta, \eta}^{\mathbf{k}, n} \frac{1}{\sqrt{N}} \sum_{\lambda} e^{i\mathbf{k} \cdot \mathbf{R}_{\lambda\beta}} \phi_{\eta}(\mathbf{r} - \mathbf{R}_{\lambda\beta}) \quad (1.7)$$

where  $\mathbf{R}_{\lambda\beta} = \mathbf{R}_{\lambda} + \tau_{\beta}$  is the position of the  $\beta^{\text{th}}$  atom in unit cell  $\lambda$ ,  $\phi_{\eta}(\mathbf{r})$  is the  $\eta^{\text{th}}$  orbital of an isolated atom and  $N$  is the number of unit cells. The eigenvalue Schrödinger problem (after projection on  $\langle \phi_{\eta, \lambda, \beta} |$  state) becomes:

$$\sum_{\lambda', \eta', \beta'} \left\{ \gamma_{\beta, \beta', \eta, \eta'}^{\lambda \lambda'} e^{i\mathbf{k} \cdot (\mathbf{R}_{\lambda' \beta'} - \mathbf{R}_{\lambda\beta})} \right\} c_{\beta', \eta'}^{\mathbf{k}, n} = (E_n(\mathbf{k}) - E_{\eta}) c_{\beta, \eta}^{\mathbf{k}, n} \quad (1.8)$$

where  $\gamma_{\beta, \beta', \eta, \eta'}^{\lambda \lambda'} = \langle \phi_{\eta, \lambda, \beta} | \hat{\Delta V} | \phi_{\eta', \lambda', \beta'} \rangle$ ,  $E_{\eta}$  is the orbital energy. The overlap terms between different orbitals  $\langle \phi_{\eta, \lambda, \beta} | \phi_{\eta', \lambda', \beta'} \rangle$  are neglected in TB model with an orthogonal basis [195, 151]. The term  $\gamma_{\beta, \beta', \eta, \eta'}^{\lambda \lambda'}$  can be further simplified by neglecting the three sites integrals [253]. The hopping integrals ( $\{\lambda, \beta\} \neq \{\lambda', \beta'\}$ ) are then given as:  $V^{\text{hop}} = \langle \phi_{\eta, \lambda, \beta} | V_{at}(\mathbf{r} - \mathbf{R}_{\lambda' \beta'}) | \phi_{\eta', \lambda', \beta'} \rangle$ . Finally, the crystal field integrals ( $\{\lambda, \beta\} = \{\lambda', \beta'\}$ ) and orbital energy are both incorporated into the on-site energy  $E^{\text{onsite}}$ .

In empirical TB,  $E^{\text{onsite}}$  and  $V^{\text{hop}}$  are fitting parameters.  $V^{\text{hop}}$  is usually restricted to nearest neighbors and only a few atomic orbitals per atom are considered. The two most common TB models in the literature are using either a  $sp^3$  basis extending coupling to the third nearest neighbors, or an  $sp^3d^5s^*$  basis accounting for first nearest neighbors only. The tenth orbital  $s^*$  in the last model was introduced to account for coupling to outmost

remote orbitals. This latter model will be used in this work. When spin-orbit coupling is introduced, the matrix size reaches  $20\times$  the number of atoms considered, making this model able to treat systems of several millions of atoms in a tractable way. Moreover the atomistic description in TB model makes it a suitable model for nanostructures, as the symmetry of the system is well described and reflected on the calculated electronic properties. As the atomic orbitals are not explicitly described, the knowledge of the local wavefunction and charge density are not available here.<sup>1</sup>

### 1.1.5 $\mathbf{k} \cdot \mathbf{p}$ theory (KP)

The  $\mathbf{k} \cdot \mathbf{p}$  (hereafter KP) theory comes from the work of J.M.Luttinger and W.Kohn, as well as E.O.Kane, in the 1950's to describe the valence and conduction band dispersion near the  $\Gamma$  point. It comes from the application of the perturbation theory to solve Schrödinger equation in a crystal around a point in the BZ.

When wavefunctions are taken as Bloch waves (Eq. (1.1)), Schrödinger equation can be written as:

$$\left\{ \frac{p^2}{2m_0} + V_s(\mathbf{r}) + \frac{\hbar^2 k^2}{2m_0} + \frac{\hbar}{m_0} \mathbf{k} \cdot \hat{\mathbf{p}} \right\} u_{n\mathbf{k}}(\mathbf{r}) = E_{n\mathbf{k}} u_{n\mathbf{k}}(\mathbf{r})$$

The Hamiltonian in bracket can be split into two parts: the first two terms are the Hamiltonian of the crystal at  $\mathbf{k} = 0$  and the last two terms include the  $\mathbf{k}$  dependency (note the term in  $\mathbf{k} \cdot \mathbf{p}$  appearing and giving the name to the method). Without loss of generality, one can write the eigenfunctions of the problem as a linear combination of the states at  $\mathbf{k} = 0$ :

$$u_{n\mathbf{k}}(\mathbf{r}) = \sum_m c_m(n, \mathbf{k}) u_{m0}(\mathbf{r})$$

The eigenvalue problem becomes:

$$\sum_m c_m(n, \mathbf{k}) \left\{ (E_{n0} - E_{n\mathbf{k}} + \frac{\hbar^2 k^2}{2m_0}) \delta_{nm} + \frac{\hbar}{m_0} \mathbf{k} \cdot \langle u_{n0} | \hat{\mathbf{p}} | u_{m0} \rangle \right\} = 0$$

The  $\mathbf{k}$ -dependent part of Hamiltonian can then be treated as a perturbation:

$$E_{n\mathbf{k}} = E_{n0} + \frac{\hbar^2 k^2}{2m_0} + \frac{\hbar^2}{m_0^2} \sum_{m \neq n} \frac{|\langle u_{m0} | \mathbf{k} \cdot \hat{\mathbf{p}} | u_{n0} \rangle|^2}{E_{n0} - E_{m0}}$$

Further, the number of basis states  $u_{n0}$  (or number of bands  $n$ ) are truncated to a few states. This truncation makes the basis incomplete and wavefunctions can be non-orthogonal. To solve this issue, remote bands have to be included in the derivation of the Hamiltonian, and a re-normalization of the basis set is then performed [195]. As expected, the more bands one explicitly treats, the more accurate the energy dispersion is described, but the computation also becomes more expensive (especially when confined structure are

---

<sup>1</sup>Note that DFTB models were also recently used to compute the electronic states of big systems with a description of the local density of charge, solving it self-consistently in an iterative way.

considered). For materials with indirect band gap, it is usually convenient to use reference basis function away from  $\mathbf{k} = 0$  point (for  $\Delta$  valleys in Si for instance), which is made in the widely used 2-band KP models for Si.

Several models have been derived during the years, for different materials and with different level of accuracy. These KP models can be divided into two categories: *low-order* models, used to describe the valence or conduction band in a small portion of the BZ and limited energy range, but that need only a few parameters and small matrix size and are therefore widely used in device solvers; and *high-order* models, which are more time-consuming and need a higher number of empirical parameters, but can describe the full-band dispersion, over the entire BZ. The full-zone KP models can reach the same order of accuracy as TB models for systems of the same size or even bigger, as they are “continuous” models and the size of the mesh can be adapted. However the truncated perturbative model doesn’t guarantee the periodicity of the band structure outside the first BZ and the continuous model doesn’t account for the symmetry breaking in nanostructures. This can be problematic when applied to confined structure, where “spurious” states can appear in the band gap, as it will be discussed in the second part of the Chapter.<sup>2</sup>

We give here a rapid overview of the different low-order and high-order KP models. For more details about the KP theory, the book of G.Fishman [95] gives a complete and broad discussion of the history and derivations of the main KP models.

### ***Low-order models***

The first KP model published was used to describe the valence band, containing three bands in bulk : so-called heavy holes (HH), light holes (LH) and spin-orbit split-off (SO) bands. The reader can refer to Refs. [75, 209] for more details about these models. For direct band gap materials such as III-As, the lowest conduction band can be added to this set, leading to a 4-band KP model where the coupling between valence and conduction bands in  $\Gamma$  is related to the optical parameter  $E_p$ . The reader can refer to Refs. [156, 19, 109] for reviews (see also Appendix A.1.1). This model allows a good description of the strongly non-parabolic  $\Gamma$  valley in these materials and has been used to derive expressions for the non-parabolic correction in EMA that are discussed in the second part of this Chapter. For the conduction  $\Delta$  valleys of Si, a 2-band model was later developed accounting for the coupling between the two closest  $\Delta$  equivalent valleys [129]. Compared to EMA, this model improves the description of  $\Delta$  valleys at high energy, in particular its non-parabolic character and can correctly describe the splitting of these valleys with stress [340].

In device and transport solvers, low-order KP models are probably the most widely used, due to their low computational cost and ease of implementation. They are thus very useful especially at low bias where carriers mainly lie close to the band edge (typically up to  $\sim 5 \times k_B T$  away from the band edge). However for high-field transport, carriers

---

<sup>2</sup>These spurious states appear in models where both negative and positive band dispersions are taken into account (such as 8-band or full-zone KP models) and are coming from remote  $\mathbf{k}$  states that are projected in the 2D/1D Brillouin zone.

are accelerated to higher energies, where low-order KP models fail to describe the band structure [228].

Note that the simplest KP model is the Effective-Mass Approximation describing the energy dispersion of a single band by the expression  $E(k) = \frac{\hbar k^2}{2m^*}$ . This expression is similar to the kinetic energy of free electrons, where the electron mass has been replaced by an effective parameter  $m^*$  where all the interactions with the crystal are hidden.

### **High-order models**

The models presented above are only describing the band structure close to a specific point in the BZ, but fail to describe the band structure over the entire BZ and at high energy. Full-zone KP models were later developed in 1966 by F.Pollak and M.Cardona [45], who extended the models to a higher number of basis states in  $\Gamma$ . These models were later extended to account for strain [35, 304, 229]. Although 30 bands were originally used, accounting for [000], [111] and [200] nearly-free electron states (see Refs. [398, 45] and Fig. 1.4), different models were also developed accounting for 12, 14, 16 or 20 bands [95], providing a wide range of models and accuracies, as well as parameters. Unfortunately, among this wide range of models, only very few studies with reference parameters for both GaAs and InAs were found [310, 299, 286]. For this reason, a parameterization of full-band KP models for InAs and GaAs materials has been performed that will be presented in the next section [237]. In this work, we extracted parameters for InAs and GaAs for the 30-band models, but also a 54-band model that will be described in more details below.

#### 54-band KP model

As said earlier, full-band KP models were first derived accounting for the 15 states corresponding to free-electron states with wavevectors [000], [111] and [200] [286, 304, 299], leading to a 30-band model. This allows a good description of the band structure in most of the high symmetry  $\mathbf{k}$  points. However, at the particular K symmetry point, the states with [220] free-electron wavevector lie at low energy and affect the local minimum, which is poorly described by the 30-band KP model, where an additional smoothing function had to be used to adapt the parameters near this point in previous works [304].

In order to improve this description, the 30-band Hamiltonian of Refs. [286, 304, 299] is extended to account explicitly for the 12 states with wavevector [220] (see Ref. [286]), leading to a 54-band Hamiltonian [237, 229]. These 12 extra bands are described in the Hamiltonian by five energy levels at the  $\Gamma$ -point and seventeen matrix coupling elements (for their definition, see Table A.4 in appendix). No additional spin-orbit terms are added to the standard ones, as they increase the complexity and they are supposed to have a negligible impact on the lowest energy band levels. For group  $T_d$  materials such as InAs and GaAs, additional non-zero matrix elements have to be accounted for compared to Si and Ge, due to centrosymmetry breaking. Four extra imaginary coupling parameters ( $S, S', U$  and  $U'$  in Table A.4) and one extra SO term ( $\Delta_{\Gamma_{15}\Gamma_{25''}}$ ) are thus added to the standard 30-band Hamiltonian used for Si.

Following the matrix elements definition in Ref. [304], the 54-band matrix is given in appendix and the coupling parameters are illustrated in Figure 1.4.

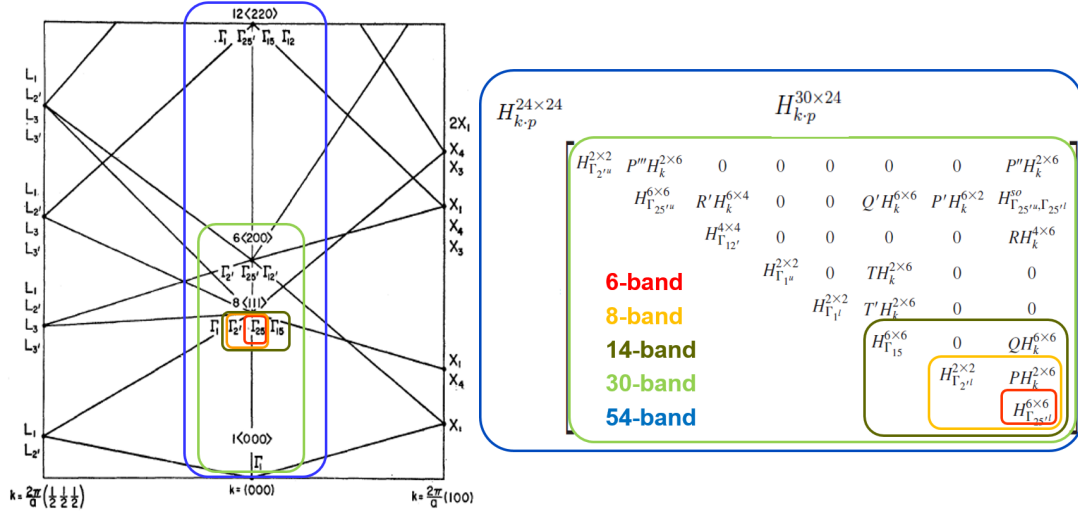


Figure 1.4. Left: nearly free electron band structure in a periodic BZ with labels of the  $O_h$  point group (figure taken from Ref. [286]). Right: KP matrix, according to the definition in Appendix A.1.2. Elements of the 6-, 8-, 14-, 30- and 54-band models are highlighted with different colors.

### 1.1.6 Si and Ge band structure

The Si band structure obtained with 30-band KP is shown in Figure 1.5(up) and compared with *ab initio* and EPM calculations. The 30- and 54-band KP models are compared in the near- $K$  point region, in the inset of the figure. One clearly notes the presence of the (220) band as low as 5 eV above valence band maximum in the  $K$  point, which was missing in the 30-band model in Ref.[304]. Moreover, without smoothing function the 30-band model predicts a conduction band edge in  $K$  that is too low, which is the reason why authors of Ref. [304] introduced a non-physical interpolation of the parameters. Such pragmatic approach is not needed with the 54-band KP model, which allows a better description of the near- $K$ -point region, while keeping a small computational cost. The computational effort for a complete bulk band structure calculation is for both KP models approximately two orders of magnitude lower than the one needed by non-local EPM method.

The Ge band structure obtained with 30-band KP is shown in Figure 1.5(down) and compared with *ab initio* and EPM calculations. A smoothing function is used in the 30-band model to improve the agreement in the near- $K$ -point region.

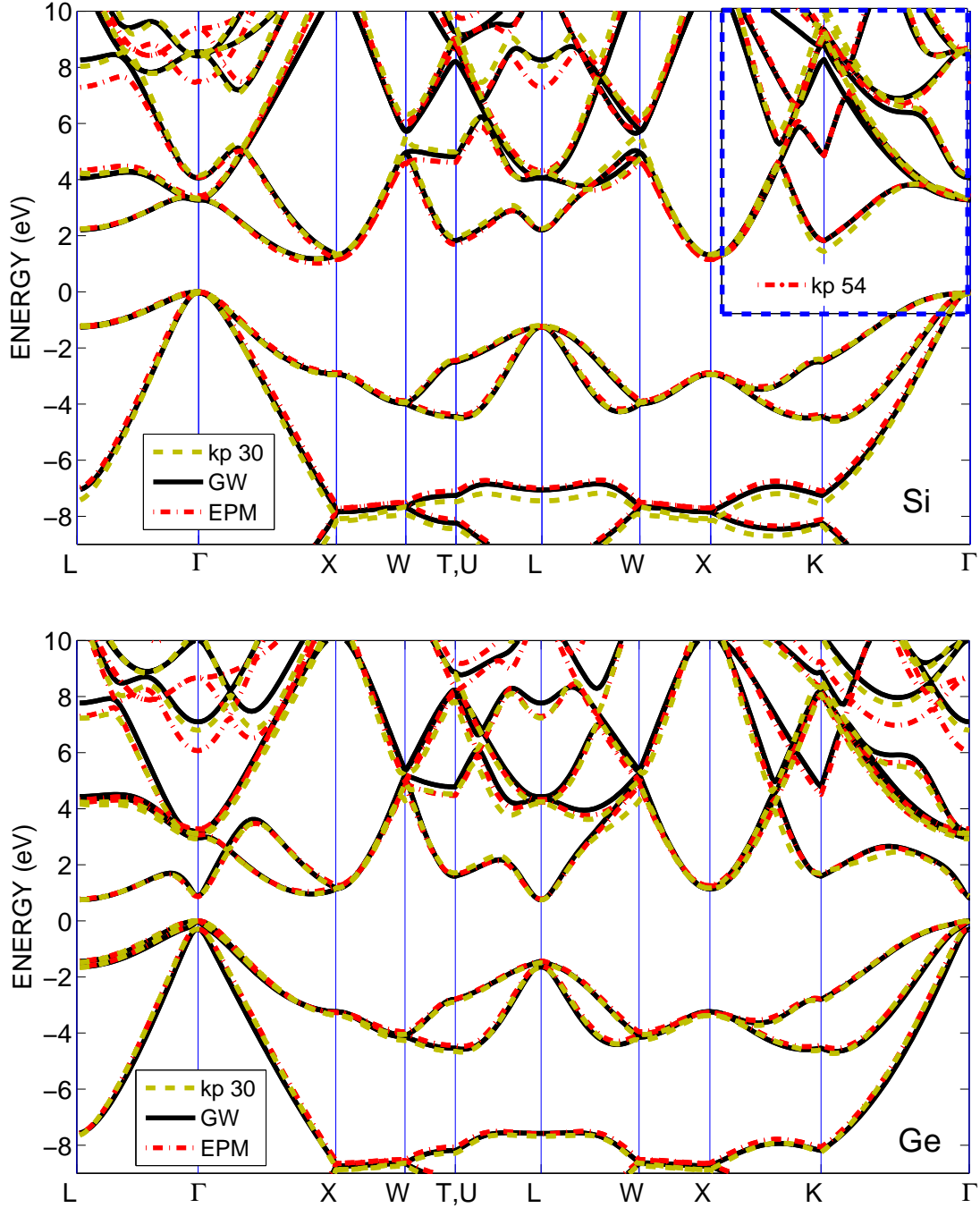


Figure 1.5. Up: Bulk Si electronic band structure using 30-band KP model without smoothing function, compared to DFT- $G_0W_0$  and NL-EPM calculations. Dashed-line blue rectangle points out the (220) band effect in the near- $K$ -region, where the 54-band KP model is plotted and shows improvement compared to 30-band KP model (see Fig.1 of Ref. [304]). Down: bulk Ge electronic band structure using 30-band KP model using smoothing function, compared to DFT- $G_0W_0$  and NL-EPM calculations. Data taken from Refs. [304, 301], computed with UTOX (KP and NL-EPM) and ABINIT [115] (DFT- $G_0W_0$ ).

### 1.1.7 GaAs and InAs band structure

While intensive studies of the band structure and electronic parameters have been made for bulk Si, Ge, as well as GaAs, some debates remain on InAs and InGaAs alloys, as pointed out by Vurgaftman *et al.* (2001) [385] and O’Regan *et al.* (2010) [264]. In particular, the position of the L and  $\Delta$  satellite valleys (local minima at L symmetry point and along the  $\Gamma$  - X line respectively) is not clearly defined, as it is shown in the next paragraph. The energy separation between these conduction band local minima and the top of the valence band will be labeled  $E_L$  and  $E_X$  hereafter. Some recent theoretical studies aims at bridging the gap and complete the description [165, 46], but no clear consensus has been found and only few experimental studies exist, mostly in the 1980’s. This difficulty and lack of trustable reference is reflected by the broad dispersion and difference of predictions found in the band structure given by different empirical models and parametrization for bulk InAs, as illustrated in Figure 1.6. For GaAs, the two available EPM parametrizations [51, 165] provide close values for band gaps. For InAs, the values of  $E_X$  obtained with the two EPM parametrizations of Refs. [51] and [165] are 1.4 and 2.1 eV respectively (see Fig. 1.6), while the exhaustive *ab initio* calculations of Ref. [171] reports  $E_X$  ranging from 1.65 to 2.09 eV and TB model with parameters from Jancu *et al.* (1998) [145] gives  $E_X$  around 2.18 eV (see Table 1.2). The only experimental value available to our knowledge for  $E_X$  is 1.9 eV [76].

Below, we give a quick overview of the recent theoretical studies and (often older) experimental works to have more insight about the knowledge that is currently available on these materials. We also present the different set of parameters available in the literature for the empirical models considered.

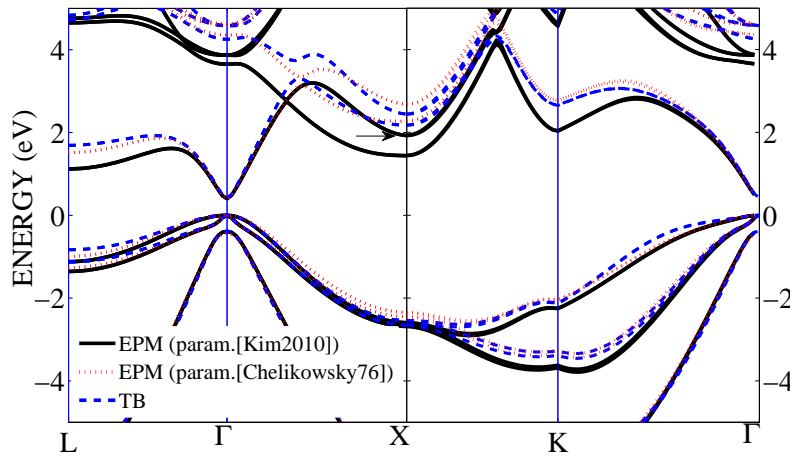


Figure 1.6. InAs band structure obtained with UTOX package based on the two NL-EPM parametrizations of Refs. [51] and [165], and with TBSim package based on the TB parametrization of Ref. [145]. The experimental value of Ref. [76] for  $E_X$  is shown with the black arrow. The NL-EPM models exhibit a clear difference, illustrating the controversy on the position of satellite valleys.

## Experimental

While the exact full-band structure cannot be observed directly experimentally, several methods can be used to extract relevant quantities such as band gaps and effective masses, as well as a mapping of the eigenvalues for different  $\mathbf{k}$  points in a region of the BZ. The review paper of Vurgaftman *et al.* (2001) [385] considers a broad range of experimental and theoretical papers, giving a good reference for the knowledge of the band structure and electronic properties of most III-V materials. For the position of valleys in GaAs, the authors mainly focus on the paper of Aspnes (1976) [14], who measured synchrotron Schottky-barrier electroreflectance spectra and compared them with previous studies. We note that the description of the valence band dispersion has been further refined by angle-resolved photoemission studies in Chiang *et al.* (1980) [53], which are needed to extract position of the satellite valleys from optical measurements of Aspnes. The corrected values given in their work are reported in Table 1.2. For the effective mass, the values in Ref. [385] are taken from Adachi [2].

For the position of satellite valleys in InAs, Vurgaftman *et al.* (2001) [385] gives no experimental reference and points out the controversy on this value. However, the study of Drube *et al.* (1987) [76] ought to be mentioned, which extracts the position of X valley by inverse photoemission study, whose value is reported in Table 1.2. Another study from Williams *et al.* (1986) [392] provides a complete study of the valence band dispersion of InAs by angle-resolved photoemission. They can unfortunately not be compared with data used by Drube [76] as the later article doesn't give them explicitly. The effective mass of lowest conduction band of InAs is also difficult to be extracted experimentally due to the strong non-parabolicity. The value suggested by the compilation in Ref. [385] is in the range of  $0.021 - 0.026 m_0$ . The effective mass of satellite valleys is more uncertain and no clear reliable experimental work was found.

## *Ab initio*

DFT calculations on small band gaps semiconductors such as InAs are difficult to perform. Indeed, standard DFT calculations usually predict InAs with negative band gap (*s*-like states below the *p*-states, as explained in Ref. [173]), and *GW* correction may fail when it is based on wavefunctions with an incorrect ordering. Hybrid functionals can be used to get a correct band gap, but these methods unfortunately depend on the amount of Hartree-Fock energy included in the functional, which can be adjusted to reproduce experimental values (see the complete study in Ref. [171]).

Table 1.1 compiles the results from several recent studies on bulk InAs. While the band gap remains relatively close to the experimental one ( $E_{\Gamma} = 0.41$  eV) in most cases (also it is 0.1 eV below in the case of  $GW_0$  in Ref. [173]), the relative position of the satellite L and X valleys are not matching in most studies and show a dispersion of  $\sim 0.3$  eV ( $> 20\%$ ) and 0.58 eV ( $> 30\%$ ) resp. This broad range of values found with these advanced tools show the difficulty to treat small band gap materials. However, one can conclude that the L and X valleys are generally lying more than 1 eV above the conduction band edge. Note that the early work of Zhu and Louie (1991) [406] offer values in the range of these studies.

Table 1.1. Band gaps at different  $\mathbf{k}$  points in bulk InAs as found in *ab initio* studies in the literature. All values are in eV and references are given in the first line.

$E_g$	$GW_0$ (PBE) [173]	$G_0W_0^{TC-TC}$ [171]	HSE06 [171]	HSE06 [163]	QP [406]
$E_\Gamma$	0.32	0.41	0.42	0.38	0.31
$E_L - E_\Gamma$	1.33	1.04	1.11	1.20	1.12
$E_X - E_\Gamma$	1.92	1.34	1.56	1.79	1.71

### Parameters for models

The band gaps at 0 K calculated in this work with the different empirical models are shown in Table 1.2 and difference with experimental values of less than 40 meV for all relevant gaps is obtained (when experimental values are available). Effective masses are also extracted by fitting the parabolic dispersion close to band extrema and shown in Table 1.2. For these computations, we used parameters from the literature with some adjustment when needed, as detailed below.

**TB** For the  $sp^3d^5s^*$  TB model used in this work, Jancu *et al.* (1998) [145] and Boykin *et al.* (2002/2004) [38, 39] provide two complete sets of parameters for a broad range of semiconductors, including GaAs and InAs. The first set of parameters reproduces the band structure at low temperature (0 K). These parameters are used to compute the parameters in Table 1.2. Note that the third valley minimum in GaAs lies in X symmetric point with this parametrization, while it is located at  $k_x \sim 0.86 [2\pi/a]$  in the other cases (including EPM and KP calculations). For InAs,  $E_X$  is about 0.5 to 0.6 eV higher than other theoretical calculations, but closer to the experimental value. The second set of parameters of Boykin [39] reproduces the band structure at room temperature and will be used in Chapters 2 and 3. A more recent set of parameters for GaAs has been given by Tan *et al.* (2014) [351] (and applied to nanostructures in Ref. [352]).

**EPM** A wide range of parameters for the local EPM can be found in the literature. The parameters used for the calculation of the valence charge density in Fig. 1.3 were taken from Cohen and Bergstresser (1966) [54] for GaAs and InAs. For the non-local EPM (NL-EPM), the reference paper of Chelikowsky and Cohen (1976) [51] gives a complete parametrization for a wide variety of semiconductors, reproducing the band structure and optical properties of these materials. This set of parameters is used for all calculations of GaAs NL-EPM band structure. A more recent parametrization was published by Kim and Fischetti (2010) [165] for InAs, GaAs and InGaAs alloys. As mentioned earlier, this latter parametrization gives different satellite valleys positions for InAs compared to Ref. [51]. As the InAs band gap is in better agreement with experimental data in Ref. [165], we choose this latter parametrization for all calculations of InAs NL-EPM band structure. In all our calculations, the parameters for spin-orbit (SO) coupling were slightly modified, as detailed in Appendix A.2. While  $m_e^{*(\Gamma)}$  is overestimated for GaAs (which is also the case in other EPM studies), all other masses lie within the experimental range of values.

Table 1.2. Band gaps (with respect to valence band maximum), spin-orbit and effective masses calculated for GaAs and InAs at T=0 K. All energies are expressed in eV and masses in unit of  $m_0$ . Experimental values are taken from Ref. [385], except when mentioned. KP and NL-PM calculations are made with UTOX, while TBSim was used for TB (see text for parameters references). Values in parentheses are calculated with 30-band KP.

	GaAs				InAs			
	Exp.	TB	EPM	KP	Exp.	TB	EPM	KP
$E_g^{(\Gamma)}$	1.519	1.519	1.526	1.527 (1.527)	0.42	0.418	0.406	0.415 (0.405)
$\Delta_{SO}^{(\Gamma)}$	0.341	0.340	0.349	0.349 (0.349)	0.39	0.380	0.390	0.390 (0.390)
$E_g^{(L)}$	1.85 <sup>1</sup>	1.837	1.855	1.942 (1.835)	N/A	1.691	1.122	1.128 (1.098)
$E_g^{(X)}$	2.18 <sup>1</sup>	1.989	2.115	2.162 (2.118)	1.90 <sup>2</sup>	2.176	1.442	1.456 (1.459)
$E_g^{(\Delta)}$	–	N/A	2.088	2.109 (2.058)		N/A		
$m_e^{*(\Gamma)}$	0.067	0.067	0.083	0.074 (0.084)	0.026	0.023	0.026	0.028 (0.027)
$m_{e,l}^{*(L)}$	1.9	1.44	1.85	1.41 (1.91)	0.64, 3.57 <sup>3</sup>	2.16	1.68	1.25 (1.43)
$m_{e,t}^{*(L)}$	0.08	0.12	0.12	0.13 (0.14)	0.05, 0.12 <sup>3</sup>	0.11	0.10	0.11 (0.12)
$m_{e,l}^{*(\Delta)}$	1.30	1.25	1.45	1.29 (1.17)	1.13, 1.98 <sup>3</sup>	1.69	2.31	0.82 (1.55)
$m_{e,t}^{*(\Delta)}$	0.23	0.24	0.24	0.23 (0.23)	0.16, 0.28 <sup>3</sup>	0.28	0.19	0.21 (0.22)
$m_{hh}^{*(001)}$	0.35	0.33		0.36 (0.36)	0.34 – 0.39	0.32		0.31 (0.31)
$m_{hh}^{*(110)}$	0.64	0.65		0.68 (0.65)	0.58 – 0.98	0.65		0.58 (0.58)
$m_{hh}^{*(111)}$	0.89	0.92		0.90 (0.84)	0.63 – 0.76	0.96		0.81 (0.80)
$m_{lh}^{*(001)}$	0.090	0.086		0.098 (0.109)	0.027 – 0.042	0.029		0.033 (0.033)
$m_{lh}^{*(110)}$	0.081	0.076		0.087 (0.096)	0.026 – 0.041	0.027		0.031 (0.032)
$m_{lh}^{*(111)}$	0.078	0.073		0.084 (0.093)	0.014 – 0.026	0.028		0.031 (0.031)
$m_{so}$	0.1165	0.161		0.198	0.09 – 0.15	0.095		0.106 (0.107)

<sup>1</sup> Ref. [53]

<sup>2</sup> Ref. [76]

<sup>3</sup> Ref. [165] and references therein.

**KP** For full-zone KP models, Richard *et al.* (2004) [299] first gave a parametrization for 30-band KP model for GaAs. Later, Ben Radhia *et al.* (2007) [292] gave parameters for In-V materials. In this work, we derived parameters to be used for InAs, GaAs and InGaAs alloys, using 30-band and the extended 54-band models presented above [237].

### Parameters extraction for full-zone $\mathbf{k} \cdot \mathbf{p}$ model

To extract parameters for III-As, we use the NL-EPM calculation based on parameters in Ref. [51] for GaAs and Ref. [165] for InAs, presented above. A non-linear optimization algorithm using Nelder-Mead method is used to minimize the least-square error function

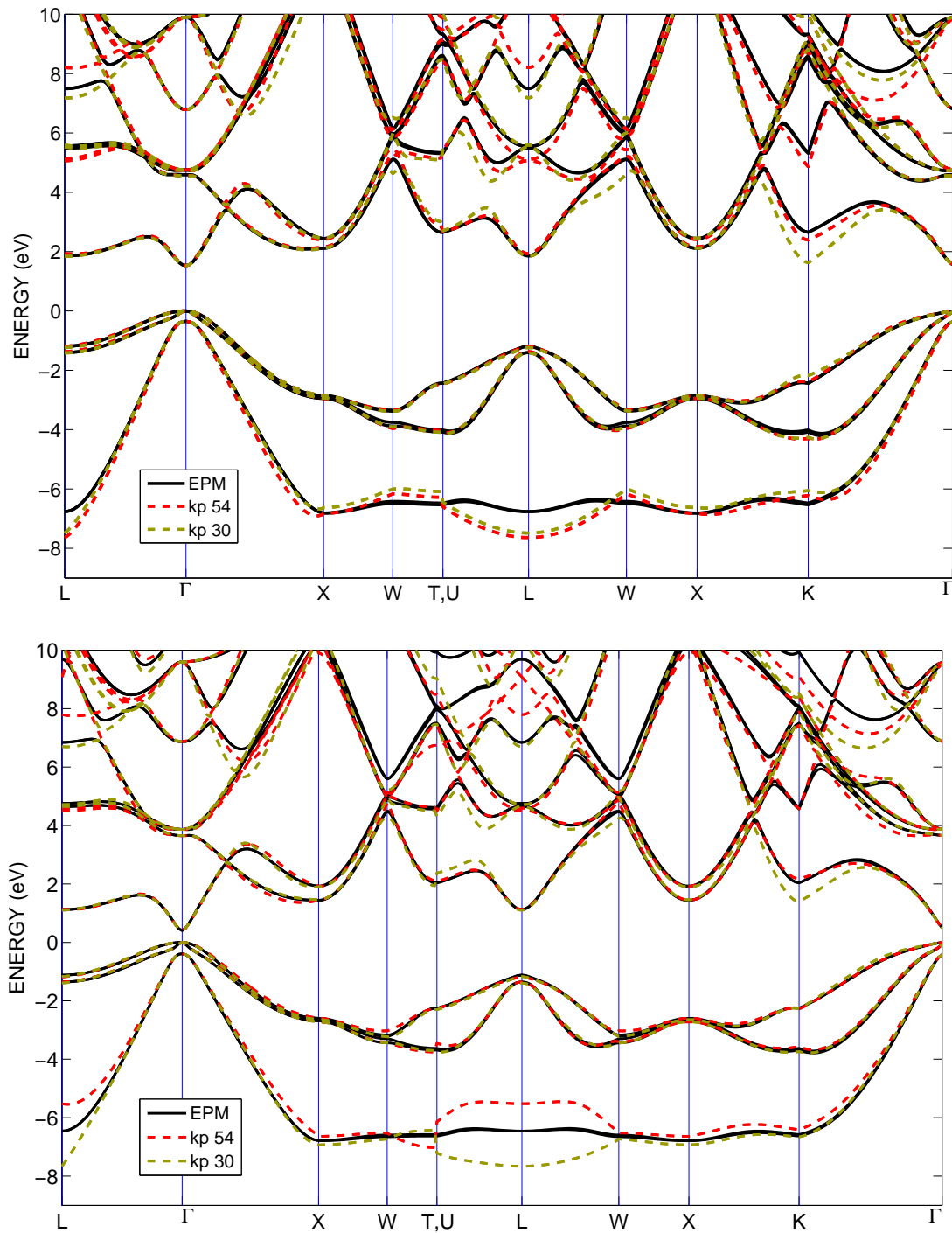


Figure 1.7. Bulk electronic band structure for GaAs (up) and InAs (down) using 30-band, 54-band KP and NL-EPM models computed with UTOX.

between KP and EPM eigenvalues on a complex and dense path throughout the Brillouin zone, as shown in Fig. 1.7. We also tried to reproduce as closely as possible the experimental values for known eigenvalues and effective masses, but some inaccuracy can remain over 10 eV and below -6 eV.

Band structures obtained for GaAs and InAs are shown in Fig. 1.7 and corresponding  $\mathbf{k} \cdot \mathbf{p}$  parameters are given in Table A.4 in appendix. Good agreement is found with EPM results and experimental data in the energy range considered, especially for the  $\Gamma$ ,  $\Delta$  and L conduction valleys involved in electronic transport. Note that the 54-band KP model allows a better description of the band structure in the near- $K$ -point region, as mentioned earlier, and reproduces more closely the band minimum in this region, which is too low in the case of the 30-band KP model. The 30-band KP model also leads to a discontinuity between eigenvalues of equivalent  $T$  and  $U$  points in BZ (as seen in Fig.1.7(b)). This discontinuity can be decreased (if not removed for bands close to the band gap) with the 54-band model. Note however that we did not try to improve valence band description below -5 eV, as it has no influence on transport.

The band gaps extracted from these parametrizations are shown in Table 1.2. While GaAs effective mass in  $\Gamma$  is still too high, it is closer to experimental value for the 54-band model and other effective masses are in line with the data mentioned in Refs. [165, 385].

### Density-of-States

Finally, the Density-of-States (DOS) has been computed by integrating the band structure over the 3D BZ with Gilat and Raubenheimer method [111]. The DOS obtained for GaAs and InAs with the present 54-band KP and NL-EPM calculations are shown in Fig. 1.8 and compared to the NL-EPM calculations of Refs. [51] and [90]. As discussed in previous section, the two EPM parametrizations for InAs give different values for indirect band gaps. This discrepancy is visible in Fig. 1.8(b), where the first peak in conduction band is shifted by  $\sim 0.5$  eV.

A zoom of the conduction band edge shows the very low DOS of the  $\Gamma$  conduction valley and the abrupt change of DOS when satellite valleys are reached (around 1.85 eV for GaAs and 1.1 eV for InAs). Although InAs has a lower DOS in the  $\Gamma$  conduction band, this abrupt transition is less pronounced. This is due to its higher non-parabolicity and the lower masses of the satellite valleys.

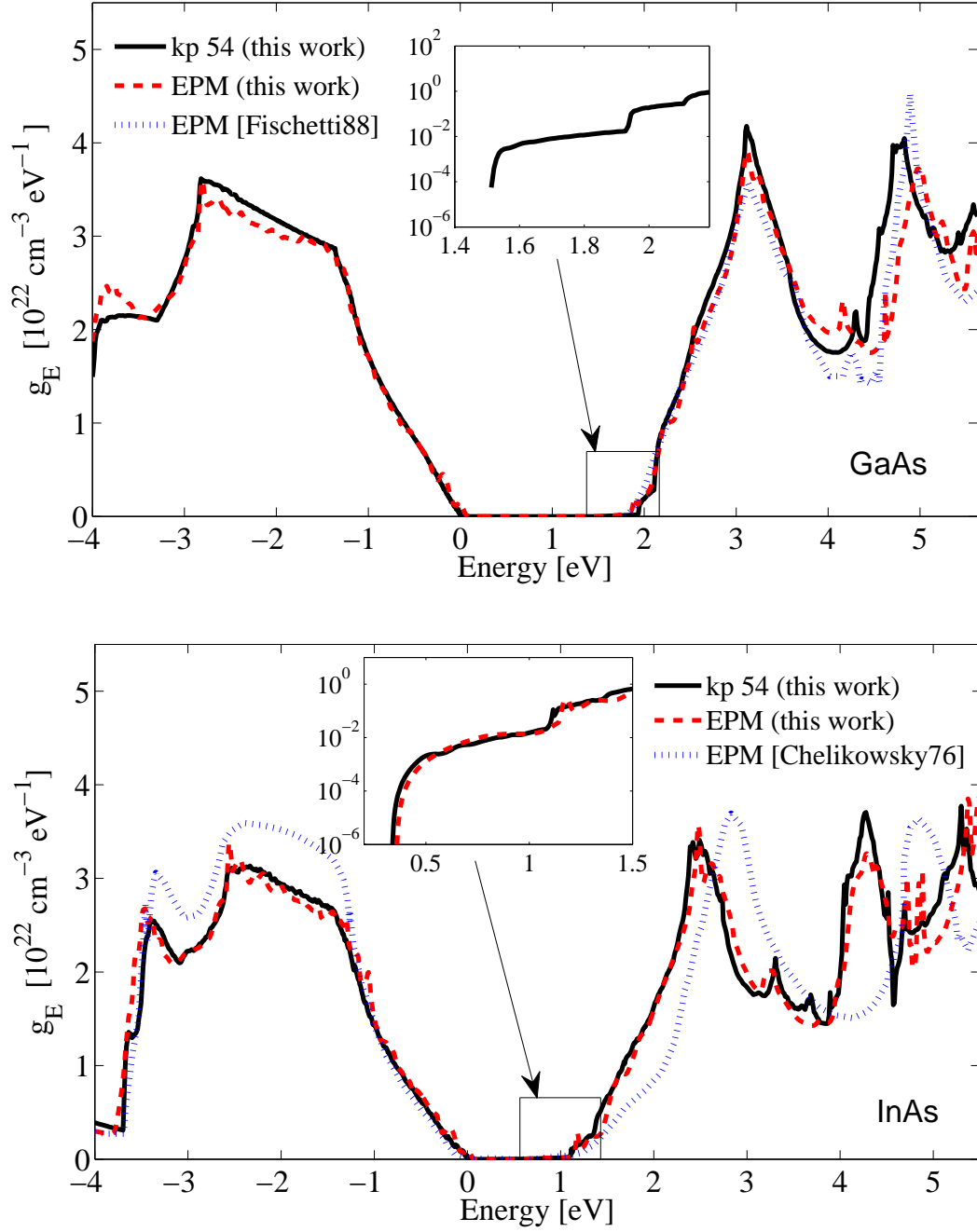


Figure 1.8. Density-of-states of GaAs (up) and InAs (down) using 54-band KP and NL-EPM models in the UTOX package. The data for the blue dotted lines were taken directly from Ref. [90] for GaAs and [51] for InAs. Other NL-EPM data were computed in this work, with parameters from Ref. [51] for GaAs and [165] for InAs (see discussion in Sec. 1.1.7).

### 1.1.8 Alloys: random supercell versus virtual crystal approximation

As mentioned in the Introduction, non-stoichiometric semiconductor alloys such as ternary  $\text{In}_x\text{Ga}_{1-x}\text{As}$  and binary  $\text{Si}_{1-x}\text{Ge}_x$  start to emerge in the semiconductor industry. The description of these alloys adds a difficulty as the crystalline structure cannot be considered as periodic anymore. In fact, it was found that the ordering of atoms in these crystals is often close to a random arrangement. In this case, the band structure of random alloys is not clearly defined, as the Bloch theorem is no longer applicable.

Two options are usually found in the literature for the calculation of the electronic structure of alloys: to build an atomistic random large supercell that won't be affected too much by periodic boundary conditions and to build a single unit cell crystal composed by virtual atoms whose parameters are interpolated.

#### Atomistic description

In models with an atomistic description, such as DFT, TB or atomistic EPM, a random crystal can be generated by building a large supercell with random distribution. For ternary alloys such as InGaAs, only the elements of the cations sublattice (Ga and In) are randomly distributed (see Fig. 1.9). When the supercell size is large enough, the spurious effect of the periodic boundary condition becomes negligible and convergence can be achieved. Studies on TB models showed that a good convergence is achieved with very large supercell of typically  $>60,000$  atoms for SiGe bulk materials [251], which is clearly not possible to treat with DFT codes. In addition, the position of all atoms has to be relaxed, which necessitates a force model and can be numerically expensive. Algorithms have been proposed to generate Special Quasirandom Structures (SQS) with a lower number of atoms which reproduce the electronic properties of larger random supercell calculations [409].

Another difficulty comes from the folding of the supercell band structure at the  $\Gamma$  point which makes the position of satellite valleys inaccessible. To solve this issue, algorithms have been proposed recently to unfold the BZ of supercell and map it to unit cell states [37, 36, 223]. These algorithms allow the reconstruction of bulk band structure and the determination of the satellite valley positions, but a big dispersion of eigenvalues is found due to the randomness of the crystal, as found in Ref. [163].

#### Virtual Crystal Approximation (VCA)

In the Virtual Crystal Approximation, a virtual crystal is constructed for which the atomic parameters are interpolated between the two elements, as shown in Figure 1.9. In this case, the results for alloys depend on the chosen interpolation scheme. Purely linear interpolation can be chosen, also known as Vegard's law, but a bowing coefficient has to be introduced in the general case to be able to reproduce experimental results. For instance, the parameters of  $\text{In}_x\text{Ga}_{1-x}\text{As}$  materials would be modified as:

$$P_{\text{InGaAs}} = P_{\text{InAs}}x + P_{\text{GaAs}}(1 - x) - Bx(1 - x) \quad (1.9)$$

where  $B$  is the so-called bowing parameter, which is usually an additional fitting parameter.

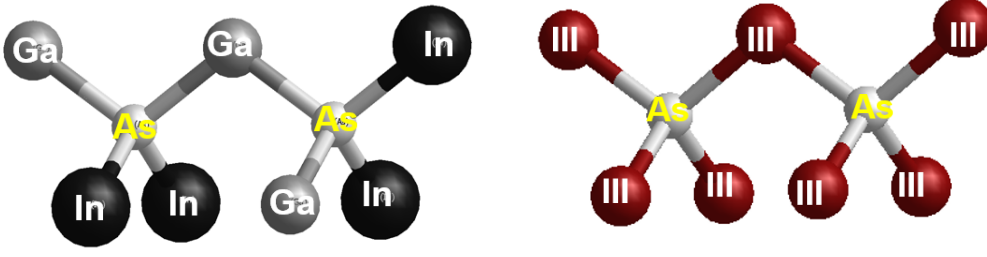


Figure 1.9. Sketch of two As anions with their neighboring III cations in the atomistic random model (left) and virtual crystal approximation (right), where “III” designs a virtual cation with interpolated parameters.

### Si<sub>1-x</sub>Ge<sub>x</sub> band structure

Figure 1.10(left) shows the band gap of SiGe alloys as a function of Ge content with TB model with both a random supercell and VCA approach, compared to experimental values. For the VCA calculation, the on-site and hopping parameters are interpolated linearly and quadratically as a function of  $x$ , shown by the following equations:

$$E_{VCA}^{on-site}(x) = (1-x)E_{Si,Si}^{on-site} + xE_{Ge,Ge}^{on-site}; \quad (1.10)$$

$$V_{VCA}^{hop}(x) = (1-x)^2V_{Si,Si}^{hop} + x^2V_{Ge,Ge}^{hop} + x(1-x)(V_{Si,Ge}^{hop} + V_{Ge,Si}^{hop}), \quad (1.11)$$

where  $E_{Si,Si}$ ,  $E_{Ge,Ge}$ ,  $V_{Si,Si}$ ,  $V_{Si,Ge}$ ,  $V_{Ge,Si}$  and  $V_{Ge,Ge}$  are the atomistic TB parameters for SiGe alloy as defined in Ref. [251]. The results with another VCA model, developed by D.Rideau and detailed in Appendix A.3, are also shown in Fig. 1.10(left) under the label “VCA model 2”. The band gap obtained with linear interpolation is also shown and a linear variation as function of  $x$  is predicted, failing to reproduce the correct experimental bowing.

### In<sub>x</sub>Ga<sub>1-x</sub>As band structure

Figure 1.10(right) shows the direct band gap of InGaAs alloys as a function of In content with TB model with both random and VCA approaches. NL-EPM results from Kim *et al.* (2010) [165] are also shown and are in good agreement with TB calculation with random supercell. Bowing coefficients given in Ref. [202] were used for the VCA model, together with binary parameters of Ref. [145]. The band gap dependence obtained with this model is in close agreement with experimental and random supercell calculations. The band gap obtained with linear interpolation is also shown in Fig. 1.10(right) and predicts a wrong sign of bowing. This model should thus not be used.

As for InAs, an uncertainty on the position of satellite valleys remains for InGaAs alloys. Below we present recent studies with DFT and different empirical models.

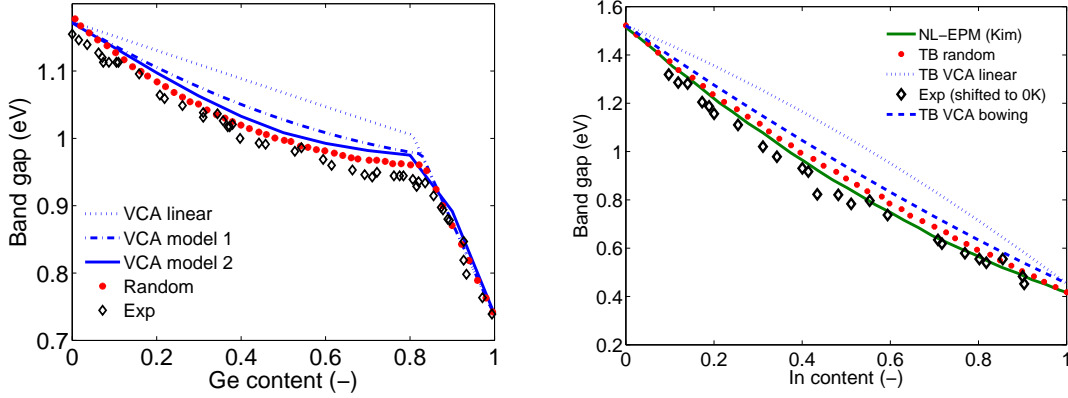


Figure 1.10. Band gap of bulk unstrained  $\text{Si}_{1-x}\text{Ge}_x$  (left) and  $\text{In}_x\text{Ga}_{1-x}\text{As}$  (right) materials as function of  $x$  content with TB model in TBSim package. The VCA calculations with different interpolation (see text) are compared with random supercell calculation. Experimental data are taken from Ref. [389] for  $\text{Si}_{1-x}\text{Ge}_x$  and Ref. [25] for  $\text{In}_x\text{Ga}_{1-x}\text{As}$ . The values of  $\text{In}_x\text{Ga}_{1-x}\text{As}$  measured at 300 K were shifted up by 70 meV to reproduce 0 K values. NL-EPM results from Ref. [165] are also shown for  $\text{In}_x\text{Ga}_{1-x}\text{As}$ .

**Experimental** As  $\text{In}_{0.57}\text{Ga}_{0.43}\text{As}$  is lattice matched with InP and has a wider gap than pristine InAs, it has been particularly investigated in the literature. In particular, Cheng *et al.* (1982) [52] studied the position of the L valley by ultraviolet photoemission and found a separation of  $\Gamma$  and L valleys of  $E_L - E_\Gamma = 0.55$  eV. For InGaAs alloys with other compositions, the optical direct band gap, spin-orbit separation of split-off valence band and lowest conduction effective mass has been studied by Berolo *et al.* (1981) [25].

**DFT** The treatment of alloys in DFT is particularly difficult, as the calculations become very heavy when the number of atoms increases. However, very recent articles [118, 163] perform calculations on InGaAs bulk materials, using Special Quasi-random Structures allowing to use a smaller supercell (typically 16 to 32 atoms). Table 1.3 compiles the band gaps and the position of satellite valleys found with these methods in  $\text{In}_{0.57}\text{Ga}_{0.43}\text{As}$  alloy. It is interesting to note that the difference  $E_L - E_\Gamma$  found with the VCA approach is generally higher than the supercell calculations. However, the experimental values reported are lower than all the values reported here. Also note that Khomyakov *et al.* (2015) [163] studied in particular the dependence of the band structure with In content and gives bowing coefficients  $B$  for  $E_\Gamma$ ,  $E_L$  and  $E_X$  of 0.55, 0.31 and 0.105 eV respectively (obtained with HSE supercell calculations with 216 atoms).

**EPM** In Kim *et al.* (2010) [165], a VCA approach is used to compute the band structure of InGaAs with NL-EPM. The position of the satellite valleys is plotted in Fig. 1.11. They found bowing coefficients for  $E_\Gamma$ ,  $E_L$  and  $E_X$  of 0.473, 0.399 and 0.421 eV resp. These values match well the values obtained by DFT-HSE calculation above, except for  $E_X$ . It is important to mention that the position of satellite valleys in pristine InAs is very

Table 1.3. Band gaps at different  $\mathbf{k}$  points for bulk  $\text{In}_{0.53}\text{Ga}_{0.47}\text{As}$  as found in *ab initio* studies in the literature. All values are in eV and references are given in the first line. To help comparison between methods, the satellite valleys are referred to bottom of the conduction band. SQS refers to Special Quasi-random Structures (with 16 atoms) as defined in Ref. [409] while SC refers to cubic supercells (with 216 atoms).

$E_g$	$G_0W_0$ [118] VCA	$G_0W_0$ [118] SQS	HSE06 [118] SC	HSE06 [163] <sup>1</sup> SC	QP [406] VCA
$E_\Gamma$	0.92	0.87/0.84	0.92	0.71	0.80
$E_L - E_\Gamma$	0.72	0.99/1.07	0.99	0.87	0.83
$E_X - E_\Gamma$	1.04	1.19/1.20	1.13	1.40	1.27

<sup>1</sup> The calculations in this reference were done for  $\text{In}_{0.5}\text{Ga}_{0.5}\text{As}$ .

different in the two cases: X valleys are higher in InAs than GaAs in the case of DFT-HSE calculation, while it is the opposite in NL-EPM calculations. NL-EPM parameters for the particular composition  $\text{In}_{0.57}\text{Ga}_{0.43}\text{As}$  have also been extracted by Dittrich *et al.* (1999) [70], which found a separation  $E_\Gamma - E_L = 0.54$  eV in agreement with experimental value and the value reported in Kim *et al.* (2010) [165]. They also found a separation  $E_\Gamma - E_X = 1.035$  eV which is in good agreement with DFT-VCA calculations, but higher than the values in Kim’s article of  $E_\Gamma - E_X = 0.804$  eV.

**TB** For the position of the satellite valleys in TB, we use here the VCA approach, as they are not available in the supercell calculation without unfolding methods. The direct band gap shown in Fig. 1.10 allows to validate the VCA approach, with the interpolation scheme of Ref. [202]. The X valleys of InAs are here higher than those of GaAs as shown in Fig. 1.12. A negative bowing is found for  $E_X$  of -0.15 eV, while the bowing for  $E_L$  is 0.29 eV in relative good agreement with the value extracted from DFT and NL-EPM.

**KP** As KP are continuous models, only VCA approach can be used to compute the band structures of alloys. Recently, parameters for InGaAs alloys have been published for full-zone KP models. Parameters for the 40-band KP model are given in Yahyaoui *et al.* (2013) [395], and parameters for the 30-band KP model for the specific  $\text{In}_{0.57}\text{Ga}_{0.43}\text{As}$  have been extracted in Verreck *et al.* (2016) [384]. Yahyaoui [395] gives two parametrizations for unstrained and strained InGaAs grown on GaAs buffers, and bowing coefficient for almost all parameters.

In our full-zone 54-band KP model, a more pragmatic linear interpolation is made for all parameters, except for the energies  $\Gamma_{12}$  and  $\Delta_{SO}$  for which the experimental bowing coefficients  $B$  suggested by Vurgafman *et al.* (2001) [385] are used ( $B = 0.477$  eV for  $\Gamma_{12}$  and 0.15 eV for  $\Delta_{SO}$ ). Although Ref. [385] also suggests a bowing coefficient for parameter  $P$ , an adequate tendency for the energy gap  $E_g$  and effective mass  $m_e^{*(\Gamma)}$  is obtained without bowing with the 54-band model, as shown in Fig. 1.11. Fitting back the band gaps  $E_L(x)$  and  $E_X(x)$  with Eq. (1.9) gives bowing coefficients of 0.72 and 1 eV respectively, which

are higher than the ones reported with previous models, but lie in the range of values suggested by Vurgaftman *et al.* (2001). The difference with experimental results for  $m_e^{*(\Gamma)}$  can be due to temperature influence, as measurements were done at 300 K.

For the 30-band KP model, additional bowing coefficients had to be introduced on parameters  $P'''$ ,  $Q'$  and  $S$  ( $B = 0.78, 0.2$  and  $0.2$  eV, respectively) in order to have a correct bowing for  $m_e^{*(\Gamma)}$  and band gaps. This can be due to the influence of remote bands not included in this model, indicating that the 54-band KP model allows a more complete description of alloys. The band gaps and effective masses with this model are also shown in Fig. 1.11. Although  $m_e^{*(\Gamma)}$  is higher than the experimental mass, the tendency is very close to NL-EPM, from which the KP parameters were extracted.

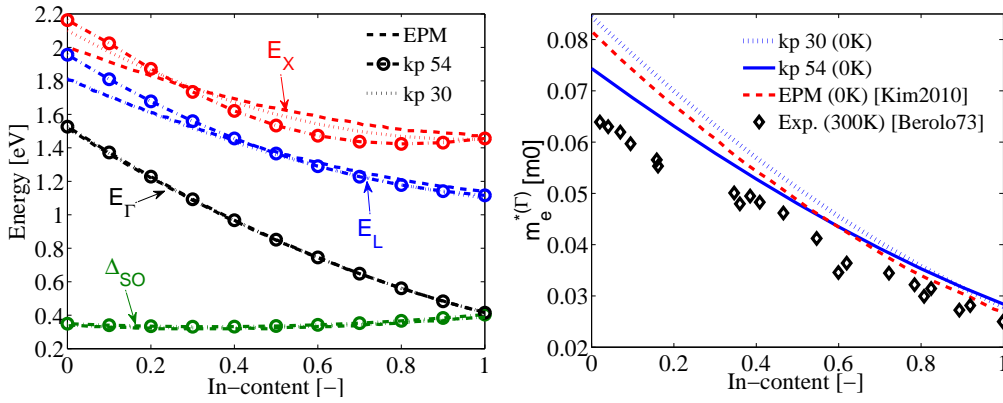


Figure 1.11. Band gaps (left) and effective mass in  $\Gamma$  (right) of InGaAs as function of In mole fraction, calculated with UTOX package and our parametrization for 54- and 30-band KP model. Dashed lines show the fits with Eq. (1.9). Data for NL-EPM are from Ref. [165], while experimental values are taken from Ref. [25]. The various band gaps are relative to the top of the valence band  $\Gamma_{25'}^l$ .

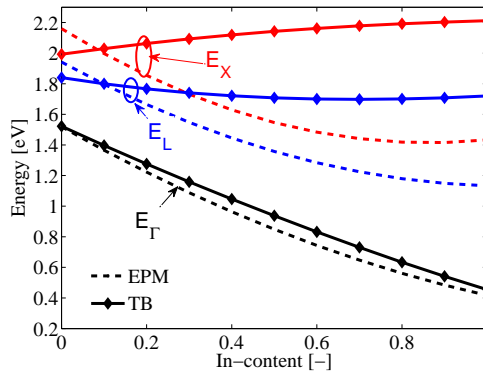


Figure 1.12. Same as Fig. 1.11 with TB model in TBSim package and parameters from Ref. [145].

### 1.1.9 Stress influence on band structure

Stress engineering has been widely used and studied in recent transistor nodes as technological boosters. Indeed, stress can have a big influence on the band structure, which can be thus adequately “tuned” to favor low-effective mass carrier and improve transport properties of both electrons and holes. In a general trend, compressive stress improves hole transport, while tensile stress improves electron transport in Si, but the picture and interaction can be very complex, especially in confined structures where an interplay exists between the confinement and stress. For electron transport in III-V materials, the stress is in general much less efficient, as the lowest valley lying in  $\Gamma$  is isotropic and single degenerate. However, it can have an influence on the position of satellite valleys, which can be populated at high gate or drain voltage. Some recent papers have studied the effect of stress, using various approaches such as DFT, EPM, KP and TB [297, 46, 401].

The influence of stress on the transport is not studied in detail in this work, but we review briefly below the incorporation of stress in the empirical models, as the knowledge of the related deformation potential is of significant importance for electron-phonon coupling and transport properties (see Chap. 3).

#### Atomistic description

In atomistic models, the description of stress is straightforward, as it is directly translated into a shift of the position of the atoms. In DFT codes, the charge redistribution due to the atoms displacement is automatically accounted for in the self-consistent calculation and the change of band structure with stress can be obtained with no further hypothesis. On the other side, in empirical models it is part of the fitting parameters, which need to be adapted. In general, the extra fitting parameters are adjusted in order to reproduce the deformation potentials, taken from experiments or *ab initio* calculations in different stress conditions (see the following subsection about deformation potential theory). These models remain valid for small stress conditions only, and are not guaranteed to work at large stress conditions (typically  $\varepsilon > 1\%$ ). The dependence of particular points in the BZ under large stress conditions could be reproduced by more accurate parametrization in TB and EPM models (see, e.g., Ref. [251]).

#### Deformation potential theory

The theory of deformation potential was introduced in the 1950’s [130, 20] and more recently reviewed by Van de Walle (1989) [369] using *ab initio* tools to extract the parameters of different materials. In the first approximation, the influence of the displacement of atoms in a strained crystal leads to a rigid shift of the band edges, modeled by a linear model in terms of the components  $\varepsilon_{ij}$  of the strain tensor. In the case of hydrostatic stress ( $\varepsilon_{xx} = \varepsilon_{yy} = \varepsilon_{zz} = \varepsilon$ ) the position of the conduction band edge at the  $\Gamma$  point is written as [398]:

$$E_{\Gamma} = E_{\Gamma}^0 + a_c \left( \frac{\partial V}{V} \right) = E_{\Gamma}^0 + 3a_c \varepsilon$$

where  $E_{\Gamma}^0$  is its position in unstrained crystal and  $a_c$  is the volume deformation potential.<sup>3</sup> Experimentally, the absolute shift of the conduction band edge is difficult to measure and optical measurements are often used to determine the band gap shift due to hydrostatic pressure. This one is equal to the relative deformation potential of valence and conduction band:  $a_g = a_c - a_v$ .

For degenerate bands, three deformation potentials are in principle needed to describe not only the shift of energy, but also the degeneracy splitting induced by shear stress component. For valence band, the pioneer work of Pikus and Bir [31] paved the way of deformation potential theory and derived expressions for these three deformation potentials. The two additional deformation potentials  $b_v$  and  $d_v$  are defined by [369]:

$$\delta E_{001} = 2b_v(\varepsilon_{zz} - \varepsilon_{xx})$$

$$\delta E_{111} = 2\sqrt{3}d_v(\varepsilon_{xy})$$

where  $\delta E_{001}$  and  $\delta E_{111}$  are the shift of the average energy of the three topmost valence band caused by strain in the [001] and [111] direction resp.

In the case of conduction band edges at  $\Delta$  and L symmetry points, two values are sufficient, due to symmetry rules, and the model derived in Herring and Vogt (1956) [130] has been the most widely used. It writes the energy shift of valley  $\nu$  as [398]:

$$\delta E_{\nu} = \Xi_{d\nu}(\text{Tr}\{\bar{\varepsilon}\}) + \Xi_{u\nu}(\mathbf{k}_{\nu}' \cdot \bar{\varepsilon} \cdot \mathbf{k}_{\nu})$$

where  $\Xi_d$  and  $\Xi_u$  are respectively the dilatation and uniaxial deformation potentials,  $\text{Tr}\{\}$  is the trace and  $\mathbf{k}_{\nu}$  is the unit vector along the direction of the valley in reciprocal space. The values of these deformation potentials for GaAs and InAs materials extracted from experimental and theoretical studies in the literature are given in Tables 1.4 and 1.5. An overall good agreement is found for  $a_g$ ,  $a_c$ ,  $b$  and  $d$  between all methods for these two materials, as well as deformation potentials of satellite valleys.

The deformation potential theory is also used in transport to model the electron-phonon interaction. In principle, the parameters extracted here are related to the acoustic phonon deformation potential entering the calculation of intravalley scattering [398]. However, although a direct relation theoretically exists between the stress-driven parameters and the ones entering the electron-phonon coupling elements [161], these values can present a net difference (see parameters and discussion in Chap. 3).

The deformation potentials for  $\text{In}_{0.57}\text{Ga}_{0.43}\text{As}$  material are presented in Table 1.6. An overall good agreement is found for  $b$  and  $d$  parameters. Note however that Khomyakov *et al.* (2015) [163] predicts a lower value for  $a_g$  compared to experimental values given in Vurgaftman [385], which was extracted from People (1988) [278] and Wilkinson (1990) [391]. This leads to an inverse sign in the bowing parameter for  $a_g$ :  $B = +2.34$  eV extracted

---

<sup>3</sup>Note that in the majority of the cases (if not all), the conduction band edge at  $\Gamma$  is shifted up to higher energy for compressive hydrostatic stress and down to lower energy for tensile stress. In what follows, we will use the convention of negative  $\varepsilon$  for compressive stress, and positive  $\varepsilon$  for tensile stress, implying a negative  $a_c$ .

Table 1.4. Deformation potentials of GaAs obtained from experimental and *ab initio* studies in the literature. All values are in eV.

Reference	$a_g$	$a_c$	$b_v$	$d_v$	$\Xi_{d,X} - a_v$	$\Xi_{u,X}$	$\Xi_{d,L} - a_v$	$\Xi_{u,L}$
Exp. [385, 283]	-8.5	-7.7	-2	-4.8	N/A			
Exp. [43, 109]	-9.77	-7.1	-1.7	-4.55	N/A			
DFT-LDA [369]	-8.33	-7.17	-1.9	-4.23	–	8.61	–	14.26
DFT-HSE [163]	-8.54	–	-2	-4.4	-1.35	8.22	-8.38	15.1

 Table 1.5. Deformation potentials of InAs obtained from experimental and *ab initio* studies in the literature. All values are in eV.

Reference	$a_g$	$a_c$	$b_v$	$d_v$	$\Xi_{d,X} - a_v$	$\Xi_{u,X}$	$\Xi_{d,L} - a_v$	$\Xi_{u,L}$
Exp. [385]	-6	-5.08	-1.8	-3.6	N/A			
Exp. [43, 109]	-6	-5.4	-1.8	-3.6	N/A			
DFT-LDA [369]	-6.08	-5.08	-1.55	-3.10	–	4.5	–	11.35
DFT-HSE [163]	-5.97	–	-1.68	-3.8	-0.16	4.83	-6.86	12.5

 Table 1.6. Deformation potentials of  $\text{In}_{0.57}\text{Ga}_{0.43}\text{As}$  obtained from experimental and *ab initio* studies in the literature. All values are in eV.

Reference	$a_g$	$a_c$	$b_v$	$d_v$	$\Xi_{d,X} - a_v$	$\Xi_{u,X}$	$\Xi_{d,L} - a_v$	$\Xi_{u,L}$
Exp. [385, 278, 391]	-7.79	-6.96	–	–	N/A			
Exp. (lin. interp.) [109]	-7.76	-6.2	-1.75	-4.04	N/A			
DFT-HSE [163]	-6.81	–	-1.79	-3.9	-0.22	5.15	-7.09	12.9

from experimental data compared to  $-1.47$  eV from DFT-HSE study. A possible explanation given by Ref. [163] is the questionable interpolation method used to extract elastic constants in InGaAs in the extraction procedure from experimental studies.

**TB** The influence of stress on the TB parameters is usually described with the use of a power law, also called “Harrison law” in reference to the complete study of Harrison [125]. The nearest-neighbor (NN) hopping integrals are assumed to vary as:

$$V = V_0 \left( \frac{d_0}{d} \right)^\eta$$

where  $d$  and  $d_0$  are the NN distances in the stressed and relaxed structure respectively, and the  $\eta$  exponent is called Harrison parameter. This model has been refined in Niquet *et al.* (2009) [251] for the treatment of large stress in SiGe alloys, adding correcting parameters on the on-site and hopping terms labeled  $\alpha$ ,  $\beta$  and  $\gamma$ .

**EPM** In strained structures, the reciprocal lattice vector are affected by the distortion of the cubic lattice [302]:

$$\mathbf{G}' = \frac{\mathbf{G}}{\bar{\mathbf{1}} + \bar{\varepsilon}}$$

where  $\bar{\mathbf{1}}$  is the unit tensor and  $\bar{\varepsilon}$  is the strain tensor.

This implies that, to describe the influence of stress, one has to know the value of the local form factors  $V_s$  and  $V_a$  at  $G'$  (norm of  $\mathbf{G}'$ ). From the six local form factors at the unstrained  $G^2 = 3, 4(8)$  and 11, different expressions are derived to describe the whole  $V(G)$  curve in the literature, using sometimes complicated interpolation functions (see, e.g., Refs. [99] and [308] for Si and Ge). For InGaAs alloys, Kim *et al.* (2010) [165] used spline cubic functions, fitting the slope of the curve by fixing the form factors at  $G \pm 0.01 [2\pi/a_0]$ . Note that Kim *et al.* (2002) [166] pointed out that the deformation potentials  $a_c$  and  $a_v$  in polar materials are not well described if local parameters are only modified as presented above, because the stress also induces charge redistribution and changes in the screening potential included in  $V_a$  and  $V_s$ . The authors thus include an additional fitting parameter in their model, which is not accounted for in the parametrization of Ref. [165].

**KP** The pioneer work of Bir and Pikus [95, 284] studied the influence of stress in the perturbative  $\mathbf{k} \cdot \mathbf{p}$  framework and derived expression for stress elements. It is included as extra terms in the Hamiltonian. When spin-orbit and strain-effect are included, the Schrödinger equations thus becomes:

$$\{H_{kp} + H_{so} + H_{strain}\} \psi_{n\mathbf{k}}(\mathbf{r}) = E_{n\mathbf{k}} \psi_{n\mathbf{k}}(\mathbf{r}) \quad (1.12)$$

The strain Hamiltonian has been derived for 30-band KP models in Rideau *et al.* (2006) [304], but to our knowledge no complete set of parameters exists for InAs and GaAs materials to describe stress. In Neffati *et al.* (2012) [242] as well as Verreck *et al.* (2016) [384], the strain in 30-band model for III-V materials is deduced from the 8-band model with no additional strain parameters.

The effect of strain in the 8-band KP model is presented in Appendix A.1.1. Note that it was found in the recent work of Rau *et al.* (2016) [297] that the standard value of deformation potential used in 8-band KP fail to reproduce stress dependence prediction of DFT and TB models and need to be re-calibrated. Unfortunately, the re-calibration was not provided in their work.

## 1.2 Band structure in nanostructures

In this second section, the electronic properties of quasi-1D (nanowires) and quasi-2D (thin films) nanostructures are investigated. These structures are of technological importance considering the novel architectures of scaled devices, where the channel in FDSOI/FinFET devices reaches thickness/width of a few nanometers. In particular, NanoWires FET (NWFETs) and Gate-All-Around (GAA) devices are considered for future nodes, allowing an improved electrostatic control and better scalability [84].

The theory of envelope function and the construction of the BZ and Hamiltonian in a confined structure are first discussed. Then band structures of InAs and GaAs thin films and nanowires are investigated with TB, KP and NP-EMA models with hard-wall boundary conditions. The models and derivations of non-parabolic corrections in the confinement direction are discussed and the lowest subband energy of  $\Gamma$  valley and effective masses are extracted.

### 1.2.1 Confinement effect on band structure

In FDSOI MOS structures, insulators with large band gap surrounding the thin semiconductor channel produce a confining potential. This can be seen in the Figure 1.13, where the conduction and valence band edges profile along a FDSOI structure is shown. When the size of the channel layer reaches the characteristic wavelength of carriers, the wavefunctions are affected by the confining potential and quantum confinement starts to play an important role. Electrical confinement can also be induced by the perpendicular electric field applied by the gate. This effect will be discussed in the next Chapter, treating the electrostatics of MOSFET structures.

This quantum confinement affects the band structure, projecting the bulk 3D BZ in lower dimensionality, along with the creation of “subbands”. The projection of the bulk BZ and position of  $\Delta$  and L valleys for different confinement orientations are schematically drawn in Figure 1.14. The different subbands and envelope functions associated in the confined FDSOI structure are also shown in Figure 1.13. This projection of the BZ can be seen as a sampling of the bulk band structure for each discrete  $k_i$  vectors ( $i$  supposed as a confined direction) labeling the different “subbands”.

### TB

In the case of atomistic methods, the physical confinement is taken into account explicitly in real space, by constructing a supercell with hard-wall boundary conditions. In unconfined direction(s), standard periodic boundary conditions are applied, as in bulk simulations. In reciprocal space, the supercell construction induces a folding (or projection) of the BZ and the transport can occur only along the unconfined direction(s).

Now, there are different ways to construct the boundary conditions at the nanostructure surface. Lee *et al.* (2004) [178] presented two methods to apply closed-boundary conditions by raising the energy of either surface atoms or dangling bonds of these atoms, to avoid charge in the empty bonds. Niquet *et al.* (2000) [247] chose to passivate the dangling bonds of surface atoms with H atoms, whose parameters can be eventually adapted

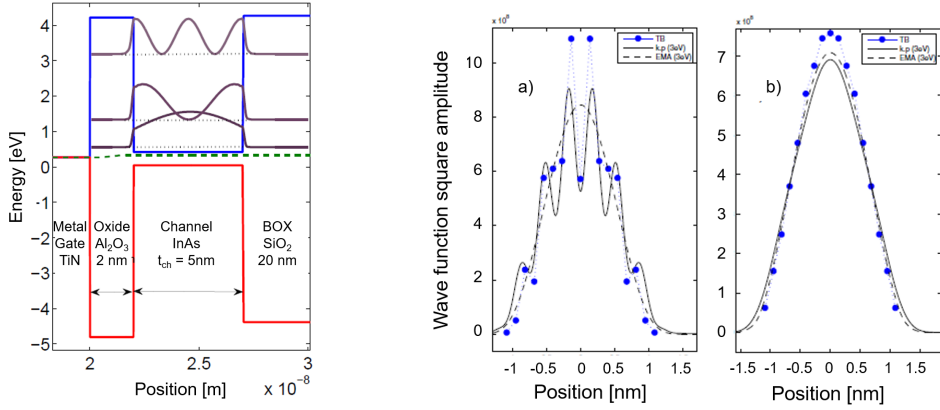


Figure 1.13. Left: Cut of the conduction (blue) and valence (red) band profiles through a FDSOI structure, in flat band conditions. We set a band offset between InAs and  $\text{Al}_2\text{O}_3$  of 3.8 eV and a metal workfunction of 5 eV. Black dashed lines show the energy level of the three lowest subbands in NP-EMA including WFP, and the envelope function associated is plotted in solid lines (in arbitrary units). Right: Comparison of the envelope functions of the lowest subbands in a Si (001) slabs coming from  $\Delta_{x,y}$  (a) and  $\Delta_z$  (b) valleys obtained with different empirical models (taken from Ref. [305]).

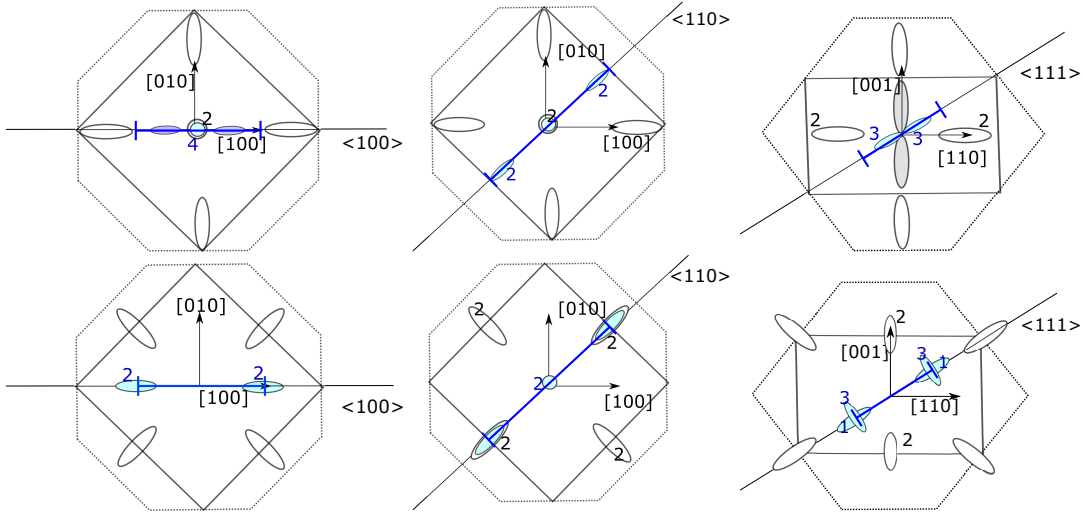


Figure 1.14. Schematic drawing of the BZ in 2D systems and projection of  $\Delta$  (up) and  $L$  (down) valleys (shown as white empty ellipsoids). The dotted lines are the projection of 3D BZ on a plane, while solid lines are the 2D BZ of confined quasi-2D layers. 1D BZ is shown with a blue solid line. The light blue ellipsoids show the position of valleys in a quasi-1D confined structure in different orientations.

to emulate different physical phenomena, such as band edge and surface dipoles [254]. Unfortunately, it is more complicated to describe the interface with an oxide with TB

models and the above boundary conditions cannot account for the finite band offset between semiconductor and oxide, inducing the wavefunction penetration (WFP) inside the oxide. These effects are however non-negligible and affect the electrostatic properties of MOSFET devices (such as capacitance), as it will be investigated in the next Chapter.

## KP

In the case of “continuous” models, such as KP model, the construction of the Hamiltonian is in principle only valid in bulk materials, due to the choice of the basis for the wavefunction expansion. In heterostructures, the envelope function approximation has been widely used, together with the appropriate boundary conditions. Nonetheless, this method can be questionable to model semiconductor/oxide interfaces, since it supposes a slow varying potential (nearly constant at the scale of the crystal unit cell) and can give different results compared with atomistic models [303, 305, 386, 82]. Moreover as the periodicity of the bulk band structure is not assured in the KP model (perturbation around one  $\mathbf{k}$  point), the projection of the 3D BZ can lead to spurious states. We will discuss the different boundary conditions and ways to filter these states below.

**Envelope function approximation and Brillouin zone construction** We recall briefly the derivation of the envelope function and construction of BZ in confined systems. The band offset due to the interface with oxides can be treated in first approximation as a potential term  $\Phi(\mathbf{r})$  in Schrödinger equation:

$$(H_0 + \Phi(\mathbf{r}))\psi(\mathbf{r}) = E\psi(\mathbf{r})$$

where  $H_0$  is the bulk Hamiltonian (Eq. (1.5)). In this case, the crystal symmetry is broken and the Bloch functions are no longer valid. As for the KP theory in bulk, the basis set for the development is taken as the wavefunctions at  $\mathbf{k} = 0$ :

$$\psi(\mathbf{r}) = \sum_n F_n(\mathbf{r})u_{n0}(\mathbf{r}) \quad (1.13)$$

where  $F_n(\mathbf{r})$  is an envelope function. By considering both  $\Phi(\mathbf{r})$  and  $F_n(\mathbf{r})$  slowly varying in space, it allows to recover a Schrödinger-like equation on the envelope functions:

$$(H^{KP} + \Phi(\mathbf{r})) F_n(\mathbf{r}) = E_n(\mathbf{r})F_n(\mathbf{r}) \quad (1.14)$$

where  $H^{KP}$  is the bulk KP Hamiltonian, function of KP matrix elements  $\sim \langle u_{n0} | \hat{p} | u_{n0} \rangle$  and where the terms  $\hbar k$  have been replaced by  $\hat{p} = -i\hbar\nabla$  and  $\hbar^2 k^2$  by  $\hat{p}^2 = -\hbar^2\nabla^2$ .

In the particular case of 1D confinement in  $z$  ( $\Phi(\mathbf{r}) = \Phi(z)$ ), the envelope function is given by  $F_{n\mathbf{K}b}(\mathbf{r}) = e^{i\mathbf{K}\mathbf{R}} f_{n\mathbf{K}b}(z)$ .<sup>4</sup> The application of  $\hat{\nabla}$  operator is thus twofold: i) in the *in-plane* direction  $\mathbf{R} = (x, y)$ , it applies on plane waves and leads to the  $\mathbf{K} \cdot \mathbf{p}$  terms

---

<sup>4</sup>We introduce here the notation:  $\mathbf{K}$  and  $\mathbf{R}$  are *in-plane* 2D vectors,  $z$  is a 1D coordinate in the confinement direction and  $b$  is the index of subband.

as in bulk, giving rise to a continuous energy dispersion versus  $\mathbf{K} = (k_x, k_y)$ ; ii) in the confinement direction  $z$ , it applies on the envelope function  $f_{n\mathbf{K}b}(z)$  and leads to a set of differential equations that need to be solved to obtain the subband energy levels (indexed by  $b$ ). The envelope functions obtained in this way in EMA in Si thin films are compared with TB calculations in Ref. [305], as shown in Figure 1.13.

Note that the confined structures considered (nanowires and slabs/thin films) are not real 1D or 2D structures, as the crystal has a finite extension and a given geometry in the confined direction(s). In some cases, it is interesting to construct a confined “Brillouin zone” (see the discussion in Esseni *et al.* (2005) [82]). In particular, the extension of the BZ in the confined direction will be important in the treatment of spurious states explained below.

**Boundary conditions** The development above considers a potential well in an homogeneous medium (no variation of the KP parameters with space coordinates). In the case of a real interface between two materials, the parameters are space-dependent and the  $u_{n0}$  basis states for KP model differ between the two bulk materials. One way to match the wavefunctions and Hamiltonian at the interfaces has thus to be determined.

A pragmatic way to do this was first proposed in the 1960’s by Harrison [124] and the corresponding KP Hamiltonian was given by Ben-Daniel and Duke (1966) [23]. The 1D EMA Schrödinger equation in this case is given by:

$$\left[ \hat{p}_z \frac{1}{2m^*(z)} \hat{p}_z + V(z) \right] f(z) = Ef(z)$$

where  $m^*(z)$  is discontinuous at the interface, but the envelope wavefunction  $f(z)$  remains continuous, as well as the quantity  $[1/m^*(z)](\partial f/\partial z)$ . Note that as  $\hat{p}_z$  and  $m^*(z)$  don’t commute, the position of each operator is important.

In the case of KP models with more than one band, the correct operator ordering was derived by Burt in 1992 [42] and applied to 8-band KP model by Foreman in 1993 [96], leading to the so-called “Burt-Foreman” operator ordering. For a more detailed analysis of the issue of operator ordering, one can refer to the PhD thesis of Veprek (2009) [374], as well as practical examples in more recent studies [98, 136].

**Spurious states** As stated earlier, spurious states can appear in the simulation of heterostructures with KP models. These states are non-physical states that appear in confined band structures, due to the non-periodicity of the bulk KP models. They appear in models where both negative and positive band dispersions are taken into account (such as 8-band or full-zone KP models) and are coming from remote  $\mathbf{k}$  states that are projected in the 2D/1D Brillouin zone. In the case of 8-band KP model, it was shown that different operator ordering and boundary conditions can affect the apparition of spurious states [375, 49].

In this work, we follow the work of Refs. [151, 383] and filter the spurious state in the reciprocal space. The idea consists in filtering the spurious states according to their spatial frequencies. The Hamiltonian is projected on  $\sin(k_z z)$  and  $\cos(k_z z)$  testfunctions that

correspond to well-determined oscillations in the confinement direction.<sup>5</sup> The maximum oscillation frequency of the testfunctions depends on the number of testfunctions  $N_{tst}$  used in the calculations, which can be more than a hundred to assure convergence. In this case, the corresponding  $k_{z,max} = \frac{N_{tst}2\pi}{L}$  goes outside the bulk BZ and/or beyond the domain of validity of the KP parametrization, leading to spurious states. These states are avoided by considering a “padding” zone: the real space length  $L_z$  is extended to  $L = L_z + L_{pad}$  in order to keep the highest  $k$  in the range of the validity of the KP parametrization:  $k_{z,max} < k_{max} = \frac{2\pi}{a}$ . The potential is then raised up in this “padding” region, allowing to filter the spurious states for any KP models and to adjust the range of spatial oscillations within the domain of validity of the KP parametrization.

### NP-EMA

For the device modeling point of view, the great advantage of EMA over full-band empirical models is that it gives an analytic expression for the  $E(\mathbf{k})$  dispersion. In this way, the integration over  $\mathbf{k}$  can be converted into an integration over the energy and the computation time is drastically decreased. For example, the knowledge of the wavefunctions at the subband minima is then sufficient to compute the charge in a thin film or nanowire. However, in III-V materials, the parabolic approximation fails as the energy dispersion close to the  $\Gamma$  point is strongly non-parabolic, due to the coupling between conduction and valence bands (see Figure 1.15). This analytic integration is in principle no longer possible, and Schrödinger equation needs to be solved on a fine  $\mathbf{k}$  mesh. To circumvent this issue, some corrections have been derived to account for non-parabolic effect in a simple analytic EMA model. In this model, the bulk energy dispersion is given as (see Appendix A.1.1 for details about the derivation of this expression):

$$\varepsilon(\mathbf{k}) = \frac{1}{2\alpha} \left\{ -1 + \sqrt{1 + 4\alpha\gamma(\mathbf{k})} \right\} \quad (1.15)$$

where  $\gamma(\mathbf{k}) = \frac{\hbar^2 k^2}{2m^*}$ . The dispersion obtained with this expression and the effect of non-parabolicity on InAs band structure and subbands energy levels are schematically shown in Fig. 1.15.

For confined structures, Schrödinger equation in the envelope function approximation has to be solved and Eq. (1.15) leads to a kinetic energy operator that depends on  $\mathbf{k}$ . Indeed, the non-parabolicity couples the modes in the confinement direction to the transverse modes  $(x, y)$  and makes it *a priori* necessary to solve a Schrödinger equation for each in-plane  $(k_x, k_y)$  point. Further approximations need thus to be made to keep the analytic advantage of EMA models and to obtain a simple NP-EMA model that is numerically efficient. To avoid simplification, some studies proposed to solve the NP Schrödinger equation by using iterative method [388, 146]. These methods were not used here for sake of computation efficiency. We rather used analytical EMA models that include NP corrections

---

<sup>5</sup>Note that this new basis also allows to reduce the size of the KP matrix in big systems, where the finite difference in real space has to be done on a fine mesh, and can thus be more computational efficient.

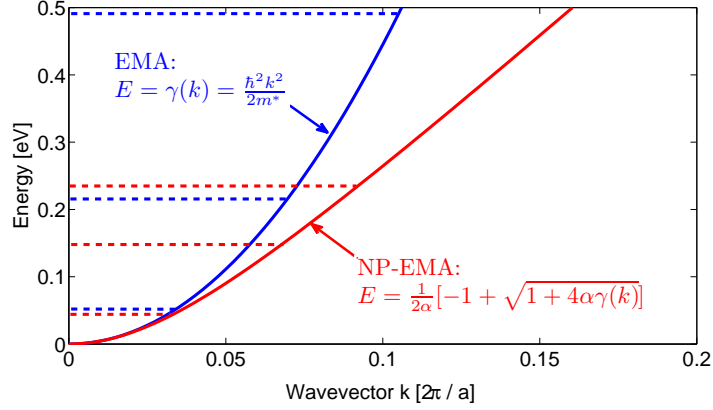


Figure 1.15. Simple schema of the energy levels in thin film and bulk dispersion obtained with EMA and NP-EMA models, using parameters of InAs  $\Gamma$  valley:  $m^* = 0.023 m_0$ ,  $\alpha = 2.6$  and  $t_{ch} = 17$  nm.

and keep the resolution as simple as parabolic EMA in numerical point of view. A few different models were proposed in the literature, such as the ones of Altschul *et al* (1992) [7], Jungemann *et al.* 1993 [153], Fischetti and Laux (1993) or Jin *et al.* (2007) [149], with different approximations. In this work, we use two models: Jungemann [153] and Jin [149] models. In the first one, kinetic energy operator's dependency on  $\mathbf{k}$  is neglected and only the in-plane  $E(k_x, k_y)$  dispersion takes into account NP corrections. In the second model, the kinetic energy operator is projected on parabolic wave-functions, allowing to take into account NP corrections in both transport and quantization direction. The position of  $\mu^{\text{th}}$  subband energy level is given in this model by:

$$E_{\mu}^{NP} = U_{\mu} + \frac{1}{2\alpha} \left\{ -1 + \sqrt{1 + 4\alpha(E_{\mu} - U_{\mu})} \right\} \quad (1.16)$$

where  $E_{\mu}$  is the parabolic level and  $U_{\mu} = \int |\zeta_{\mu}^P(z)|^2 U(z) dz$ , with  $\zeta_{\mu}^P$  the parabolic wave function and  $U(z)$  the total potential energy.

### 1.2.2 GaAs and InAs thin films

We compare in this section the TB and NP-EMA models in quasi-2D thin layers of GaAs and InAs, corresponding to thin films in FDSOI technologies (confined along the gate stack direction). As the treatment of boundary condition is still under debate and degree of accuracy differs between the methods, we will consider free standing films with hard-wall boundary conditions (the wavefunction is considered as zero outside the semiconductor).

#### TB

Semi-empirical atomistic  $sp^3d^5s^*$  TB model with spin-orbit is used to compute the band structure of InAs and GaAs nanostructures (thin films and nanowires). The hopping and on-site parameters are taken from Ref. [38] and boundary conditions are set as in Ref. [250], with a surface passivated with pseudo-H atoms. The coupling parameters of these pseudo-H is chosen so that the surface states are well separated and lie far from the conduction and valence band edges of the semiconductor. This leads to nearly hard-wall boundaries and negligible wave-function penetration (WFP). This allows to compare the different models without the influence of the up-to-now unresolved problem of semiconductor/oxide interfaces.

The effective masses at the bottom of the subbands are extracted from the second derivative of the energy dispersion, calculated by the Hellman-Feynman theorem:

$$\frac{\partial^2 E}{\partial k^2} = \langle \psi | \frac{\partial^2 \hat{H}}{\partial k^2} | \psi \rangle + 2 \Re \left\{ \left( \frac{\partial \langle \psi |}{\partial k} \right) \frac{\partial \hat{H}}{\partial k} | \psi \rangle \right\}$$

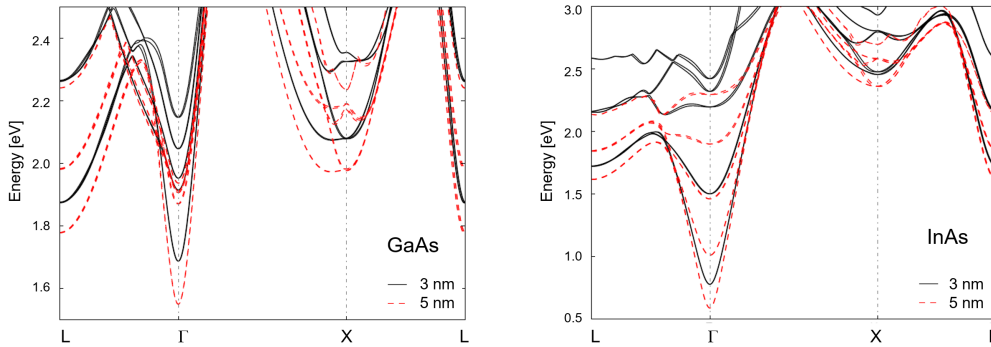


Figure 1.16. Conduction band structure for  $t_{ch}$  of 3 nm (black solid lines) and 5 nm (red dashed lines) for GaAs (left) and InAs (right) (001) thin films passivated with pseudo-H atoms, obtained with TB model in TBSim [238].

The full band structure for thin films of InAs and GaAs confined in (001) direction and film thicknesses  $t_{ch} = 2$  and 5 nm are plotted in Figure 1.16. One first notes that the lowest subband remains at the  $\Gamma$  point and the study of wavefunction symmetry shows that it has the  $s$ -like character of the  $\Gamma$  bulk valley for thickness down to 2 nm.

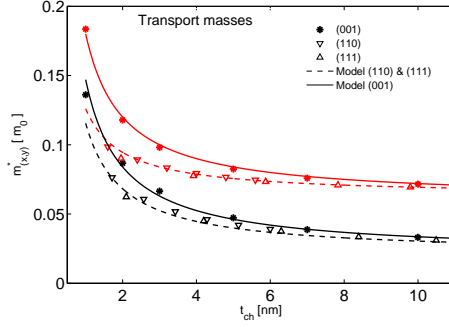


Figure 1.17. Transport effective mass  $m_{(x,y)}$  in InAs and GaAs thin films obtained with TB model in TBSim, as a function of film thickness.

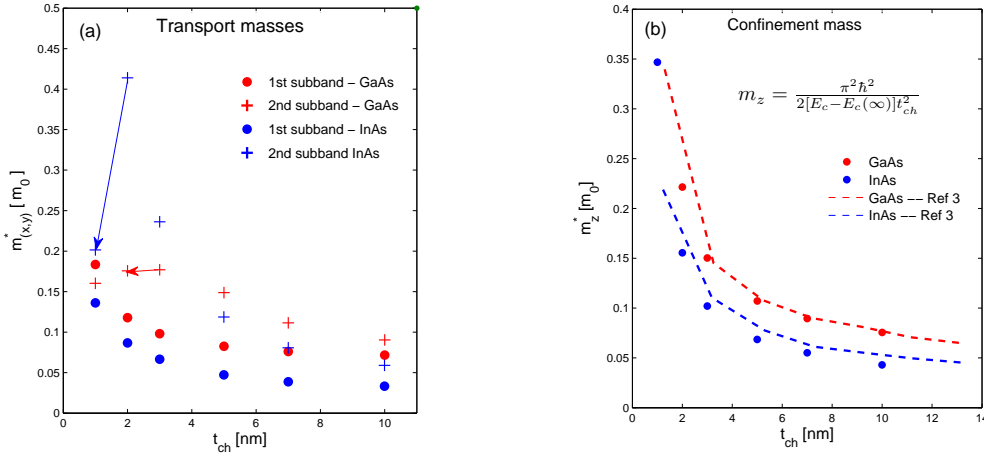


Figure 1.18. Transport  $m_{(x,y)}$  (a) and confinement  $m_z$  (b) effective masses at the  $\Gamma$  point in GaAs (red) and InAs (blue) obtained by TB, as a function of film thickness. The arrows show the transition where  $\Delta_z$  valleys become lower than  $\Gamma$  valley (see Fig. 1.16 and text). Results from Ref. [190] are also shown in (b) for comparison.

The transport effective masses of the lowest subband for thin films with different confinement orientations are plotted in Figure 1.17. Their dependence can be modeled with an analytic formula used in compact models [134]:  $m(d) = m_{\text{bulk}} \left(1 + \frac{d_0}{d}\right)$  where  $d$  is the confinement dimension (film thickness in this case) and  $d_0$  is a fitting parameter (equal to 6.5 nm (2 nm) for InAs (GaAs) film confined in (001) orientations and 4.5 nm (1 nm) for InAs (GaAs) films confined in the two other orientations). The lowest conduction band edge remains at the  $\Gamma$  point, but the effective mass in (001) films increases more rapidly with confinement, maybe due to the influence of boundary conditions.

Figure 1.18(a) also shows the in-plane effective mass of the second subband in (001)

films and the arrow shows the transition point where the  $\Delta_z$  bulk valley projected in the 2D BZ center has an impact on the 2nd subband. Figure 1.18(b) shows the “quantization effective mass” recast from the energy shift of the subband. Indeed, in the case of infinite quantum well, the wave-vector along the confinement direction (supposed along  $z$  axis) is given by  $k_z = \frac{n\pi}{t_{ch}}$ , where  $n \in \mathbb{N}$  and  $t_{ch}$  is the thickness of the well. The energy level of the different subbands can be expressed in a first approximation (parabolic model) as:

$$E_{c,n} = E_c^0 + \frac{\hbar^2 k_n^2}{2m_z} = E_c^0 + \frac{n^2 \pi^2 \hbar^2}{2m_z t^2} \quad (1.17)$$

where  $E_c^0$  is valley minimum in bulk,  $n$  is the index of subband and  $m_z$  is the effective mass along the confinement axis  $z$  (defined here as the “quantization effective mass”). The energy shift  $\Delta E_c = E_{c,1} - E_c^0$  as a function of  $1/t_{ch}^2$  obtained by TB is plotted in Fig. 1.19, and compared with the analytic parabolic formula above. As expected, the energy shift extracted from TB doesn’t follow a  $1/t_{ch}^2$  trend due to NP effects and the parabolic EMA leads to strongly overestimated subband energies for films with  $t_{ch} < 10$  nm. This is also more pronounced for InAs than GaAs, due to its higher NP coefficient (see Table 1.7). To better account for this effect, the bulk NP dispersion in Eq. (1.15) can be used to derive an analytic expression of the subband energy [277], when no WFP is taken into account. In that case, the subband energy level is approximated by:

$$E_{c,n} = E_c^0 + \frac{-1 + \sqrt{1 + 4\alpha \frac{\hbar^2 k_z^2}{2m_z}}}{2\alpha} = E_c^0 + \frac{-1 + \sqrt{1 + 2\alpha \frac{\hbar^2}{m_z} \left(\frac{n\pi}{t_{ch}}\right)^2}}{2\alpha} \quad (1.18)$$

where  $\alpha$  is a non-parabolic coefficient and  $k_z$  is defined as previously  $k_z = \frac{n\pi}{t_{ch}}$ . The result obtained with this expression is also plotted in Figure 1.19 and we see that a very good agreement between the analytic model and TB can be found with a single effective mass  $m^*$  equal to the bulk one but with a boosted  $\alpha$  parameter (see Table 1.7 and discussion about NP-EMA model below).

### NP-EMA

Subbands energy levels extracted with the NP-EMA model of Jin *et al.* (2007) [149] are also plotted in Fig. 1.19, with parameters given in Table 1.7.

As explained above, the relation  $\Delta E(1/t_{ch}^2)$  is no more linear due to NP effect. Moreover, in order to obtain good agreement with TB, the NP coefficient  $\alpha$  has to be boosted compared to the theoretical value given by Eq.(A.3). This observation together with the different behavior in transport and quantization direction of  $m^*$  extracted by TB indicates that NP effects in transport and quantization directions may behave differently with confinement thickness and might thus need to be described with different NP coefficients. One notes here the almost perfect agreement between the NP-EMA PS numerical resolution and the analytic model in Eq. (1.18).

By comparing our results with the recent publication of Zerveas *et al.* (2016) [401], one finds an overall good agreement with the different empirical method and *ab initio* tools, including the simple NP-EMA. This tends to comfort our idea and validate the approach used for device modeling, based on NP-EMA model.

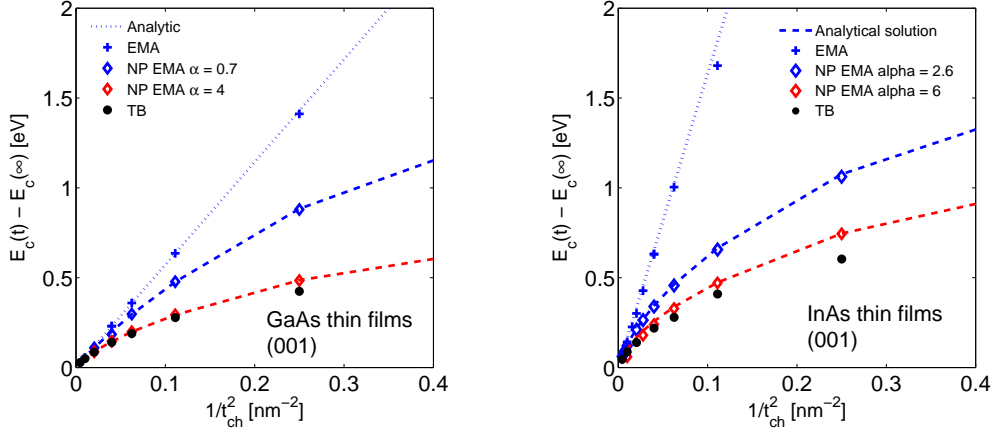


Figure 1.19. Lowest subband energy levels difference  $E_{\Gamma} - E_{\Gamma}(\text{bulk})$  in GaAs (left,  $E_g(\text{bulk}) = 1.41$  eV) and InAs (right,  $E_g(\text{bulk}) = 0.37$  eV) simulated with EMA and NP-EMA models in UTOX and TB model in TBSim. Results do not include WFP effects. Symbols are PS simulations, while lines are analytic results (see text).

Table 1.7. Parameters used for EMA and NP-EMA calculations, extracted from bulk TB calculation with TBSim for InAs and GaAs and from Ref. [264] for InGaAs.  $\alpha$  values in parenthesis are extracted by fitting the TB data for confined structures (see text). For  $\Delta$  valley both transverse and longitudinal masses are given.

Material	Valley	$E_g$ [eV]	$m^*$ [ $m_0$ ]	$\alpha$ [ $\text{eV}^{-1}$ ]
InAs	$\Gamma$	0.37	0.023	2.6 (6)
$\text{In}_{0.57}\text{Ga}_{0.47}\text{As}$	$\Gamma$	0.74	0.041	1.3
GaAs	$\Gamma$	1.41	0.066	0.7 (4)
	L	1.7	0.09 / 1.73	0.2
	$\Delta$	1.9	0.18 / 1.86	0.1

## KP

The band structure obtained with 8-band KP model in InAs thin film in (001) confined direction is compared with TB in Figure 1.20. The Burt-Foreman Hamiltonian was resolved here in real-space in a finite difference scheme and a coupling parameter  $E_p = 18$  eV. The theoretical  $E_p = 20$  eV leads to spurious solutions, as shown in Ref. [96]. The comparison with TB model shows that the conduction band structure is well described with 8-band KP model close to  $\Gamma$  point, but that the confinement effect on valence band is overestimated. The spin splitting due to symmetry breaking effects in nanostructures, inducing a lift of the spin degeneracy for  $k \neq 0$  in TB band structure, is also missing in the KP description.

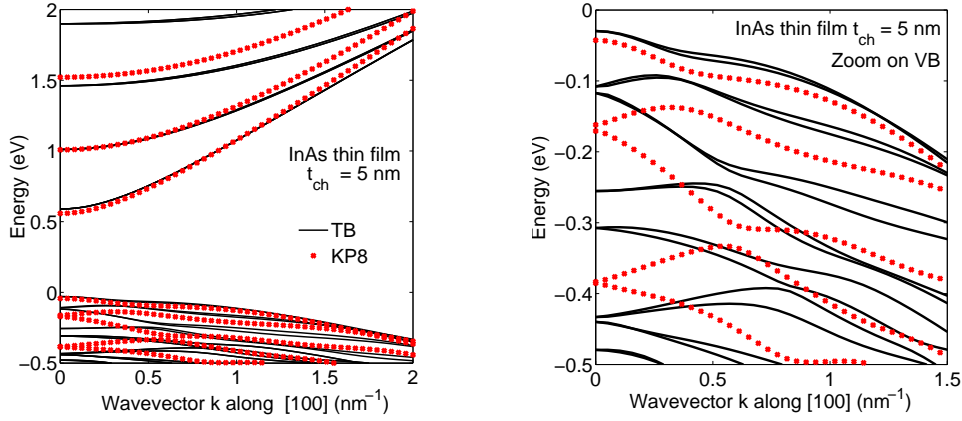


Figure 1.20. Band structure around the  $\Gamma$  point of (001) InAs thin films with  $t_{ch} = 5$  nm obtained with 8-band KP ( $E_p = 18$  eV) and TB models in TBSim package.

Moreover, the full-band structure over the entire 2D BZ of GaAs thin films in (001) confined direction is also computed with the 27-band KP model (54-band without spin-orbit), with a reciprocal space resolution of the Hamiltonian projected on sinusoidal functions, allowing the filtering of the spurious states as explained above. The band structure is shown in Figure 1.21 and compared with TB model. An overall good agreement is found for the two models. Some discrepancies are found for the  $\Delta_z$  valleys projected in the  $\Gamma$  point (second and third subbands of TB model) and the  $\Delta_x$  and  $\Delta_y$  valleys at the X point which are lying lower in TB model with the parameters given by Jancu *et al.* (1998) [145]. This difference, also encountered in the bulk band structure, is due to the parametrization.

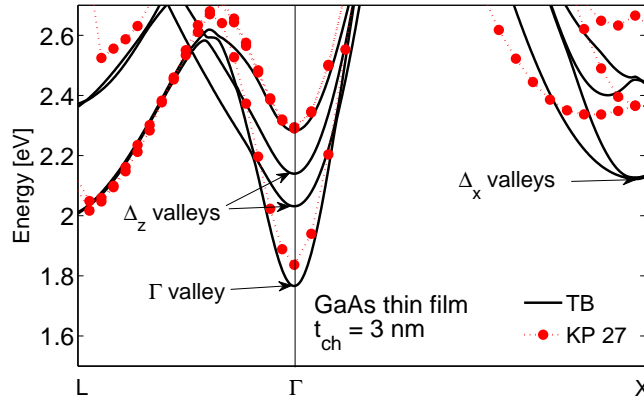


Figure 1.21. Band structure of (001) GaAs thin films with  $t_{ch} = 3$  nm obtained with 27-band KP and TB models in UTOX package.

## LCBB

Finally confined thin-film structures are simulated with a Linear Combination of Bulk Band (LCBB) approach with local EPM bulk model and following the methodology of Esseni *et al.* (2005) [82] and Rideau *et al.* (2007) [302, 303]. Unlike calculations in Si and Ge, both conduction and valence bands need to be included in the LCBB calculations in order to reproduce the correct position of the  $\Gamma$  valley in III-As materials, which increases the difficulty and computational cost of this method. The results obtained and the comparison with TB simulations for GaAs and  $\text{In}_{0.57}\text{Ga}_{0.43}\text{As}$  thin films with thickness of  $t_{ch} = 3$  nm are shown in Figure 1.22. A VCA approach is used for  $\text{In}_{0.57}\text{Ga}_{0.43}\text{As}$  materials for both LCBB and TB calculations. A linear interpolation is used for EPM parameters, while the interpolation method presented in Section 1.1.8 is used for TB.

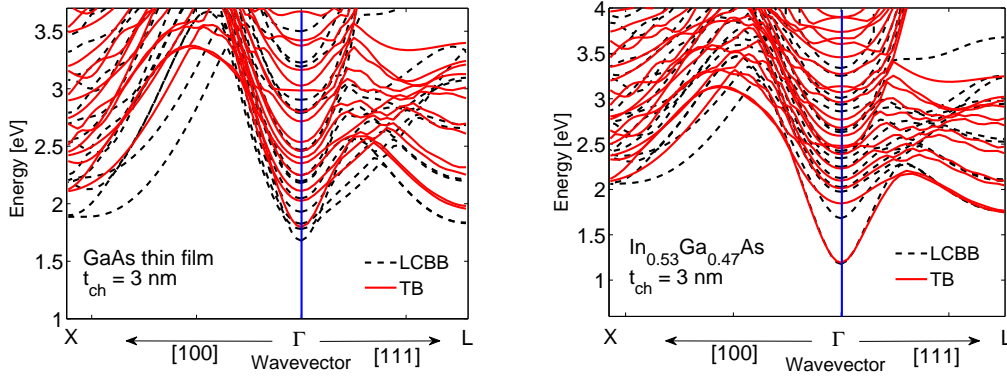


Figure 1.22. Band structure of (001) GaAs (left) and  $\text{In}_{0.53}\text{Ga}_{0.47}\text{As}$  (right) thin films with  $t_{ch} = 3$  nm obtained with LCBB (EPM) and TB models in UTOX package.

For the GaAs thin films, the lowest subbands lie at lower energy in LCBB compared to TB. The energy difference between the lowest subbands at  $\Gamma$  and along the  $\Delta$  line are also reduced in LCBB compared to TB. These effects are probably due to the bulk parameterization. For  $\text{In}_{0.57}\text{Ga}_{0.43}\text{As}$  thin films, an overall good agreement is found between the two approaches for the lowest conduction bands. In the LCBB calculation, the valley minimum along the  $\Delta$  line is shifted away from X symmetry point, while it remains at X in the TB calculation, due to the parametrization used (as mentioned in Section 1.1.4).

### 1.2.3 III-As and SiGe nanowires

The band structure and electronic properties of III-As and SiGe nanowires are investigated in this section with an atomistic TB approach, with the  $sp^3d^5s^*$  TB model in TB\_Sim package and parameters for SiGe discussed in Section 1.1.8. The VCA and random supercell approaches are compared in the case of SiGe NWs.

**III-As NWs** The conduction band edge and transport effective masses of the lowest subband for InAs and GaAs nanowires with different orientations are plotted in Figure 1.23. One notes that the variation of lowest subband effective mass is similar in the  $\langle 110 \rangle$  and  $\langle 111 \rangle$  directions, but increases more rapidly in the  $\langle 001 \rangle$  direction. As for thin films, its dependence can be modeled with the same analytic formula, where  $d$  is the wire radius in this case and  $d_0$  is a fitting parameter (equal to 8 nm (3.5 nm) for InAs (GaAs) in  $\langle 001 \rangle$  orientation and 4.5 nm (1.2 nm) for InAs (GaAs) NWs in the two other orientations). The position of the conduction band edge is rather independent on the wire orientation, as seen in Fig. 1.23, due to the isotropic character of the  $\Gamma$  valley and confirming that the lowest subband remains from the bulk  $\Gamma$  valley.

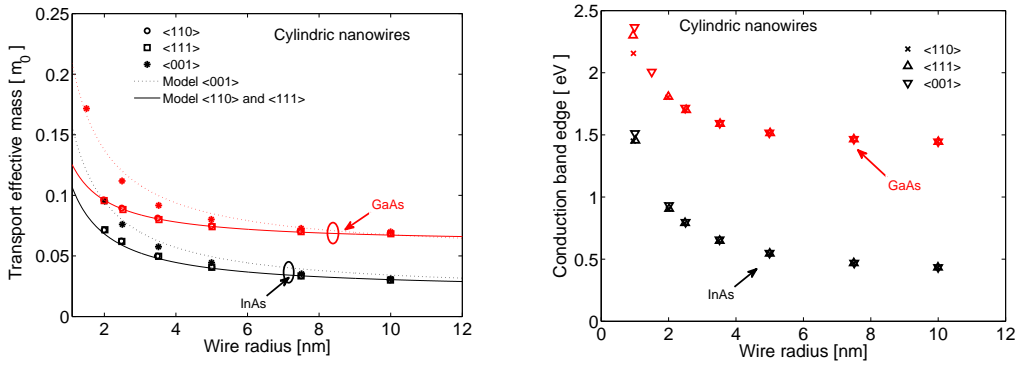


Figure 1.23. Transport effective mass  $m_x$  (left) and conduction band edge (right) in InAs and GaAs nanowires obtained with TB model in TBSim, as a function of wire radius.

**SiGe NWs** In Si and Ge materials, the conduction band minima are not isotropic anymore and the influence of the confinement on the band structure can be more complex. The band structures of pristine Si and Ge NWs with diameter  $d=8$  nm and different orientations are shown in Figure 1.24. Unlike III-As materials, the confinement direction affects the character of the lowest conduction subband, whose effective mass and degeneracy are summarized in Table 1.8.

In SiGe NWs, a discontinuity in the band gap and effective mass is found around  $x \simeq 0.8$  as in the bulk case, as shown in Figure 1.25. The sharp transition can be accompanied with a decrease (in the  $\langle 110 \rangle$  and  $\langle 111 \rangle$  orientations) or increase (in the  $\langle 001 \rangle$  orientation) of the effective mass of the lowest subband. The calculation with random distribution of Si and Ge atoms is compared with the VCA model presented in the previous section and a good agreement is found, especially for the effective mass of the lowest subband which is the most relevant for transport (as discussed in the Chapter 3).

Orientation	Si NW subbands		Ge NW subbands		
	A	B	A	B	C
$\langle 001 \rangle$	$\Delta_4$ (0.22)	$\Delta_2$ (0.91)	$\Delta_4$ (0.20)	$\Delta_2$ (0.85)	$L_4$ (0.60)
$\langle 110 \rangle$	$\Delta_2$ (0.19)	$\Delta_4$ (0.56)	$L_2$ (0.09)	$\Delta_4$ (1.31)	$L_2$ (1.14)
$\langle 111 \rangle$	$\Delta_6$ (0.44)	-	$\Delta_6$ (0.42)	$L_3$ (0.27)	$L_1$ (1.61)

Table 1.8. Properties of the NW subbands indicated in Fig. 1.24: Origin of the subband (projected valley  $\Delta$  or L), degeneracy (subscript), and effective mass in atomic unit (in parenthesis).

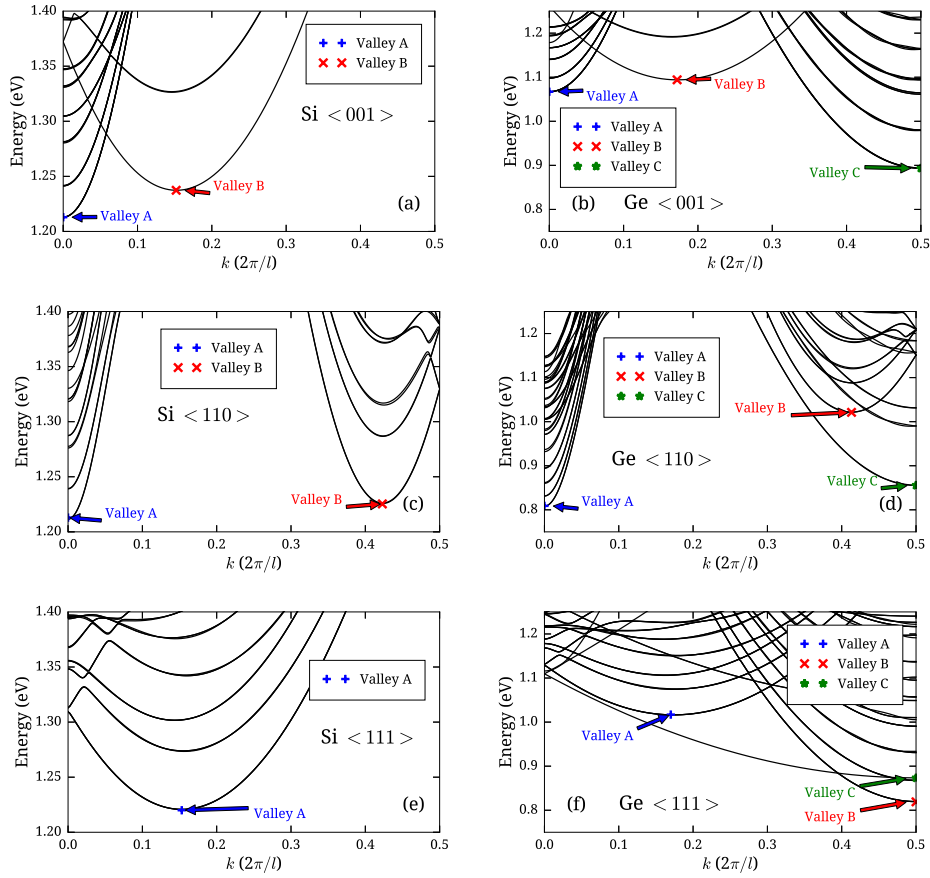


Figure 1.24. Conduction band structure of pristine Si (left) and Ge (right) NWs with 8 nm diameter oriented in  $\langle 001 \rangle$  (a-b),  $\langle 110 \rangle$  (c-d) and  $\langle 111 \rangle$  (e-f) directions, obtain with TB model in TBSim. Properties of the subbands indicated in each figure are summarized in Table 1.8. The origin of the vertical energy axis is set to the top of the bulk valence band.

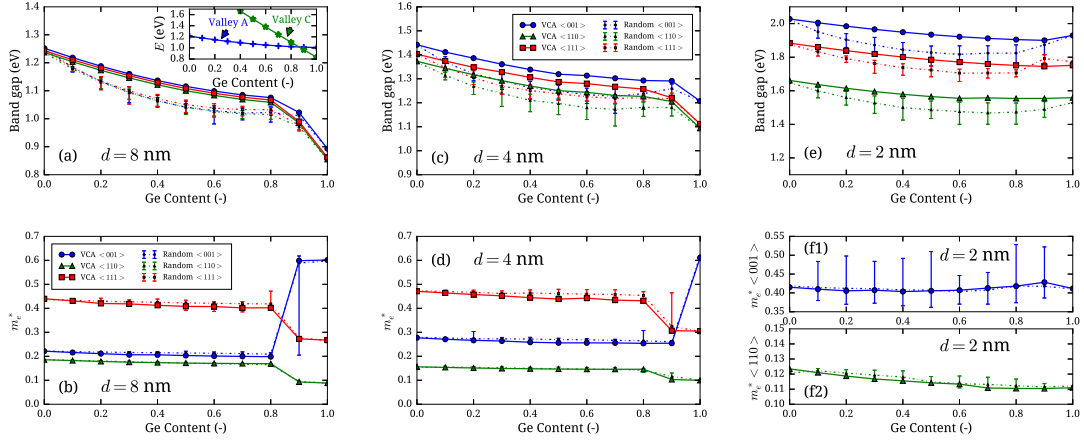


Figure 1.25. Band gap (up) and electron effective mass of the lowest subband (down) in SiGe NWs with three orientation and diameters of 8nm (a-b), 4nm (c-d) and 2nm (e-f). The symbols with solid lines are VCA calculations, while dashed lines are calculations with random distribution of atoms (one hundred samples were randomly generated, the error bar showing the minimum and maximum values obtained; see text for details). Valley labels in the inset of (a) are defined in Fig. 1.24(a-b). Lines are guides to the eye.

### 1.3 Conclusion of the Chapter

In this Chapter, we investigated the electronic properties of bulk and confined  $\text{In}_x\text{Ga}_{1-x}\text{As}$  and  $\text{Si}_{1-x}\text{Ge}_x$  materials. The effective masses and position of the different valleys as well as the total density-of-states were extracted from the bulk band structure and the values of deformation potentials were reviewed. This study gave us insight in the knowledge of the electronic structure of these materials and the controversy on the position of satellite valleys in InAs and InGaAs materials.

The effective mass and band structure of quasi-2D and quasi-1D nanostructures were also computed with different approaches and the effect of the non-parabolicity in the confinement direction in III-As thin films were discussed.

Moreover, different empirical models were introduced, that will be used along the next Chapters for the calculation of electrostatic and transport properties. For electrostatic calculations, presented in Chapter 2, the NP-EMA model will be used and compared with atomistic TB to model capacitance in thin-films. For calculations of transport properties presented in Chapter 3, NP-EMA and low-order KP models will be used to compute the carrier low-field mobility in planar structures, while TB model will be used for the calculation of carrier effective mobility and drift velocity at high field in nanowires. In Chapter 4, quantum transport calculations in a whole device are performed within the EMA and low-order KP model framework only.

## Chapter 2

# Electrostatics and trap dynamics

In transistors based on Metal-Oxide-Semiconductor (MOS) structures, the current is enabled by the creation of a charge inversion in the channel. The switching capability of the device is thus strongly dependent on the electrostatic characteristics of the structure, namely the inversion charge achievable by the application of a gate voltage  $V_{gs}$ .

One of the major concern in III-V MOSFETs is the charge inversion achievable, which is limited by the low density-of-states of the  $\Gamma$  valley available as well as the high traps density present at the interface between III-V semiconductor and oxides. These effects hinder the performance gain of their high electron mobility, as the overall current needs both high carrier velocity and density:  $\mathbf{j} = n\mathbf{v}$ .

In this Chapter, the electrostatic characteristics of long-channel devices are investigated by Poisson-Schrödinger simulations in the TB and NP-EMA approaches. The capacitances obtained with the different models in bulk and Ultra-Thin Body and BOX (UTBB) ideal devices (without traps) are compared with each other. In the second part of the Chapter, the influence of trap response at room-temperature is discussed by analysis of experimental data of MOSCAP devices fabricated at CEA-LETI and the models available for the simulation are exposed.

## 2.1 Capacitance of ideal MOS devices

### 2.1.1 Modeling strategy

#### Non-linear Poisson solver

When a difference of potential is applied at the two terminals of a MOS structure, the system is polarized and a charge can be achieved in the semiconductor. At equilibrium, the potential and the charges in the system must satisfy the Poisson equation:

$$\nabla \cdot (\epsilon_r \mathbf{E}) = \frac{\rho(\mathbf{r})}{\epsilon_0} \quad (2.1)$$

where  $\mathbf{E} = -\nabla V$  is the electric field and  $\rho = e(p - n + N_{ch})$  is the electric charge density, accounting for electrons  $n$  and holes  $p$  free carriers and dopant concentration  $N_{ch} = N_D - N_A$  ( $N_D$  and  $N_A$  denoting the donor and acceptor ions resp.). For bulk

MOSFET at low gate voltage  $V_{gs}$ , the quantum confinement is negligible and we can consider a classical formula for the free carrier charge density:

$$n(\mathbf{r}) = N_c^{3D} \mathcal{F}_{1/2} \left( \frac{E_c(\mathbf{r}) - E_F}{k_B T} \right) \quad (2.2)$$

where  $N_c^{3D}$  is the classical effective density-of-states related in bulk to the effective mass  $m^*$  through the relation ( $g_s = 2$  is the spin degeneracy):

$$N_c^{3D} = g_s \left( \frac{m^* k_B T}{2\pi \hbar^2} \right)^{3/2}$$

and  $\mathcal{F}_i(\eta)$  is the Fermi-Dirac integral of order  $i$  defined as:

$$\mathcal{F}_j(\eta) = \frac{1}{\Gamma(j+1)} \int_0^\infty dt \frac{t^j}{1 + \exp(t - \eta)}$$

The self-consistent resolution of Eqs. (2.1) and (2.2) can be performed with iterative solvers, often referred to as “non-linear Poisson solvers”. The high non-linearity comes from the exponential dependancy of the density over the potential and makes the convergence of the system hard to assure. To get a good convergence, the system is transformed into a set of linear equations solved iteratively, in a predictor-corrector scheme [359] (see, e.g., Refs. [280, 131, 359] or [316] for details).

### Poisson-Schrödinger solvers

When  $V_{gs}$  is increased, the electric field at the SC-oxide interface increases and produces a V-shape potential profile. This electrical confinement leads to the creation of 2D electron gas (2DEG) and quantified energy levels (subbands). 2DEG can also be created by physical confinement in thin-films or NWs. In these cases where the confinement is strong, the subbands energy levels need to be computed through the resolution of the Schrödinger equation. In order to simulate numerically, e.g., the capacitance of a MOS structure, the Poisson and Schrödinger equations are then solved self-consistently in the scheme presented in Figure. 2.1.

The free carrier charge density is here given at equilibrium as a function of the wavefunctions  $\psi_{n\mathbf{K}}^\sigma$  at wavevector  $\mathbf{K}$  in the band  $n$  and with spin  $\sigma$ :

$$n(\mathbf{r}) = -e \sum_{n, \mathbf{K}, \sigma} |\psi_{n\mathbf{K}}^\sigma(\mathbf{r})|^2 f \left( \frac{E_n(\mathbf{K}) - E_F}{k_B T} \right) \quad (2.3)$$

As mentioned in the previous Chapter, the use of the EMA simplifies greatly the calculation of the density, as an analytic relation between  $E$  and  $K$  exists and the wavefunctions and energy levels at the  $\Gamma$  point are sufficient to determine the charge density. In this case, the calculation of the charge density can be simplified as follows. First, the discrete summation over in-plane wavevectors  $\mathbf{K}$  is transformed into a continuous integral and

the norm of the plane wave part of the wavefunctions are averaged, leading to a simple renormalization factor  $1/L^2$  and only the 1D envelope function  $\phi_n(z)$  remains:

$$n(z) = -eg_s \sum_n \frac{\mathcal{L}^{\mathcal{Z}}}{(2\pi)^2} \int d^2K \frac{1}{\mathcal{L}^{\mathcal{Z}}} |\phi_n(z)|^2 f\left(\frac{E_n(\mathbf{K}) - E_F}{k_B T}\right) \quad (2.4)$$

Then the analytic relation between  $E$  and  $K^2$  is used to transform the integral:

$$\int d^2K = \int \frac{2\pi m^* dE}{\hbar^2}$$

Finally, the definition of the Fermi-Dirac integrals shown above is used to obtain the expression of the charge density:

$$n(z) = -e \sum_n |\phi_n(z)|^2 N_c^{2D} \mathcal{F}_0\left(\frac{E_n(0) - E_F}{k_B T}\right) \quad (2.5)$$

where the expression of the 2D effective density-of-state is used:  $N_c^{2D} = g_s \frac{m^* k_B T}{2\pi \hbar^2}$ . In the case of an anisotropic dispersion, as  $\Delta$  and L valleys that are modelled by ellipsoids with transversal mass  $m_t$  and longitudinal mass  $m_l$ , the effective mass  $m^*$  entering the equation needs to be determined. A “density-of-states” effective mass  $m_{DOS}^* = \sqrt{m_x m_y}$  is defined in practice, where  $m_x$  and  $m_y$  depend on the confinement orientation and their relation to  $m_t$  and  $m_l$  can be determined through the change of coordinate references and the “generalized effective mass approach” for arbitrary device orientation developed and discussed in details in Refs. [83, 196, 296].

For NP-EMA models, the charge density calculated in the self-consistent loop is corrected according to the model used. For Jin’s model, it is given by [149]:

$$n_{2D}(z) = -eg_s \frac{k_B T}{2\pi \hbar^2} \sum_{\mu} m_d^{\mu} \left\{ [1 + 2\alpha(E_{\mu}^{NP} - U_{\mu})] \mathcal{F}_0(\eta) + 2\alpha k_B T \mathcal{F}_1(\eta) \right\} |\zeta_{\mu}(z)|^2$$

where  $\mu$  indexes the different valleys and subbands and  $m_d^{\mu}$  is the DOS effective mass. The NP energy level  $E_{\mu}^{NP}$  is determined through the relation given in the Chapter 1 Eq.(1.16). The charge density given by Jungemann’s model [153] follows the same expression, replacing  $(E_{\mu}^{NP} - U_{\mu})$  by  $E_{\mu}^P$ .

In TB, this analytic transformation cannot be performed and the charge density must be computed on the TB atomic mesh ( $z_i$  being the position of the  $i^{\text{th}}$  atom) by integration over a refined  $\mathbf{K}$  mesh on which the wavefunctions and energies are computed:

$$n(z_i) = -e \sum_{n, \mathbf{K}, \sigma} |\psi_{n\mathbf{K}}^{\sigma}(z_i)|^2 f\left(\frac{\mathcal{E}_n(\mathbf{K}) - \mathcal{E}_F}{k_B T}\right)$$

where here  $|\psi_{n\mathbf{K}}^{\sigma}(z_i)|^2$  denotes the weight of the wavefunction on the atomic orbitals of the atom at  $z_i$ . This charge is then transferred (interpolated) to the Poisson solver, which uses a finite difference square mesh, extended in the oxides and metal gate contacts.

### Numerical resolution: Newton-Raphson iteration scheme

The schematic Poisson-Schrödinger self-consistent loop is shown in Figure 2.1. A potential guess  $V(z)$  is first set in Schrödinger equation and eigenvalues and eigenvectors are computed. They are then used to compute the charge density and its derivative as a function of the potential, and re-injected in the non-linear Poisson equation, in the framework of a Predictor-Corrector Newton-Raphson scheme. In this scheme, the potential at the  $i^{\text{th}}$  step is computed from the previous  $(i - 1)^{\text{th}}$  step as [280, 359]:

$$[\nabla \cdot \varepsilon(\mathbf{r})\nabla + \delta\rho^{i-1}(\mathbf{r})]V^i(\mathbf{r}) = \delta\rho^{i-1}(\mathbf{r})V^{i-1}(\mathbf{r}) - \rho^{i-1}(\mathbf{r}) \quad (2.6)$$

where  $\delta\rho(\mathbf{r}) = \frac{\delta\rho(V,\mathbf{r})}{\delta V(\mathbf{r})}$  denotes the local derivative of the charge density with respect to the potential (or Jacobian).

The self-consistent resolution of Poisson and Schrödinger equations resembles the non-linear Poisson solver, where the charge density depends on the outputs from the eigenvalue Schrödinger solver. In this case, the derivative of the density over the potential is not analytic and needs to be performed numerically. Some approximations are usually used to compute it.

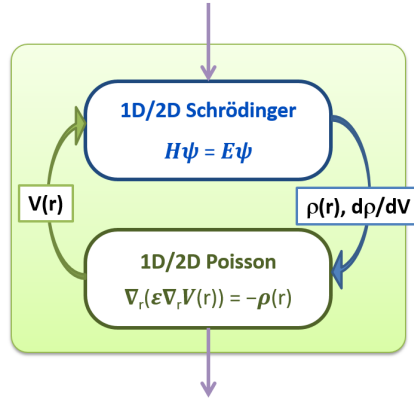


Figure 2.1. Schema for the self-consistent resolution of Poisson and Schrödinger equations.

Another self-consistent scheme was used in Pereira (2015) [280], using an “effective” density prefactor  $N_c^{3D}$  in a non-linear Poisson solver, calculated from the Schrödinger charge density. This can be useful when the Schrödinger equation is particularly numerically expensive, or in the framework of Quantum Drift-Diffusion, as it will be discussed in the Chapter 4.

In UTOXPP, the linear system for Poisson equation is solved with either a standard LU factorisation technique or a Successive Over-Relaxation (SOR) method, as implemented and discussed in Pereira (2015) [280]. Schrödinger equation is solved with either Lanczos or QR eigenvalues solvers, implemented in the Lapack package and libraries available for

C/C++. The self-consistency is assured by a predictor-corrector scheme presented above. A simpler Kerker mixing was also used and compared in Pereira (2015) [280].

In `TB_Sim`, Poisson equation is solved with a conjugate gradient method. Schrödinger equation is solved with a Jacobi-Davidson sparse matrix solver for TB and Lanczos solver for EMA and KP models. The self-consistency is performed by a Newton-Raphson method to insure convergence. DIIS (Direct Inversion of the Iterative Subspace) method has also been used, using the errors vectors from the previous iterations (up to four) to extrapolate the next iteration, thus improving the simple Kerker mixing.

### 2.1.2 Quantum and non-parabolic effects on $C(V)$

The structure of the Intel’s device of Radosavljevic *et al.* (2011) [294] is first simulated, consisting in a 40 nm thick  $\text{In}_{0.57}\text{Ga}_{0.43}\text{As}$  channel with a front oxide with  $\text{EOT}=1.2$  nm. Figure 2.2(left) shows the capacitance simulated with classical non-linear Poisson solvers (with a Maxwell-Boltzmann and Fermi-Dirac statistics) and Poisson-Schrödinger simulations in the EMA and NP-EMA approximations. It is found that classical solvers with parabolic models are unable to reproduce the quantum effects presented in III-V materials. The use of Maxwell-Boltzmann statistic is clearly wrong, due to low density-of-states of InGaAs and the high position of the Fermi-level inside the conduction band in accumulation (positive gate to source bias  $V_{gs}$ ), as pictured in Fig. 2.3. The discrepancy between parabolic EMA model and classical simulation with Fermi-Dirac statistic can be explained by the quantum effects such as the dark space (maximum of charge centroid shifted away from interface, see Fig. 2.3) or wave function penetration (WFP) in the oxide (which is higher in III-V than in Si, due to a stronger effective mass discontinuity at interface). The first effect tends to decrease the quantum capacitance (as it increases the effective thickness). This is the reason why classical simulation at moderate inversion overestimates the capacitance. When the gate voltage is increased, the dark space decreases (due to the electrical confinement pushing the maximum of charge towards the interface) and the difference between classical and quantum capacitance decreases. The second effect tends to increase the capacitance, as it is shown in Figure 2.2 where the simulation with (red) and without (blue) WFP is compared. Note that similar results were found in Lind *et al.* (2010) [188] in bulk MOSCAPs.

Figure 2.2(right) compares the experimental measurement done at 1 MHz in Radosavljevic *et al.* (2011) [294] with the NP-EMA simulations with UTOXPP *in-house* solver and another Poisson-Schrödinger solver developed at IMEP by Quentin Rafhay [133]. A small discrepancy is found between the two solvers, probably due to the difference of treatment for the WFP and effective mass interpolation [131]. A good match is obtained between measurements and simulation in the NP-EMA approach, while parabolic EMA underestimates the  $C(V)$ , for both solvers. No traps are included in the simulation, indicating that the Intel’s device figures surprisingly good semiconductor/oxide interface quality. Although Ref. [294] gives no details about the nature of the high- $\kappa$  material used for the gate oxide, the previous paper from Intel presented at IEDM 2010 (Ref. [295]) mentions  $\text{TaSiO}_x$  used as a gate oxide, which could be a promising candidate for III-V MOSFETs. As pointed out later by Stanojevic *et al.* (2015) [337], the gate stack used by Intel could

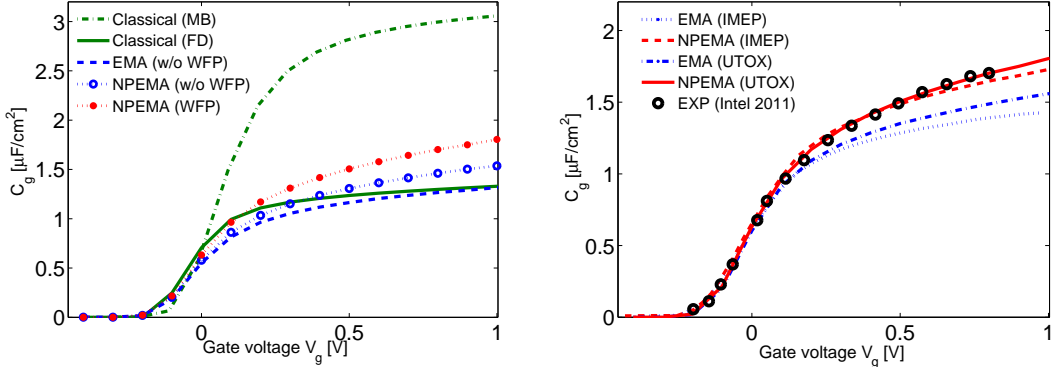


Figure 2.2. Comparison between classical and quantum PS models in the parabolic EMA and NP-EMA approximation with UTOXPP solver (left) and comparison with IMEP PS solver including WFP and the experimental data from Ref. [294] (right).

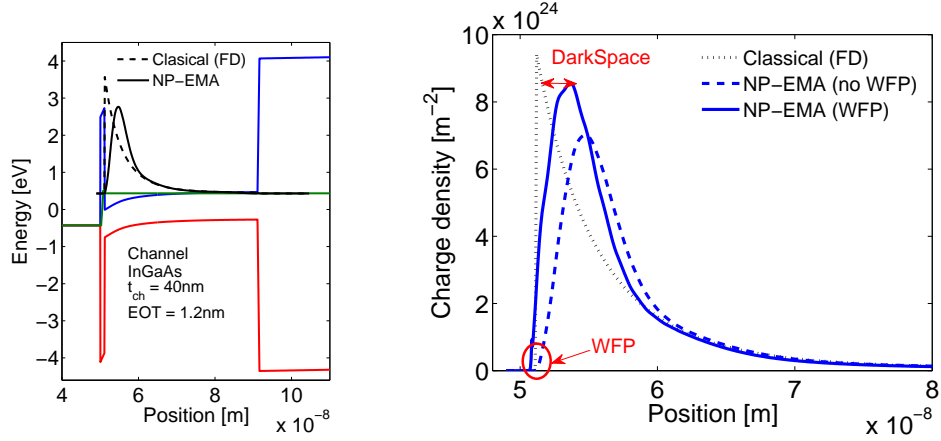


Figure 2.3. Left: Band diagram of the structure of Ref. [294] at  $V_{gt} = V_{gs} - V_{th} = 1\text{ V}$  obtained with NP-EMA model in UTOXPP package. The charge distribution obtained with NP-EMA and Classical model with Fermi-Dirac distribution are also shown at  $V_{gt} = 1\text{ V}$  in arbitrary units (same scaling applied to both curves). Right: zoom of the charge distribution, showing the darkspace (DS) due to quantum confinement and the effect of WFP (reducing the DS).

actually be made of a layered structure made of  $\text{Ta}_2\text{O}_5$  and  $\text{SiO}_2$  layers, which composition was fitted to obtain a dielectric constant  $\varepsilon_{\text{TaSiO}_x} = 8.97$ .

### 2.1.3 Bulk MOSCAPs

The capacitance of bulk MOSCAPs with semiclassical and Poisson-Schrödinger simulation were already compared in Lind *et al.* (2010) [188], showing the importance to use non-parabolic models to describe the capacitance of InAs and InGaAs MOSCAPs and obtaining

a good agreement with experimental data. O'Regan *et al.* (2010) [264] modeled InGaAs bulk MOSCAPs over a wider range of gate voltage with NP-EMA models with different positions of satellite valleys and showed their effect on capacitance. However the recent studies on DFT detailed in Chapter 1 showed that the satellite valleys probably lie higher in energy than the values used in Ref. [264]. In this section, we compare NP-EMA and TB calculation with experimental data measured at low temperature and high frequency, in order to avoid the contribution of traps.

### Experimental growth at CEA-LETI

$\text{Al}_2\text{O}_3/\text{In}_{0.57}\text{Ga}_{0.43}\text{As}$  MOSCAPs structures were fabricated at CEA-LETI by the LTM team (Mathilde Billaud and Hervé Boutry in particular). Different thicknesses (25, 27, 75 and 150 nm) of unintentionally doped ( $N_D \simeq 10^{15} \text{ cm}^{-3}$ )  $\text{In}_{0.57}\text{Ga}_{0.43}\text{As}$  were epitaxially grown by MOCVD on InP n-doped (001) substrates ( $N_D \simeq 1 \times 10^{18} \text{ cm}^{-3}$ ). Different surface treatment were performed to obtain a good surface quality (in particular a surface cleaning process with a solution of  $\text{NH}_4\text{OH}$  4%). 8 nm of  $\text{Al}_2\text{O}_3$  were then deposited by Atomic Layer Deposition (ALD). Finally a Ni/Au metallic gate was deposited as contact. Figure 2.4 shows a Transmission Electron Microscopy image of the cross section of the MOSCAP structure. One can refer to Billaud *et al.* (2015) [29] for more details about the fabrication and characterization.

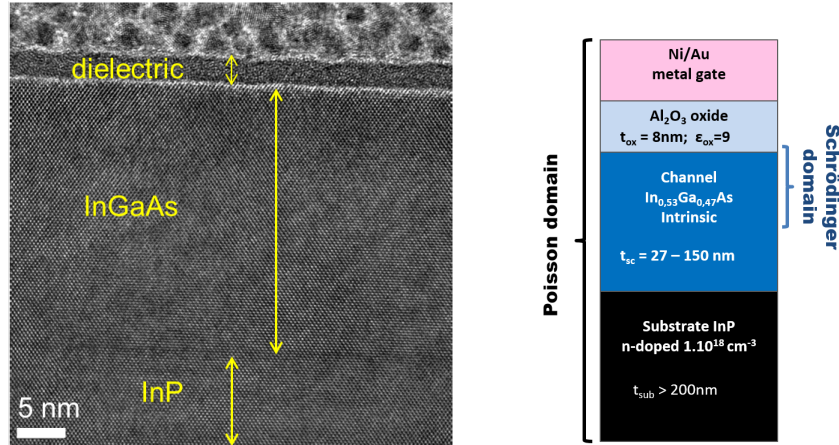


Figure 2.4. Left: TEM image of the cross section of a  $\text{In}_{0.57}\text{Ga}_{0.43}\text{As} / \text{Al}_2\text{O}_3$  MOSCAPs grown on InP substrates. The thickness of the  $\text{In}_{0.57}\text{Ga}_{0.43}\text{As}$  layer is 27 nm (reproduction from M.Billaud's presentation at EUROSOI-ULIS 2015 [29]). Right: schematic view of the simulated structure.

The capacitance of these structures is then measured with an Agilent impedance analyzer in the frequency range from 100 Hz to 1 MHz connected with a cryostat for measurement at low temperature down to 4 K.

The  $\text{Al}_2\text{O}_3$  oxide deposited in this way is amorphous, but its quality and dielectric constant can vary. In order to extract the dielectric constant of the film deposited, a

series of samples with different oxide thickness has been grown and characterized. The capacitance for 40, 60, 87 and 100 ALD cycles (corresponding to around 4.2, 5.9, 8.1 and 9.4 nm  $\text{Al}_2\text{O}_3$  thicknesses as measured by ellipsometry) are shown in Figure 2.5. In a simplest model, one can write the capacitance as:

$$\frac{1}{C_g} = \frac{1}{C_s} + \frac{1}{C_{ox}}$$

where  $C_s = \frac{\epsilon_0 \epsilon_{sc}}{DS}$  is the semiconductor capacitance due to the darkspace  $DS$  and  $C_{ox} = \frac{\epsilon_0 \epsilon_{ox}}{t_{ox}}$  is the oxide capacitance. If one considers that  $C_s$  doesn't vary strongly at high gate voltage (not always true, as explained below), one can easily relate the slope of  $1/C_{max}$  vs.  $t_{ox}$  to the dielectric constant of the oxide. The capacitance at  $V_g = 2$  V for 50 and 300 K are plotted as a function of the oxide physical thickness in Figure 2.5, as well as the linear fit of these curves. The dielectric constant extracted from these fits are  $\epsilon_{ox} = 8.16$  and  $\epsilon_{ox} = 7.76$  at 50 and 300 K respectively. In the literature, the dielectric constant of dense amorphous  $\text{Al}_2\text{O}_3$  deposited by ALD is usually close to 9 [309] but can vary from 8 to 10 [397, 28]. The low dielectric value can suggest that the deposited alumina presents a high uncontrolled porosity [276].

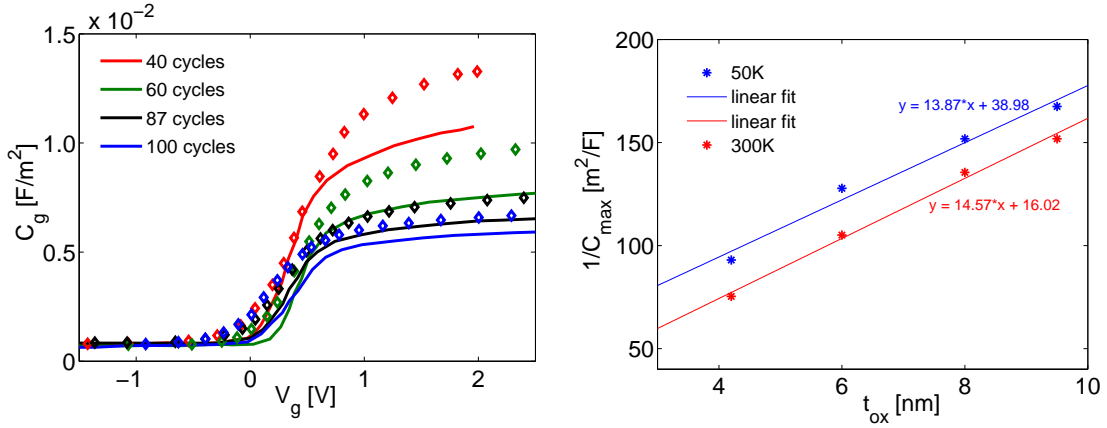


Figure 2.5. Left: gate capacitance at 100 kHz measured in sample with varying  $\text{Al}_2\text{O}_3$  thicknesses at 50 K (symbols) and 300 K (lines). Right:  $1/C_{max}$  taken at  $V_g = 2$  V as a function of oxide thickness  $t_{ox}$  used to extract the dielectric constant (see text).  $\epsilon_r = 8.16$  is extracted at 50 K and  $\epsilon_r = 7.76$  at 300 K.

Moreover, the extraction technique based on a particular  $V_g$  can be questionable for III-V, where no real saturation of the capacitance is obtained. The approximation of constant  $C_s$  can thus be invalid because, unlike Si MOSCAPs, InGaAs MOSCAPs generally present a higher darkspace and don't reach  $C_{ox}$  even at high  $V_g$ , due to their low DOS. Moreover, due to the rather high variability in these devices, the threshold voltage  $V_{th}$  can vary from different samples and the extraction of the maximum capacitance  $C_{max}$  is not straightforward. This technique was nonetheless used in several studies in the literature, e.g., Refs. [404, 399].

Furthermore, some comparisons with simulation results are performed to better understand this behavior and validate the parameter extraction. We suppose that at sufficiently low temperature, the traps begin to have very long time response dynamic and can be considered as “frozen” (or fixed charge). In this case, they don’t influence the shape of the capacitance (acting mainly as a rigid horizontal shift) and one can recover the “ideal”  $C(V)$  obtained by the simulation without traps. The capacitance measured at 1 MHz for different temperatures is presented in Figure 2.6. Measurements from 300 down to 4 K show a decrease in accumulation capacitance and a steeper slope, indicating the lower influence of traps. A similar behaviour was found in Ref. [74] for the temperature dependency of  $\text{Al}_2\text{O}_3/\text{In}_{0.57}\text{Ga}_{0.43}\text{As}$  MOSCAPs. Note that a brutal shift in  $V_{th}$  is observed when temperature is decreased from 100 to 75 K which reason is not well established. From 75 to 4 K, the  $C_g(V_g)$  curve doesn’t change significantly and their dispersion in frequency is very small, indicating that the traps can be considered as frozen. The comparison between measurement at 10 K and 1 MHz and the simulated ideal  $C(V)$  curve is shown on Fig. 2.6. The simulations were performed with UTOXPP Poisson-Schrödinger solver in the NP-EMA approximation accounting for the  $\Gamma$  valley and a non-parabolic coefficient  $\alpha = 1.3$ , allowing a good description of the charge distribution. A good agreement is found between experimental and simulation data with an alumina thickness of 8 nm and a dielectric constant of 8, without traps. The threshold voltage was here adjusted to the experimental value, as no particular attention was given to the metal workfunction (set to 5 eV in the simulation) or the fixed charge in the gate stack. The value of the capacitance for negative voltage is due to the depletion of the InP layer and we find a good agreement with the expected InP doping of  $10^{18} \text{ cm}^{-3}$ . The small staircase observed around -0.2 V in the measurements is not reproduced in the simulations and might be due to some artifacts from the equipment.

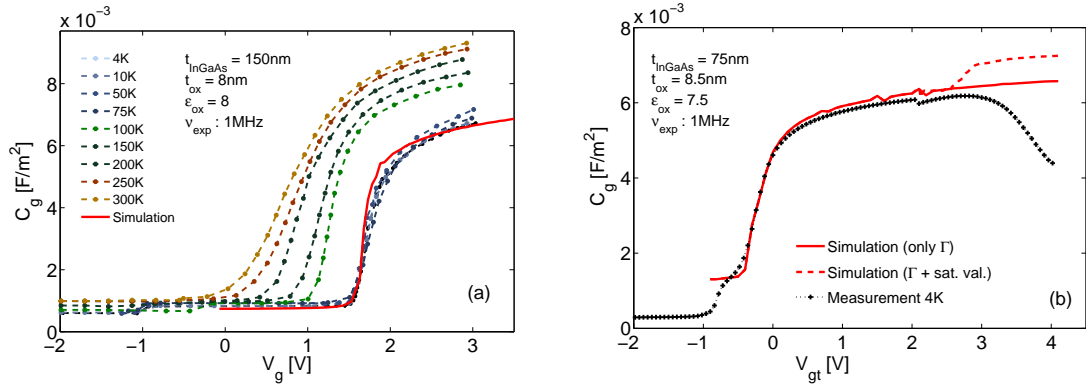


Figure 2.6. (a) Capacitance measurements for IGA2 sample at different temperature at 1 MHz. NP-EMA simulations at low temperature obtained with UTOXPP package are also shown. (b)  $\text{Al}_2\text{O}_3/\text{In}_{0.57}\text{Ga}_{0.43}\text{As}$  capacitance measured at low temperature and high frequency (4 K and 1 MHz) matching well the ideal  $C(V)$  without traps simulated with UTOXPP package.

In Figure 2.6(b) the measurement of  $\text{Al}_2\text{O}_3/\text{In}_{0.57}\text{Ga}_{0.43}\text{As}$  MOSCAPs grown on Si (001) substrate are shown. The  $\text{In}_{0.57}\text{Ga}_{0.43}\text{As}$  thickness is here 75 nm and GaAs and InP buffer layers were epitaxially grown on Si substrate to obtain an good quality of  $\text{In}_{0.57}\text{Ga}_{0.43}\text{As}$  without defect. This makes the process compatible with the 300 mm CMOS production plants (for more details, see Ref. [30]). The measurement at 4 K and 1 MHz were performed up to higher voltage to investigate the influence of satellite valleys. The drop of capacitance around  $V_{gt} = V_g - V_{th} = 3$  V might be due to the dielectric breakdown or the loss of contact (difficult to achieve at these low temperature) and no higher gate voltage could be applied. The small instability around  $V_{gt} = 2$  V is an artifact due to the change of regime of the impedance analyzer. The simulation with NP-EMA models were performed with the same band structure parameters as before, while the alumina thickness and dielectric constant had to be slightly adjusted to reproduce the experiments ( $t_{ox} = 8.5$  nm and  $\epsilon_{ox} = 7.5$ ). These values remain in the range extracted with the above analysis on dielectric constant and the ellipsometry studies. When compared to the experimental measurements, a good agreement is found up to  $V_{gt} = 3$  V where only the  $\Gamma$  valley is occupied. When  $\Delta$  and L satellite valleys are included in the simulation, a bump appears in the capacitance when the Fermi-level reaches their energy, due to the increase of density-of-states. The bump's position depends on the position of satellite valleys, which values are taken following Ref. [264]. For lower values ( $E_L = 1.2$  eV and  $E_\Delta = 1.33$  eV), the bump is around  $V_{gt} = 2.5$  V, while for the higher values ( $E_L = 1.49$  eV and  $E_\Delta = 1.98$  eV) the bump is shifted to gate voltage higher than 4 V. Due to the breakdown of the alumina oxide, the exact position of the satellite valleys could not be extracted here, but the experimental  $C_g(V_g)$  curve shows that the satellite valley have to lie higher than 0.6 eV above the conduction band edge, in agreement with the upper range in Ref. [264] and DFT values given in Chapter 1.

#### 2.1.4 Ultra-Thin Body and BOX (UTBB) MOSCAPs

In this section, TB and NP-EMA models are applied to UTBB MOSCAPs and compared. The accurate description of physical confinement of the NP-EMA model discussed in Chapter 1 is here extended to self-consistent calculation of  $C(V)$  characteristics. The structure presented in Fig. 2.7(a) is considered, consisting in a 5 nm thin semiconductor film, a 1 nm  $\text{Al}_2\text{O}_3$  front oxide (EOT  $\simeq 0.43$  nm) and a 5 nm  $\text{Al}_2\text{O}_3$  BOX. A sketch of the atomistic cell used in TB calculations is also shown. Poisson and Schrödinger equations are solved self-consistently in the 1D slice of the structure with TB and NP-EMA models. The channel is made of InAs, GaAs or  $\text{In}_{0.57}\text{Ga}_{0.43}\text{As}$  materials and confinement orientation is along the (001) direction in all cases. In order to compare the different models, fixed boundary conditions were first used, as described in the previous Chapter.

Figure 2.7(b) compares the results in InAs UTBB MOSCAPs obtained with the *in-house* UTOXPP solver and the IMEP PS solver, with parabolic EMA and NP-EMA models and without WFP [133]. A good agreement with the different solvers is found again in UTBB structures. The second bump in the capacitance corresponds to the point where the second subband is populated, in agreement with subband position found in Chapter 1. Parabolic EMA leads to flat stair-like capacitance with a bump at high  $V_g$  and

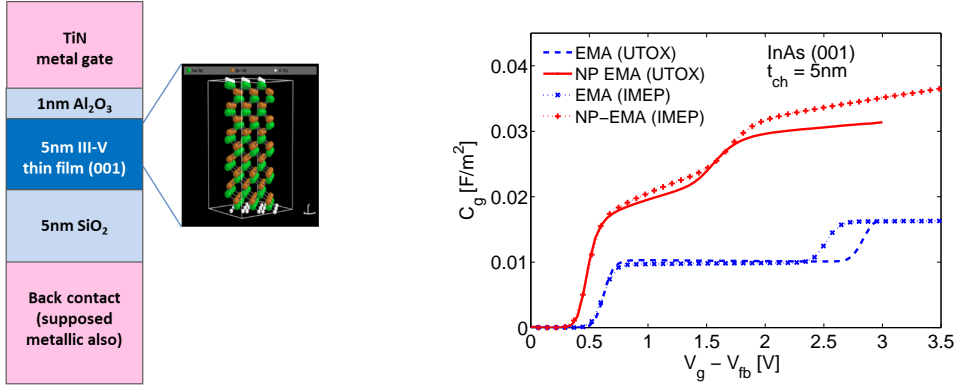


Figure 2.7. Left: Sketch of UTB MOSCAP structure considered. Atomistic structure used in TB is also shown. Right: Gate capacitance of InAs UTBB structure simulated with *in-house* UTOX software and compared with IMEP-LAHC’s software [133].

strongly underestimates the capacitance compared to NP-EMA model.

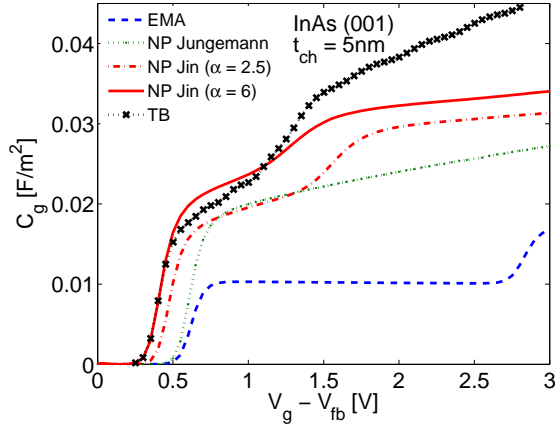


Figure 2.8. Capacitance of InAs UTBB MOSCAPs with  $t_{ch} = 5$  nm and confinement in the (001) direction, modelled with TB, Jin’s and Jungemann’s NP-EMA and EMA models.

Results obtained with TB model are shown in Figure 2.8, together with the NP-EMA model of Jungemann [153]. One first notes that NP-EMA models proposed by Jungemann [153] and Jin [149] give two different results. While the slope of the capacitance is similar, if the subband energy levels are not corrected (in Jungemann’s NP-EMA model) the bump is pushed to higher values and the  $V_{th}$  shift is not accounted for (up to 0.2 V in this case). This model thus fails to capture the correct capacitance of InAs UTBB MOSCAPs. On the other side, the agreement between Jin’s NP-EMA and TB models is not perfect either. As it has been noted in Chapter 1, the second subband position is still overestimated with NP-EMA Jin’s model compared to TB, unless  $\alpha$  is boosted.

For boosted  $\alpha$ , the bump position for InAs agrees well with TB, while the slopes still have some discrepancy. Note that this phenomenon was not found in bulk InAs and InGaAs MOSCAP [188] where the theoretical  $\alpha$  could be used without correction of the subband position to find good agreement with TB. This difference can be explained by the enhanced NP effects by physical confinement and the need to treat NP quantization effect with boosted  $\alpha$ . The difference in boundary condition can also affect strongly the results, as it will be discussed in the next section.

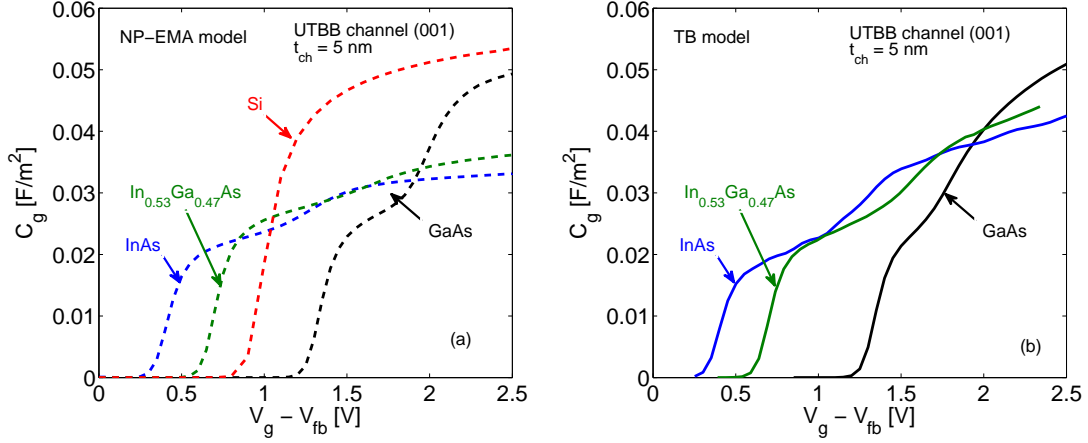


Figure 2.9. Capacitance of III-V and Si UTBB MOSCAPs with  $t_{ch} = 5$  nm and confinement in the (001) direction, modeled with Jin’s NP-EMA model with boosted  $\alpha$  (left) and TB (right).

Figure 2.9 compares the capacitance of (001) films with channels made by III-V and Si materials, obtained with NP-EMA and TB model. The voltage reference is set to the flat-band voltage  $V_{fb}$ . One notes the clear  $V_{th}$  shift due to the different band alignments and gaps, but also the different  $C_{max}$  obtained and steep slope. InAs and  $\text{In}_{0.57}\text{Ga}_{0.43}\text{As}$  channels display only half gate capacitance compared to Si, due to the low density-of-state of the  $\Gamma$  valley, even with non-parabolicity with boosted  $\alpha$  and population of other subbands. In GaAs thin films, satellite L valleys become populated before the second subband in  $\Gamma$  (as shown in Fig. 1.16), increasing the density-of-state. This leads to a higher gate capacitance, reaching values close to Si UTBB at high gate voltage.

### Boundary conditions

**TB** As discussed in Chapter 1, the parameters set for the H-passivation in TB can affect the band structure of thin films. These parameters can also influence the charge density present on the H passivating atoms and the self-consistent calculation of the  $C_g(V_g)$  characteristics. Figure 2.10(a) plots the capacitance obtained with TB models with parameters for In-H and As-H bonds from Y.-M.Niquet *et al.* (2002) [248], and with H-atoms on-site parameters increased by 4 eV. When the on-site energy term is increased, less charge is present on H-atoms, but they also become less efficient in passivating the surface. The

agreement with NP-EMA model is here improved up to  $V_g \simeq 1.5$  V, before the 2nd subband become populated. However the results obtained with the two passivation parameters are quite close.

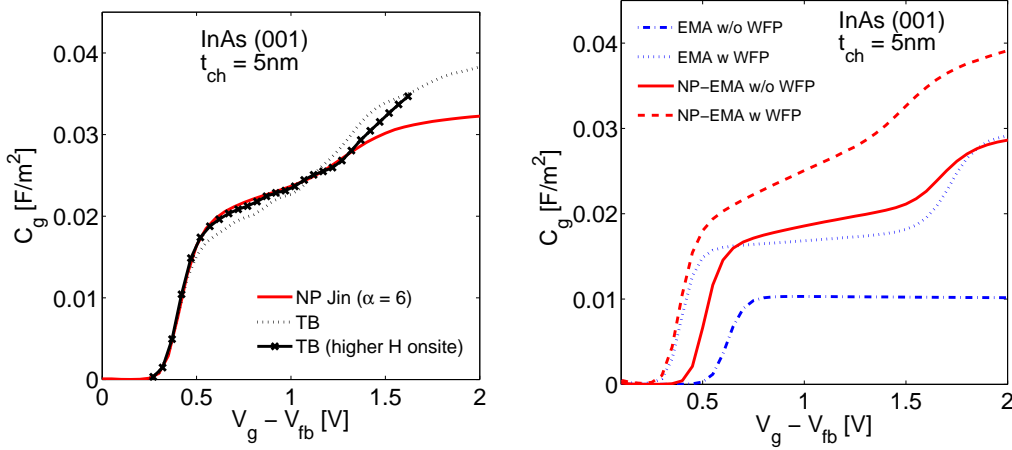


Figure 2.10. Left: influence of the TB parameters of H passivating atoms on the  $C_g(V_g)$  curve. Right: influence of the wave-function penetration (WFP) on the NP-EMA  $C_g(V_g)$ .

**NP-EMA** Figure. 2.10(b) shows the impact of the wave-function penetration (WFP) on the  $C_g(V_g)$  characteristics of a InAs thin film. One notes that the WFP has a strong impact on the  $C_g(V_g)$  characteristics: i) the accumulation capacitance is strongly increased (almost doubled in the case of parabolic EMA) and ii) the  $V_{th}$  is also shifted to lower value, resulting in a similar  $V_{th}$  value for both the EMA and NP-EMA models. This was expected, as the energy subbands discussed in Chapter 1 show lower values when WFP is included in the calculations. One thus concludes that the effect of WFP is important to account for and that, in TB, an important goal for the future will be to have a proper description of the oxide layer. Recent studies go in this direction, as, e.g., J.Li *et al.* (2016) [181].

## 2.2 Capacitance with defects

In the first part of this Chapter, the capacitance of MOS structures was computed for bulk and UTBB devices. In these computations, ideal electrostatics was considered, with defect-free materials and interfaces. In real devices, defects are always present in bulk materials (oxide, semiconductor) as well as at their interfaces. These defects are usually complicated to characterize and depend on the material crystallography, the possible diffusion of species, the stress (induced by the fabrication process for example), the thermionic budget endured during process, the chemical reaction and other mechanisms that can occur at atomic scale. These defects affect the capacitance measured experimentally, because they are in many cases electrically charged. They are called “fixed charges” in the case where their electric charge doesn’t vary with the applied gate voltage or signal frequency (in the range on the experiment) and they will mainly act as an horizontal rigid shift of the capacitance (i.e., a shift of threshold voltage  $V_{th}$ ). This effect is not considered here, as it doesn’t affect the shape of the capacitance, and we don’t try to extract the exact  $V_{th}$  on our device (it is considered as a fitting parameter). In the case where the defects interact with the inversion charge and capture or emit one (or more) free carrier(s), they are called “traps”. The charge state of the defect is modified as a function of the gate voltage and/or frequency of the signal  $\nu$ , inducing an additional capacitance  $C_{it}(V_g, \nu) = \frac{\partial Q_{it}}{\partial V_{gs}}$  (as shown in Fig. 2.11). This capacitance typically affects the shape of the static DC capacitance as a stretch of the  $C_g(V_g)$  and an increase or decrease of  $C_{max}$  [71]. It also induces a frequency dispersion of the capacitance, due to the characteristic response time of the traps [80].

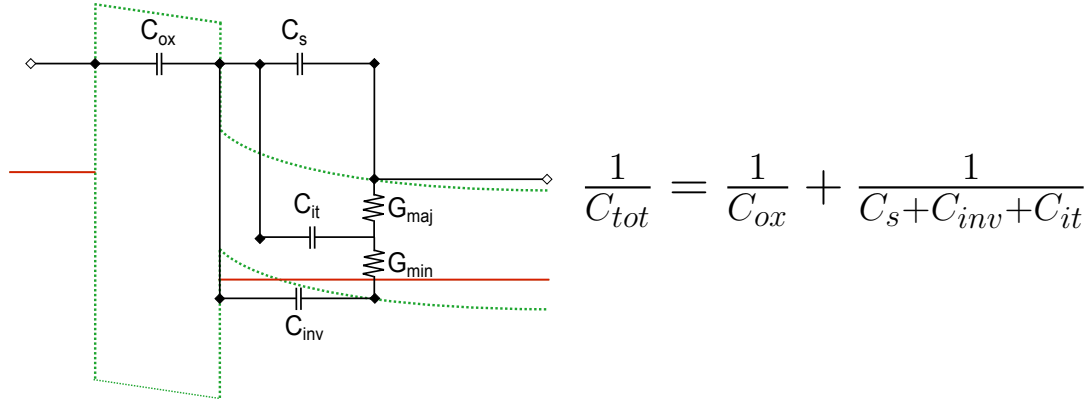


Figure 2.11. Schema of the electric equivalent circuit (capacitances  $C$  + conductances  $G$ ) of a MOS structure, including interface traps. It shows the trap capacitance  $C_{it}$ , the oxide capacitance  $C_{ox}$  as well as the capacitance due to depletion in the semiconductor  $C_s$  and the darkspace  $C_{inv}$ .

In the following sections, we present different *ab initio* studies found in the literature on the defects in III-As, oxides and their interfaces and discuss their influence on the capacitance. We distinguish here two different categories of traps: interfacial traps and border traps. We then present the model used to simulate the electrical response of a

MOSCAP system in presence of traps, based on the multi-phonon approximation (MPA). Finally we present some experimental and simulation studies for the extraction of trap characteristics from  $C_g(V_g)$  measurements, focusing on the results from an experimental team at CEA-LETI and the comparison with simulations performed with UTOXPP software.

Note that the deposition process of oxide materials on  $\text{In}_{0.57}\text{Ga}_{0.43}\text{As}$  is still under improvement, as it can be observed from the number of papers presented on this topic at the last Semiconductor Interface Specialists Conference (SISC) conference on December 2016. The electrical characterization of InGaAs/oxide MOSCAPs can thus differ from samples to samples and the experimental understanding of these interfaces is still under investigation. The role of these sections is thus more to give a bibliographic overview of the studies and models available, rather than a complete study on this complex topic.

### 2.2.1 Point defects in III-As/oxide structures

We briefly present here a bibliography of DFT studies on defects in the oxide and at the III-V/oxide interface. Let us first give two definitions for categories of traps that are often used in the literature:

- “Border traps” is used to describe bulk traps inside the oxide, at a distance close enough to interact with the charges inside the SC (in particular by tunnel effect). These defects are the same as in the bulk oxide, but their position with regard to the SC band edge depends on the band alignment of the two materials, that needs to be determined.
- “Interfacial traps” or  $D_{it}$ , in the other side, is used for traps caused by the interface formation between semiconductor and oxide. They can be due to surface defects inherent to a particular interface model, to lattice mismatch or chemical reactions between SC and oxide (this includes the diffusion of chemical species), leading to dislocations or point defects such as dangling bonds or interstitial atoms. The defect levels can be located in different energy ranges, inside the SC band gap, above the conduction band minimum or below the valence band maximum. As the SC/oxide interface usually extends over more than one monolayer (up to several nm in some case, as in Ref. [147]), these defects can be located at a tunneling distance from the inversion charge.

Note that the difference between these two denominations can be rather blurred in reality, as the diffusion of species and the interface extension can be large and the high- $\kappa$  thickness are pushed down to only a few nanometers. In the literature, the “border traps” denomination is sometimes used for any defect at a tunneling distance from the inversion 2DEG (thus differing from our definition).

### Alumina $\text{Al}_2\text{O}_3$

Let’s first consider the case of bulk alumina  $\text{Al}_2\text{O}_3$ , which is probably the oxide material the easiest to deposit on III-As SC. The band gap of amorphous alumina is around

6.7 eV [175], while its crystalline phases have usually higher band gap: around 9 eV for the high-density  $\alpha$  phase (sapphire) [97], 7.9 eV for the  $\kappa$  phase [390] and 6.5 eV for the  $\gamma$  phase [222]. L.Masoero (2012) [222] studied different point defects in the  $\gamma$  phase of  $\text{Al}_2\text{O}_3$  with DFT-LDA and  $\text{G}^0\text{W}^0$  approaches, including H-related defects present in ALD-deposited alumina with  $\text{H}_2\text{O}$  precursors. It was found that the most stable electrically active defects with energy levels in the band gap are H interstitial and O vacancy. Weber, Janotti and Van de Walle (2011) [390] also studied numerous defects inside the bulk  $\text{Al}_2\text{O}_3$  and its band alignment with III-As materials. They used HSE06 functionals and considered the  $\kappa$  phase of  $\text{Al}_2\text{O}_3$  that presents a similar density, but higher band gap compared to amorphous  $\text{Al}_2\text{O}_3$ . They found that the Al interstitial and Al vacancy would certainly produce fixed charges in the transistor gate stack (respectively positive and negative); while the O vacancy would lead to thermodynamic levels in the energy range of the III-V band gaps (from 0.74 below to 0.11 above the CBE of  $\text{In}_{0.57}\text{Ga}_{0.43}\text{As}$  for the (+2/+1) and (+1/0) transitions). However, a more recent study by Colleoni *et al.* (2015) [57] studied in details the band alignment of amorphous  $\text{Al}_2\text{O}_3$  / GaAs interface with HSE06 functionals and found a conduction band offset of 1.3 eV and valence band offset of 3.8 eV, in good agreement with XPS experimental studies. This indicates that the position of III-As band edges in Weber *et al.* (2011) were probably lying  $\sim 1$  eV too low and that the transition associated with  $V_O$  would probably lie slightly below the valence band of SC. In conclusion, O vacancy can be potential border traps affecting the  $C_g(V_g)$  characteristics, acting as a donor-type traps close to the SC valence band edge. H interstitials could also be present in ALD  $\text{Al}_2\text{O}_3$ .

### III-As/ $\text{Al}_2\text{O}_3$ interface

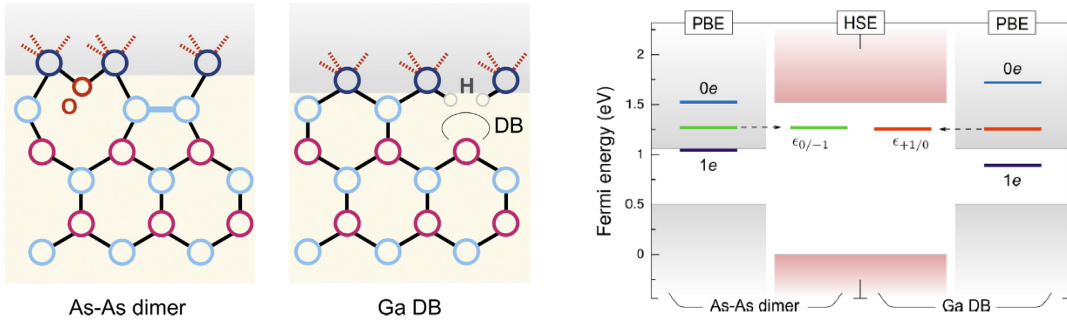


Figure 2.12. Left: schema of possible defects at GaAs/ $\text{Al}_2\text{O}_3$  interfaces. Right: their thermodynamic energy levels calculated by Miceli and Pasquarello (2014) (figures taken from Ref.[227]).

Interfacial traps are more difficult to model with DFT models, as it involves different elements (Ga, In, As, Al and O), it requires an accurate interface model and it is necessary to include a big number of atoms in the calculation. Moreover, the number of possible defects is huge and clusters of defects can form, which are needed to explain the

Fermi-level pinning at GaAs/Al<sub>2</sub>O<sub>3</sub> interface [55]. However, recent *ab initio* studies were able to model III-V/high- $\kappa$  interfaces and to study the interfacial defects. They mainly focus on Ga dangling bonds and As-As dimer (antibonding states) [186, 226, 187] (see Fig. 2.12). Lin and Roberston (2011) [186] studied a broad range of GaAs/high- $\kappa$  interfaces, such as GaAs/HfO<sub>2</sub>, GaAs/Gd<sub>2</sub>O<sub>3</sub> and GaAs/Al<sub>2</sub>O<sub>3</sub>. They studied the effect of Ga- or As- terminated interface and the position of dangling bonds and As-As bonding. They found that Ga-dangling bonds (DB) lie above conduction band edge (CBE) when referred to InAs, GaAs or InP (about 0.3 eV above GaAs CBE). However, As-As antibonding state lies at lower energy and can be slightly below the conduction band edge for InAs. According to them, In-rich (001) InGaAs surfaces can be used to avoid these As-As antibonding states. Miceli and Pasquarello (2014) [227] later studied more specifically these two major interface defects between GaAs and Al<sub>2</sub>O<sub>3</sub>: the Ga dangling bond and As-As dimer. They found in their calculations (correcting the gap with HSE06) that both defects lead to a thermodynamic level about 0.3 eV below the CBE of GaAs, with different nature (see Fig. 2.12): Ga DB leads to donor traps with transition (+1/0) while As-As dimer leads to acceptor traps with transition (0/-1). Other recent studies investigated the interface between Al<sub>2</sub>O<sub>3</sub> and In<sub>0.53</sub>Ga<sub>0.47</sub>As alloy (Miceli (2013) [226] and Colleoni *et al.* (2015) [56]). They found that the As-As antibonding state actually lies above InGaAs CBE (see Ref. [354] and the next section for further discussion). This level was found to be quite independent on the chemical environment in the InGaAs layer.

Remarks:

I) Note that the dielectric constant of Al<sub>2</sub>O<sub>3</sub> is quite low for application in advanced transistors technology which needs to achieve high capacitance together with low leakage current (i.e. thick oxide). For this reason, high- $\kappa$  materials such as HfO<sub>2</sub> ( $\epsilon \simeq 20$ ), ZrO<sub>2</sub> ( $\epsilon \simeq 22$  [135]), LaAlO<sub>3</sub> ( $\epsilon \simeq 20 - 27$  [78]) or Ta<sub>2</sub>O<sub>5</sub> ( $\epsilon \simeq 25$  [337]) are also intensively investigated in the literature. The interface between In<sub>0.57</sub>Ga<sub>0.43</sub>As and these high- $\kappa$  materials is usually less known than for In<sub>0.57</sub>Ga<sub>0.43</sub>As /Al<sub>2</sub>O<sub>3</sub> and very few *ab initio* studies exist on these interfaces.

II) Intensive experimental studies are moreover performed on the effect of surface treatment to passivate point defect at the interface, such as the role of sulfur atoms (surface treatment with (NH<sub>4</sub>)<sub>2</sub>S [4]); the use of plasma-PH<sub>3</sub> passivation [347]; plasma-enhanced ALD (PEALD) method [72] or plasma-O<sub>2</sub> postoxidation treatment for the densification of Al<sub>2</sub>O<sub>3</sub> [177].

III) Note that the determination of the energy of a defect at an interface is a complex problem and some discrepancy can remain among results. Moreover, in above mentioned *ab initio* studies, perfect stoichiometry, abrupt interface and relaxed strain condition were usually considered and only specific defects were treated. In supercell calculations, the problem of interactions between defects in neighbor cells remains a critical issue. In addition, in experimental devices, some additional chemical species can remain due to exposition to air or growth catalysts/precursors (such as H<sub>2</sub>O in case of Al<sub>2</sub>O<sub>3</sub> ALD) leading to additional defects. Interfaces are usually not abrupt and a transition layer can remain (in particular Ga<sub>2</sub>O<sub>3</sub> oxide are very often encounter at InGaAs/high- $\kappa$  interfaces [319]). A third additional effect can be due to local strain, influencing the energy levels of the defect. For all these reasons, a rather broad distribution of trap energy levels is usually

considered in the models, when macroscopic quantities such as capacitance are computed. In our case, we will consider double-Gaussian profiles in position and energy, representing a type of defects characterized by its intrinsic parameters, such as Huang-Rhys factor (as explained below).

### 2.2.2 Influence of traps on electrostatics and capacitance

As it has been seen, different defects are usually present at InGaAs/oxide interfaces or close to it, and some of them can interact with the inversion charge in the channel. This interaction leads to a modification of the ideal  $C_g(V_g)$  curve, as it can be seen on Fig. 2.6(a) and 2.13(a). As said in the section 2.2, traps in the band gap usually stretchout the  $C_g(V_g)$  curve, while traps above the conduction band can increase the capacitance in accumulation, as they induce an additional capacitance in parallel (see Fig. 2.11). As this transfer of carriers between the delocalized states in SC (CB or VB) and the trap states is a dynamical process, with a characteristic time, the modification of the AC capacitance depends on the signal frequency, and a broad dispersion is often found in the measurements (Fig. 2.13(b)). Note that in Fig. 2.13(b), the very broad dispersion with frequency at negative voltage is mainly due to the non-radiative generation-recombination of minority carrier (holes in this case) [80]. This non-radiative generation-recombination occurs through traps in the band gap, and can be due to point defects inside the semiconductor itself (“intrinsic GR”), as well as interfacial or border traps.

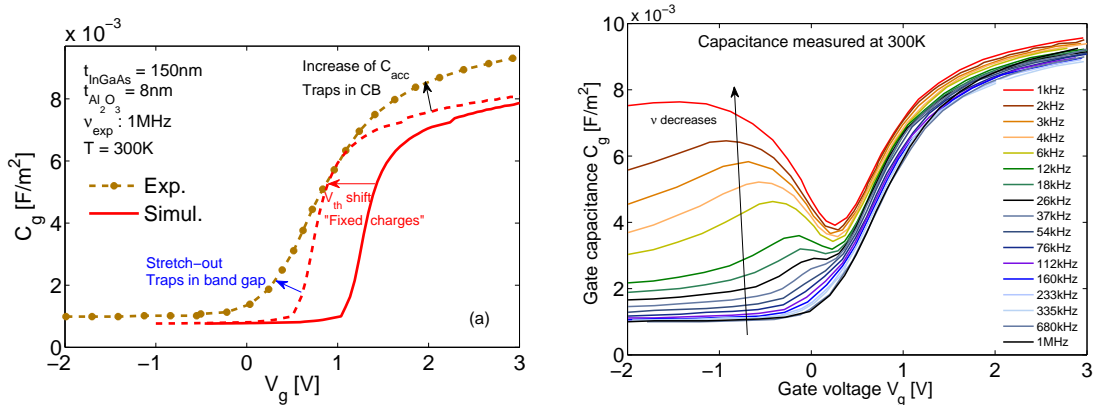


Figure 2.13. Room temperature  $C_g(V_g)$  of  $\text{In}_{0.57}\text{Ga}_{0.43}\text{As} / \text{Al}_2\text{O}_3$  MOSCAPs fabricated and measured at CEA-LETI: experimental measurement is compared with simulated ideal  $C_g(V_g)$  in (a), while the frequency dispersion is shown in (b).

To characterize these effects and take them into account in the simulation, it is important to understand the mechanism of charge transfer and the parameter associated, such as the trap capture/emission cross section  $\sigma_{c/e}$  (or equivalently the capture/emission rate  $\tau_{c/e}^{-1}$ ). These parameters can then be used to model the non-radiative capture and emission of carriers in the channel through the well-known Shockley-Read-Hall theory.

## Literature

Many recent studies have been published on the comparison between experimental and simulation MOS capacitance, to extract information on traps. We can cite for example: Djara *et al.* (2013) [71] from IBM, that extracted the traps distribution profile in InGaAs/Al<sub>2</sub>O<sub>3</sub> structure by fitting experimental DC  $C_g(V_g)$  curve with a simple model. Later, Sereni *et al.* (2015A/B) [320, 318] used a multiphonon model to simulate AC capacitance, conductance and leakage current measurement and extract traps profiles in InGaAs/Al<sub>2</sub>O<sub>3</sub> structures; Sereni *et al.* (2015C) [319] applied it to temperature measurements at 300 and 400 K. IMEC also published very recent studies on the temperature dependence of trap response, such as Vais *et al.* (2015A) [367] and Dou *et al.* (2014) [74]. In Vais (2015B) [368] the influence of the InGaAs thin film thickness is also investigated and it is found that the InP buffer can influence the  $C_g(V_g)$  curve.

While Djara (2013) only extracted a distribution of traps projected on the interface (effective “ $D_{it}$ ” profile) from DC characteristics, the very complete study of Sereni (2015) managed to simulate both the  $C_g(V_g)$  and  $G_g(V_g)$  characteristics of In<sub>0.57</sub>Ga<sub>0.43</sub>As /Al<sub>2</sub>O<sub>3</sub> systems over a broad range of frequencies with the traps distribution map in space and energy reported on Figure 2.14.

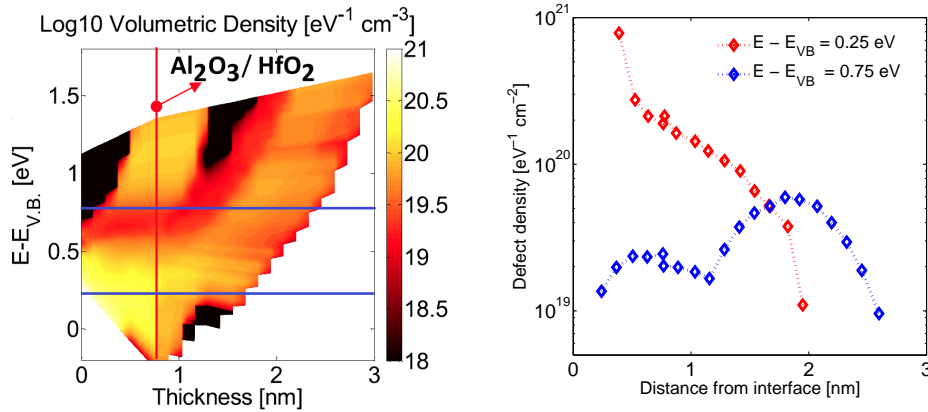


Figure 2.14. Left: traps distribution map in space and energy of In<sub>0.57</sub>Ga<sub>0.43</sub>As /Al<sub>2</sub>O<sub>3</sub>/HfO<sub>2</sub> MOSCAPs extracted from the fit of  $C_g(V_g)$  and  $G_g(V_g)$  profile for frequency range from 100 Hz to 1 MHz (figure taken from Ref. [320]). Right: cuts along the horizontal blue lines in left figure (data taken from Ref. [320]).

These studies can be used to characterize the usually accepted profiles for distribution of traps in the In<sub>0.57</sub>Ga<sub>0.43</sub>As /Al<sub>2</sub>O<sub>3</sub> system. Two different categories can be distinguished:

- Donors traps in the band gap, slightly closer to the SC valence band edge, that are responsible for the stretch-out of the capacitance in DC and can influence the dispersion in inversion and the GR, as it will be discussed later. In the study of Sereni (2015), these traps seem to be mainly located inside the Al<sub>2</sub>O<sub>3</sub> layer, at less than 1 nm away from interface.

- Acceptors traps in the conduction band, that are responsible for the dispersion in frequency of the capacitance in accumulation  $C_{acc}$ , as well as its increase with temperature. These traps are very important, as they are believed to deteriorate the performance of the MOSFETs, inducing a pinning of the Fermi-level above the SC CBE and preventing to achieve a high density of free carriers (see Taoka *et al.* (2013) [354] and Caruso *et al.* (2014) [47], as well as the discussion below). However it is not clear where these traps are located in space and how they communicate with the free charges in the BC of the SC.

Some studies consider this second category of traps as border traps inside the oxide, implying an interaction with SC free charge through tunneling. However the DFT studies presented above didn't find point defects in the oxide fulfilling these characteristics (acceptor character with transition energy about 0.3 eV above SC CBE). Some studies consider them as interfacial traps, that can be due to the As–As antibonding defects pointed out by DFT. Note that the key study of Taoka *et al.* (2013) [354, 353] shows that these traps hinder the performance of MOSFETs. They found that the charge density extracted by  $C_g(V_g)$  measurement overestimates the free electron density in the SC compared to Hall measurements, which reaches a plateau around  $5 \times 10^{12} \text{ cm}^{-2}$ . This can be translated and explained by an exponential “effective” interfacial trap density profile that reaches values of  $10^{15} \text{ cm}^{-2} \text{ eV}^{-1}$  about 0.3 eV above the SC CBE, where the Fermi-level is pinned. This phenomenon was later modeled by Caruso *et al.* (2014) [47]. However, it is not clear how a localized state can trap electron for the SC CB at the interface and how it can interact with the SC free charge. An interesting study using a DFT/NEGF approach was presented at ESSDERC 2016 by QuantumWise and showed how a localized state can form at the  $\text{In}_{0.57}\text{Ga}_{0.43}\text{As} / \text{Al}_2\text{O}_3$  interface without defects. Greene-Diniz (2014) [119] also investigated this issue with DFT (HSE06) and determined a transition energy about 0.7 eV above SC CBE for the (0/-1) transition of the As–As dimer. However, it is difficult for DFT to model accurately system with a Fermi-level above SC CBE, as excited states are not taken into account. Finally,  $1/f$ -noise and charge pumping studies have been performed to gain a deeper understanding of these defects. Scapirno (2014) [314] investigated the role of border traps in the  $1/f$ -like noise; Stemmer (2012) [342] and Galatage (2014) [102] also investigated the frequency dispersion in positive bias regime (accumulation of electrons) and both concluded that it is more probably due to interfacial traps in the mid-gap region (or disorder-induced gap states – DIGS) communicating through two-step process: i) tunneling of an electron from occupied traps to the gate, ii) recombination of the remaining hole with an electron in the SC CB.

Considering the numerous studies performed on the topic, we will not here make a more detailed review of these studies, but rather conclude that although many discrepancies can be found in the literature (due to the large variety of interface quality, fabrication process, extraction methods as well as strong variability of these devices), the vast number of literature studies tends to distinguish two distributions of traps that affect respectively the hole inversion Generation-Recombination process and the frequency dispersion of electron accumulation in n-MOSCAPs.

In the next section we briefly discuss the modeling strategy to take into account the trap dynamic in our solver, as well as how the calculation of the model parameters are done

through a multi-phonon theory. We then briefly present an early analysis of experimental results obtained at LETI and a qualitative comparison with our simulations.

### 2.2.3 Model

The model to account for traps dynamics presented below comes from the work of D.Rideau [306, 301], and part of the work of D.Garetto [105].

#### Electrostatics

First, let us introduce the rate equation:

$$\frac{\delta \rho_T(x, t)}{\delta t} = \Phi_c(x, t) - \Phi_e(x, t) - \tilde{\Phi}_c(x, t) + \tilde{\Phi}_e(x, t) \quad (2.7)$$

relating the variation of the trap charge density  $\rho_T(x, t)$  in time with the electrons (holes) capture and emission flows  $\Phi_c(x, t)$  and  $\Phi_e(x, t)$  ( $\tilde{\Phi}_c(x, t)$  and  $\tilde{\Phi}_e(x, t)$ , respectively) at position  $x$  and time  $t$ . These flows are depicted in Fig. 2.15.

Let us consider the left-hand term. Similarly to inversion charge, the trap charge  $\rho_T(x, t)$  can be calculated in a general way using

$$\rho_T(x, t) = e \int dE N_T(x, E, t) f_T(x, t, E - E_F(x, t)) \quad (2.8)$$

where  $f_T(x, t, E - E_F(x, t))$  is the occupation function of the trap, i.e., the probability that a trap placed at energy  $E$  and position  $x$  is occupied by an electron at time  $t$ . The quasi-Fermi level at position  $x$  is indicated with  $E_F(x, t)$ . As mentioned earlier, traps distribution  $N_T(x)$  is taken as a 2D Gaussian distribution in space and energy in the oxide layer. In this study degradation models are not investigated and thus  $N_T$  has been considered time independent  $N_T(x, E, t) = N_T(x, E)$ .

Introducing Eq.(2.8) in Eq.(2.7), the rate equation can be rewritten as:

$$e \int N_T(x, E) \frac{\partial f_T(x, t, E - E_F(x, t))}{\partial t} dE = \int \left( \Phi_c(x, E, t) - \Phi_e(x, E, t) - \tilde{\Phi}_c(x, E, t) + \tilde{\Phi}_e(x, E, t) \right) dE \quad (2.9)$$

Now the expression of the flows in the right-hand side of Eq. (2.7) can be expressed as functions of the capture and emission rates  $\tau_c^{-1}$  and  $\tau_e^{-1}$  for electrons as:

$$\begin{aligned} \Phi_c(x, E, t) &= N_T(x, E) \left( 1 - f_T(x, t, E - E_F(x, t)) \right) \tau_c^{-1}(x, E, t) \\ \Phi_e(x, E, t) &= N_T(x, E) f_T(x, t, E - E_F(x, t)) \tau_e^{-1}(x, E, t) \end{aligned} \quad (2.10)$$

and for holes as:

$$\begin{aligned} \tilde{\Phi}_c(x, E, t) &= N_T(x, E) f_T(x, t, E - E_F(x, t)) \tilde{\tau}_c^{-1}(x, E, t) \\ \tilde{\Phi}_e(x, E, t) &= N_T(x, E) \left( 1 - f_T(x, t, E - E_F(x, t)) \right) \tilde{\tau}_e^{-1}(x, E, t) \end{aligned} \quad (2.11)$$

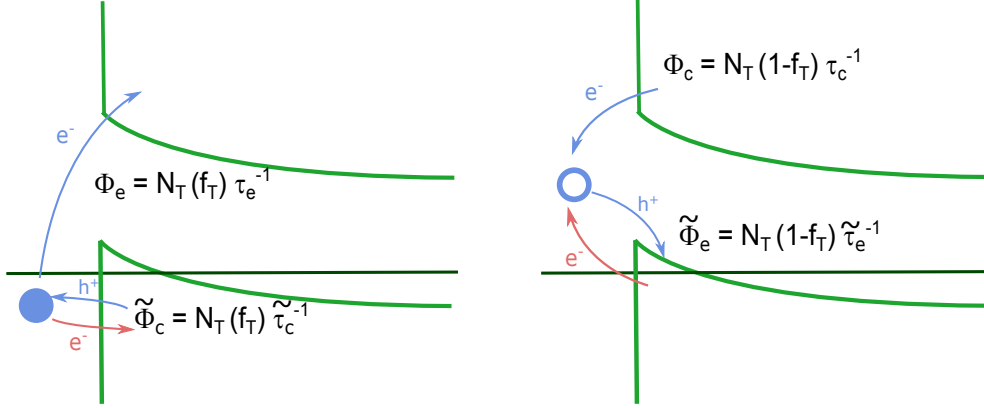


Figure 2.15. Schema of the flow defined in our code and characterizing the charge transfer between inversion charge and traps. Left: In the case where the trap energy level is below semiconductor Fermi-level (black horizontal line), it is filled with an electron, and transfer occurs through emission of electrons in CB (or capture of holes in VB). Right: When the trap energy level is above the Fermi-level, it is filled with hole (empty of electron), and it can capture electrons in CB (or emit holes in VB).

When these equations are inserted in Eq.(2.7), one can recognize a final equation very similar to the Shockley-Read-Hall recombination model [322, 132]:

$$\frac{\partial f_T}{\partial t} = \tau_e^{-1}(1 - f_T) - \tau_c^{-1} f_T$$

In order to model accurately the trapping mechanisms, the occupation function  $f_T(x, t, E - E_F(x, t))$  (or equivalently the quasi-Fermi level  $E_F$ ) is determined through resolution of this equation.

Finally, from this quantity, one can calculate the negative/positive trap charge caused by  $e^-/h^+$  occupying the trap using:

$$\begin{aligned} \tilde{\rho}_T(x, E, t) &= -e f_T(x, t, E - E_F(x, t)) N_T(x, E, t) \\ \rho_T(x, E, t) &= e(1 - f_T(x, t, E - E_F(x, t), t)) N_T(x, E, t) \end{aligned} \quad (2.12)$$

This trapped charge later enters into the Poisson equation (2.1), which is solved self-consistently with the Schrödinger equation in our 1D PS solver:

$$\rho(x, t) = e \left( p(x, t) - n(x, t) + N_{ch}(x) + N_{fixed}(x) \right) + \rho_T(x, t) \quad (2.13)$$

where  $\rho(x, t)$  identifies the electric charge density at position  $x$  and time  $t$ , where  $N_{fixed}(x)$  is the net concentration of fixed charges after degradation and  $\rho_T(x, t)$  the position-dependent trapped charge density evolving in time.

### Capture and emission parameters

In the case we exposed above, an important physical property has to be determined in order to perform the resolution of Eq.(2.7): the capture/emission rates  $\tau_{c/e}^{-1}$ . These quantities

can be expressed in term of the capture cross section  $\sigma$  as [3, 110]:

$$\tau_c^{-1} = \sigma Q_i v_{th} \quad (2.14)$$

$$\tau_e^{-1} = \sigma Q_{itrap} v_{th} \quad (2.15)$$

where  $Q_{itrap}$  is the surface carrier concentration when  $E_F$  equals the traps energy level  $E_T$  and  $v_{th}$  is the average thermal velocity. The dependence of  $\sigma$  over the temperature can be taken into account by the relation  $\sigma = \sigma_0 \exp(-E_B^*/k_B T)$ , where  $E_B^*$  can be understood as an effective activation energy of the process.

However, this way of doing hides the main physical phenomenon in one empirical parameter that is unable to take into account effects such as lattice relaxation involved in multiphonon assisted transitions (see discussion below). Moreover, it doesn't describe accurately the dependence of the capture and emission rates with the position in the oxide [105]. In our model, the temperature, position and time dependent capture and emission rates are written in terms of the capture/emission probabilities  $W_{c/e}$ ,

$$\begin{aligned} \tau_c^{-1}(x, \tilde{E}_T, t) &= \sum_i \int_{2DBZ} W_c(x, \varepsilon_i(\mathbf{K}), \tilde{E}_T, t) f(x, \varepsilon_i(\mathbf{K}), t) d\mathbf{K} \\ \tau_e^{-1}(x, E_T, t) &= \sum_i \int_{2DBZ} W_e(x, \varepsilon_i(\mathbf{K}), E_T, t) (1 - f(x, \varepsilon_i(\mathbf{K}), t)) d\mathbf{K} \end{aligned} \quad (2.16)$$

where  $\varepsilon_i(\mathbf{K})$  is the energy of the  $i^{\text{th}}$  subband at the 2D wavevector  $\mathbf{K}$  and  $E_T$  is the energy level of the trap considered.

### Non-radiative multiphonon theory

The transition probabilities  $W_{c/e}$  are determined through a model derived from multiphonon non-radiative theory. The application of the multiphonon theory to non-radiative transitions is a complex and broad topic and we will not go into detailed description here, nor show the derivation of Eq. (2.17) (see Appendix B for a general and short review). This theory is used to describe the lattice relaxation involved in the charge trapping/detrapping phenomenon. During the capture process, a carrier (electron or hole) is transferred from the free state (conduction or valence band) to the defect level. This capture induces a change of the electric charge of the defect, which affects the equilibrium coordinate of the system (from  $Q_A$  to  $Q_B$  in the Figure 2.16).

A so-called configuration-coordinate diagram can be used to have a graphical illustration of this phenomenon. Here the defect is supposed to be strongly coupled to one single mode of vibration, which is defined by its single coordinate  $Q$  (see Appendix B) and its phonon energy  $\hbar\omega$ . In this picture, the harmonic total energy of the system in the state  $A$  (where the trap is empty) and state  $B$  (where the trap is occupied) is plotted as function of the normal coordinate  $Q$ , as shown in Figure 2.16. This plot shows the shift in coordinate from the free state  $Q_A$  to the trapped state  $Q_B$ , as well as the relaxation energy associated  $S\hbar\omega$  (also called Franck-Condon energy) which is released to the lattice. This energy is intimately related to the Huang-Rhys factor  $S$ , defined as:

$$S\hbar\omega = \frac{\omega^2}{2} (Q_B - Q_A)^2$$



the second term in Eq. 2.17 can be usually neglected. The expressions of  $|V|^2$  and  $S$  as a function of oxide parameters in the case of a simple model for the defect wavefunction are given respectively in Eq. (B.4) and (B.5) in appendix. In our calculation,  $S$  is also considered as an adjustable parameter and is fixed to 15 (a reasonable value for a deep level [320, 244]). The term  $R(\Delta E)$  comes from the vibration overlap and is expressed as [113]:

$$R(\Delta E) = \frac{1}{\hbar\omega} \exp \left[ -(2\bar{n} + 1)S + \frac{\Delta E}{2kT} \right] \sum_m I_m(\xi) \delta(m\hbar\omega - \Delta E) \quad (2.18)$$

where  $m$  is the number of phonons involved in the transition,  $I_m(z)$  is the reduced Bessel function of order  $m$ ,  $\xi = 2S\sqrt{\bar{n}(\bar{n} + 1)}$  and  $\delta$  is the Dirac delta function.

The cross section obtained with this model for characteristic defects at Si/SiO<sub>2</sub> interface is shown in Fig. 2.17.

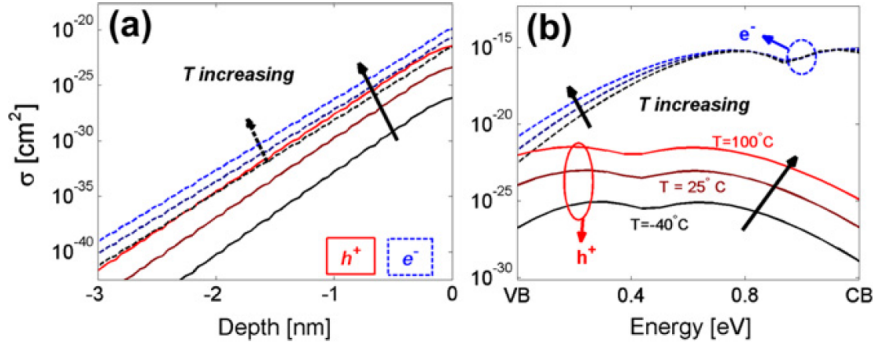


Figure 2.17. Capture cross section maps in depth in oxide (a) and energy (b) extracted from multiphonon model by Garetto (2012) [108] in an Si NMOS with 5nm of SiO<sub>2</sub>. (Figure taken from Ref. [108])

## 2.2.4 Comparison with experiment

Literature studies of In<sub>0.57</sub>Ga<sub>0.43</sub>As / Al<sub>2</sub>O<sub>3</sub> MOSCAPs and similar devices were reviewed in Section 2.2.2. In this section, we present a study on the MOSCAPs devices fabricated in LETI and characterized at low temperature in Section 2.1.3. The multi-phonon model is used, as implemented in UTOXPP software. The model derived above has been used in previous studies to simulate the influence of traps on the  $C_g(V_g)$  and  $G_g(V_g)$  in Si/SiO<sub>2</sub> structure, in the framework of a Poisson-Schrödinger solver [108, 106, 107]. Although we first suppose that this model can be extended to InGaAs/Al<sub>2</sub>O<sub>3</sub> structures with the same approximations made and same physics, the simulation of III-V MOS structures can be more complex, as the interfaces suffer from numerous defects and we have less knowledge about the microscopic nature of these defects. Moreover some additional effects can be encountered, due to the low density-of-states and non-parabolic nature of III-V materials, as well as interfacial traps inside the conduction band.

### Measurement at CEA-LETI

We showed a study of the capacitance of  $\text{In}_{0.57}\text{Ga}_{0.43}\text{As} / \text{Al}_2\text{O}_3$  MOSCAPs at low temperature and frozen traps condition in Section 2.1.3. A good agreement between theory and experimental data was found with the extracted oxide parameters (dielectric constant and physical thickness of alumina layer).

At higher temperature, a strong frequency dispersion is observed on the measurements, due to the traps dynamical response (see Fig. 2.19). To study the influence and nature of traps, further electrical characterization are performed on the same sample, as AC capacitance/conductance measurements at different frequencies (ranging from 1 kHz to 1 MHz) and different temperatures (ranging from 4 to 300 K). Considering the high number of data and the discrepancy in the measurements for different samples with the same process, and also different measurements on the same sample, some care should be taken in the interpretation of the data. It is not clear whether the discrepancy comes from errors or artifacts in the measurements or from the aging of the samples, due to relaxation of traps with long characteristic time for example. For this reason, we tried to reproduce the dispersion of the measurements qualitatively only, rather than obtaining a perfect quantitative agreement.

### Simulation results

Figure 2.18 shows the dispersion of traps considered in this study. It represents a narrow distribution with a spatial variance of 1 nm situated  $2 \text{ \AA}$  away from the interface. Two Gaussian distributions in energy are included: i) one distribution increasing inside the SC CB and ii) one smaller distribution close to the SC VBE. The first distribution peaks at about  $4.5 \times 10^{19} \text{ cm}^{-3} \text{ eV}^{-1}$  and is set as acceptor traps. The second distribution peaks at about  $5 \times 10^{19} \text{ cm}^{-3} \text{ eV}^{-1}$  and is set as donor-type. These two distributions of traps represent the two categories mentioned in Section 2.2.2 and the position in the oxide and peak values of the Gaussian were adjusted to reproduce qualitatively the experimental  $C_g(V_g)$ .

A small-signal analysis is used with a 30 mV amplitude signal and frequencies in the range of the measurement (1 kHz to 1 MHz). The same band structure and dielectric parameters are used in the NP-EMA PS solver as the one used in Section 2.1.3. For the parameters of the MPA model of Eq. (2.17), we set the phonon energy  $\hbar\omega = 60 \text{ meV}$  [319], close to the value of the optical phonons in  $\text{Al}_2\text{O}_3$ . For the Huang-Rhys factor, we arbitrarily choose  $S = 15$ , as its value for interface traps in  $\text{In}_{0.57}\text{Ga}_{0.43}\text{As} / \text{Al}_2\text{O}_3$  is not known and that the cross-section of these traps is also under debate [80]. The AC  $C_g(V_g)$  characteristics obtained are shown on Figure 2.19 and compared with the experimental measurement. A qualitative agreement is obtained with a frequency dispersion in accumulation and inversion with the two distribution of traps considered. However the slope of the capacitance at moderate accumulation is steeper in the simulation compared to the experimental one and the capacitance dispersion in accumulation is higher in the simulation than in experiments.

Figure 2.20 shows the influence of the  $S$  factor when varied from 9 to 15 on the accumulation AC  $C_g(V_g, \nu)$  characteristics of the nMOSCAP considered. One observes

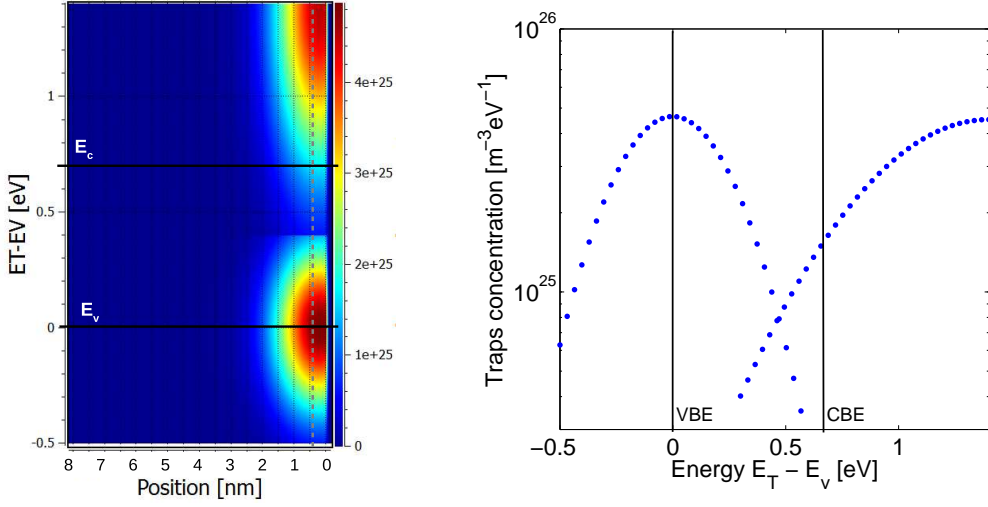


Figure 2.18. Maps of traps distribution considered in this study, consisting in a Gaussian distribution in space and energy. The origin of energy is set to the top of valence band  $E_V$ , and the scale for colors is given in  $m^{-3}eV^{-1}$ . The vertical cut along the grey dashed line is shown on the right plot.

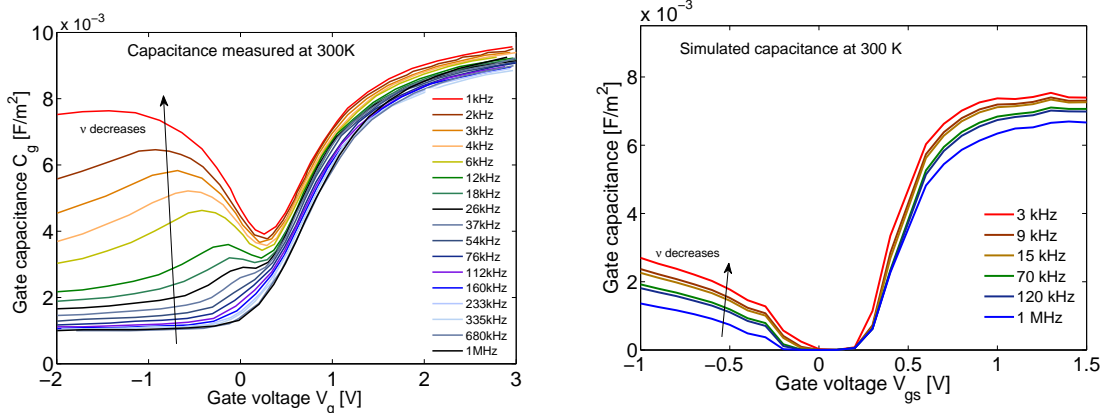


Figure 2.19. Left: frequency dependent  $C_g(V_g)$  measured at 300 K. Right: simulated  $C_g(V_g)$  at 300 K including two distributions of traps above CBE and close to VBE shown in Fig 2.18.

that when  $S$  is decreased, the  $C_g(V_g, \nu)$  curve presents an overall shift to the left (acting as a shift of the threshold voltage  $V_{th}$  to lower gate voltage) and the influence of the traps on the  $C_g(V_g)$  characteristics is generally found at higher frequency.

For the dispersion in inversion (negative  $V_{gs}$ ), the trap-assisted generation of inversion holes makes it difficult to distinguish between trap response and holes generation. This generation of inversion charge was not taken into account in our solver, as infinite

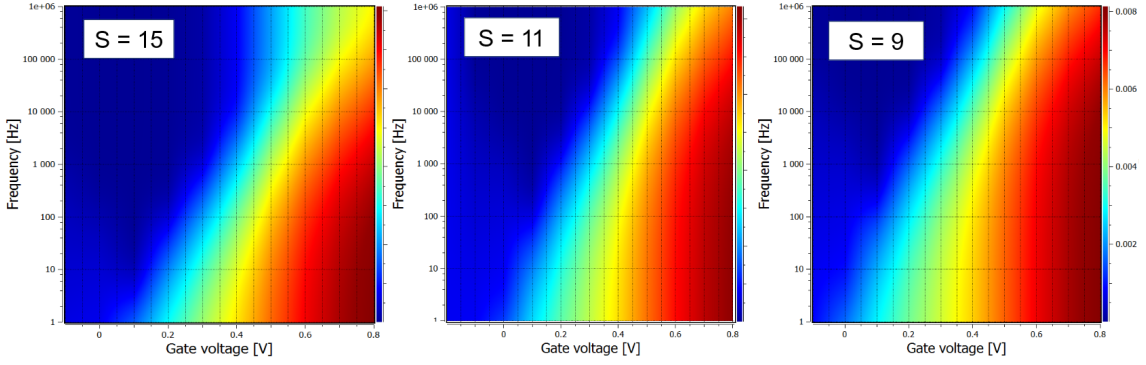


Figure 2.20. Small signal AC gate capacitance of nMOSCAP in accumulation ( $V_{gs}$  varying from  $-0.2$  to  $0.8$  V) for different values of Huang-Rhys factor  $S$ .

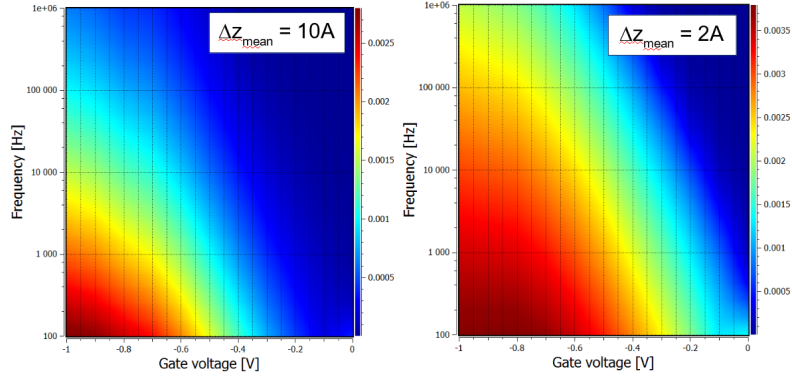


Figure 2.21. Small signal AC gate capacitance of nMOSCAP in inversion ( $V_{gs}$  varying from  $-1$  to  $0$  V) for a donor traps distribution close the VBE with a mean space Gaussian located  $1$  nm and  $2$  Å away from the SC/oxide interface.

reservoirs of carriers are supposed to be available (which is not the case in experimental MOSCAP devices without source/drain reservoirs). However, it is possible to introduce this effect in the solver by “freezing out” the DC holes inversion charge during the AC small signal simulations leading to a zero influence on capacitance, while the trap-assisted hole generation-recombination signature was still taken into account through the multi-phonon non-radiative transition model. It is interesting to note here that the distribution of traps in the oxide was sufficient to reproduce the dispersion at inversion and the generation of inversion charges, without generation-recombination centers in the III-As SC itself, which should be incorporated in the model and probably influence the hole generation. This shows that different traps distribution and parameters can be used to reproduce a  $C_g(V_g)$  characteristics and that the traps distribution obtained with a similar fitting procedure would probably not be unique, especially when the intrinsic parameters and atomic nature of the traps are not well characterized.

The inversion AC  $C_g(V_g, \nu)$  characteristics when the trap distribution is pushed away from the interface are shown in Figure 2.21. One observes that when the trap distribution is shifted from 2 Å to 1 nm away from the interface, the capacitance in inversion drastically diminishes, due to the lower transition probability and thus lower hole generation mechanism.

## 2.3 Conclusion of the Chapter

In this Chapter, we investigated the electrostatic characteristics of III-As/Al<sub>2</sub>O<sub>3</sub> MOSCAPs. Classical, parabolic EMA, NP-EMA and atomistic TB PS simulations were compared in the case of ideal MOSCAPs without traps and the important influence of non-parabolicity and boundary conditions on the electrostatics in UTBB MOSCAPs were investigated.

In the second part of the Chapter, a literature review of the knowledge of the traps in In<sub>0.57</sub>Ga<sub>0.43</sub>As /Al<sub>2</sub>O<sub>3</sub> structures and a model to take into account their effects on electrostatic  $C_g(V_g)$  characteristics were presented. A review of the state-of-the-art devices and their interface quality was given, as well as models for the simulation of traps response. This Chapter pointed out the limitations of different models in the simulation of the electrostatics of III-V materials, as well as the intrinsic bottleneck of these materials concerning the low DOS of their  $\Gamma$  valley. Due to this low DOS, the Fermi-level can travel far inside the SC conduction band and can scan traps at high energy. These traps not only induce a frequency-dispersion of the capacitance at positive  $V_g$  bias but also limit the free carrier density achievable and thus the overall current of the device. In addition, electrically active defects can affect the transport properties and current achievable through Coulomb scattering, as pointed out in Refs. [331, 366].

In this Chapter, the gate capacitance of long-channel planar devices was considered. The transport properties of long-channel devices and the electrostatics and transport properties of short-channel devices will be investigated in the next two Chapters.

## Chapter 3

# Semi-classical transport

To model the diffusive transport in long-channel MOSFET transistors, the current is usually given in terms of the low-field mobility and the high-field saturation velocity, describing the transport properties of the channel material. These properties may depend on various parameters, such as the transverse electric field, the carrier density, the confinement, the doping concentration and the interface properties (surface roughness and interface charges). Empirical models are often used in TCAD to account for these effects, that introduce numerous fitting parameters and that need intensive calibration. More advanced physical-based models can be used to predict and understand (de-embed) the contribution of different scattering mechanisms on the overall mobility.

In this Chapter, the diffusive transport properties of electrons and holes in nanostructures are investigated by means of semi-classical methods, based on the resolution of the Boltzmann transport equation (BTE). The derivation of the low-field mobility based on the relaxation time approximation (RTA) and the exact resolution of the linearized BTE are first presented. The derivation of the scattering matrix elements for the main mechanisms, such as Polar Optical Phonon (POP), Deformation Potential acoustic and optical phonon, Surface Roughness (SR) and Ionized Impurity (Local Coulomb LC) are then discussed within continuous KP and EMA models and used to compute the mobility in planar FDSOI structures. The calculation of phonons and alloy disorder scattering matrix elements in an atomistic TB approach is then presented and used to compute the mobility in SiGe nanowires. The resolution of the BTE at high electric field is then used to compute the saturation velocity of SiGe nanowires and to investigate the effect of confinement, band structure and nanowire orientation on the saturation velocity.

### 3.1 Low-field mobility

The mobility is an important parameter for electronic transport, linking the electric field  $\mathbf{E}$  with the average carrier velocity  $\mathbf{v}$ , and thus with current  $\mathbf{j} = n\mathbf{v}$ . This relation can be assumed to be linear at low electric field (low source-drain voltage  $V_{ds}$ ):

$$\mathbf{v} = \mu\mathbf{E}$$

This relation enters the calculation of the drift current of a MOSFET device in the linear regime, in the simple drift-diffusion (DD) model, written for electrons as:

$$\mathbf{J} = e(n\mu\mathbf{E} + D\nabla n) \quad (3.1)$$

where  $\mathbf{J}$  is the total current,  $e$  the elementary charge,  $n$  the electrons carrier density and  $D$  the diffusivity coefficient. At high electric field (saturation regime), the relation is no more linear. The drift velocity tends to saturate and the electronic transport (and saturation current) depends on the so-called saturation velocity  $v_{sat}$ , which will be discussed in Section 3.2.1.

The low-field mobility is, at first approximation, given by the simple formula (predicted by the classical Drude’s theory [13]):

$$\mu_{\text{eff}} = \frac{e\tau_r}{m^*} \quad (3.2)$$

where  $\tau_r$  is the momentum relaxation time and  $m^*$  is the effective mass of the carrier. The relaxation time expresses an average lapse of time between two collisions, changing the energy and/or wavevector orientation of an electron. This quantity can be computed with semi-classical or quantum pictures and is not trivial to extract. Moreover, Eq. (3.2) is over simplified and, in an inversion layer in a scaled device, more accurate quantum calculations of the mobility have to be performed. To calculate mobility at low field in an inversion layer in a MOSFET device, the so-called “Kubo-Greenwood” formula is used in our solver [88]:

$$\mu_{xy} = -\frac{e}{\hbar} \left\langle \tau_x v_x \left( \frac{\partial f}{\partial K_y} \frac{1}{f} \right) \right\rangle_{th}$$

where  $x, y$  stands for the direction in the 2D plane,  $v$  is the group velocity and  $f$  is the Fermi-Dirac distribution function.  $\langle \cdot \rangle_{th}$  denotes the thermal average:

$$\langle \zeta \rangle = \sum_{i,\nu} \frac{g_\nu}{n_i} \int \frac{d\mathbf{K}}{(2\pi)^2} \zeta(\mathbf{K}) f_i(\mathbf{K})$$

where  $i$  is the index of the subband and  $\nu$  the index of the valley. This formula comes from the much more general linear response theory of the electric conductivity, derived in the quantum transport framework in the work of Kubo (1957) [176] and Greenwood (1958) [120].

### 3.1.1 Linearization of Boltzmann transport equation

The semi-classical formulation of the KG formula can be obtained from the linearization of the Boltzmann transport equation (BTE):

$$\frac{\partial f_i}{\partial t} + \mathbf{v} \cdot \nabla_{\mathbf{r}} f_i + \frac{\mathbf{F}}{\hbar} \cdot \nabla_{\mathbf{k}} f_i = \left. \frac{\partial f_i}{\partial t} \right|_{col} \quad (3.3)$$

where the right hand side of the equation is the collision term due to scattering mechanisms (no generation-recombination processes are considered here),  $f_i(\mathbf{k}, \mathbf{r}, t)$  is the carrier distribution function of subband  $i$ ,  $\mathbf{v}(\mathbf{k}) = \frac{1}{\hbar} \nabla_{\mathbf{k}} \varepsilon$  is the group velocity and  $\mathbf{F} = -e(\mathbf{E} + \mathbf{v} \times \mathbf{B})$  is the external Lorentz force ( $\mathbf{E}$  and  $\mathbf{B}$  being the electric and magnetic fields, resp.).

We usually assume a stationary, homogeneous distribution function  $f_i = f_i(\mathbf{k})$ , and no magnetic field applied. Under these assumptions (generally true for long-channel devices), Equation (3.3) becomes:

$$-\frac{e\mathbf{E}}{\hbar} \cdot \nabla_{\mathbf{k}} f_i(\mathbf{k}) = \left. \frac{\partial f_i}{\partial t} \right|_{col} \quad (3.4)$$

Moreover, we can express the collision term as a function of transition rate matrix  $S_{ij}$  as:

$$\begin{aligned} \left. \frac{\partial f_i}{\partial t} \right|_{col} = & \sum_j \frac{\Omega}{(2\pi)^d} \int d^d k' \left( S_{ji}(\mathbf{k}', \mathbf{k}) \left\{ f_j(\mathbf{k}') [1 - f_i(\mathbf{k})] \right\} \right. \\ & \left. - S_{ij}(\mathbf{k}, \mathbf{k}') \left\{ f_i(\mathbf{k}) [1 - f_j(\mathbf{k}')] \right\} \right) \end{aligned} \quad (3.5)$$

where the first term in the sum corresponds to in-scattering events (from state  $\mathbf{k}'$  in subband  $j$  to state  $\mathbf{k}$  in subband  $i$ ) and the second term to out-scattering events (from state  $(\mathbf{k}, i)$  to state  $(\mathbf{k}', j)$ ),  $\Omega$  is the volume considered,  $d$  is the dimensionality and  $S_{ij}$  can be determined using Fermi's golden rule (first-order of the scattering perturbation):

$$S_{ij}(\mathbf{k}, \mathbf{k}') = \frac{2\pi}{\hbar} |M_{ij}(\mathbf{k}, \mathbf{k}')|^2 \delta(\varepsilon_j - \varepsilon_i \pm \Delta\varepsilon) \quad (3.6)$$

where  $\delta$  is the Dirac delta function and  $M_{ij}(\mathbf{k}, \mathbf{k}')$  is the matrix element of transition from state  $\mathbf{k}$  to  $\mathbf{k}'$  defined as:

$$M_{ij}(\mathbf{k}, \mathbf{k}') = \langle \mathbf{k}', j | \hat{V}^p | \mathbf{k}, i \rangle = \frac{1}{\Omega} \int_{\Omega} d^d r \psi_j^\dagger(\mathbf{k}', \mathbf{r}) V^p(\mathbf{r}) \psi_i(\mathbf{k}, \mathbf{r})$$

where  $V^p$  is the perturbation potential, depending on the scattering mechanism considered.

To solve Equations (3.4) and (3.5), assumptions are made on the dependence of the distribution function on the electric field. It is hereafter expanded to the first-order (linearization of BTE). However, higher orders are needed to describe the distribution at high electric field. To treat this case, the full Boltzmann equation can be solved in different ways, such as Monte Carlo simulation or using Spherical Harmonic functions to expand distribution function in higher momenta. In our case, we will show how to solve Equations (3.4) and (3.5) without further approximation in next section.

### Order zero

Under equilibrium, the distribution function  $f(\mathbf{k})$  is given by Fermi-Dirac statistics:

$$f_i^0(\mathbf{k}) = \frac{1}{1 + e^{\beta(\mathcal{E}_i(\mathbf{k}) - \mathcal{E}_F)}}$$

where  $\mathcal{E}_F$  is Fermi energy, and  $\beta = \frac{1}{k_B T}$ . The terms in bracket in Equation (3.5) thus become:

$$f_j^0(\mathbf{k}') [1 - f_i^0(\mathbf{k})] = \frac{1}{1 + e^{\beta(\mathcal{E}_j(\mathbf{k}') - \mathcal{E}_F)}} \frac{e^{\beta(\mathcal{E}_i(\mathbf{k}) - \mathcal{E}_F)}}{1 + e^{\beta(\mathcal{E}_i(\mathbf{k}) - \mathcal{E}_F)}}$$

When no electric field is applied  $\mathbf{E} = 0$ , Equation (3.4) equals zero and the detailed balance equation is obtained by setting the integrand in Equation (3.5) to zero:

$$S_{ji}(\mathbf{k}', \mathbf{k}) \left\{ f_j^0(\mathbf{k}') [1 - f_i^0(\mathbf{k})] \right\} = S_{ij}(\mathbf{k}, \mathbf{k}') \left\{ f_i^0(\mathbf{k}) [1 - f_j^0(\mathbf{k}')] \right\}$$

Combining these two equations, one obtains:

$$\begin{aligned} S_{ji}(\mathbf{k}', \mathbf{k}) &= S_{ij}(\mathbf{k}, \mathbf{k}') \frac{f_i^0(\mathbf{k}) [1 - f_j^0(\mathbf{k}')] }{f_j^0(\mathbf{k}') [1 - f_i^0(\mathbf{k})]} \\ &= S_{ij}(\mathbf{k}, \mathbf{k}') e^{\beta(\mathcal{E}_j - \mathcal{E}_i)} \end{aligned} \quad (3.7)$$

This equation translates the fact that, in order to have equilibrium, the number of transitions  $(i, \mathbf{k}) \rightarrow (j, \mathbf{k}')$  must be equals to the number of opposite transitions  $(j, \mathbf{k}') \rightarrow (i, \mathbf{k})$ . It can be proved for each scattering mechanism by using time-reversal symmetry. In the case of inelastic phonon scattering, the energy difference  $(\mathcal{E}_j - \mathcal{E}_i)$  is equal to the phonon energy  $\hbar\omega$  and the exponential term in Eq. 3.7 compensates the ratio of phonon occupation factors due to the difference between phonon emission and absorption processes (see Sec. 3.1.2).

### First order

The distribution function is now expanded at first order in  $\mathbf{E} = \mathbf{E}\mathbf{u}$ :

$$f_i^1(\mathbf{k}) = f_i^0(\mathbf{k}) + e\mathbf{E}g_i(\mathbf{k}) \quad (3.8)$$

The terms in bracket in Equation (3.5) now become <sup>1</sup>:

$$(f_j^0 + e\mathbf{E}g_j) [1 - (f_i^0 + e\mathbf{E}g_i)] = f_j^0 [1 - f_i^0] + e\mathbf{E} (g_j(1 - f_i^0) - g_i f_j^0)$$

Keeping only the first order, Equation (3.4) becomes:

$$-\frac{e}{\hbar} \mathbf{E} \cdot \nabla_{\mathbf{k}} f_i^0 = \sum_j \rho_d \int d^d k' e\mathbf{E} \left( S_{ji} \{ g_j [1 - f_i^0] - g_i f_j^0 \} - S_{ij} \{ g_i [1 - f_j^0] - g_j f_i^0 \} \right)$$

---

<sup>1</sup>For sake of readability, we simplify here the notation, not writing explicitly the function variables

where  $\rho_d = \frac{\Omega}{(2\pi)^d}$ . Simplifying by  $eE$  and re-arranging the terms in  $g_i$ :

$$-\frac{1}{\hbar} \mathbf{u} \cdot \nabla_{\mathbf{k}} f_i^0 = \sum_j \rho_d \int d^d k' \left( g_j \{ S_{ji} [1 - f_i^0] + S_{ij} f_i^0 \} - g_i \{ S_{ji} f_j^0 + S_{ij} [1 - f_j^0] \} \right)$$

Now using chains rule for derivative and the definition of group velocity:

$$\begin{aligned} [\mathbf{u} \cdot \mathbf{v}] \frac{\partial}{\partial \mathcal{E}} f^0(\varepsilon_i) &= \sum_j \rho_d \int d^d k' \left( g_i \{ S_{ji} f_j^0 + S_{ij} [1 - f_j^0] \} \right. \\ &\quad \left. - g_j \{ S_{ji} [1 - f_i^0] + S_{ij} f_i^0 \} \right) \end{aligned} \quad (3.9)$$

This expression can be expressed as a linear system  $\mathbf{b} = A\mathbf{g}$  where the matrix  $A$  is composed of transition rate matrix and equilibrium distribution function. At first order, the time reversal symmetry is conserved and one needs to add the condition of  $g_i(\mathbf{k}) = g_i(-\mathbf{k})$  to solve the system (i.e.  $\sum_{\mathbf{k}} g_i(\mathbf{k}) = 0$ ). This numerical resolution of this system can be used to calculate the distribution function and to get the conductivity and mobility from its first and second order momenta.

### Relaxation time approximation

Another way to compute the mobility, often found in the literature, comes from the introduction of a so-called relaxation time  $\tau(\mathbf{k})$ . It is indeed very common to see the collision term expressed as:

$$\left. \frac{\partial f}{\partial t} \right|_{col} = -\frac{f(\mathbf{k}) - f^0(\mathbf{k})}{\tau(\mathbf{k})}$$

where the parameter  $\tau$  expresses the time that the distribution function needs to come back to equilibrium and is related to the momentum relaxation time  $\tau_r$  introduced in Equation (3.2). In this approximation, BTE (3.4) becomes:

$$-\frac{e\mathbf{E}}{\hbar} \cdot \nabla_{\mathbf{k}} f(\mathbf{k}) = -\frac{f(\mathbf{k}) - f^0(\mathbf{k})}{\tau(\mathbf{k})}$$

We will now assume that the relaxation time  $\tau(\mathbf{k}) = \tau$  is isotropic and drop the function variables in our notation. As before, the distribution function is considered to vary linearly with the electric field  $E$  and Eq. (3.8) is used. Keeping terms in first order in  $E$ , it comes:

$$\frac{e\mathbf{E}}{\hbar} \nabla_{\mathbf{k}} f_0 = \frac{eEg}{\tau}$$

Simplifying by  $eE$  and using chain's rule of derivative:

$$\frac{g}{\tau} = \frac{\mathbf{u}}{\hbar} \nabla_{\mathbf{k}} \varepsilon \frac{\partial f_0}{\partial \varepsilon} = [\mathbf{v} \cdot \mathbf{u}] \frac{\partial f_0}{\partial \varepsilon}$$

Finally we obtain:

$$g = \tau v_u \frac{\partial f_0}{\partial \varepsilon} \quad (3.10)$$

where  $v_u$  is the component of the group velocity in the direction of electric field and where the derivative of  $f_i^0$  over energy can be written as:

$$\frac{\partial f_i^0}{\partial \varepsilon} = -\beta f_i^0 (1 - f_i^0)$$

Now the scattering collision term in Eq. (3.5) can also be written as:

$$\frac{g_i}{\tau_i} = \sum_j \frac{\Omega}{(2\pi)^d} \int d^d k' \left( S_{ji} \{g_j [1 - f_i^0] - g_i f_j^0\} - S_{ij} \{g_i [1 - f_j^0] - g_j f_i^0\} \right)$$

After some algebra and using Eq. (3.10) and the zeroth-order balance equation (3.7), the expression of scattering rate  $1/\tau_i$  can be obtained:

$$\begin{aligned} \frac{1}{\tau_i} &= \sum_j \frac{\Omega}{(2\pi)^d} \int d^d k' S_{ij} \frac{1 - f_j^0}{1 - f_i^0} \left( 1 - \frac{\cancel{\beta f_j^0 (1 - f_j^0)} \tau_j v_{u,j}}{\cancel{\beta f_i^0 (1 - f_i^0)} \tau_i v_{u,i}} \left\{ \frac{f_i^0}{f_j^0} \frac{1 - f_i^0}{1 - f_j^0} \right\} \right) \\ &= \sum_j \frac{\Omega}{(2\pi)^d} \int d^d k' S_{ij} \frac{1 - f_j^0}{1 - f_i^0} \left( 1 - \frac{\tau_j v_{u,j}}{\tau_i v_{u,i}} \right) \end{aligned} \quad (3.11)$$

This last expression is commonly found in the literature, expressing the relaxation time for a given subband  $i$  and a given scattering mechanism determined by  $S_{ij}$ . Finally, writing explicitly the expression of  $S_{ij}$ , the scattering rate reads:

$$\frac{1}{\tau_i} = \frac{2\pi}{\hbar} \sum_j \frac{\Omega}{(2\pi)^d} \int d^d k' \left| \langle \mathbf{k}', j | \hat{V}^p | \mathbf{k}, i \rangle \right|^2 \delta(\varepsilon_j - \varepsilon_i \pm \hbar\omega) \frac{1 - f_j^0}{1 - f_i^0} \left( 1 - \frac{\tau_j v_{u,j}}{\tau_i v_{u,i}} \right) \quad (3.12)$$

At this step, there is no additional approximation and this equation is equivalent to Eq. (3.9). As it still links  $\tau_i$  with  $\tau_j$ , this equation must be solved self-consistently, as Eq. (3.9). To avoid this time-consuming treatment, the last term is often approximated as:

$$\left( 1 - \frac{\tau_j v_{u,j}}{\tau_i v_{u,i}} \right) = (1 - \cos \theta) \quad (3.13)$$

where  $\theta$  is the scattering angle between vector  $\mathbf{k}$  and  $\mathbf{k}'$ . Moreover, for elastic scattering,  $\varepsilon_i = \varepsilon_j$  and  $f_i^0 = f_j^0$  so the distribution function term in Eq. (3.12) is set to 1. On the other hand, for inelastic but isotropic scattering, one usually neglects the second term in parenthesis and keep only the distribution function term. These approximations were investigated in recent studies [214, 334] and found to be invalid in the case of anisotropic and inelastic mechanisms, such as POP in III-V polar materials.

### 3.1.2 Scattering rates within KP models

We discuss below the different scattering mechanisms relevant to the transport properties of  $\text{In}_x\text{Ga}_{1-x}\text{As}$  and  $\text{Si}_{1-x}\text{Ge}_x$  channels. These mechanisms include:

- the interaction with Polar-Optical Phonons (POP) through the Fröhlich potential, which is the limiting mechanism in bulk polar materials such as III-V;
- the interaction with Non-Polar Phonons (PH) through the Deformation-Potential theory, which includes the Acoustic and Optical Phonons and is the limiting mechanism in bulk covalent materials at room temperature;
- the interaction with Surface Roughness (SR) or interface roughness, which importance significantly increases when the front gate voltage increases (high inversion) or the confinement increases (very thin channel);
- the Coulomb interaction with ionized impurities in the channel (Local Coulomb LC) or remote charges in the gate stack (Remote Coulomb RC), which hinders the mobility in highly doped materials or degraded gate stack, respectively. These processes are particularly important at low inversion, where the screening of the scattering potential is unefficient;
- the interaction with Alloy Disorder (AD) in random alloys, which particularly hinders the mobility in SiGe bulk channels [91].

The dependence of some of the mechanisms on temperature and electric field is shown in Figure 3.1.

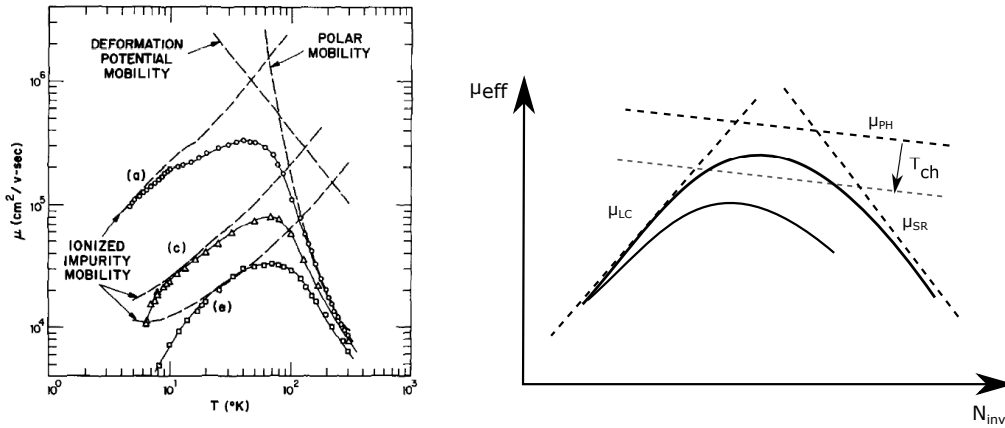


Figure 3.1. Left: Hall mobility in n-type GaAs with dopant concentrations:  $5 \cdot 10^{13}$  (a);  $1 \cdot 10^{15}$  (c) and  $5 \cdot 10^{15}$  (e)  $\text{cm}^{-3}$ , showing the temperature dependence of the different scattering mechanisms (Figure taken from Ref. [344]). Right: schematic plot of the effective low-field mobility in FDSOI devices as a function of the inversion charge  $N_{inv}$  for different scattering mechanisms. The arrow shows the enhancement of electron-phonon coupling when the channel thickness  $t_{ch}$  is decreased.

### Polar optical phonons

As said in the Introduction, to compute the effective mobility in a channel made of III-V materials, it is necessary to take into account a scattering mechanism that is not present in Si: the scattering of carriers by Polar-Optical Phonons (POP).

This mechanism comes from the creation of an oscillating electric field by lattice vibrations in a polar crystal, such as III-V. The scattering potential describing this mechanism in the bulk is the so-called Fröhlich potential [100, 101]:

$$V_{\text{POP}}(\mathbf{r}) = e \left\{ \frac{\hbar\omega_{LO}}{2q^2\Omega} \left[ \frac{1}{\epsilon(\infty)} - \frac{1}{\epsilon(0)} \right] \right\}^{1/2} e^{i\mathbf{q}\mathbf{r}} (a_{-\mathbf{q}}^+ + a_{\mathbf{q}}) \quad (3.14)$$

where  $\omega_{LO}$  is the frequency of LO-phonons,  $\epsilon(\infty)$  and  $\epsilon(0)$  are static and optical dielectric constants,  $\Omega$  is the volume considered,  $e$  is the electron charge,  $\mathbf{q}$  and  $\mathbf{r}$  are vectors in reciprocal and real space respectively ( $q$  being the norm of  $\mathbf{q}$ ) and  $a_{-\mathbf{q}}^+$  and  $a_{\mathbf{q}}$  are the phonon creation and annihilation operators. This potential can be obtained by solving the equations of oscillating polarization, local electric field and atoms movement in presence of an electric field, keeping in mind the dielectric behavior of an ionic crystal and the well-known Lyddane-Sachs-Teller relation that links phonon frequencies and dielectric constants:

$$\frac{\epsilon(0)}{\epsilon(\infty)} = \frac{\omega_{LO}^2}{\omega_{TO}^2}$$

In thin films of thickness  $T$ , the scattering matrix element for this mechanism is expressed as (see Appendix C for the complete derivation):

$$|M_{ij}(Q)|^2 = \left\{ \frac{e^2\hbar\omega_{LO}}{4S} \left[ \frac{1}{\epsilon(\infty)} - \frac{1}{\epsilon(0)} \right] \right\} \left( N_{\text{LO}} + \frac{1}{2} \mp \frac{1}{2} \right) \frac{H_{i,j}(Q)}{Q}$$

where  $S$  is the surface normalization factor,  $N_{\text{LO}}$  is the phonon occupation factor,  $Q$  is the norm of the in-plane phonon wavevector  $\mathbf{Q} = \mathbf{K}' - \mathbf{K}$  and  $H_{i,j}$  is the overlap integral:

$$H_{i,j}(Q) = \int_0^T dz_1 \int_0^T dz_2 \psi_i(z_1) \psi_i^\dagger(z_2) \psi_j(z_2) \psi_j^\dagger(z_1) e^{-Q|z_1 - z_2|}$$

From this expression, the momentum relaxation time in a 2DEG can be found for the absorption and emission processes (respectively upper and lower signs) [285] (see Appendix C):

$$\begin{aligned} \frac{1}{\tau_{i,j,\nu}^{\text{POP}}(\varepsilon_i)} &= \frac{g_s g_\nu e^2 m_\nu^* \omega_{LO}}{8\pi\hbar^2} \left( \frac{1}{\epsilon(\infty)} - \frac{1}{\epsilon(0)} \right) \left( N_{\text{LO}} + \frac{1}{2} \mp \frac{1}{2} \right) \frac{1 - f(\varepsilon_i \pm \hbar\omega_{LO})}{1 - f(\varepsilon_i)} \\ &\times [1 + 2\alpha(\varepsilon_i - U_i)] \int_0^{2\pi} d\theta \frac{H_{i,j,\nu}(Q_\pm)}{Q_\pm} \left( 1 - \frac{\tau_j v_{u,j}}{\tau_i v_{u,i}} \right) \end{aligned} \quad (3.15)$$

where  $g_s$  is the spin degeneracy,  $\nu$  the index of the valley with degeneracy  $g_\nu$ ,  $\theta$  is the angle between  $\mathbf{K}$  and  $\mathbf{K}'$  and the term in square parenthesis accounts for the NP corrections [263]

( $\alpha$  being the NP coefficient and  $U_i$  the averaged potential as computed in Eq. (1.16)). As it decreases as  $1/Q = 1/|\mathbf{K} - \mathbf{K}'|$ , this mechanism is treated as an intravalley scattering. Moreover, as the main valley contributing to low-field mobility in III-V is the  $\Gamma$  valley, an isotropic effective mass  $m^*$  is considered here.

Note that in this approach, the bulk scattering potential is used, which is valid only in the case where the dielectric response of the thin film environment can be approximate by  $\epsilon(\infty)$  and  $\epsilon(0)$  dielectric constants. This is generally not the case in nanostructures. In the literature, one can find some recent publications performing simulations of mobility in III-V nanostructures using Kubo-Greenwood formalism, such as O'Regan *et al.* (2010) [263], Poljak *et al.* (2012) [285] and Marin *et al.* (2014) and (2015) [216, 215]. The treatment of the POP scattering can sometimes differ from one study to another and some further refinements can be included, in particular concerning the screening effects. O'Regan *et al.* (2010) [263] included screening effects in the Random Phase Approximation for interaction with bulk LO-phonons, while they include an additional scattering mechanism for the interaction of carriers with surface-optical modes of phonons (SO-phonons) and plasmons, which may influence the overall mobility in some cases. Another model to treat POP scattering was also presented by Stanojevic (2015) [336, 337], using the properties of the Poisson's Green function to express the scattering by the dipole created by the polar nature of phonons. In this way, the screening of the gate and dielectric environment was correctly taken into account and treated in a continuous way. Beside, Marin investigated the mobility in InAs [216, 217] and GaAs [215] nanowires and showed that the approximation in Eq. (3.13) is not valid for anisotropic and inelastic scattering mechanisms such as POP, and that the coupled system must be resolved with iterative and linear system solvers. This issue will be investigated in thin films in Section 3.1.3.

### Deformation-potential theory: acoustic and optical phonons

In non-polar materials, the scattering with phonons remains the main limiting mechanism at room temperature and moderate inversion, particularly by acoustic phonons. It is generally described through the deformation potential theory, writing the electron-phonon interaction for small atom displacement within a linear development [83, 398]:

$$V_{e-ions} \simeq \sum_{\alpha} \left( \frac{\partial H_e}{\partial \mathbf{R}_{\alpha}} \right) \Big|_{\mathbf{R}_{\alpha 0}} \cdot \delta \mathbf{R}_{\alpha}$$

where  $\delta \mathbf{R}_{\alpha}$  is the displacement of the  $\alpha^{\text{th}}$  atom and  $\mathbf{R}_{\alpha 0}$  is its position at equilibrium. In the case of long-wavelength acoustic phonon, the lattice deformation can be considered as a strain field and the strain deformation potentials described in Chapter 1 Sec. 1.1.9 can be used to compute the electron-acoustic phonon coupling (see Ref. [161] for the derivation and expression linking the two quantities). In this case, the perturbative potential reads:

$$V_{AC} = D_{ac}(\mathbf{q} \cdot \delta \mathbf{R})$$

where  $D_{ac}$  is the deformation potential in unit of [eV] ( $D_{ac} = a_{c/v}$  is the absolute strain deformation potential for longitudinal acoustic (LA) mode),  $\mathbf{q}$  is the phonon wavevector

and  $\delta\mathbf{R}$  is the atomic displacement that can be expressed in term of phonon creation and annihilation operators [398]. The momentum relaxation time in 2DEG in this case writes (see Refs. [83, 206] for the complete derivation):

$$\frac{1}{\tau_{i,j,\nu}^{\text{LA}}(\varepsilon_i)} = \frac{g_s m_{\text{DOS},\nu}^* k_B T D_{ac,\nu}^2}{2\hbar^3 \rho v_s^2} F_{i,j,\nu} \int_0^{2\pi} d\theta (1 - \cos \theta) \quad (3.16)$$

where  $\rho$  is the material volume density and  $v_s$  is the sound velocity of the acoustic phonons.  $F_{i,j,\nu}$  is the wavefunction form factor defined as:

$$F_{i,j,\nu,\nu'} = \int dz |\psi_{i,\nu}(z)|^2 |\psi_{j,\nu'}(z)|^2$$

This mechanism is treated as an elastic and intravalley ( $\nu = \nu'$ ) scattering. In the case of an anisotropic elliptic valley, the DOS effective mass can be replaced inside the integration over  $\theta$  by the expression:

$$m_{\text{DOS}}^* \rightarrow \left( \frac{\cos^2 \theta}{m_x} + \frac{\sin^2 \theta}{m_y} \right)^{-1}$$

In the case of optical phonon, the perturbative potential is written as:

$$V_{\text{OP}} = D_{op,q} \delta R$$

where  $\delta R$  is the norm of the phonon displacement and  $D_{op,q}$  is the optical deformation potential of the transition of wavevector  $q$  in units of [eV/Å]. The momentum relaxation time in 2DEG for this mechanism writes (see Refs. [83, 206] for the complete derivation):

$$\frac{1}{\tau_{i,j,\nu,\nu'}^{\text{OP}}(\varepsilon_i)} = \frac{g_s m_{\text{DOS},\nu}^* D_{op,\nu}^2}{4\rho\hbar^2 \omega_{OP}} \left( N_{\text{OP}} + \frac{1}{2} \mp \frac{1}{2} \right) \frac{1 - f(\varepsilon_i \pm \hbar\omega_{OP})}{1 - f(\varepsilon_i)} F_{i,j,\nu,\nu'} (1 - \cos \theta) \quad (3.17)$$

where  $\hbar\omega_{OP}$  is the optical phonon energy, the upper and lower sign are for the absorption and emission of a phonon and  $F_{i,j,\nu}$  is the same form factor as for AC phonons. This mechanism involves the optical phonon energy and is thus inelastic. It can be either intravalley or intervalley ( $\nu$  and  $\nu'$  different) interaction. The intervalley scattering and its role in the high field velocity in III-V materials will be discussed in more details in the Section D.

Although a constant optical energy is often considered (Einstein phonon), a simple analytic expression is used here to describe the phonon band structure, following Refs. [228, 288]:

$$\omega(q) = \omega_{OP} + v_s q + c q^2 \quad (3.18)$$

Figure 3.2 shows the fit of the phonon band structure of GaAs and InAs materials from experimental data from Refs. [346] and [265] resp. The parameters used are given in Table 3.1. For intervalley scatterings, the LA and TA modes at the band edge are included in the calculation in the Eq. (3.17) with energy extrapolated with this relation. The values of deformation potentials are discussed in Section D. The calculation of phonon band structures with more advanced models based on a Valence Force Field approach is discussed later in Section 3.1.4 in the case of atomistic simulations.

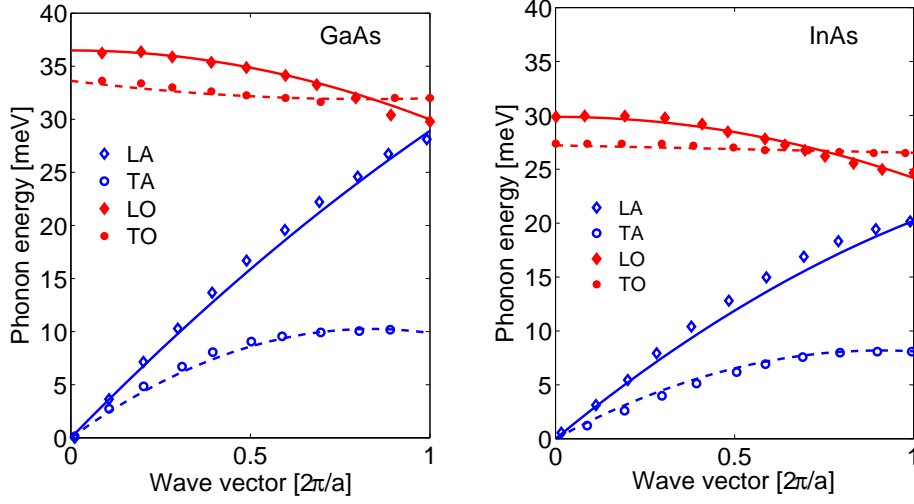


Figure 3.2. Phonons band structure of GaAs (left) and InAs (right) bulk materials along [001] direction. Experimental data are in symbols and come from Strauch *et al.* (1990) [346] for GaAs and Orlova *et al.* (1983) [265] for InAs. Lines are the fit with Eq. (3.18) and parameters in Table (3.1).

Table 3.1. Parameters for the phonon band structure in Eq. (3.18).

Parameter	GaAs				InAs			
	LA	TA	LO	TO	LA	TA	LO	TO
$\omega_{op}$ [meV]	0	0	36.5	33.6	0	0	29.9	27.2
$v$ [m/s]	4730	3350	0	-570	4000	2640	0	-100
$c$ [ $\times 10^{-7}$ m <sup>2</sup> /s]	-0.7	-1.8	-0.8	-0.31	-1	-1.4	-0.8	0

Note that, in this approach, bulk phonons are usually considered, while the confinement effects in thin film affect the phonon band structure and can have an impact on the mobility [73]. More importantly, the values of the deformation potentials used in thin films have been under debate for long time [260], and it was found that the acoustic deformation potential need to be increased in Si confined structure in order to reproduce the mobility measured experimentally. In the case of electron mobility the value goes from  $D_{ac} = 10.2$  eV in Si bulk MOSFET to 16.5 eV in Si FDSOI MOSFET. The reason for this is still unknown, and more advanced atomistic models could not fully explain this phenomenon [181]. In the case of III-V, it is not clear whether this is also the case.

### Surface roughness

As it can be seen in Figure 3.1(b), the Surface Roughness is in most cases the main scattering mechanism at high inversion charge, as the carriers are pushed close to the

surface by the electric field. This mechanism is however not straightforward to treat in a perturbative manner, as the potential barrier at the interface between SC and oxide is important (of the order of several eV). Several models have been developed in the literature, some of them very recently (e.g., Lizzit *et al.* (2014) [192] and Badami *et al.* (2016) [17]) going beyond the original formulation of Prange and Nee (1968) [290]. In the other side, non-perturbative quantum transport methods have also been used to model the SR-mobility and can be used as reference for this mechanism, as they treat the surface in a geometrical description without further approximation. Approaches going beyond the first order perturbative Fermi golden rule have also been proposed recently [231], which provide a more accurate description of the scattering mechanism. In our study, we follow the derivation of Jin *et al.* (2007) [149], which extends the original derivation of Prange-Nee with 2D corrections. In this approach, the scattering matrix elements are given by:

$$|M_{ij}(\mathbf{q})|^2 = \left| \left[ \Gamma_{ij}^{GPN} + \Gamma_{ij}^{\mathbf{q}} \right] \Delta_{\mathbf{q}} \right|^2$$

where  $\Gamma_{ij}^{GPN}$  is the matrix element given by the Generalized Prange Nee model:

$$\begin{aligned} \Gamma_{ij}^{GPN} = & -\frac{\hbar^2}{t_{ch}} \int dz \psi_i(z) \frac{\partial}{\partial z} \left[ \frac{1}{m_z} \frac{\partial \psi_j(z)}{\partial z} \right] \\ & + \int dz \psi_i(z) \frac{\partial V(z)}{\partial z} \left( 1 - \frac{z}{t_{ch}} \right) \psi_j(z) \\ & + (\varepsilon_i - \varepsilon_j) \int dz \psi_i(z) \left( 1 - \frac{z}{t_{ch}} \right) \frac{\partial \psi_j(z)}{\partial z} \end{aligned}$$

and  $\Gamma_{ij}^{\mathbf{q}}$  is the correction added by Jin *et al.* (2007) [149] to account for the charge fluctuations, due to three different effects:

$$\Gamma_{ij}^{\mathbf{q}} = V_{\mathbf{q}}^n + V_{\mathbf{q}}^{\sigma} + V_{\mathbf{q}}^{im}$$

where  $V_{\mathbf{q}}^n(z)$  accounts for the redistribution of electrons in 2DEG and is the main correction,  $V_{\mathbf{q}}^{\sigma}(z)$  accounts for the shift of the polarization charge at the interface and  $V_{\mathbf{q}}^{im}$  is due to the fluctuation of the image charge potential. All these terms are included in our calculation, following the derivation of Ref. [149], except the last term  $V_{\mathbf{q}}^{im}$  for sake of computational simplicity. Indeed, this term requires a burdensome numerical integration over  $\mathbf{k}$  mesh, that forced authors of Ref. [149] to resort to a tabulation of the integral. A roughness profile with an exponential auto-covariance function is considered in all cases, yielding the following amplitude for the 2D spatial Fourier coefficients::

$$\langle |\Delta_{\mathbf{q}}|^2 \rangle = \pi \Delta^2 \Lambda^2 (1 + q^2 \Lambda^2 / 2)^{-3/2}$$

where  $\Delta$  is the root mean square (rms) amplitude and  $\Lambda$  is the correlation length of the surface roughness profile.

The momentum relaxation time is finally written as:

$$\frac{1}{\tau_{i,\nu}^{\text{SR}}} = \frac{g_s}{2\hbar^3 \pi} \int_0^\pi d\theta \ m_{\text{DOS},\nu}^* \frac{|M_{ii,\nu}(q)|^2}{\varepsilon_D^2(q)} (1 - \cos \theta) \quad (3.19)$$

where  $\varepsilon_D(q)$  is the scalar screening factor of the dielectric function computed in Section 3.1.2. This mechanism is treated as elastic, and only intravalley and intrasubband transitions are considered ( $\nu' = \nu$  and  $j = i$ ).

### **Ionized impurities**

Coulomb interaction with ionized impurity in the channel is a major scattering mechanism in highly doped regions such as access regions (which include source and drain, but also the region below the spacer with a high gradient of doping concentration) and at low inversion in the channel. In gate stack with high- $\kappa$  materials, a high concentration of electrically charged defects may be present in the gate stack, acting as remote scattering centers and degrading the mobility at low inversion. This mechanism is referred to as remote Coulomb (RC) scattering, as opposed to the scattering with ionized impurities referred to as local Coulomb (LC). When the inversion charge increases, the free carriers are able to efficiently screen the perturbative potential and both the LC-limited and RC-limited mobilities increase significantly and become of low influence. These two mechanisms can be treated by the mean of the Poisson Green function formalism, which was adopted in this work. The Coulomb potential of a point charge located at  $z_0$  is here obtained by resolving the equation:

$$\left[ \frac{\partial}{\partial z} \varepsilon(z) \frac{\partial}{\partial z} - q^2 \right] G(q, z, z_0) = -4\pi\delta(z - z_0)$$

where  $q$  is the norm of the wavevector parallel to the film, and  $G(q, z, z_0)$  is the Poisson Green function entering the calculation of the scattering matrix element of a point charge:

$$M_{ij}^0(q, z_0) = e \int dz \psi_j^\dagger(z) \psi_i(z) G(q, z, z_0)$$

The final scattering matrix elements for electric charges inside the semiconductor (ionized impurities)  $N_{ch}$  and electric charges (fixed charges or traps) inside the gate stack  $N_{rc}$  is given by:

$$|M_{ij}(q)|^2 = \int dz_0 [ |M_{ij}^0(q, z_0)|^2 N_{ch}(z_0) + |M_{ij}^0(q, z_0)|^2 N_{rc}(z_0) ]$$

where  $N(z_0)$  is the volumic density of fixed charges at position  $z_0$ . By applying appropriate boundary conditions for  $G(q, z, z_0)$ , the screening by the metal gate can be appropriately accounted for, which has a strong impact for scaled high- $\kappa$  thicknesses [245].

The momentum relaxation time is finally given as:

$$\frac{1}{\tau_{i,j,\nu,\nu'}^{LC/RC}} = \frac{g_s}{2\hbar^3\pi} \int_0^\pi d\theta m_{\text{DOS},\nu}^* \frac{|M_{ij,\nu\nu'}(q)|^2}{\varepsilon_D^2(q)} (1 - \cos\theta) \quad (3.20)$$

This scattering mechanism is supposed to be elastic and can be either inter or intravalley.

### Screening effects

In Eqs. (3.19) and (3.20), the dielectric response of the system  $\varepsilon_D(q)$  comes into play for SR and LC/RC mechanisms. In order to account for the screening effect of the free charge on the scattering potential of these mechanisms, the dielectric response can be calculated in the Random Phase Approximation (RPA). The effect of different approximations, such as tensorial versus scalar and dynamical versus static screening were investigated intensively in the literature (see, e.g., Toniutti *et al.* (2010) [357]). The effect of the coupling with plasmon modes can also have a strong impact at high inversion, as seen in Ref. [85]. Here, the static scalar dielectric constant is computed with the formula:

$$\varepsilon_D(q) = 1 + \sum_i F_{ii}(q)\Pi_{ii}(q) \quad (3.21)$$

where  $\Pi_{ii}(q)$  is the diagonal term of the polarization factor:

$$\Pi_{ii}(q) = \frac{2g_s}{(2\pi)^2} \int dk \frac{f_i(k+q) - f_i(k)}{\varepsilon_i(k+q) - \varepsilon_i(k)}$$

and  $F_{ii}(q)$  is the diagonal term of the screening form factor:

$$F_{ii}(q) = \int dz \int dz' \psi_i(z) \psi_i^\dagger(z) G(q, z, z') \psi_i(z') \psi_i^\dagger(z')$$

### Alloy scattering

The model to treat alloy disorder in continuous theory, in its most common form, is derived from Nordheim (1931) [258] and describes the perturbation as hard spheres of fixed potential. This model is somehow empirical and has been questioned by Fischetti and Laux (1996) [92]. In particular, the value to choose for the “alloy potential”  $\Delta U_{AD}$  is not clear and often used as a fitting parameter. It was shown later that this parameter can be extracted from atomistic TB models [225]. The treatment of alloy disorder in atomistic models will be discussed later in Section 3.1.4.

### Other scattering mechanisms

Finally, let us mention that other scattering mechanisms should be taken into account in some cases for the correct modeling of the carrier transport in advanced transistors. In particular, it was shown that the use of SiO<sub>2</sub>/HfO<sub>2</sub> high- $\kappa$  gate stack in advanced nodes can degrade the effective mobility in the channel [332]. This effect was attributed to different mechanisms. In addition to the previously mentioned RC scattering, the Remote SR scattering was investigated in Refs. [103, 249] and the Remote-Phonon scattering due to polar-optical phonons in the high- $\kappa$  polar material were studied in Refs. [93],[81] and [358]. Other scatterings were recently investigated by Z.P.Zeng (2016) [400], such as the dipole fluctuations and the metal work function fluctuations. These last effects are particularly important at low inversion, but mainly vanish at high inversion where the perturbative potential is screened by the inversion charge. Apart from RC scattering, none of these mechanisms were included in the present study, as their influence on the mobility in high inversion is supposed to be low for the size considered.

### Combination

From the expressions (3.15) – (3.20) the scattering rate for each mechanism is computed by integration over all final states  $(j, \nu')$ . These scattering rates are then put together following a “Matthiessen” rule as:

$$\frac{1}{\tau} = \sum_m \frac{1}{\tau^{(m)}}$$

where  $m$  indexes the scattering mechanisms (POP, PH, SR, LC, RC and/or AD) accounted for. The mobility is finally computed with the KG formula:

$$\mu_{xy}^\nu = \frac{e}{k_B T} \frac{1}{n_\nu} \frac{g_s g_v}{(2\pi)^2} \int d^2k \tau_{xy}^\nu v_x^\nu v_y^\nu f^0(\varepsilon_\nu) (1 - f^0(\varepsilon_\nu))$$

where  $v_\lambda^\nu = 1/\hbar \partial\varepsilon_\nu/\partial k_\lambda$  is the group velocity in the  $\lambda^{\text{th}}$  direction ( $\lambda = (x, y)$ ) and  $n_\nu$  is the carrier density of valley  $\nu$ . The total mobility tensor is finally given by:

$$\mu_{xy} = \sum_\nu \frac{\mu_{xy}^\nu n_\nu}{\sum_\nu n_\nu}$$

### 3.1.3 Mobility in planar thin films

In this section, we use the Kubo-Greenwood formalism described above to study the mobility in UTBB structures. We study the hole mobility in Si and SiGe FDSOI structure and the electron mobility in III-V UTBB structures.

We note here that the technologies are often compared in  $\mu(E_{\text{eff}})$  plots, where the effective field  $E_{\text{eff}}$  is extracted from experimental data with the equation:

$$E_{\text{eff}} = e \frac{Q_{\text{depl}} + \eta Q_{\text{inv}}}{\epsilon_s} \quad (3.22)$$

where the parameter  $\eta$  was given to be 1/2 in the case of electron and 1/3 for holes in Si and Ge (as suggested in Takagi *et al.* (1994) [350]). This plot is used to recover a so-called “universal” mobility behavior in bulk MOSFET. Note that the parameter  $\eta$  can be extracted experimentally but its value remains quite controversial, as well as the “universal” picture of the mobility in advanced architecture [62, 279]. When the effective field at the interface or at the maximum of charge is extracted from the simulation, the relation (3.22) would require a value for  $\eta$  closer to 1/2 for holes in bulk and FDSOI MOSFET. This implies that the effective field and  $\eta$  parameters are not well defined physically and should be regarded as “effective” empirical parameters. For III-V materials, the value of  $\eta$  that should be used in order to recover a “universal” picture of the mobility is not clear, as the dependence of POP mechanism on  $E_{\text{eff}}$  is different from the acoustic phonon mechanism that limits the mobility in Si (see, e.g., Hiblot (2015) [131]). Sonnet *et al.* (2011) [330, 329] investigated the mobility in  $\text{In}_x\text{Ga}_{1-x}\text{As}$  devices and found that a value of  $\eta = 1/4$  could recover a “universal” curve in bulk MOSFET. However, this study was not mentioned in other papers. In particular the references used in Section 3.1.3 and Figure 3.5 were performed before 2011 and they did not specify the value of  $\eta$  used in their extraction. We chose to use the value advised by Takagi for electron mobility in Si of  $\eta = 1/2$ , as it remains the most commonly used value for electron mobility extraction from experimental split C-V method.

#### Electron transport in $\text{In}_x\text{Ga}_{1-x}\text{As}$ : effect of approximation in the RTA

We investigate here the POP-limited mobility in planar UTBB devices, neglecting the effect of SO phonons, but showing the importance of resolving the coupled system in Eq. (3.9) (exact method) without approximation on the RTA in Eq. (3.12) (RTA method), as pointed out by Ref. [216] in nanowires and explained above.

Figure 3.3 shows the scattering rate  $1/\tau_m$  for PH and POP scattering mechanisms in an  $\text{In}_{0.57}\text{Ga}_{0.43}\text{As}$  film with thickness  $t_{ch} = 5$  nm and 50 nm and parameters of Table 3.2. One notes that the PH-limited scattering rate is constant in each subbands in 2DEG, as expected from the Eqs. (3.16) and (3.17) and presents discontinuities at each subband edges, due to the Van Hove singularities. Due to the strong confinement in 5 nm thin film, the two first subbands from the  $\Gamma$  valleys are separated by 0.48 eV, leading to a long flat plateau in the scattering rate. The first subband from the L valleys is about 0.6 eV above the conduction band edge, where the scattering rate increases significantly. When the gate voltage is increased from 0 to 0.7 V, the Fermi-level goes inside the conduction

Table 3.2. Band structure and physical parameters used for the calculation of electron mobility in Figures 3.3 and 3.4. Deformation potentials are taken from Ref. [285] for  $\text{In}_{0.57}\text{Ga}_{0.43}\text{As}$  and Refs. [89, 86] for GaAs.

	GaAs	$\text{In}_{0.57}\text{Ga}_{0.43}\text{As}$		GaAs	$\text{In}_{0.57}\text{Ga}_{0.43}\text{As}$
$m_{\Gamma}^*$ [ $m_0$ ]	0.065	0.048	$D_{ac,\Gamma}$ [eV]	7.1	5.42
$\alpha_{\Gamma}$	0.7 (4)	1.3 (5)	$D_{ac,L}$ [eV]	9.2	9.0
$m_L^*$ [ $m_0$ ]	0.85	0.436	$D_{ac,\Delta}$ [eV]	9.27	9.2
$m_{\Delta,l/t}^*$ [ $m_0$ ]	1.86/0.17	2.26/0.25	$D_{op,\Gamma-L}$ [eV/Å]	5.25	5.43
$E_L - E_{\Gamma}$ [eV]	0.29	0.76	$\varepsilon(\infty)$ [ $\varepsilon_0$ ]	10.9	11.6
$E_{\Delta} - E_{\Gamma}$ [eV]	0.49	1.25	$\varepsilon(0)$ [ $\varepsilon_0$ ]	12.9	13.9

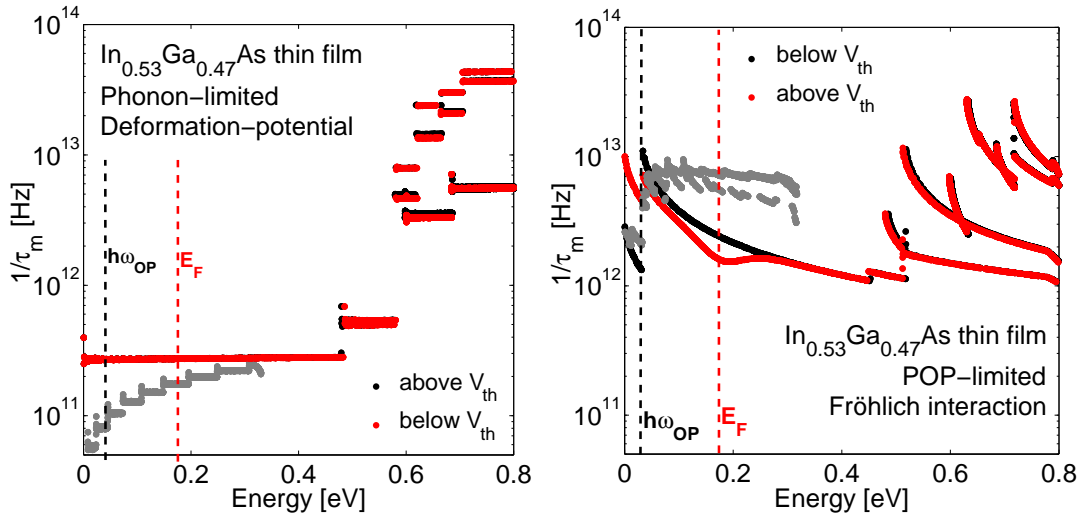


Figure 3.3. Scattering rate for AC+OP deformation potential interaction (PH, left) and Fröhlich interaction (POP, right) in a 5 nm  $\text{In}_{0.57}\text{Ga}_{0.43}\text{As}$  UTBB FDSOI at  $V_{gs} = 0$  (black) and 0.7 V (red) as a function of energy of the initial state. The scattering rate in a 50 nm  $\text{In}_{0.57}\text{Ga}_{0.43}\text{As}$  film is also plotted in grey up to 0.35 eV. Simulation parameters are given in Table 3.2.

band but the scattering rate is not strongly affected here. In the case of the 50 nm thick film, the confinement is weaker and the subbands are much closer in energy to each other. The scattering rate follows an overall  $\sqrt{E}$  trend, expected in bulk material with 3D density-of-state (see e.g. Ref. [206]). For POP-scattering, the scattering rate decreases with increasing energy in each subbands, as it goes as  $1/q$  in Eq. (3.15). One notes a net discontinuity around 30 meV above the conduction band edge, corresponding to the energy of LO phonons and the onset of the phonon emission processes. When the gate voltage is increased above threshold, the scattering rate presents a dip at the Fermi-level position, due to the occupation factor. The occupation factor term for absorption process  $\frac{1-f(\mathcal{E}_i+\hbar\omega)}{1-f(\mathcal{E}_i)}$  in Eq. (3.15) also leads to an increase of the scattering rate between 0 and

30 meV when the Fermi level goes above the conduction band edge.

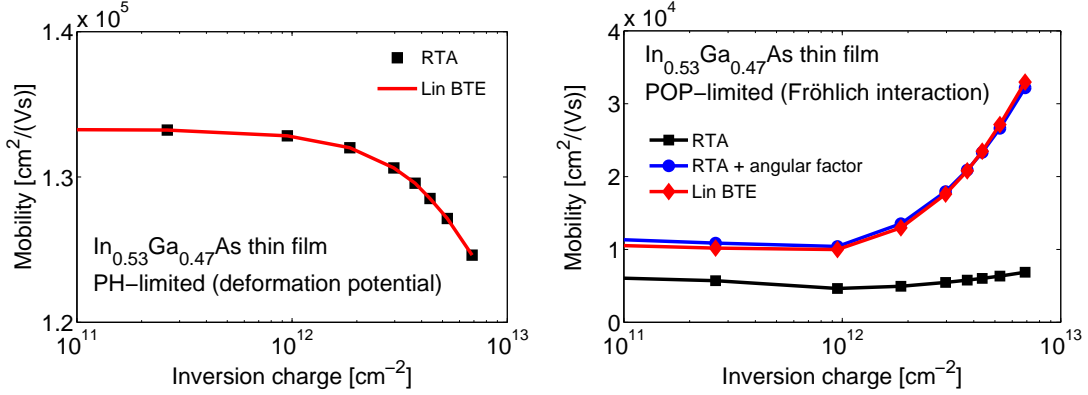


Figure 3.4. PH-limited (left) and POP-limited (right) electron mobility as a function of electron sheet density for a  $\text{In}_{0.57}\text{Ga}_{0.43}\text{As}$  UTBB MOSFET with a channel thickness of  $t_{ch} = 5$  nm. The exact and RTA resolution are compared, together with the effect of the angular term  $(1 - \cos \theta)$  is Eq. (3.13).

Figure 3.4 shows the PH-limited and POP-limited mobility in  $\text{In}_{0.57}\text{Ga}_{0.43}\text{As}$  UTBB FDSOI channels computed within the KG formalism, in the exact resolution of the linear system and RTA approach. We consider here a gate stack with Equivalent Oxide Thickness (EOT) of 1 nm and a  $\text{SiO}_2$  Buried Oxide (BOX) of 25 nm. The channel thickness is 5 nm and unintentionally doped. We consider only the [001] confinement orientation and the transport along (100). However, as the  $\Gamma$  valley is isotropic and satellite valleys are not populated under  $V_g = 1$  V, the results should be similar in the other confinement and transport directions. As expected, the PH-limited mobility is higher than POP-limited mobility (about one order of magnitude higher) and has a low impact on the overall mobility. Moreover, the exact and RTA results give an almost identical results for this mechanism, as it doesn't depends on  $q$  and is thus perfectly isotropic for the  $\Gamma$  valley. For the POP-limited mobility however, the exact and RTA methods give two very different results. The exact resolution of the linear BTE gives a mobility almost two times higher than the isotropic RTA approximation, when the factor in Eq. (3.13) is totally neglected. When the factor  $(1 - \cos \theta)$  is included in the calculation, the situation is improved and the RTA result is closer to the exact resolution, but some small discrepancies remain.

Finally, the electron mobility as a function of effective field in  $\text{In}_{0.57}\text{Ga}_{0.43}\text{As}$  bulk MOSFETs with all scattering processes is shown in Figure 3.5. The  $\eta$  parameter for the calculation of effective field in Eq. (3.22) was set to 1/2. The SR parameters were adjusted to reproduce the experimental values. Note that the r.m.s values used for SR are large, which can be due to the limitations of the SR model used in our KG calculations, as pointed out by Lizzit *et al.* (2014) [192, 17]. Moreover, the mobility in  $\text{In}_{0.57}\text{Ga}_{0.43}\text{As}$  MOSFET structures is mainly impacted by the interfacial charges and surface roughness parameters and far from the intrinsic POP-limited mobility (which is around  $10^4$  cm<sup>2</sup>/Vs). The growth of an InP or InAlAs layer between the  $\text{In}_{0.57}\text{Ga}_{0.43}\text{As}$  channel and the gate stack oxide can improved the mobility, as the defects and rough interface are pushed away

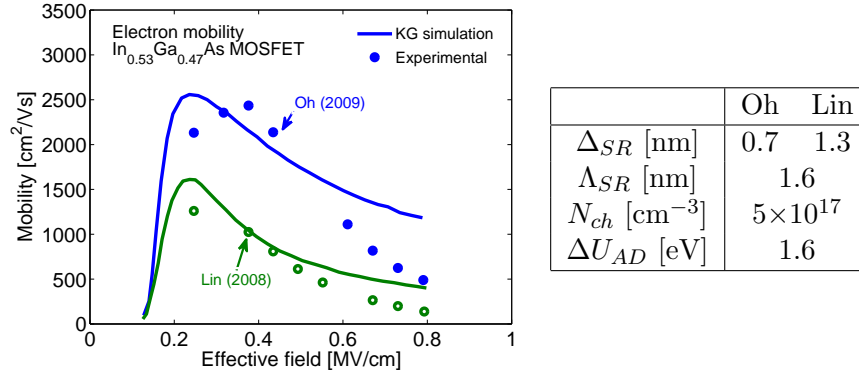


Figure 3.5. Electron mobility in  $\text{In}_{0.57}\text{Ga}_{0.43}\text{As}$  MOSFET computed with KG solver (lines) with parameters given in the right table compared with experimental values from Oh *et al.* (2009) [259] (blue) and Lin *et al.* (2008) [184] (green).

from the inversion layer [403, 183, 24]. In the case of these “buried channels”, the mobility can be increased to more than  $6000 \text{ cm}^2/\text{Vs}$ , close to the POP-limited mobility. However, the dielectric control by the gate is also reduced, as the equivalent EOT is increased. An inversion charge can also form in the InP buffer layer, thus reducing the transport properties of the device. Although interesting in a technological perspective, the detailed study of these combined effects will not be discussed here, as they have been studied in previous work [131].

### Hole transport in Si

The mobility in pMOS FDSOI structures with channels made of Si is investigated by mean of semi-classical KG approach and compared with the mobility extracted from NEGF simulations. A 3-band KP model is used for the band structure of holes, with parameters given in Table 3.3 on page 99.

The phonon-limited mobility is plotted in Figure 3.6. One single optical deformation potential is used for all transition set to  $15 \text{ eV}/\text{\AA}$  with a phonon energy of  $62 \text{ meV}$ , while the acoustic deformation potential is set to  $16.5 \text{ eV}$ . The agreement between KG and NEGF simulation is quite poor for phonon-limited hole mobility, while a good agreement was found in the case for electron mobility (see Ref. [245]). This discrepancy could be attributed to the inter-valley scattering between HH, LH and SO valence bands, which is not account for in NEGF calculations.

The surface-roughness-limited mobility is plotted in Figure 3.7(left). In both KG and NEGF simulation, an exponential profile is used, with  $\Delta_{SR} = 0.47 \text{ nm}$  and  $\Lambda_{SR} = 1.3 \text{ nm}$ . The SR-limited mobility in NEGF was extracted by the inverse Mathiessen rule, as explained in Ref. [257]. In this case, a good agreement is found between KG and NEGF approach for channel of 7 and 5 nm. For the thinner channel of 3 nm, the KG overestimates the mobility and the perturbative KG approach faces some issues at these short scales. One can see in Figure 3.7(right) that the KG model doesn’t predict the

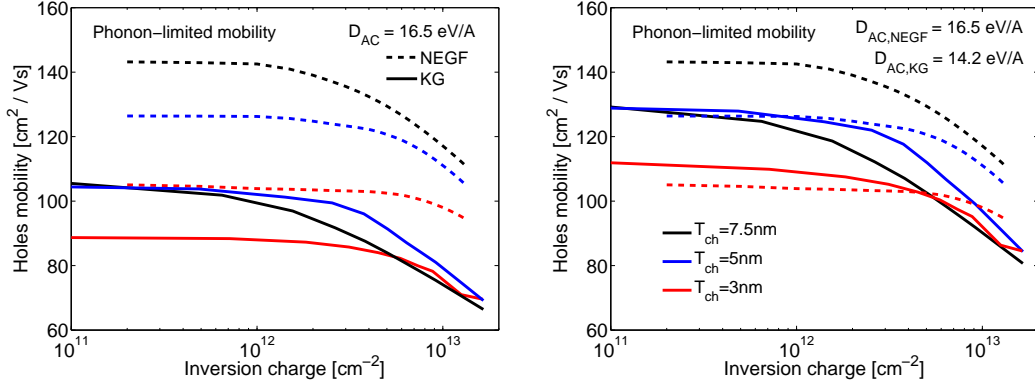


Figure 3.6. Left: PH-limited mobility as a function of electron sheet density in Si pMOS FDSOI devices with different channel thicknesses. Right: The agreement of KG simulation with NEGF is improved when the acoustic deformation potential  $D_{AC}$  is lowered to 14.2 eV (the one used in NEGF is in all cases  $D_{AC} = 16.5$  eV). NEGF calculation are shown in dashed lines, while KG simulation are shown with solid lines.

correct dependency of the mobility with the channel thickness, while the NEGF mobility is in very good agreement with the experimental data of Uchida *et al.* (2002) [363]. The mobility values are however quite close to experimental values with both models.

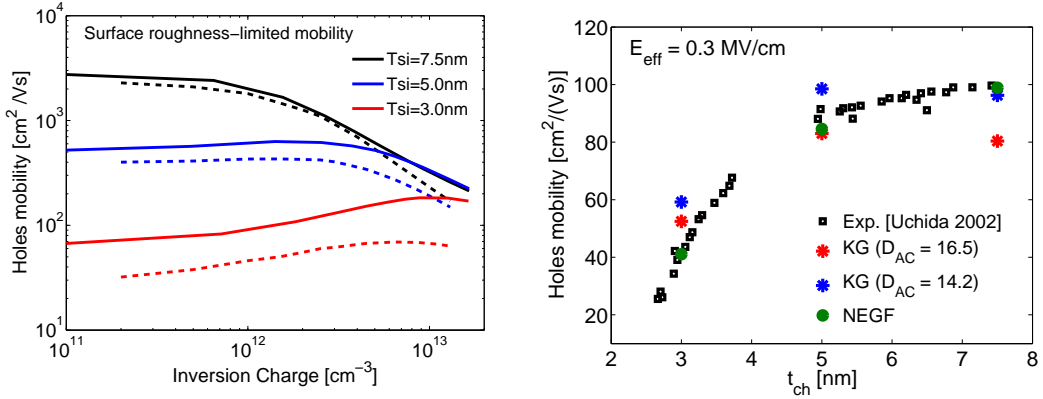


Figure 3.7. Left: SR-limited mobility as a function of electron sheet density. NEGF calculation are shown in dashed lines, while KG simulation are shown with solid lines. Right: SR- and PH-limited holes mobility as a function of the channel thickness of Si PMOS FDSOI, compared with experimental data of Uchida *et al.* (2002) [363].

### Hole transport in Ge and SiGe

When SiGe is grown on top of a Si substrate, the lattice mismatch induces a biaxial compressive stress inside the SiGe thin layer. This compressive stress is generally advantageous for the hole mobility, due to the enhancement of the light-hole character of the highest subband (decrease of the transport effective mass) and the band splitting between light-hole (LH) and heavy-hole (HH) bulk valley (decrease of the intervalley scattering) (see, e.g., Ref. [304]). On the other side, it is known that the alloy scattering plays an important role in bulk SiGe materials and hinders the mobility compared to pristine Si and Ge devices (see, e.g., Ref. [92]). It was shown in bulk materials that the mobility of unstrained devices as a function of Ge concentration presents a U shape, with minimum of mobility ranging from 30 to 50% of Ge [92, 193]. For strained SiGe layer grown on Si, the minimum is shifted to lower values of Ge, around 15-20% and an improvement of the total holes mobility over pristine Si is found only for  $x_{Ge} > 0.3$ . However, the interplay of stress, alloy disorder, combined with the influence of the confinement in thin SiGe-On-Insulator (SGOI) layers, can lead to complex behavior of the mobility and can be difficult to predict in empirical models used in common TCAD solvers. Moreover, it is not clear whether the bulk value of alloy scattering potential remains valid in SGOI thin layers for 14FD application, where the random distribution of Si and Ge atoms can be altered in the 6 nm thick channel and scattering potential parameter can be different. The investigation of these effects with KG solvers is thus interesting and an important work in this direction was done by Nier (2015) [245]. As evidenced in experimental studies, and by the choice made by the microelectronics industry recently, adequate process flow allows the fabrication of SGOI structures with high value of biaxial stress and the hole mobility can be almost doubled in SiGe PMOS compared to Si PMOS with only 20% of Ge, as shown in Ref. [11].

We show in Figure 3.8(left) the mobility of Si, Ge and SiGe bulk MOSFETs simulated with the parameters given in Table 3.3 and compared to numerous experimental works [301]. We used  $\eta = 1/3$  for the extraction of the effective field in Eq. 3.22. A 6-band KP model was used with a spin-orbit coefficient  $\Delta_{SO}$  of 0.044 for Si and 0.29 for Ge. The SR profile and fixed charge concentration were adjusted to reproduce the experimental data. The value of deformation potential in bulk is used here [348, 92], which is lower than the one for thin-films used in previous section, as mentioned in Sec. 3.1.2.

Table 3.3. Left: Physical-based parameters used in the KG solver for the calculation of hole mobility [301]. Right: band structure and strain parameters for 3-band KP models for Si and Ge materials.

	Si	Ge		Si	Ge
$\Delta_{SR}$ [nm]	0.22	0.2	L	-6.64	-31.6
$\Lambda_{SR}$ [nm]	3	2.3	M	-4.61	-5.2
$\Delta U_{AD}$ [eV]	0.9		N	-8.68	-33.6
$D_{ac}$ [eV]	9.03	13	l	-2.13	-3.75
$D_{op}$ [eV/Å]	10	10	m	4.14	4.95
$\hbar\omega_{OP}$ [meV]	57	64	n	-8.24	-5.89

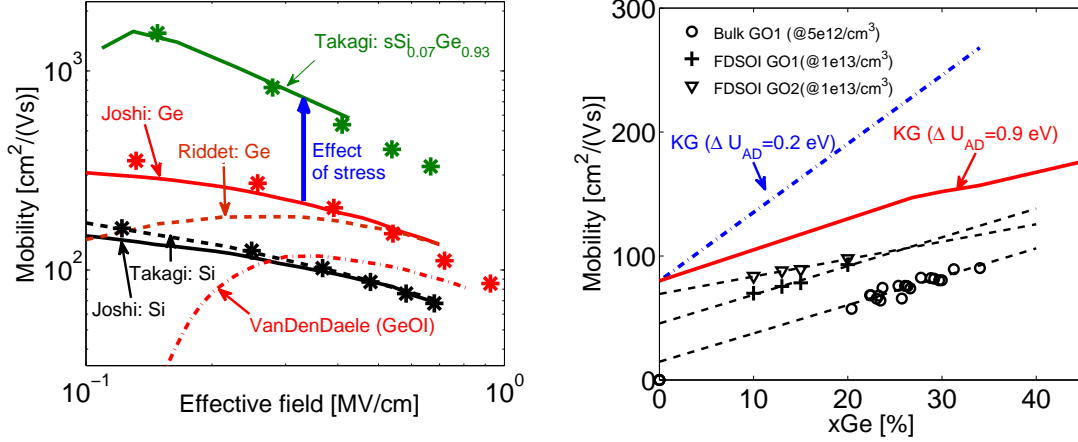


Figure 3.8. Left: effective hole mobility computed with KG solver shown by symbols for Si (blue), Ge (red) and  $\text{Si}_{0.07}\text{Ge}_{0.93}$  strained devices (green) [301]. The lines show experimental data from the following references: Joshi (2007) [152] and Takagi (1994) [350] for Si, VanDenDaele (2011) [370], Riddet (2010) [300] and Joshi (2007) [152] for Ge and Takagi (2006) [349] for SiGe. The effective field is computed with  $\eta = 1/3$  (see text). Right: effective hole mobility of biaxially stressed SGOI structures, as a function of the Ge content. Symbols are measurements from STMICROELECTRONICS devices. Solid lines are KG simulations for different AD potentials [301]. Dashed lines are guides to the eye.

We see that KG calculations are able to reproduce the so-called “universal” hole mobility tendency for both Si and Ge channels, with strain and different concentration of Ge. Moreover, we see that the Ge mobility generally increases by a factor two compared to Si mobility, and that strain greatly enhances this tendency to reach maximum mobility of more than  $1000 \text{ cm}^2/(\text{V.s})$ . Note that a discrepancy exists for pure Ge mobility among different experimental studies, probably due to the different interface quality with oxide or impurities in the channel. Also note the high value of the SR roughness correlation length  $\Lambda_{SR}$  used in Table 3.3.

Figure 3.8(right) shows the measured total holes mobility in biaxial compressive strained channel in bulk MOSFET and SGOI MOSFET (for GO1 and GO2 architecture) of STMICROELECTRONICS (STM) as a function of Ge concentration. As it was found in Andrieu *et al.* (2014) [11], the experimental measurements show a quasi-linear tendency when Ge content is increased up to 40%, which is recovered with KG simulation. The slope of the curve depends on the alloy scattering potential used in the calculation and a slope in agreement with experiments for SGOI was recovered with  $\Delta U_{AD} = 0.9 \text{ eV}$ . This value is in good agreement with the one found for bulk materials in Ref. [92] and for SGOI MOSFET in Ref. [11], but higher than the one found by the Monte Carlo calculation in Ref. [228], which was  $\Delta U_{AD} = 0.4 \text{ eV}$ . As mentioned earlier, the physical value for the alloy potential  $\Delta U_{AD}$  to be used in KG simulation is still controversial and atomistic model such as the one presented in Sec. 3.1.4 is of high interest.

### 3.1.4 Scattering rates within TB models

Tight-binding (TB) Hamiltonians, coupled with valence-force field models for the phonons, have been used in recent papers to study the electron-phonon interaction in NWs [255, 200, 256] and thin films [181] in a fully atomistic description. In this approach, the scattering matrix element are computed directly from the derivation of the TB Hamiltonian with respect to the atom positions. It allows to investigate the phonon-limited mobility without the need of deformation-potential parameters. Moreover, the alloy disorder (AD) scattering can also be treated in an atomistic approach, following the work of Mehrotra *et al.* (2011) [225].

In this section, we apply these methods to  $\text{Si}_{1-x}\text{Ge}_x$  and  $\text{In}_x\text{Ga}_{1-x}\text{As}$  NWs to investigate the effect of AD on these systems. The phonon-limited mobility is also computed in  $\text{Si}_{1-x}\text{Ge}_x$  systems and compared to the AD-limited mobility. For  $\text{In}_x\text{Ga}_{1-x}\text{As}$  nanowires, the mobility is limited by POP scattering rather than a deformation potential type of interaction [214]. This type of scattering could in principle be treated in a fully atomistic TB approach, but requires the treatment of long-range Coulomb interaction that make the calculation heavy and not easy to implement. While the Ewald summation technique was proposed in bulk for the calculation of phonons [341], the separation between a long-range and short-range interaction in nanostructures is less trivial and it is not guaranteed to work. For these reasons, the electron-phonon coupling in III-V nanowires was not investigated here and we limit the study to AD-limited mobility.

#### Non-polar phonons

The method used here is derived from previous works on pristine NWs [402, 255, 256]. An atomistic  $sp^3d^5s^*$  TB model is employed to determine the electronic band structure and electron wave functions, and a valence-force field is used for the phonons. The  $sp^3d^5s^*$  TB Hamiltonian were described and discussed in Chapter 1 Section 1.1.4 and we use the parameters for SiGe and InGaAs materials given in Section 1.1.8.

The phonons states are computed by diagonalization of the dynamical matrix [180]. For Si and Ge materials, the VFF model developed by Vanderbilt (1989) [371] is used, which includes bonds-centered interactions (no anharmonic terms were used here). The parameters for Si are taken from Vanderbilt (1989) [371] while the ones for Ge are taken from Tubino (1972) [362]. For III-V materials, the enhanced Keating model developed by Steiger *et al.* (2011) [341] is used, considering the five atoms-centered interactions depicted in Figure 3.9(a). The phonon band structure of GaAs obtained with this model is plotted in Figure 3.9(b) using the parameter set of model P5/C from Ref. [341] and compared with the experimental data of Ref. [346]. The parameters for InAs are taken from Salmani-Jelodar *et al.* (2012) [312]. The Coulomb interaction term in the energy calculation in Ref. [341] is not included in our calculation, because the treatment of this term in nanostructures is complex and implies the description of the dielectric environment. In the same way, the scattering with POP would necessitate more advanced implementation. As said above, the phonon-limited mobility in III-V materials were not studied here and only used to extract the AD-limited mobility.

In the case of alloys, we use the virtual crystal approximation (with parameters and

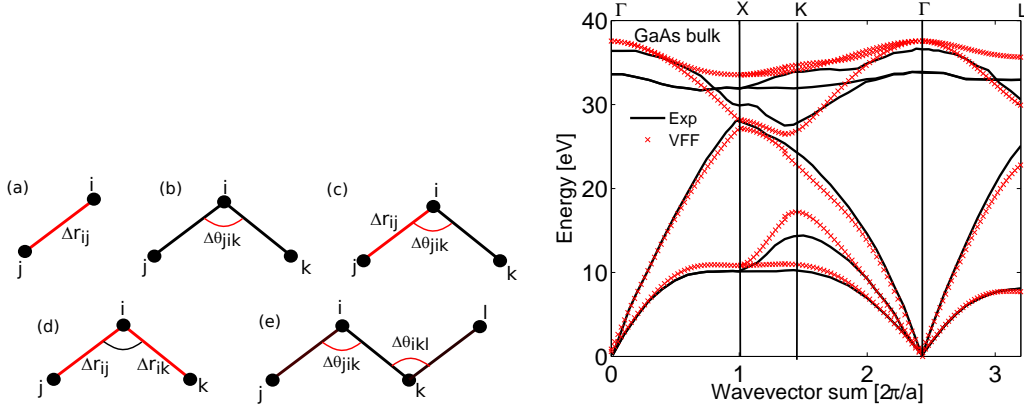


Figure 3.9. Left: schema of the valence force field parameters used representing: (a) bond stretching, (b) bond bending, (c) interaction of 2 neighbour bonds stretching, (d) bond stretching + bending interaction and (e) coplanar bond bending interaction. Right: Phonon band structure of GaAs obtained with EVFF models of Ref. [341] (P5/C parameter set used in Fig.4 of Ref. [341]) compared to experimental band structure from Ref. [346].

models described in Chapter 1 Section 1.1.8) and a linear interpolation of valence-force field parameters between pristine compounds. We have verified in test cases that the electron mobility is almost identical (within 2%) if we consider a random alloy supercell to calculate the phonons. In spite that the random distribution of Si and Ge masses strongly affects the phonons spectra at high energy, it was also found in Ref. [240] that VCA is sufficient to obtain correct electron-phonon scattering and mobility in bulk SiGe.

Once the electronic and phononic states are known, all possible electron-phonon (e-ph) scattering events are searched by considering full phonon bands, and electron states up to 0.25 eV from the conduction band minimum. The e-ph scattering matrix elements that enter the Fermi golden rule in Eq. (3.6) are given as [402]:

$$\begin{aligned}
 M_{q,j}^{k,\nu,\nu'} &= \sum_{\alpha,i} \frac{1}{\sqrt{NM_\alpha}} \sqrt{\frac{\hbar}{2\omega_{q,j}}} e_{\alpha,i}^{(j)}(q) \sum_{\substack{\beta,\eta \\ \beta',\eta'}} (c_{\beta',\eta'}^{k+q,\nu'})^* c_{\beta,\eta}^{k,\nu} \\
 &\times \sum_{m,m'} e^{i\mathbf{K}\mathbf{R}_{m\beta}} e^{-i(\mathbf{k}+\mathbf{q})\mathbf{R}_{m'\beta'}} \langle \phi_{\eta'}(\mathbf{r} - \mathbf{R}_{m'\beta'}) | \frac{\partial \hat{H}}{\partial s_{\eta\alpha i}} | \phi_{\eta}(\mathbf{r} - \mathbf{R}_{m\beta}) \rangle
 \end{aligned}$$

where the coefficients  $c_{\beta,\eta}^{k,\nu}$  and  $\phi_{\eta}(\mathbf{r})$  describe the TB electron wavefunction as defined in Chapter 1 Section 1.1.4 and  $e_{\alpha,i}^{(j)}$  are the eigenvectors of the dynamical matrix.

## Alloy disorder

AD scattering rates are calculated from VCA Bloch states, which are developed along a random alloy supercell with  $N_k$  unit cells, where  $N_k$  is also the number of  $k$ -points considered in the Brillouin zone (from 420 to 1024, depending on the NW orientation [256]). Following Ref. [225], the AD scattering matrix elements are defined as  $\langle \psi_{\text{VCA}}^f | H_{\text{alloy}} | \psi_{\text{VCA}}^i \rangle$ , where  $H_{\text{alloy}}$  is the Hamiltonian of the random alloy supercell and  $\psi_{\text{VCA}}^{i/f}$  are the VCA Bloch initial and final states. The squared norms of the scattering matrix elements are averaged over 10 configurations of AD. This is sufficient to obtain good convergence of the mobility. The scattering rate of each event is evaluated via the Fermi golden rule and the total mobility is finally obtained by including all scattering rates into the linearized Boltzmann equation which is solved exactly. Due to the random generation of alloy supercells, particular  $\mathbf{k}$  vectors can be weakly scattered and travel almost ballistically when only AD is considered (with a matrix elements associated clearly higher than others). These states may induce an artificially high AD-limited mobility. The inclusion of phonon scattering rates before the resolution of the Boltzmann equation helps to avoid this, as it leverages the contribution of these states (which are scattered by phonons). Matthiessen rule can then be used to obtain the AD-limited mobility alone.

Calculating scattering rates from the electronic states of random alloy supercells would better capture disorder effects but would be problematic due to carrier localization [10]. This leads to an exponential decrease of the group velocities when increasing the supercell length, [162, 201] thus to an exponential decrease of the mobility which is not physical at room temperature. For this reason, electron-phonon and AD scatterings are both treated as perturbations of the VCA Bloch states in alloyed NWs.

### 3.1.5 Mobility in nanowires

#### SiGe nanowires

In the complex case of SiGe NWs, the effect of alloy disorder (AD) on the hole mobility has been studied with atomistic [162, 224] and  $\mathbf{k} \cdot \mathbf{p}$  models [220] but phonon scattering was only considered using approximate deformation potentials. Importantly, while AD is the main source of scattering in bulk SiGe [92], electron-phonon interactions have comparable influence in confined structures [224].

We investigate here the effects of both scattering mechanisms on the electron and hole mobility in SiGe NWs using a fully atomistic description. While the hole mobility in SiGe NWs is interesting in a technological point of view, electron mobility is also of both technological and scientific interest for nMOS structures. Indeed, considering the conduction band structure of Si and Ge NWs and the transition in valley described in Chapter 1 Section 1.2.3, it is interesting to study how these effects will affect the intrinsic electron mobility [234]. A quite similar study has been recently performed by another group for two-dimensional SiGe structures [269, 270].

The phonon-limited hole mobility in SiGe NWs in different orientation ( $\langle 001 \rangle$ ,  $\langle 110 \rangle$  and  $\langle 111 \rangle$ ) is plotted in Figure 3.10(left) and compared to the results within the deformation potential theory of Ref. [224]. We see that the phonon-limited mobility increases

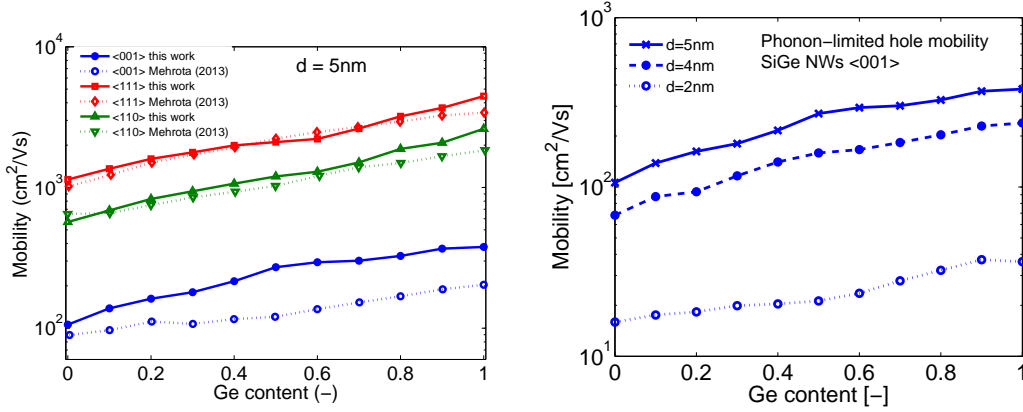


Figure 3.10. Left: hole mobility versus Ge concentration in SiGe NWs with  $d=5$  nm and orientation, compared to the results in the deformation potential approximation from Ref. [224]. Right: hole mobility in the  $\langle 001 \rangle$  direction for different diameters.

roughly monotonously with the Ge concentration for all orientations. While the hole mobility of pristine Si is in good agreement with Ref. [224], the hole mobility of pristine Ge is generally higher in our calculation [255]. This might be due to the deformation potential values chosen in Ref. [224]. As it was found in Ref. [255] for Ge NWs and Ref. [256] for Si NWs, the NWs present higher hole mobility in the  $\langle 111 \rangle$  direction for the diameters considered, due to the light-hole character of the highest valence subband with an effective mass  $m^* < 0.1m_0$ . The hole mobility of  $\langle 001 \rangle$  SiGe NWs with diameters  $d = 2, 4$  and  $5$  nm is plotted in Figure 3.10(right) and shows the strong dependence of the phonon-limited mobility with the NWs size, due to the enhanced e-ph coupling in small NWs.

The electron mobility of SiGe NWs for the same three orientations and diameters  $d = 2, 4$  and  $8$  nm is plotted in Figure 3.11. In general, the phonon-limited electron mobility of NWs with  $d = 8$  nm is more or less constant with the increase of Ge concentration up to  $0.8$ , after which the mobility increases in  $\langle 110 \rangle$  and  $\langle 111 \rangle$  NWs, but decreases in  $\langle 001 \rangle$  NWs. This sharp transition is intimately related to the transition from  $\Delta$  to L valleys studied in Chapter 1 Section 1.2.3. The lowest subband transits from large effective mass valley to low effective mass valley in  $\langle 110 \rangle$  and  $\langle 111 \rangle$  NWs ( $m_e^* = 0.19 \rightarrow 0.09$  and  $0.44 \rightarrow 0.27$  respectively), but this is reversed in  $\langle 001 \rangle$  NWs ( $0.22 \rightarrow 0.60$ ). This behavior is preserved in  $4$  nm NWs but the transition occurs at higher Ge concentration, consistently with our analysis of the band structure and transition point in Chapter 1 Section 1.2.3. For  $2$  nm NWs, the variation of mobility is very small for  $\langle 001 \rangle$  and  $\langle 110 \rangle$  oriented NWs, mainly because of the stable effective mass. For  $\langle 111 \rangle$  NWs, because of the change in effective mass, there is an abrupt change in mobility at  $x \approx 1$ .

In addition, the mobility in  $4$  nm and  $8$  nm NWs presents a marked dip at the transition point, for all orientations including  $\langle 001 \rangle$  (Fig. 3.11). The mobility suddenly decreases when the subbands originating from  $\Delta$  and L valleys become close in energy in such a manner that intervalley scattering is strongly enhanced. To study this effect, we performed

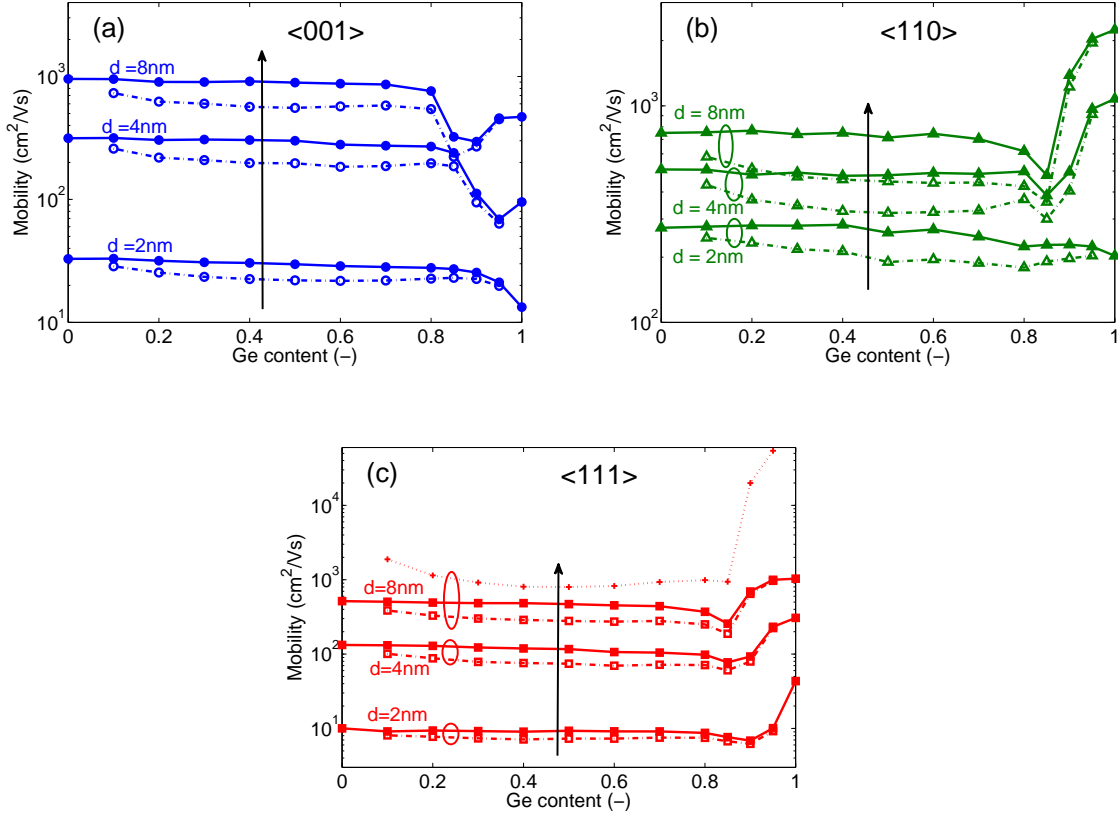


Figure 3.11. Electron mobility versus Ge concentration in SiGe NWs of different diameter and orientation:  $\langle 001 \rangle$  (a),  $\langle 110 \rangle$  (b) and  $\langle 111 \rangle$  (c). Solid lines with filled symbols represent the phonon-limited mobility, while dashed line with open symbols correspond to the mobility including both e-ph and AD scattering. The AD-limited mobility is shown with dotted lines and crosses for  $\langle 111 \rangle$  NWs with  $d = 8$  nm. The arrow shows the increasing diameter trend.

calculations including only transitions satisfying  $|k^f| - |k^i| < 0.2 \times 2\pi/a$  in  $\langle 001 \rangle$  NWs with  $d = 4$  nm. In this way, the intervalley transitions between subbands originating from  $\Delta$  valleys and subbands from L valleys are omitted (the norm assures that the transitions  $k^f = -k^i$  among subbands with same types are preserved). The results in Figure 3.12(a) show that these transitions influence the mobility only close to the transition point at  $x \approx 0.9$ , as expected. When intervalley scattering is omitted, the dip of the mobility at  $x = 0.9$  is thus removed and the mobility drops monotonously from  $x = 0.8$  to 1. To better understand the phonon modes involved in these transitions, we included progressively intervalley transitions with phonon energy up to a cut-off value  $\hbar\omega$ . The mobility as a function of the cut-off value on intervalley scattering  $\mu(\hbar\omega)$  is shown in Figure 3.12(b). It evolves from the mobility without intervalley scattering to the one including all transitions. In particular, sharp drops of mobility are specifically found at

phonon energies around 9 and 24 meV. These modes corresponds to acoustic phonon modes in bulk, which have energies of 8.6 (TA1), 9.4 (TA2) and 24.9 (LA) meV for the intervalley wavevector  $\mathbf{q} = \mathbf{k}_\Delta - \mathbf{k}_L$  in bulk Ge. Two minors drops are also identified at phonon energies around 31 and 38 meV, corresponding to optical phonons in the bulk band structure. The same study was performed on SiGe NWs in  $\langle 111 \rangle$  orientation and  $d = 2$  nm and shows similar phonon energies involved in the intervalley scattering.

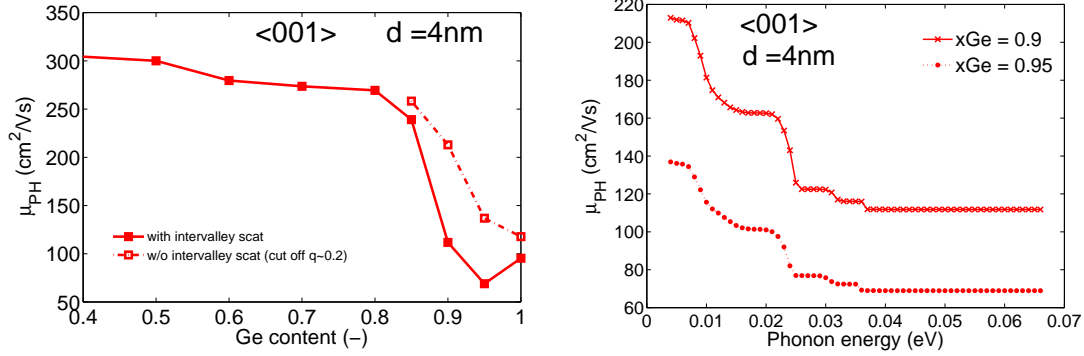


Figure 3.12. Left: phonon-limited electron mobility of  $\langle 001 \rangle$  SiGe NWs with  $d = 4$  nm, with and without intervalley scattering. Right: phonon-limited mobility at Ge concentration  $x = 0.9$  and  $0.95$  as a function of the cut-off energy on intervalley scattering (see text). Sharp drops of the mobility are clearly identified at phonons energy around 9 and 24 meV.

When the NWs diameter is decreased, the mobility is also strongly reduced, especially for  $\langle 001 \rangle$  and  $\langle 111 \rangle$  orientations. Like in pristine NWs, this is due to confinement-enhanced e-ph coupling. [255, 200, 256]

The effect of the AD scattering on the electron mobility is also shown in Fig. 3.11. When the NWs diameter is decreased, AD scattering is also enhanced. But the AD-limited mobility decreases less rapidly than the phonon-limited mobility. The contribution of the AD scattering is non-negligible: at concentration  $x = 0.5$ , the mobility reduction with respect to the phonon-limited mobility is around 40% for  $d = 8$  nm, 35% for  $d = 4$  nm and 25% for  $d = 2$  nm. These ratio do not depend much on the NW orientation. However, it is found that the sharp transition at the turning point remains when AD is included and that e-ph scattering dominates in all the considered configurations.

Finally, note that SR scattering was not included in our calculation and may become equally important or even dominant for small diameters or at high carrier density, as shown by simulations of SR-limited mobilities in Si NWs, using effective mass [149, 339] or TB models [281].

### InGaAs nanowires

For InGaAs materials, the contribution of alloy-disorder scattering mechanism on the electron mobility has been under investigation for a long time [189, 15, 126, 21], and is still under debate. Some recent works consider this mechanism as negligible [263, 22],

while other works consider it should be included in the calculation [285] and might even be dominant in some cases [218]. Moreover, there is no clear reference for the value of the alloy disorder potential that should be used in KG calculations, in bulk as in nanostructures. It is thus interesting to investigate this scattering mechanism with the atomistic model presented above.

As stated earlier, the phonon-limited mobility is difficult to compute with atomistic models, due to the polar nature of longitudinal optical modes in III-V materials. However, the AD-limited can be obtained in thin nanowires, and can give insight on the strength of this scattering mechanism in nanoscale devices.

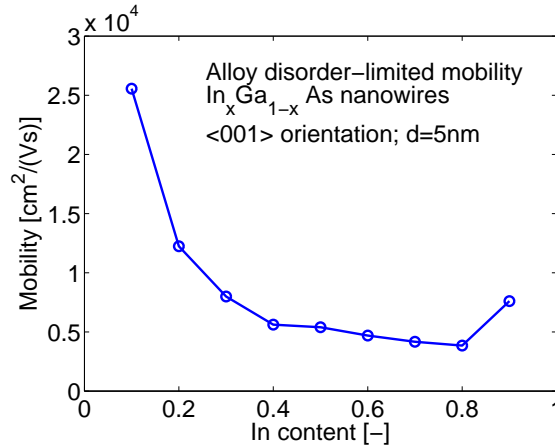


Figure 3.13. AD-limited mobility in InGaAs  $\langle 001 \rangle$  nanowires with  $d = 5$  nm computed with atomistic model.

The AD-limited electron mobility computed in  $\langle 001 \rangle$  InGaAs NWs with  $d = 5$  nm is shown in Figure 3.13 as a function of the In content. It was found that, as opposed to SiGe NWs, the mobility doesn't depend significantly on the nanowire orientation (not shown), due to the isotropic nature of the  $\Gamma$  valley. One can see that the AD-limited mobility presents a  $U$ -shape and varies significantly with In content: it is close to about  $5,000 \text{ cm}^2/(\text{Vs})$  for In content between 0.4 and 0.8, while it increases significantly for  $x$  lower than 0.3 and reaches  $25,000 \text{ cm}^2/(\text{Vs})$  for  $x = 0.1$ .

For  $x = 0.5$ , the AD-limited electron mobility at low inversion is here  $\approx 5,400 \text{ cm}^2/(\text{Vs})$ , which is about half of the value found in Ref. [218] in rectangular cross-sections of size  $5 \times 30$  nm. This could indicate that, as mentioned in Ref. [218], the AD scattering mechanism might be of same order as POP scattering mechanisms, or even dominant in ultra small nanowires.

Note however that bulk phonons modes were used to compute the POP-limited mobility in Ref. [218] and that it should be interesting to investigate the effect of confinement with an atomistic approach on the POP-limited mobility, in order to compare these two mechanisms in more details.

### 3.2 Saturation velocity

As said in Section 3.1, the low-field mobility describes the linear relation between the drift velocity  $\mathbf{v}$  and the electric field  $\mathbf{E}$ . This expression is valid in steady state at low transverse electric field  $E = V_{ds}/L_g$ , where  $V_{ds}$  is the source-drain voltage and  $L_g$  the channel length, which is supposed to be long enough so that the electric field is constant under the gate. When the electric field is increased, the linear relation breaks and the slope  $\partial v/\partial E$  drops until  $v$  eventually saturates. The Canali's formula can be used to model this saturation of velocity in a single-valley system:

$$v = \frac{\mu_0 E}{1 + \frac{\mu_0 E}{v_{sat}}} \quad (3.23)$$

where  $v_{sat}$  is the saturation velocity and  $\mu_0$  the low-field mobility. In the case of multi-valley band structure, such as the case of GaAs, negative differential mobility effects can occur, which might be better described by the extended Chang's formula [48]:

$$v(E) = \frac{\mu_0 E}{\left(1 + \left(\frac{\mu_0(E-E_0)}{v_{sat}}\right)^2\right)^{1/2}} \quad (3.24)$$

where  $E_0$  is a critical field, where the curvature is inverted.

In bulk Si, the electron velocity saturates at about  $10^7$  cm/s (at 300 K) when the electrons accelerated in one of the six equivalent conduction band valleys are dragged back to lower energy states in another valley after emission of an optical phonon (see Refs.[58, 141]). In bulk GaAs, the situation is much different because the conduction band is made of a single low-mass valley and four heavy-mass valleys 0.3 eV higher in energy. As a consequence, the velocity continuously increases with the field as long as the electrons only occupy the lowest valley but reaches a maximum and then drops considerably when electrons get scattered to heavy-mass valleys [143]. These features have been investigated long ago in bulk materials and the velocity versus electric field curve in GaAs could be used to explain the Gunn effect observed in these materials. This indicates that the saturation velocity at high field strongly depends on the band structure at high energy, on the intervalley scattering mechanisms and on the emission of optical phonons.

Note that the saturation velocity by emission of optical phonons is an important parameter for the modeling of MOSFET devices. In TCAD model, the saturation is often taken into account by modifying the effective mobility at high field with the following formula:

$$\mu = \mu_0 \left\{ 1 + \left( \frac{\mu_0 E}{v_{sat}} \right)^\beta \right\}^{-1/\beta} \quad (3.25)$$

where  $\beta$  can be adjusted and the local electric field can be computed either from the gradient of Fermi-level or electric potential (see Chapter 4). However, the  $v_{sat}$  and  $\beta$  parameters are often adjusted to reproduce the overall saturation of the current in scaled devices in TCAD, which is due to different phenomena (pinch-off, injection velocity, ...). Moreover velocity overshoot can occur in short-channel devices where the transport is

out-of-equilibrium and the carriers are accelerated to velocity higher than the theoretically optical phonon saturation velocity. The extraction of  $v_{sat}$  and its physical meaning can thus be subject to interpretation, in particular when the effect of confinement on the high-field transport properties and saturation velocity by emission of optical phonon are not well known and understood.

It is thus interesting to study the saturation velocity by emission of phonons in a long-channel NWs and thin film, in order to better understand this mechanism and its effect on the saturation current, that will be investigated in the Chapter 4.

In this section, we first present the methodology used to compute the saturation velocity at high field, extending the resolution of Boltzmann equation presented in Section 3.1. We then compare the results obtained with KP and TB methods in the case of Si NWs, as well as the influence of the Ge content in SiGe NWs.

### 3.2.1 Methodology: resolution of Boltzmann transport equation (BTE)

Modelling high-field transport is a difficult task, mostly performed using Monte Carlo methods in the case of bulk Si [141, 266] and Si layers [89, 154, 197]. In the latter case, subbands induced by the confinement are considered in the envelope-function approximation. More recently, Monte Carlo simulations have been applied to Si NWs using band structures calculated in TB [382]. All these calculations assume that carriers are coupled to bulk phonons. However, recent studies [201, 402, 200, 256] on the low-field transport in small-diameter Si NWs based on fully-atomistic descriptions of electron and phonon states such as the one presented in Section 3.1.4 show that carriers couple in a complex manner to many phonon modes due to the strong confinement. In high-field transport, the situation is even worse since, in principle, hot carriers have enough energy to excite phonon modes in the whole spectrum. Therefore, it is interesting to explore high-field transport considering all electron-phonon scattering processes.

Unlike precedent theoretical works that mainly employ Monte Carlo method to solve BTEs, a non-linear equation solver (MINPACK) is used here to determine the distribution function (occupation probability) directly, from Eqs. (3.4) and (3.5), considering uniform transport along the NWs. In the case of NW, the BTE related to a given electronic state  $i$  is repeated here:

$$\frac{-eE}{\hbar} \nabla_k f_i = \sum_{j \neq i} [S_{ji} f_j (1 - f_i) - S_{ij} f_i (1 - f_j)] \quad (3.26)$$

where  $f_i$  is the electron occupation probability in state  $i$  and the scattering rates  $S_{ij}$  are computed using the same method as in the previous section for low-field transport, using Fermi golden rule in either KP or TB approaches (Sections 3.1.2 and 3.1.4 respectively). The energy up to 1 eV from the band extrema are taken into account here, which was found sufficient to compute the full distribution function and carrier velocity for electric field up to 1 MV/cm. The gradients  $\nabla_k f_i$  are evaluated numerically on a regular grid of  $k$  in 1D. In addition to BTEs, we impose the charge conservation in the system (e.g.,  $\sum_i f_i = \text{number of electrons}$ ). Hereafter, the carrier density is set to  $10^6 \text{ cm}^{-3}$ . The BTEs together with the extra equation are then solved exactly using MINPACK [232], which

is a solver based on the Levenberg-Marquardt non-linear algorithm. The drift velocity is finally given by  $v = \sum_i f_i v_i / \sum_i f_i$ .

### 3.2.2 Si nanowires

In this section, we investigate the drift velocity in Si NWs with small diameter that have caught significant attention over the last decade [210, 393, 114]. The EMA and TB approaches are first compared in  $\langle 110 \rangle$  NWs. The influence of the temperature is then discussed and results at 77 and 300 K are compared. The drift velocity is obtained by full resolution of the non-linear BTE including the e-ph scattering matrix elements computed within a continuous EMA method based on the deformation-potential theory or a full atomistic TB approach described in the Section 3.1.4, including all possible electron-phonon scattering processes. The same parameters as in the previous section are used for TB model. For the EMA calculation, the acoustic deformation potential is set to 14.6 eV and both f- and g-type phonons are considered with phonons energies and deformation potential given in Ref. [257].

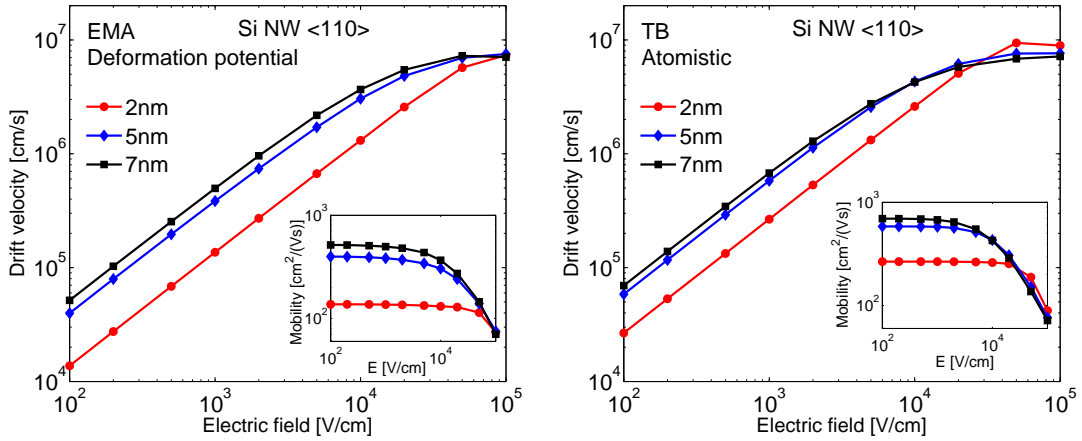


Figure 3.14. Electrons drift velocity and mobility (inset) as a function of the strength of the electric field in  $\langle 110 \rangle$  Si NW at room temperature with different diameters computed with continuous KP (left) and atomistic TB (right) approaches.

The drift velocity versus electric field in Si NWs in the  $\langle 110 \rangle$  direction at room temperature for different diameters is plotted in Figure 3.14, together with the effective mobility defined as  $\mu = v(E)/E$ . The vertical shift in the  $v(E)$  plots is due to the decrease of the electron low-field mobility with the NW diameter, as found in the previous section. Similar behavior is found in the EMA and TB approach, but the electron mobility is usually lower in EMA than in TB, due to the enhanced value of the acoustic deformation potential (as explained in Section 3.1.2). In all cases, when  $E$  is increased from 100 to  $10^5$  V/cm,  $v$  is found to be increasing at low field, then saturating after a certain threshold, or eventually dropping after a maximum. The threshold field strength, from where the saturation region starts, varies from wire to wire, and depends on the size of NW and temperature.

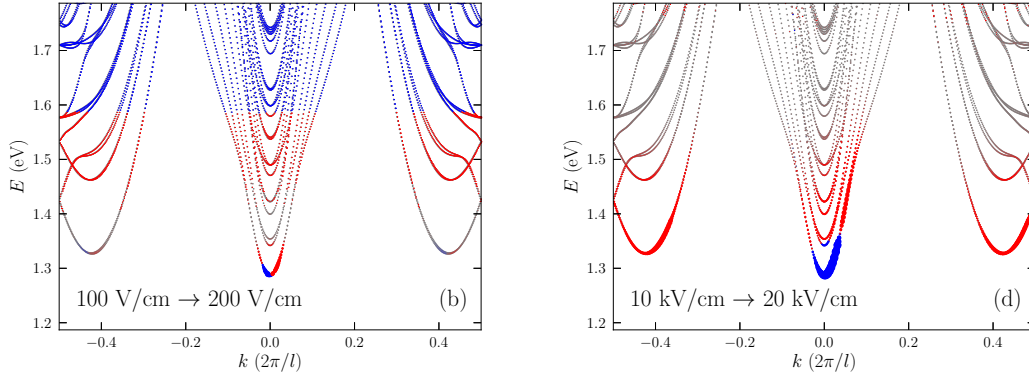


Figure 3.15. Conduction band structure of a  $\langle 110 \rangle$  Si NWs of 5 nm in diameter. The size of the dots represents the change in the electron occupation probabilities at 77 K by varying the strength of the electric field from 100 to 200 V/cm (b), or 10 to 20 kV/cm (d). Blue dots indicate a decrease in the occupation probability, red dots an increase.

One generally notes that the drift velocity in the saturation regions is usually of the same order. Therefore it is obvious to notice that wire with higher mobility has lower threshold field strength, and its mobility starts to degrade at lower field (inset of Fig. 3.14). This behavior is tightly related to the band structure of the  $\langle 110 \rangle$  Si NW and the intervalley scattering [182].

We discuss the case of the 5 nm Si NWs in details below, based on the atomistic TB approach. In order to facilitate the analysis, we discuss the change of the distribution function at low temperature (77 K). Indeed, the temperature widens the distribution function and smoothens out the effects of valley transfer, which is less pronounced at room temperature. The comparison between results at 77 K and 300 K is found in Fig. 3.16 and is discussed later.

With the presence of external electric field, the occupation probability of electron departs from the Fermi-Dirac distribution, which results from the balance between carrier acceleration by the electric field and carrier scattering by the phonons. At low electric field, the distribution function looks (almost) symmetric with respect to the conduction band minima; yet, the electric field accelerates and drags the electrons from the negative to positive group velocity states. Some of these electrons are backscattered to the negative group velocity states by the phonons. This can be seen in Fig. 3.15(left) where the change of electron occupation probability is plotted on top of the Si NWs band structure and the increase of carrier population with positive group velocity is clearly shown. At high electric field, the distribution function becomes clearly asymmetric with respect to the conduction band edge, most of the electrons being accelerated in the positive group velocity states. When most of electrons are already in positive velocity states, further increase in electric field does not help electrons to gain more velocity, but accelerate electrons to high-energy states, which facilitate phonon emission. This can be seen in Fig. 3.15(right). In this case, the average drift velocity eventually reaches a maximum and saturates. A few of

the electrons are, however, transferred from the low mass valleys at  $k = 0$  to the heavy mass valleys at  $k \pm 0.42 \times 2\pi/l$ . This intervalley process transfers electrons to state with lower group velocity, similarly to the intervalley scattering responsible for the Gunn effect in III-V bulk materials.

This analysis helps to explain why, unlike bulk Si, the saturation velocity may not be a constant in Si NWs where the confinement leads to two different types of valleys separated in energy and with different transport masses. This drop of the velocity after a peak value is particularly pronounced at low temperature, where the distribution function is steeper and the effect of valley transfer is more important. This is clearly seen in Figure 3.16, where the drift velocity at 300 K and 77 K are compared for both electrons and holes.

In general, the drift velocity in the saturation region is comparable to that of bulk Si. At 300 K, for a field of  $E = 10^5$  V/cm, the drift velocity is  $0.743 \times 10^7$  cm/s in 5 nm diameter Si NW, somewhat below the bulk value of  $\sim 10^7$  cm/s. This reduction may be explained by the stronger e-ph coupling in Si NWs [402, 256]. Following the same trend as in bulk Si, the drift velocities at  $E = 10^5$  V/cm slightly increase from 300 K to 77 K, reaching  $0.935 \times 10^7$  cm/s [141].

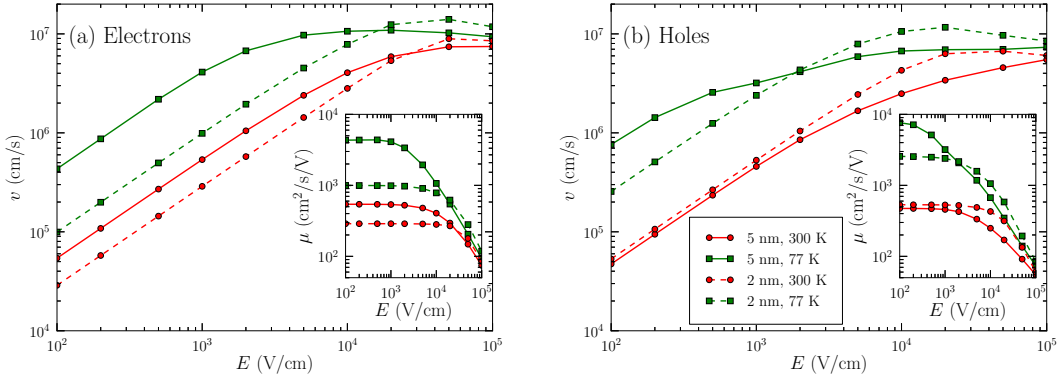


Figure 3.16. Drift velocity and mobility of electrons (a) and holes (b) as functions of the strength of the electric field in  $\langle 110 \rangle$  SiNW with diameter of 2 nm (dashed line) and 5-nm (solid line) at 77 K (green lines with squared markers) and 300 K (red lines with dotted markers).

The evolution of the distribution function of holes with respect to an increasing electric field is analogue to that of electrons. As discussed in Section 3.1.5, the highest hole subbands have a strong light-hole character in  $\langle 110 \rangle$  Si NWs, leading to a high low-field mobility. In a 5 nm NW, the first heavy hole subband is the fourth one, so that the splitting between heavy and light-hole subbands is about 46 meV. At a very high electric field, the holes can be transferred from the top light-hole to the nearby heavy-hole subbands, causing the peak value and further decrease of the hole drift velocity, as seen in Figure 3.16(b). At  $E = 10^5$  V/cm, the hole drift velocity is  $v = 0.56 \times 10^7$  cm/s at  $T = 300$  K and  $v = 0.75 \times 10^7$  cm/s at  $T = 77$  K for a 5 nm diameter Si NW. It is slightly smaller than the drift velocity of electrons, although similar saturation velocities are expected for

electrons and holes in the bulk Si (around  $10^7$  cm/s).

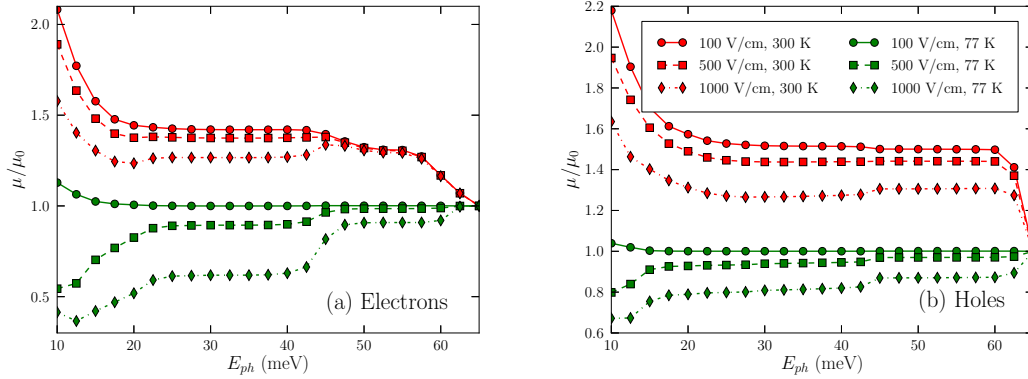


Figure 3.17. Ratio  $\mu(\hbar\omega)/\mu$  calculated for electrons (a) and holes (b) in a 5-nm  $\langle 110 \rangle$  SiNW.  $\mu(\hbar\omega)$  is the mobility at 77 K (green lines) and 300 K (red lines) calculated taking into account only the phonons with energy below  $\hbar\omega$  and  $\mu$  is the total mobility including all phonons [ $\mu \equiv \mu(\hbar\omega > 65\text{meV})$ ]. The results are shown for  $E = 100, 500$  and  $1000$  V/cm.

Figure 3.17 illustrates which phonon modes influence the drift velocity in these NWs. We plot  $\mu(\hbar\omega)/\mu$ , where  $\mu(\hbar\omega)$  is the mobility calculated including only the scattering by phonons of energy below  $\hbar\omega$ . In the bulk Si, the  $f$ -type intervalley scattering (e.g.,  $X \rightarrow Y, Z$ ) is dominated by phonons with energies around 19, 47, and 59 meV, while the  $g$ -type intervalley scattering (e.g.,  $+Z \rightarrow -Z$ ) is dominated by phonons with energies around 12, 19, and 62 meV [58, 144]. In the case of holes, the carriers are mostly coupled to the acoustic phonons and to the LO/TO branches near  $\Gamma$  ( $\hbar\omega \simeq 62$  meV). Clearly, the active phonon modes in Si NWs belong to the same categories but are distributed in broader ranges of energy because selection rules are partially lifted due to the confinement (Fig. 3.17). Also, the role of the different modes is strongly dependent on the temperature and electric field. At low field (100 V/cm), only low energy acoustic phonons contribute to inelastic scattering at 77 K [402]. Phonons of increasing energy contribute progressively when the field is increased. The influence of optical phonons ( $> 50$  meV) becomes visible only for  $E = 1$  kV/cm. At high field, the mobility increases when more phonons are taken into account, which seems rather counter-intuitive. It takes place because high-energy phonons scatter carrier from high-mass to low-mass subbands. This is the case in the conduction band of  $\langle 110 \rangle$  Si NWs in which the valley with the smallest effective mass is the lowest one (Fig. 3.15). Likewise, the emission of high-energy phonons packs holes in the top light-hole bands and limits the population of the heavy-hole bands. At 300 K, all phonons have sizeable effect whatever be the field. Yet, the high energy phonons backscatter carriers in the lowest sub-bands and limit the mobility at the low electric field, while they again hinder valley transfer and increase the drift velocity at the high electric field.

### 3.2.3 SiGe nanowires

The resolution of the BTE and methodology presented in Section 3.2.1 is applied here to SiGe NWs with different concentration and orientation, extending the atomistic study of low-field electron mobility of Section 3.1.5. The e-ph scattering matrix elements are computed with the TB fully atomistic approach and no AD scattering where included here.

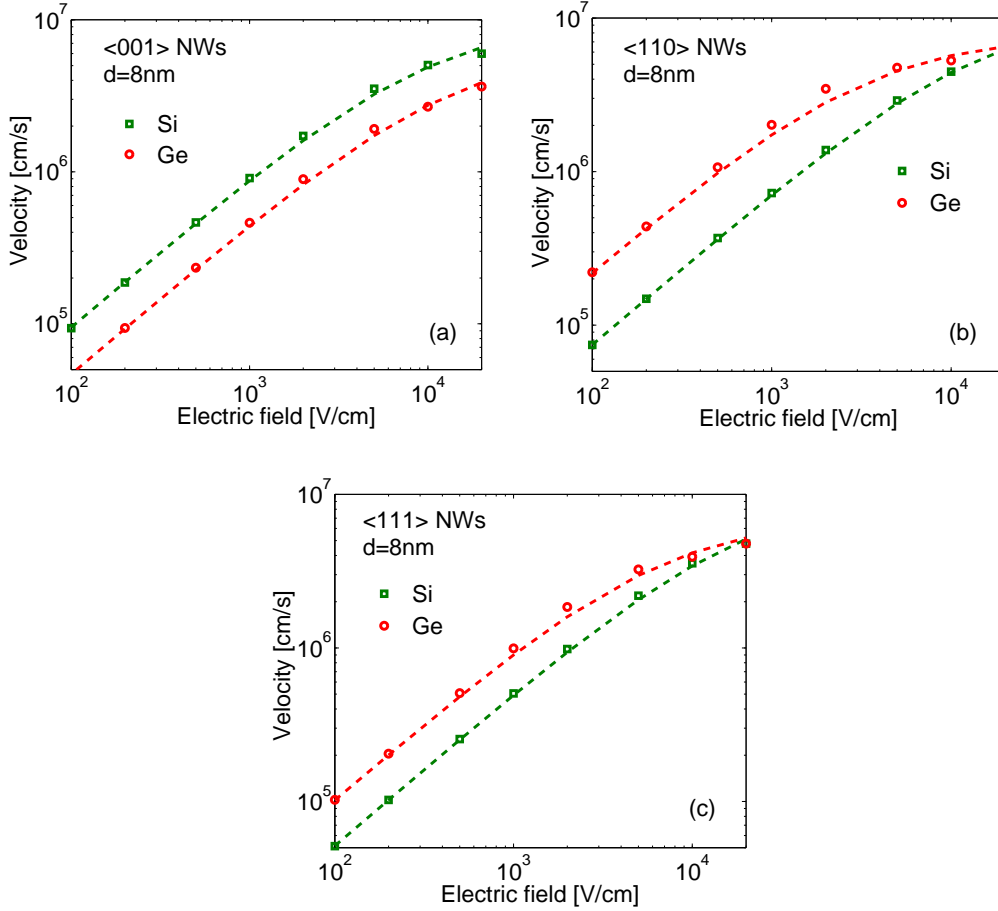


Figure 3.18. Electron drift velocity versus electric field at 300 K for pristine Si (green) and Ge (red) wires with diameter  $d=8$  nm and in the  $\langle 100 \rangle$  (a),  $\langle 110 \rangle$  (b) and  $\langle 111 \rangle$  (c) orientations. The symbols are results from resolution of BTE with TB e-ph scattering matrix elements, while lines are the fits with Canali's formula Eq. (3.23).

Figure 3.18 shows the drift velocity versus electric field of electrons in pristine Si and Ge NWs with diameter  $d=8$  nm at room temperature and with different orientations. The electric field could not be increased higher than  $2 \times 10^4$  V/cm here, due to the energy threshold used (0.25 eV) in the calculation of the scattering rates. A higher energy threshold would unfortunately increase significantly the computational cost and needed

memory for NWs with this size.<sup>2</sup> As it was studied in Section 3.1.5, the NW orientation and Ge concentration strongly impacts the low-field mobility, due to their particular band structure. In  $\langle 001 \rangle$  orientations, Si NWs present a higher mobility, while in the other two directions, Ge NWs present a higher mobility. This effect on low field mobility acts as a rigid shift of the curves in Fig. 3.18.

At high field, the velocity of Ge NWs saturates and eventually drops to lower values in  $\langle 110 \rangle$  and  $\langle 111 \rangle$  orientations, as it was observed in previous section in the case of 2 nm  $\langle 110 \rangle$  Si NWs. This is due to the multivalley character of the Ge NWs band structure (see Figure 1.24 in Section 1.2.3). This effect is less pronounced for Si NWs with  $d=8$  nm, as the splitting of the valley induced by confinement is less important. At room temperature, the saturation velocity of electrons in bulk Ge is about  $6 \times 10^6$  cm/s [142] and thus almost two times lower than the one in bulk Si ( $\sim 1 \times 10^7$  cm/s [141]). It also saturates at lower critical field. Similar effect is found in NWs, where the saturation velocity in Ge NWs is also generally lower than the one in Si NWs, as well as the critical field of the peak velocity. In Figure 3.18, the fit of the  $v(E)$  curve using the Canali formula (Eq. (3.23)) is also shown in dashed lines. The fit matches generally quite well the TB simulations, except for the case where the valley transfer is pronounced such as Ge NWs in  $\langle 110 \rangle$  and  $\langle 111 \rangle$  orientations, where the model cannot reproduce the peak velocity at field around  $3 \times 10^3$  V/cm.

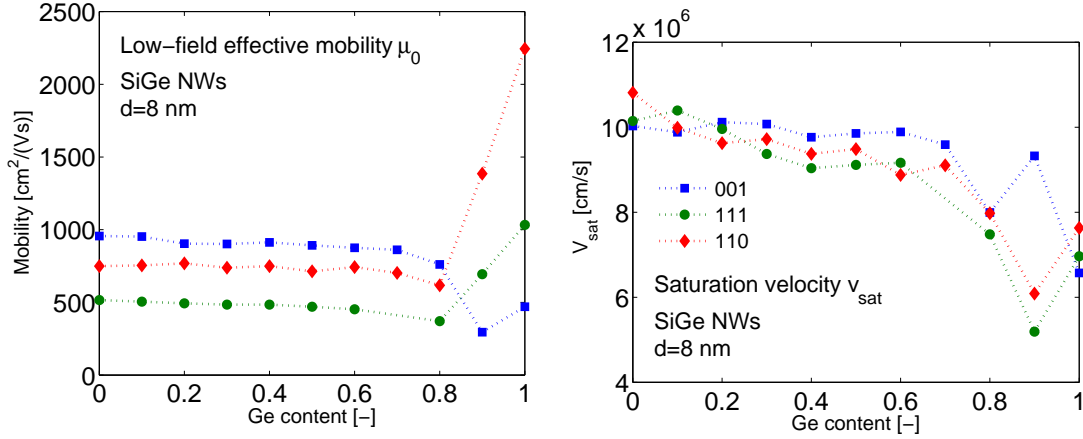


Figure 3.19. Low-field effective mobility  $\mu_0$  (left) and saturation velocity  $v_{\text{sat}}$  (right) parameters as functions of the Ge content in SiGe NWs with  $d=8$  nm and different orientations. The saturation velocity was extracted by fitting the Canali formula on TB-BTE results. The dotted lines are guide to the eye.

To perform these fits, the low-field mobility was fixed to the values calculated in Section 3.1.5 for the same NWs and the  $v_{\text{sat}}$  parameter was adjusted to minimize the

<sup>2</sup>The present calculation of the scattering rate took on average, for NWs in the  $\langle 111 \rangle$  direction, 96 hours on 64 CPUs and created  $\approx 50$  Go of data, for each Ge content.

error between the model and the simulation over the range of field considered ( $E$  between  $10^2$  and  $2 \times 10^4$  V/cm). The procedure was applied to SiGe NWs with Ge concentration varying from 0 to 1 and the value of the saturation velocity  $v_{sat}$  extracted in this way is plotted in Figure 3.19(right). As one can note, the saturation velocity extracted in pristine Si and Ge NWs with  $d=8$  nm is close to the value for bulk materials. Moreover, as opposite to the low-field mobility, the saturation velocity in pristine NWs with different orientations is similar.

When  $x$  is varied from 0 to 0.8, the saturation velocity variation is low and monotonous, regardless on the orientation. However, as for the low-field mobility, the saturation velocity shows strong variation at  $x \approx 0.8$ , due to the transfer from  $\Delta$  to L valleys. When  $x$  is increased to 0.9, the saturation velocity increases in  $\langle 001 \rangle$  NWs while it decreases for  $\langle 110 \rangle$  and  $\langle 111 \rangle$  NWs. This trends is opposite to the low-field effective mobility shown in Fig 3.19(left). Interestingly, the saturation velocity converges to a value close to the bulk value for all direction in pristine Ge NWs. However, when different valleys are close to each other in energy in such a way that intervalley is enhanced, the extraction of the saturation velocity through the single-valley Canali formula is questionable and fails to capture peaks in the  $v(E)$  curves as shown in Fig. 3.18. The saturation velocity extracted for SiGe NWs with  $x$  between 0.8 and 1 can thus be erroneous due to the fitting procedure, especially for  $\langle 110 \rangle$  and  $\langle 111 \rangle$  NWs.

### 3.3 Conclusion of the Chapter

In this Chapter, we investigated the low and high field transport properties of thin films and nanowires made of  $\text{Si}_{1-x}\text{Ge}_x$  and  $\text{In}_x\text{Ga}_{1-x}\text{As}$  materials. Physical-based models based on continuous (EMA and KP) or atomistic (TB) approaches were used to extract the transport properties such as the low-field mobility and the high-field saturation velocity.

The exact resolution of the linearized BTE was discussed in the case of inelastic anisotropic mechanisms such as POP and compared with the often used RTA approach. The effect of alloy disorder scattering on the effective mobility in nanostructures was also investigated. KG models were used to investigate effective mobility in UTBB devices and to compare it with experimental measurements, while TB models were used to investigate the mobility in NWs. The high field properties of Si NWs derived with these two approaches were compared, and the TB simulations analyzed in details.

We show that in order to model the transport properties in channel materials such as  $\text{Si}_{1-x}\text{Ge}_x$  and  $\text{In}_x\text{Ga}_{1-x}\text{As}$  it is necessary to include additional scattering mechanisms, such as POP and AD, which can be challenging to describe accurately. Moreover, the interplay between confinement and the different scattering mechanisms can be complex, and the result difficult to predict. For these reasons, it is important to have sophisticated physical-based models in order to predict the characteristics of an advanced device without need of calibration. As it will be shown in the next and last Chapter, local empirical mobility models sometimes fail to capture the correct mobility (e.g., in region below the spacer) and physical-based models such as KG model can be incorporated in a TCAD solver to compute transport parameters such as mobility and saturation velocity, in order to have a good predictability.

## Chapter 4

# Device simulation and quantum transport

In the previous Chapters, the electronic properties and transport parameters used in TCAD models, particularly relevant for long-channel devices, were simulated. However, advanced short-channel devices feature particular characteristics and physical phenomenon due to the short length of the channel, such as a lower electrostatic control by the gate, source-drain tunneling and quasi-ballistic transport. The architecture of the access regions also becomes essential in the correct modeling of the device performances. As discussed in the Introduction, the standard classical models used in TCAD face prediction power issues for nanoscale devices and several empirical models are needed to reproduce the device characteristics.

In this Chapter, the different models used to simulate the whole device are first introduced. The Quantum-corrected Drift-Diffusion (QDD) model based on the resolution of the Schrödinger equation with closed or open boundary conditions is introduced in particular. A physical-based approach is adopted, which involves the resolution of the Schrödinger equation not only for the charge distribution density, but also for quantum mechanical effects along the transport, such as source-drain tunneling. The extraction of transport parameters such as low-field mobility and saturation velocity is also discussed. In the second section, the QDD model is then used to simulate an FDSOI device. The description of confinement and transport properties by means of models based on physical parameters is investigated and compared with empirical approaches. In the third section, the quantum and ballistic features of transport in FDSOI structures are finally investigated by means of QDD and Non-Equilibrium Green Function (NEGF) codes. The saturation mechanisms in short-channel FDSOI devices are studied in particular.

### 4.1 Devices solvers

#### 4.1.1 Overview of models

One can generally divide the tools used in device modeling in two categories: semi-classical tools (such as Monte-Carlo (MC), Drift-Diffusion (DD) and Hydrodynamics

(HD)) and quantum tools (such as Landauer-Büttiker, Quantum Transmission Boundary Matrix (QTBM) and NEGF approaches). Studies have been performed to address the discrepancies among these modeling techniques and predictions of transport in nanodevices [1, 268, 372]. These studies show that each method has advantages and shortcomings (making each of them useful for a particular application) and that there is no perfect solution to model any device. This section gives a brief introduction of the different models, as well as the choice of models made in this work.

### Semi-classical models

Semi-classical tools are based on the resolution of the BTE (keeping the spatial derivative in Eq. (3.3) for non-homogeneous transport), either directly through Monte-Carlo algorithm or after integration and derivation of macroscopic quantities. The most commonly used models in TCAD are based on the method of moments, which allows a convenient approximation of the BTE and an efficient and stable resolution. To derive these models, the BTE (Eq. (3.3)) is multiplied by weighing functions (such as the carrier momentum  $\mathbf{p}$  (1<sup>st</sup> order), the energy  $\varepsilon$  (2<sup>nd</sup> order),  $\mathbf{p}\varepsilon$  (3<sup>rd</sup> order),  $\varepsilon^2$ , ...) and then integrated over the  $k$ -space. A system of equations is thus obtained, which is usually under determined. In order to solve and simplify this system, closure relations have to be introduced, implying approximations on the physics. These models are called macroscopic, as they involve the integration of BTE over the  $k$ -space and the moments obtained are related to macroscopic quantities (such as the carrier density  $n$ , carrier velocity  $v_s$  or the flux density). In the simple Drift-Diffusion (DD) model, the moments of order 0 (direct integration of the BTE) and 1<sup>st</sup> order are used, together with the approximation that the carrier are at thermal equilibrium with the lattice, allowing to have a closure relation. In this model, the current is given as [316, 117]:

$$\begin{aligned}\mathbf{J}_n &= e \left[ n\mu_n \mathbf{E} + D_n \nabla_{\mathbf{r}} n \right] \\ \mathbf{J}_p &= e \left[ p\mu_p \mathbf{E} - D_p \nabla_{\mathbf{r}} p \right]\end{aligned}\tag{4.1}$$

where  $\mathbf{J}$  is the current,  $\mu$  is the mobility,  $D$  is the diffusion coefficient,  $n$  and  $p$  are the electron and hole densities (the indexes  $n$  and  $p$  stand for electrons and holes).  $D$  and  $\mu$  are related through the Einstein relation:

$$D_i = \frac{\mu_i k_B T}{e}$$

where  $i = (n, p)$ . When quasi-Fermi level  $\phi_F$  is introduced, Eqs. (4.1) can be transformed to:

$$\begin{aligned}\mathbf{J}_n &= en\mu_n \nabla_{\mathbf{r}} \phi_{Fn} \\ \mathbf{J}_p &= ep\mu_p \nabla_{\mathbf{r}} \phi_{Fp}\end{aligned}\tag{4.2}$$

The Hydrodynamic (HD) model includes additionally the 2<sup>nd</sup> order moment and allows carrier temperature to be different from the lattice. The closure relation comes here

from the conservation of the energy flux (Fourier law). Moments of higher orders can be included to improve the models, such as it was done in Grasser *et al.* (2001) [116], allowing to extend the accuracy of the models to shorter channels and get results close to MC methods [372].

All the moment-based models usually make the assumption of a single-valley isotropic effective mass and a local carrier density computed from the classical Maxwell-Boltzmann statistics:

$$n(\mathbf{r}) = \langle \mathcal{N}_{c/v}^{3D} \rangle \exp(\eta(\mathbf{r})) \quad (4.3)$$

where  $\langle \mathcal{N}_{c/v}^{3D} \rangle$  is the spatial average of the 3D carrier density-of-state of conduction band (c) or valence band (v) and  $\eta = \frac{\mathcal{E}_{Fn}(\mathbf{r}) - \mathcal{E}_c(\mathbf{r})}{k_B T}$  for electrons and  $\eta = \frac{\mathcal{E}_v(\mathbf{r}) - \mathcal{E}_{Fp}(\mathbf{r})}{k_B T}$  for holes. Moreover, the calculation still involves transport parameters through the scattering integrals (moments of the scattering operator). A local mobility is used in DD model, based on empirical expressions that are fitted on experimental or advanced tools. For high-field, the mobility is further modified through the Eq. (3.25) to account for saturation of the velocity. Methods to compute moments of the inverse scattering operator to higher orders have also been discussed in, e.g., Refs [274, 41], allowing to avoid empirical models.

The microscopic BTE equation can also be solved directly by mean of the well-known stochastic Monte Carlo (MC) method. These MC models are widely used for the simulation of transport and allow a physical description of the scattering matrix elements and the resolution of the BTE to any order. However, they require more heavy numerical resources, in particular when confinement effects are included in Multi-Subband MC approaches [83, 356]. Moreover, the statistical description requires a large number of particles and these methods generally suffer from noise under the threshold voltage [94]. Other methods for the resolution of the microscopic BTE exist, such as the Spherical Harmonic Expansion (SHE) [316, 311], the use of wavelets [275] or the phase-space resolution [335, 336] but they will not be discussed here.

Quantum-corrections can be included in these semi-classical models to account for quantum mechanical properties such as quantum confinement and tunneling effects. Several methods to include quantum-correction exist and the general justification of these corrections can be obtained from the Bohmian interpretation of quantum mechanics and the so-called Bohm potential. Models including these corrections are, e.g., Multi-Subband Monte Carlo (MSMC) [356], Multi-Subband BTE [150] or Quantum-Corrected DD (see below). These models generally involve the resolution of the Schrödinger equation and the incorporation of quantum mechanical effects through an additional electric potential to the classical one.

The Quantum-corrected DD (QDD) models will be discussed in more details in the next section. The solver used in this work provides two different implementations [279, 280], that will be detailed in Section 4.1.2. They are used to study the transport in FDSOI devices in Sections 4.2 and 4.3.

## Quantum models

Quantum transport methods are also often encountered in the literature and are well suited for the modeling of nanoscale devices, close to the quantum limit. Landauer-Büttiker formalism can be used to model quantum transport at an acceptable numerical cost, and can be used to simulate ballistic devices. The interactions of carriers with ionized impurity and surface roughness beyond the first-order perturbation (Fermi-golden rule) can also be included [282, 281, 179]. Moreover, QTBM techniques allow to solve Schrödinger equation and describe quantum transport in open systems [167, 194]. However, to model real device working at room-temperature, non-coherent and out-of-equilibrium transport has often to be considered. NEGF formalism has been widely used and successfully applied to study the transport in nanoscale devices in ballistic or diffusive regime [257, 34, 204, 203]. Atomistic (TB or DFT) band structures can be used to have an accurate description of the electronic states [198] and the interactions of carriers can be treated in a geometrical description in real-space (surface roughness) or through the self-consistent resolution with Poisson equation (e.g., Coulomb interactions with ionized impurities). Electron-phonon coupling can be included in these tools through self-energies, computed using the self-consistent Born approximation (SCBA) and deformation potential theory. These self-consistent iterations however increase the cost of the calculation and make the atomistic description hardly applicable, while EMA/KP models are preferred (e.g., Refs. [257, 34]). Moreover, in NEGF solvers, the electronic Green function is described in real-space  $G(\mathbf{r}, \mathbf{r}')$  and its size increases very quickly with the size of the simulation domain. Modespace approaches have been widely used to decrease this numerical cost, where the Green function is projected on envelope function in the confinement direction and NEGF equations are solved only in the transport direction (1D) [204, 246, 373]. While uncoupled modespace approaches are efficient and allow to strongly reduce the numerical cost, they fail to describe the transport in inhomogeneous channels and coupled modespace approach need to be used. These approaches generally require high computational cost and need to be run on super-computers.

These models, discussed in more details in Section 4.1.3, are used to study the diffusive character of transport in nanoscale devices in Section 4.3.

### 4.1.2 Quantum-drift diffusion (QDD)

In this work, we aim at using methods that are compatible with TCAD and numerically efficient so they can run standalone on a single PC. In the same time, we try to avoid fitting parameters and empirical models, to improve the predictability of TCAD and investigate physical phenomenon involved in nanoscale devices.

In this context, it is important to investigate whether DD model can be used to model the current in a nanoscale transistor, where quasi-ballistic and out-of-equilibrium transport can occur. It was demonstrated by C.Jungemann *et al.* (2005) [155] that semi-classical models based on the first order moments of the BTE fail to model the current in a nanoscale transistor. However, it was also noted recently by M.Lundstrom *et al.* (2015) [207] that the DD formalism can be surprisingly successful in TCAD simulations,

provided that the parameters of the model are correctly extracted/calibrated. Quantum-corrected DD (QDD) models were developed and applied to nanoscaled devices in studies ten years ago [65, 239]. Their theoretical foundations were investigated in Baccarani *et al.* (2008) [16], based on the interpretation of quantum mechanics of D.Bohm [33], and it was shown that the ballistic and quantum features of transport occurring in the nanoscale devices can be, in theory, accurately described by a QDD solver, “so long as the mobility model implemented in the code accounts for subband formation, anisotropic effective-masses and strain-induced subband splitting, if any” [16].

### Overview of QDD models

We would like to highlight here that behind the label “Quantum Drift Diffusion”, we can find a wide range of solutions: from the density-gradient corrected DD solver [213] to multi-subband Poisson-Schrödinger DD solver [16], as well as sliced Schrödinger resolution, coupled or not with KG solver [279, 157] and 2D Schrödinger resolution accounting for source-drain tunneling (SDT) effects [239, 65].

In the density-gradient model, the carrier density is modeled as [9, 213]:

$$n = \mathcal{N}_c^{3D} \mathcal{F}_{1/2} \left( \frac{\varepsilon_{Fn} - \varepsilon_c - \Lambda_n}{k_B T} \right) \quad (4.4)$$

where:

$$\Lambda_n = \frac{\gamma \hbar^2}{5m_{DOS}^*} \frac{\nabla^2 \sqrt{n}}{\sqrt{n}} \quad (4.5)$$

where  $\gamma$  is a fitting parameter. The parameter  $\Lambda_n$  acts as an additional driving force, or potential energy, and can account for the quantum confinement in the direction perpendicular to the transport (e.g. darkspace effect). This model is popular among users of TCAD tools based on DD framework such as Sentaurus Device or PADRE. Other empirical models included in these solvers are, e.g., the Modified Local Density Approximation (MLDA) [267]. However, these models need to be calibrated and they are usually not well suited for the transport direction (e.g. SDT).

Baccarani *et al.* (2008) [16] showed that, based on the formulation of D.Bohm [33], the additional driving force (or “so-called” Bohm’s quantum potential) can be deduced from the resolution of the Schrödinger equation. It is given in the confinement direction  $y$  (perpendicular to the transport) in the EMA approach by:

$$Q^i(y) = -\frac{\hbar^2}{R^i} \left( \nabla_y \cdot \frac{\nabla_y R^i}{m_y^*} \right) = \varepsilon^i - U(y) \quad (4.6)$$

where  $m_y^*$  is the effective mass in confinement direction,  $U(y)$  is the classical potential energy,  $\varepsilon^i$  is the energy of the subband  $i$  and  $R^i = |\psi^i(y)|$  is the norm of the envelope wavefunction (interpreted in Bohm’s theory as the quantum field where the particles evolve). In this case, the driving force depends on the subband index and a continuity equation should be solved for each subband, with additional intersubband scattering

terms, leading to a quite cumbersome computation. However, if the variation of the subband energy along the transport direction  $x$  is equal for each subband, or if only one subband is occupied, a single equation can be recovered:

$$J_n = \mu_n n \nabla_x \varepsilon + e D_n \nabla_x n \quad (4.7)$$

where  $\mu_n$  is the average of the subband effective mobilities:  $\mu_n = \sum_i \frac{\mu_n^i n^i}{n}$ ,  $n$  being the total electron concentration  $n = \sum_i n^i$  and  $i$  the subband index. As the electric field can be written as  $eE = \nabla_x \varepsilon$ , this equation is equivalent to Eq. (4.1), provided that the electron density is replaced here by a “quantum” electron density computed as:

$$n = n_q = \sum_i |\psi^i|^2 f \left( \frac{\varepsilon^i - \varepsilon_{Fn}}{k_B T} \right) \quad (4.8)$$

For the self-consistent resolution of the Continuity and Poisson equations, the so-called “Slotboom transformation” [328] is usually used, which requires a direct analytic relation between  $n$  and  $\phi_{Fn}$ , such as Eq. (4.3). To include quantum-corrections from the models mentioned above, the charge density in Eq. (4.4) or (4.8) is, in practice, recast into a quantum potential energy  $G_n$ , which is the driving force added to the classical potential energy in the DD equation. The expression of this quantum potential energy can be determined by writing that:

$$\begin{aligned} n_q(y) &= \langle \mathcal{N}_{c/v}^{3D} \rangle \exp \left( \frac{\varepsilon_F - \varepsilon_c(y) - G_n(y)}{k_B T} \right) \\ &= n_c(y) \exp \left( \frac{-G_n(y)}{k_B T} \right) \end{aligned}$$

The quantum potential energy is then obtained [280]:

$$G_n(y) = -k_B T \ln \left( \frac{n_q(y)}{n_c(y)} \right) \quad (4.9)$$

A similar approach can be used to include an additional driving force (recast in the electrostatic potential) in the direction of transport, as it was shown by several studies such as Refs. [239, 233, 64]. In these works, a generalized 2D Poisson-Schrödinger QDD (PS-QDD) framework was derived, to model the quantum effects along the transport direction (such as source-drain tunneling SDT). The quantum potential energy is here a 2D spatial function:

$$G_n(x, y) = -k_B T \ln \left( \frac{n_q(x, y)}{n_c(x, y)} \right) \quad (4.10)$$

where the quantum charge is obtained from a 2D Schrödinger solver:

$$n_q(x, y) = \sum_i |\psi^i(x, y)|^2 f \left( \frac{\varepsilon^i - \varepsilon_{Fn}}{k_B T} \right) \quad (4.11)$$

The penetration of the 2D wavefunction inside the potential barrier induced by the gate creates here a strong ratio  $n_q/n_c$ , so that the potential energy  $G_n$  acts as a driving force along the transport able to account for tunneling effects [64]. However the assumption on the variation of the subband energy  $\nabla_x \varepsilon^i$  might not be satisfied here and a “multi-subband” version of this model should be developed to be more rigorous.

## Methodology adopted

In this work, an *in-house* PS-QDD solver is used, including quantum corrections and physical models to compute the effective mobility. We developed a QDD framework, where the non-linear Poisson and Continuity equations are solved self-consistently within a Scharfetter-Gummel scheme [316, 315]. The resolution of the Schrödinger equation is included in the self-consistent scheme, as sketched in Figure 4.1.

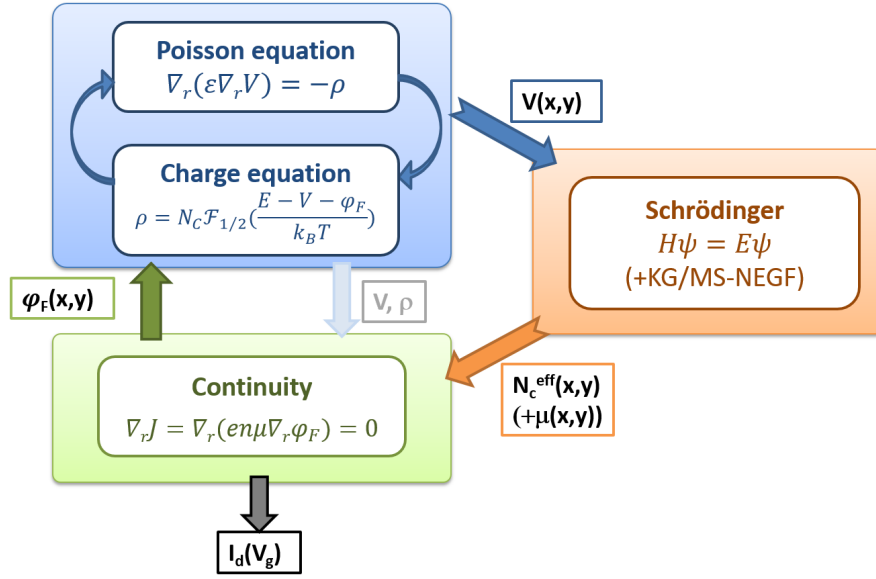


Figure 4.1. Schema of the self-consistent resolution of non-linear Poisson and Continuity equations in a QDD framework, and the inclusion of Schrödinger resolutions.

In our QDD model [279], we use two different approaches. In the first approach, the closed-boundary Schrödinger equation is solved in slices in the confinement direction  $y$  (perpendicular to the channel). The Schrödinger equation is solved in 1D here, while the Poisson and Continuity equations are solved in 2D, leading to what we called a “1.5D” PS solver. In this case, the low-field mobility can be computed either by empirical models, or by a KG approach based on the envelope function of the 1D Schrödinger solver (see Section 3.1.2). In the second approach, the NEGF equation is projected on the envelope functions of the slices and solved in an uncoupled modespace (MS) approach (see details below in Section 4.1.3). An “apparent” position-dependent mobility is recovered from the NEGF charge and current by inverting the DD equations, as explained in details in the next subsections. This second approach allows to describe quantum effects in the transport direction and brings a few improvements to the 2D PS-QDD model previously implemented.

**Electrostatics** The quantum potential energy that enters the Continuity equation is computed as explained before, with Eq. (4.9) or (4.10). It depends on the ratio of quantum density over classical density and includes the usual confinement (DS) effects near SC/oxide interfaces, in both PS-QDD models used in this study. To be consistent with the non-linear Poisson solver (blue box in Fig. 4.1), the density prefactor  $\langle N^{3D} \rangle$  used in the Slotboom transformation and non-linear Poisson equation is also modified and computed as [280]:

$$\langle N_q^{3D} \rangle = \frac{n_q(x, y)}{\mathcal{F}_{1/2}((\varepsilon_C - \varepsilon_F)/k_B T)}$$

The map of quantum corrected density factor obtained in this way is plotted in Fig. 4.2.

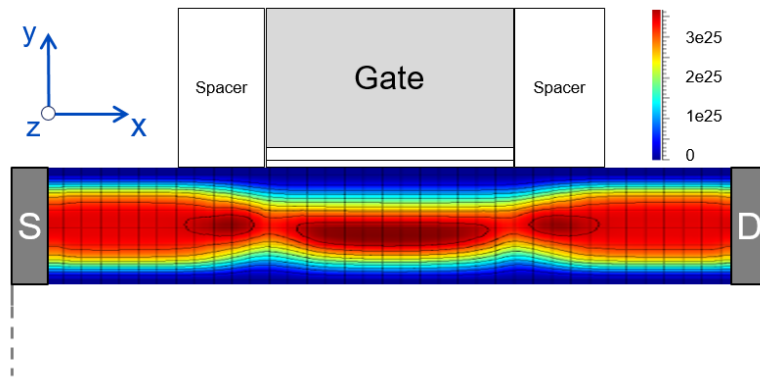


Figure 4.2. Effective density prefactor accounting for quantum corrections (see text for details) in an FDSOI NMOS device at  $V_{gs} = 0.9$  V and  $V_{ds} = 50$  mV.

Additionally, in the second QDD approach, the quantum potential computed with Eq. (4.10) includes a driving force along the transport direction, and accounts for SDT effects as explained in Ref. [65]. Note that previous studies with PS-based QDD models were mainly based on the resolution of the closed boundary system. To account for effects such as SDT in the transport direction, the limitation of the 2D Schrödinger equation is twofold: the closed boundary condition imposes the quantum charge to be zero at the quantum domain border, which implies a proper position of the simulation box. Additionally, the description of high  $V_{ds}$  regime requires a big number of subbands (typically  $\geq 1000$  in an architecture like Fig. 4.2 in saturation regime) to account for the high energy difference between source and drain levels. This limits the methods to low source-drain bias  $V_{ds}$  (1 mV in Ref. [65]) or to ultra-thin devices ( $t_{ch} = 1.5$  nm in Ref. [239]). The present NEGF-based approach allows to investigate thicker channel devices at high  $V_{ds}$ .

**Transport parameters** In the first PS-QDD approach used in this work, the low-field mobility can be computed with KG solver, based on the outputs of the 1D Schrödinger solver, as explained in Section 3.1.2. Although the KG solver increases the numerical cost of the simulation, it allows to compute the mobility based on physical-based parameters

and avoid empirical models and fitting parameters. It also allows to capture the effect of confinement on the different scattering mechanisms. A similar approach was used in, e.g., Stanojevic *et al.* (2015) [338]. This method allows to improve the prediction power of device solvers for the low-field mobility used in linear regime.

However, it does not describe the saturation mechanisms and one still needs to adjust the saturation velocity parameter to describe the current in saturation regime. Although this parameter could be calculated with the methodology introduced in Section 3.2.1, it would only describe the saturation of current through the emission of optical phonon and would not capture the ballistic effect in short channel devices (e.g., the saturation due to the injection velocity at the top-of-the-barrier [205]).

In the second PS-QDD approach used in this work, we propose to extract an “apparent” position-dependent mobility from the NEGF current based on Scharfetter-Gummel DD equations [316]. It corresponds to the mobility in a DD solver that gives the same overall drain current as the NEGF solver. It can be computed by inverting the DD formula (4.1), as detailed below. The first issue comes from the “non-locality” of the NEGF current, which is an integrated value over the channel thickness. In the view to compute a local mobility, the quantum current is first averaged over the NEGF charge distribution.

In the finite difference 2D mesh of a Scharfetter-Gummel scheme, the current density in a given mesh node  $(i, j)$  can be established by their neighbor’s mid-nodes (see Ref. [316] for the derivation of this expression):

$$J_n(i, j) = \sqrt{\left(\frac{J_{nx}|_{i+1/2,j} + J_{nx}|_{i-1/2,j}}{2}\right)^2 + \left(\frac{J_{ny}|_{i,j+1/2} + J_{ny}|_{i,j-1/2}}{2}\right)^2} \quad (4.12)$$

where the 1/2 indexes denote mid-points nodes of the 2D mesh. The required electron current density components of each of the intervals, which are the parameters of the respective differential equations for the carrier concentrations, are evaluated to:

$$\begin{aligned} J_{nx}|_{i+1/2,j} &= D_n|_{i+1/2,j} B|_{i+1/2,j} \\ J_{nx}|_{i-1/2,j} &= D_n|_{i-1/2,j} B|_{i-1/2,j} \\ J_{ny}|_{i,j+1/2} &= D_n|_{i,j+1/2} B|_{i,j+1/2} \\ J_{ny}|_{i,j-1/2} &= D_n|_{i,j-1/2} B|_{i,j-1/2} \end{aligned}$$

where  $D_n$  is the diffusivity coefficient obtained from the Einstein relation  $D_n = \frac{\mu_n k_B T}{e}$  and is given as a simple linear interpolation for the mid-interval. The functions  $B|_{i\pm 1/2,j}$  are defined as:

$$B|_{i\pm 1/2,j} = \frac{B(\varphi(i^\mp, j) - \varphi(i^\pm, j)) n(i^\mp, j) - B(\varphi(i^\pm, j) - \varphi(i^\mp, j)) n(i^\pm, j)}{\Delta_x(i^\pm)}$$

where the Bernoulli functions are given by  $B(x) = x/(1 + \exp(x))$ ,  $\Delta_x$  is the mesh step and the indexes  $i^\pm = i + 1/2 \pm 1/2$  and  $i^\mp = i - 1/2 \mp 1/2$ . The function  $B|_{i,j\pm 1/2}$  are defined the same way, interchanging  $i$  with  $j$ . Eq. (4.12) is then further transformed into:

$$J_n(i, j) = \sqrt{\left(\frac{\mu_n(i, j) k_B T (B|_{i+1/2,j} + B|_{i-1/2,j})}{2e}\right)^2 + \left(\frac{\mu_n(i, j) k_B T (B|_{i,j+1/2} + B|_{i,j-1/2})}{2e}\right)^2}$$

And therefore:

$$\mu_n(x, y) = 2J_n(x, y) \left( \frac{e}{k_B T} \right)^{3/2} \sqrt{\frac{1}{\tilde{B}^2(x, y)}} \quad (4.13)$$

where  $\tilde{B}^2(x, y)$  is the average squared Bernoulli function calculated on the half-nodes of a Scharfetter-Gummel scheme:

$$\tilde{B}^2(x, y) = (B|_{i+1/2, j} + B|_{i-1/2, j})^2 + (B|_{(i, j+1/2)} + B|_{(i, j-1/2)})^2$$

An “apparent” position-dependent mobility that is compatible with DD framework is obtained in this way from the non-local NEGF current. Carrier-phonon interactions are included in the MS-NEGF calculation, while other types of scattering that require a geometrical description and greatly increase the numerical cost of the simulation, may be later included via standard empirical models through a Matthiessen rule.

### 4.1.3 Non-equilibrium Green function (NEGF)

To study the validity of the QDD model and the diffusive character of nanoscale devices, we will compare in Section 4.3 physical quantities extracted from QDD simulations to the ones extracted from full-quantum NEGF simulations in linear and saturation regimes. The NEGF solver used there is the one implemented in `TB_Sim` [381] in the EMA/KP formalism and includes a geometrical description of the device in 3D, including surface roughness and discrete dopants. Details about the code and its implementation can be found in, e.g., Ref. [257].

In this work, we also perform NEGF simulation in the uncoupled modespace (MS-NEGF) approach, with electron-phonon interactions included with local self-energies following Ref. [8]. This solver, implemented in `U2OXPP` code, is included in the PS-QDD module and used to extract the “apparent” mobility through the method mentioned above. Other scattering mechanisms are not included in this MS-NEGF solver, but may be included *a posteriori* in the PS-QDD module, via Matthiessen rule.

The EMA is used for all calculations and will be assumed in the following derivations.

### Some definitions

The electronic one-body Green’s function  $G(\mathbf{r}, t, \mathbf{r}', t')$  represents the probability to find an electron at position  $\mathbf{r}$  and time  $t$  when an electron was initially injected at position  $\mathbf{r}'$  at time  $t'$ . For a time-independent Hamiltonian (no exterior perturbation), it is more convenient to transform the time-resolved Green’s function into an energy-resolved Green’s function  $G(\mathbf{r}, \mathbf{r}', \varepsilon)$  [361]. This function allows to describe quantum transport. However it needs to be extended to non-equilibrium Green function (NEGF) formalism to treat systems driven out-of-equilibrium or polarized by, e.g., source-drain electrodes [160]. In this subsection, we follow the definitions and derivations presented in Ref. [360].

The electronic stationary states are described by the retarded Green’s function:

$$G^r(\varepsilon) = \lim_{\eta \rightarrow 0^+} [\varepsilon + i\eta - H - \Sigma_L^r - \Sigma_R^r - \Sigma_{PH}^r]^{-1} \quad (4.14)$$

where  $\varepsilon$  is the energy usually taken on a fine mesh,  $\Sigma_L^r$  and  $\Sigma_R^r$  are the self-energies of left and right contacts resp., and  $\Sigma_{PH}^r$  is the self-energy of electron-phonon scattering.  $H$  is the KP/EMA Hamiltonian of the simulation domain. The broadening of the states induced by the contacts is related to the imaginary part of their self-energies, defined as:

$$\Gamma_C = i(\Sigma_C^r - (\Sigma_C^r)^\dagger)$$

where  $C = (R, L)$ . In the NEGF formalism, the lesser Green's function is furthermore introduced, defined as:

$$G^<(\varepsilon) = G^r(\Sigma_L^< + \Sigma_R^< + \Sigma_{PH}^<)G^a$$

where  $G^a = (G^r)^\dagger$  is the advanced Green's function and  $\Sigma_C^<$  are the lesser self-energies. These are all complex operators. The lesser and retarded self-energies are related to each other through the relation:

$$\Sigma_C^< = i\Gamma_C f(\varepsilon - \varepsilon_{FC})$$

where  $\varepsilon_{FC}$  is the Fermi-level energy at the contact considered ( $R$  or  $L$ ).

From these quantities, the energy-resolved electronic density and electronic current flowing from slice  $i$  to slice  $i'$  (along the transport direction  $x$ ) can be computed as [361]:

$$\rho(\varepsilon) = g_\nu g_s \frac{1}{2\pi} \Im \{ G^<(\varepsilon) \} \quad (4.15)$$

$$I_i(\varepsilon) = -g_\nu g_s \frac{2e}{h} \Re \left\{ \text{Tr} \left[ G_{i',i}^<(\varepsilon) H_{i,i'} \right] \right\} \quad (4.16)$$

where  $\Im$ ,  $\Re$  and  $\text{Tr}$  are the imaginary part, real part and trace operators respectively.

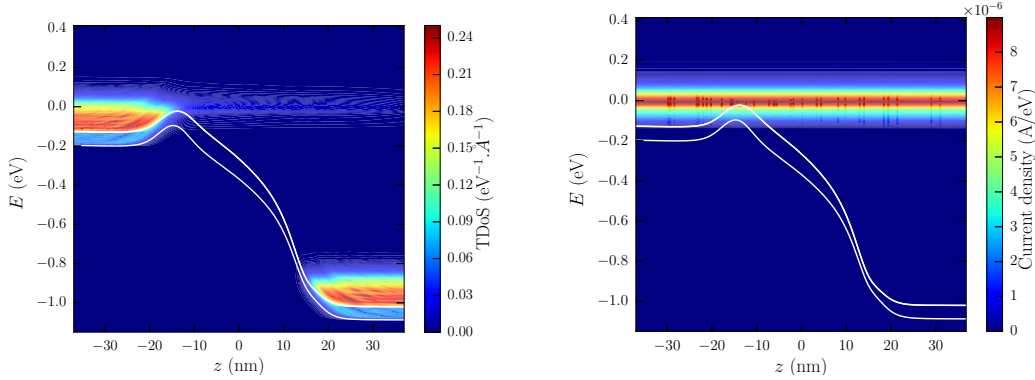


Figure 4.3. Occupied local density-of-states (left) and current density (right) maps in an FDSOI NMOS device including acoustic electron-phonon coupling in saturation regime ( $V_{ds} = 0.9$  V), computed with Eqs. (4.15) and (4.16).

In the following subsections, the methods to compute  $\Sigma_C$  and  $\Sigma_{PH}$  are presented. We consider here a 2D cross-section of an FDSOI device, as sketched in Fig. 4.5 on page 131. The device is supposed to be invariant in the width ( $z$  direction) and a  $k$ -space dispersion can be considered in this direction, discretized on a mesh with step  $\Delta k_z = \frac{2\pi}{L_z}$ .

### Contact self-energies

To account for open-boundary condition, contacts are included at the edge of the simulation domain. These contacts are treated as quasi-infinite leads, coupled with the simulation domain as depicted in Fig. 4.4. The influence of the contacts is included in the simulation domain through the use of self-energies  $\Sigma_C^r$ , modifying the eigenvalues of the Hamiltonian  $H$  and inducing a broadening of the energy levels, therefore enabling a current to flow through the device.



Figure 4.4. Schema of contact leads coupled with the simulation domain through coupling terms  $t_L$  and  $t_R$ .

In our case, the contacts are supposed quasi-infinite along the transport  $x$  direction, and coupled with nearest neighbors only, with coupling matrices  $t_L$  and  $t_R$ . In the EMA approach, the coupling between the last mesh point of left lead and the first mesh point of the simulation domain is given by  $t_L = \hbar^2/(2m_x^*\Delta x^2)$  where  $\Delta x$  is the mesh step. The left contact self-energy, projected on one transverse mode, is analytic in this case:

$$\begin{aligned}\Sigma_L(1) &= -t_L e^{ik\Delta x} \\ \Sigma_L(x) &= 0 \quad \forall x > 1\end{aligned}$$

where “1” is a point at the left edge of the simulation. The right contact self-energy  $\Sigma_R$  is given by:

$$\begin{aligned}\Sigma_R(x) &= 0 \quad \forall x < N_x \\ \Sigma_R(N_x) &= -t_R e^{ik\Delta x}\end{aligned}$$

where “ $N_x$ ” is a point at the right edge of the simulation ( $N_x$  being the number of mesh point in  $x$  direction in the simulation domain).

When a contact with a finite size along  $y$  direction is treated in real space or for general KP models, the contact self-energies are not analytic. They need to be computed numerically, with recursive methods. The decimation technique is used here to compute them, following Ref. [313].

The self-energy calculations presented here can also be used in other open-boundary solvers, such as QTBM. In our simulation, we include two electrodes contacts (source and drain), but more contacts can be included in principle in the simulation [148].

### Uncoupled modespace approach

As stated earlier, the real-space description of the Green’s function makes NEGF method numerically expensive. For this reason, a mode-space approach is often used in NEGF

studies in order to reduce the computational burden [204]. In this approach, the 2D spatial Green's function is projected on the closed-boundary eigenvectors perpendicular to the transport ( $y$  direction) as:

$$G_{i,i',y,y'}(\varepsilon, k_z) = \sum_{n,m} G_{i,i',n,m}(\varepsilon, k_z) \psi_n^i(y) \psi_m^{i'}(y') \quad (4.17)$$

where  $i$  and  $i'$  are slice indexes (i.e., position along the  $x$  direction),  $n$  and  $m$  are subband indexes along the confinement  $y$  direction (so-called “modes”) and  $\psi_n^i(y)$  and  $\psi_m^{i'}(y')$  are the eigenvectors in the slices obtained by solving the closed-boundary Schrödinger equation. Remember that the device is supposed to be invariant in the  $z$  direction, so the dependency of the Green function on the transverse wavevector  $k_z$  in this direction has been introduced here.

In this way, the real-space Green's function  $G_{i,i',y,y'}$  with size  $(N_x \times N_y)^2$  is reduced to the mode-space Green's function  $G_{i,i',n,m}$  with smaller size  $(N_x \times N_m)^2$ , where  $N_m$  is the number of modes (that can be significantly smaller than  $N_y$ , as it was seen in Chap. 1). The EMA Hamiltonian in the coupled mode-space approach is generally non-diagonal, as the modes of different slices may be coupled to each other. However, in the case of a homogeneous thin film, one can consider that the shape of the modes varies slowly along the  $x$  direction:

$$\psi_n^i(y) \simeq \psi_n^{i\pm 1}(y)$$

In this case, the EMA Hamiltonian  $H$  projected on the modes becomes block tridiagonal and the equation of motion can be solved for each mode independently, leading to the uncoupled mode-space approach and reducing the size of Hamiltonian for each equation to  $(N_x)^2$  [373].

We have verified in the case of FDSOI device with homogeneous film thickness (no raised source/drain) that the overall current obtained in the coupled and uncoupled mode-space approaches is almost identical, even when electron-phonon coupling is taken into account. When raised source/drain regions (thicker than the channel) are considered, the uncoupled mode-space approach fails and the current obtained significantly differs from the coupled mode-space and real-space approaches.

### Phonon self-energy: self-consistent Born approximation (SCBA)

In this study, electron-phonon interactions are treated in the deformation-potential theory, following Ref. [8]. The Dyson equation is used to solve the electron-phonon scattering self-energy:

$$G^r = G^{r0} + G^r \Sigma_{PH}^r(G^r) G^{r0}$$

where  $G^{r0}$  is the Green's function of the un-pertubated system (no  $\Sigma_{PH}^r$  in Eq. (4.14)). The energy dependencies have been omitted here. This equation can be solved iteratively, leading to the so-called SCBA.

Phonon scattering processes are considered isotropic, leading to diagonal self-energies in real space:

$$\langle z_i | \Sigma_{PH}^{r/\hat{<}}(\varepsilon) | z_i \rangle = K_{PH} \langle z_i | G^{r/\hat{<}}(\varepsilon) | z_i \rangle \quad (4.18)$$

where  $\langle z_i | \hat{A} | z_i \rangle$  are  $N_x \times N_m$  matrices,  $z_i$  is a point of the mesh in  $z$  direction and  $K_{PH}$  is a phonon coupling constant. In the case of acoustic phonon, it is related to the acoustic deformation potential through:

$$K_{AC} = \frac{D_{ac}^2 k_B T}{\rho v_s^2 \Delta x \Delta y \Delta z}$$

where  $\rho$  is the material density,  $v_s$  is the sound velocity and  $\Delta x \Delta y \Delta z$  is the volume of a mesh node. As the device is invariant in  $z$  direction, it is more convenient to express Eq. (4.18) in  $k$ -space:

$$\Sigma_{PH}^{r/<}(\varepsilon) = K'_{PH} \times \frac{1}{N_z} \sum_{k_z} G^{r/<}(\varepsilon, k_z) \quad (4.19)$$

where we used the fact that the self-energy in  $k$ -space is independent of  $k_z$  and equal to the self-energy in real-space. The normalization of the coupling constant transforms here as:

$$K'_{PH} = K_{PH} \Delta z \delta k$$

where  $\delta k = 2\pi/L_z$  is the step in  $k_z$ . The same derivation can be performed for intravalley optical phonon and intervalley f- and g-processes.

Note here that these equations contain the coupling between the different  $k_z$ -vectors by phonons. Even if the Green's functions are block diagonal in  $k_z$ -space, the different blocks interact at each self-consistent Born iteration through these phonon self-energies. As opposed to Ref. [246], a numerical integration over  $k_z$  is thus needed to account for electron-phonon interactions in the NEGF formalism presented and an analytic integration is not possible.

## 4.2 Poisson-Schrödinger-based QDD: linear regime

In this section, we perform simulations of a Si FDSOI PMOS structure corresponding to nowadays technological node [235]. We compare “standard” TCAD simulations accounting for empirical mobility and density-gradient (DG) models with PS-QDD simulations, where the quantum confinement normal to the channel is taken into account by solving the Schrödinger equation within the 3-band KP model, and the mobility is calculated with a KG solver with PH, LC and SR scattering models (see Section 3.1.2 in previous Chapter). The difficulty to calibrate the empirical models is pointed out and we show the need for physical-based models in industrial TCAD framework. The impact of the mobility models used in the LDD region on the overall current is also investigated, showing the difficulties to tackle physical effects with empirical models depending only on local quantities.

### 4.2.1 Device considered: FDSOI PMOS architecture

The device simulated in this section and its geometrical parameters are given in Figure 4.5, corresponding to the architecture of a FDSOI device in current technological node. The gate stack is composed of 1 nm of SiON interfacial layer (IL) ( $\epsilon = 6.6$ ) and 1.8 nm of HfO<sub>2</sub> ( $\epsilon = 20$ ), leading to an EOT of about 0.94 nm (for the so-called GO1 architecture). The metal gate workfunction is set to 4.62 eV for unstrained Si device. The channel is 6 nm thick and 24 nm long. The spacers are 6 nm long.

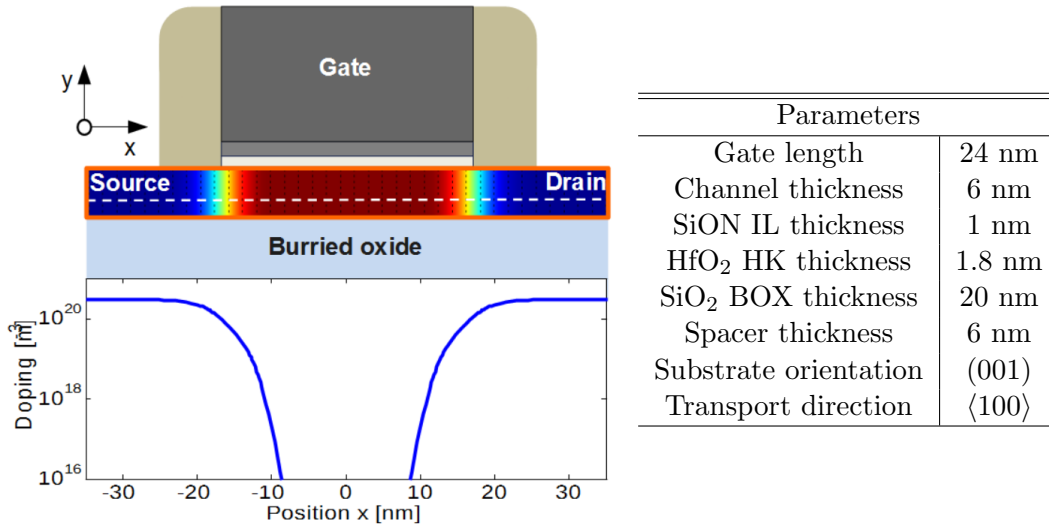


Figure 4.5. FDSOI device architecture used in this study, with a gate length  $L_g = 24$  nm. A sketch of the device is shown in the left figure, while the geometrical and physical parameters are detailed in the right table. The doping profile along the horizontal  $x$  direction is also plotted in bottom left figure. The orange rectangle shows the quantum simulation domain.

Although the width of the device was shown to affect the stress in the channel [27, 26],

it is considered infinite in this study and the equations are solved only in 2D. Indeed, the stress is considered as an input in the simulations, and the device are too wide to induce a significant quantum confinement on the carrier ( $W \approx 170$  nm). An homogeneous version of the device is considered, where the thickness is constant and equal to 6 nm in the channel but also source and drain areas (no raised source and drain contacts). The p-type doping profile along the source-drain transport direction  $x$  is depicted in Fig. 4.5 and is described by the following equation:

$$f(x) = 3 \cdot 10^{20} \frac{1}{1 + 10 \frac{x+6}{4}} \frac{1}{1 + 10 \frac{x}{1.5}}$$

where  $x$  is the direction of transport with the origin at the center of the channel and  $f(x)$  is the acceptor doping concentration in [ $\text{cm}^{-3}$ ]. This equation was used to reproduce the doping profile obtained by process simulations [280].

#### 4.2.2 Charge confinement: Poisson-Schrödinger vs Density-Gradient

To benchmark the models and study the effect of charge confinement in the direction perpendicular to the transport, the current obtained with our QDD is first compared with SDevice solver in test cases (not quantitative). Figure 4.6 shows the transfer characteristics of the FDSOI PMOS device with a constant mobility (set to  $470.5 \text{ cm}^2(\text{Vs})^{-1}$ ) and with classical and quantum approaches. The simulation is performed with the TCAD SDevice solver and the *in-house* U2OXPP solver.

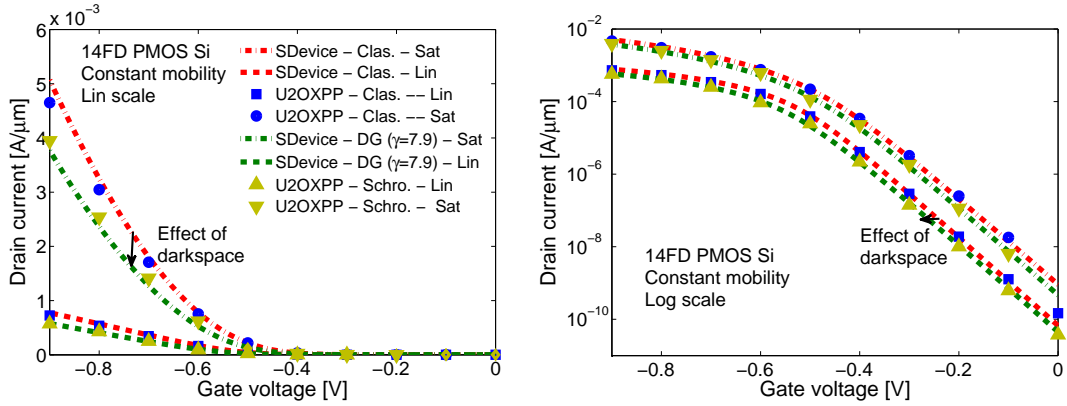


Figure 4.6. Transfer characteristics: drain current  $I_{ds}$  versus gate voltage  $V_{gs}$  in linear ( $V_{ds} = -50$  mV) and saturation regime ( $V_{ds} = -0.9$  V) with classical and quantum solvers. The SDevice and U2OXPP solvers are compared, based on different quantum correction approaches (see text). The left plot is in linear scale and the right plot in logarithmic scale.

The comparison of classical simulations allows to benchmark the solvers and validate the implementation in the *in house* U2OXPP solver. The results obtained with both solvers are very similar and give a current within  $< 7\%$  difference.

To account for quantum effects, the DG method is used in SDevice, while the resolution of the Schrödinger equation with a 3-band KP model along the confinement  $y$  direction is used in U2OXPP (with parameters given in Section 3.1.3 Table 3.3). 100 slices are typically used perpendicular to the transport direction and along the 74 nm long device. EMA model accounting for HH, LH and SO bands were also used and showed similar results, providing that the DOS mass were properly set (not shown here). In Fig. 4.6, it is found that the vertical quantum confinement in thin channels has an impact on the overall current in both linear and saturation regimes. It reduces slightly the current at high inversion and shifts the threshold voltage to more negative gate voltage, due to the decrease of the energy of the highest valence subband due to confinement.

More importantly, the distribution of the charge density is strongly affected. Figure 4.7 shows the quantum charge and current density along an homogeneous channel at high inversion ( $V_{gs} = -0.9$  V) in the case of linear ( $V_{ds} = -50$  mV) and saturation ( $V_{ds} = -0.9$  V) regime obtained with the U2OXPP PS-QDD solver with 3-band KP model.

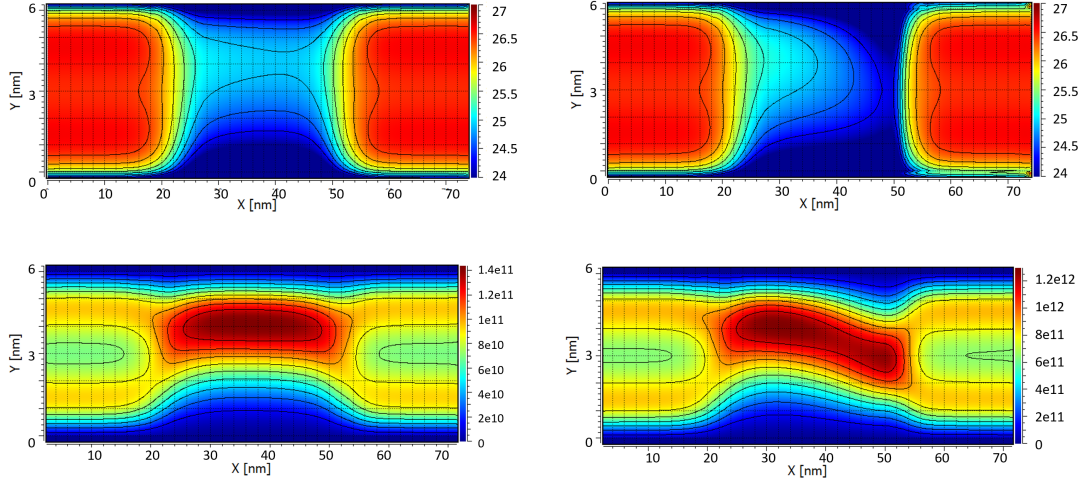


Figure 4.7. Hole charge (up) and current (down) density maps in the orange rectangular region of Fig. 4.5 at high-inversion ( $V_{gs} = -0.9$  V) in linear (left,  $V_{ds} = -50$  mV) and saturation (right,  $V_{ds} = -0.9$  V) regimes, obtained with self-consistent PS-QDD simulations. Charge density is in unit of [ $\text{m}^{-3}$ ] (log scale) and current density is in [ $\text{A}/\text{m}^2$ ].

The cut of these distributions along the confinement  $y$  direction is plotted in Figure 4.8. The maximum of charge and, as a consequence, the maximum of current density are pushed away from the Si/SiO<sub>2</sub> interface, due to the well-known dark-space effect (see Section 2.1.2). In the DG approach, this distribution is strongly dependent on the  $\gamma$  parameter entering Eq. (4.5), that needs to be fitted on PS simulations. The value used here to reproduce 3-band KP simulation ( $\gamma = 7.9$ ) is in good agreement with the one extracted by Pons *et al.* (2013) [287]. Note that this value is only valid for holes in the [001] confinement direction considered here, and needs to be adjusted for other wafer

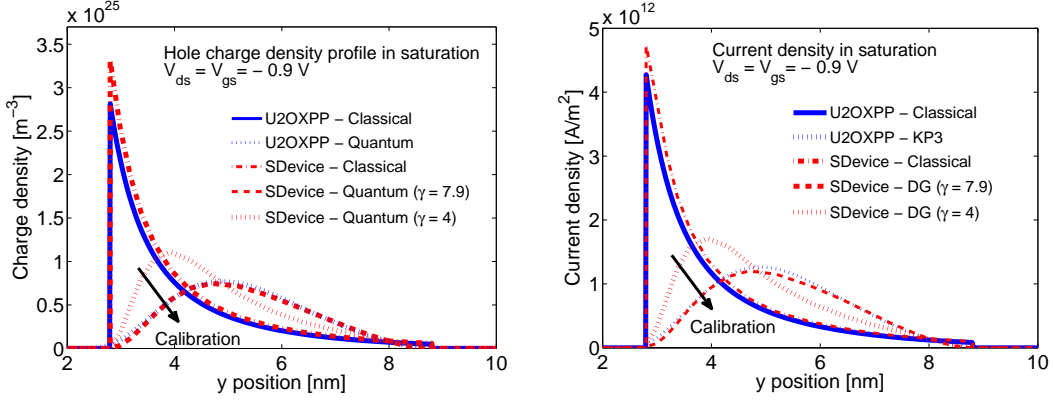


Figure 4.8. Hole charge (left) and current (right) density distributions cut in the middle of the channel in the confinement direction. The classical and quantum resolutions are compared, showing the effect of darkspace on both charge and current distributions. The arrow indicates the effect of DG calibration, when the  $\gamma$  parameter entering Eq. (4.5) is changed from 4 (default value) to 7.9 (calibrated value).

orientations, as it was shown in Ref. [287]. We found however that it doesn't depend strongly on the channel thickness and that the same  $\gamma$  value can be used for different values of  $t_{ch}$ .

### 4.2.3 Mobility: empirical models vs Kubo-Greenwood

Two empirical models are used here: the Philips Model (PhuMob) [213, 172], taking into account the PH and LC scattering in bulk materials (as function of temperature and dopant concentration) and the  $E_{normal}$  model from Takagi *et al.* (1994) [350], taking into account the effect of vertical effective field on PH and SR.

The PhuMob model describes the bulk PH- and LC-limited mobility with:

$$\begin{aligned} \mu_{PH} &= \mu_{max} \left( \frac{T}{300} \right)^{-\theta} \\ \mu_{LC} &= \left( \frac{\mu_{max}^2}{\mu_{max} - \mu_{min}} \right) \left( \frac{N_{REF}}{N_{ch}} \right)^\alpha \left( \frac{T}{300} \right)^{3\alpha-1.5} \\ &\quad + \left( \frac{\mu_{max}\mu_{min}}{\mu_{max} - \mu_{min}} \right) \left| \frac{-n-p}{N_{ch}} \right| \left( \frac{T}{300} \right)^{-0.5} \end{aligned}$$

where  $T$  is the temperature in [K], and  $\mu_{max}$ ,  $\mu_{min}$ ,  $\theta$ ,  $N_{REF}$  and  $\alpha$  are fitting parameters. The first term in  $\mu_{LC}$  takes into account the unscreened Coulomb scattering due to dopants in the channel, while the second term models the impact of screening by the inversion charge.

The  $E_{normal}$  model adds the two contributions:

$$\mu_{PH,normal} = A \left( \left| \frac{\nabla\phi}{0.1} \right| \right)^{\alpha_{PH}} \left( \frac{T}{300} \right)^{-\theta_{PH}}$$

$$\mu_{SR} = B \left( \left| \frac{\nabla\phi}{0.1} \right| \right)^{\alpha_{SR}}$$

where  $\phi$  is the local potential and  $A, B, \alpha_{PH}, \alpha_{SR}$  and  $\theta_{PH}$  are additional fitting parameters.

These scattering mechanisms are finally combined with a Matthiessen rule:

$$\frac{1}{\mu_{tot}} = \frac{1}{\mu_{PhuMob}} + \frac{1}{\mu_{Enormal}}$$

$$= \frac{1}{\mu_{PH}} + \frac{1}{\mu_{LC}} + \frac{1}{\mu_{PH,normal}} + \frac{1}{\mu_{SR}}$$

The transfer characteristics obtained on the FDSOI device with SDevice and U2OXPP solvers with the calibrated empirical models are shown on Fig. 4.9. Additional fitting corrections are included in SDevice, such as an effective doping concentration for screening of  $\mu_{LC}$  and a slightly different  $E_{normal}$  model [213], which can explain the small discrepancy observed for saturation current in linear scale, but an overall good agreement is found with both solvers. The empirical parameters used here were fitted to reproduce experimental data and can be found in Pereira (2015) [280].

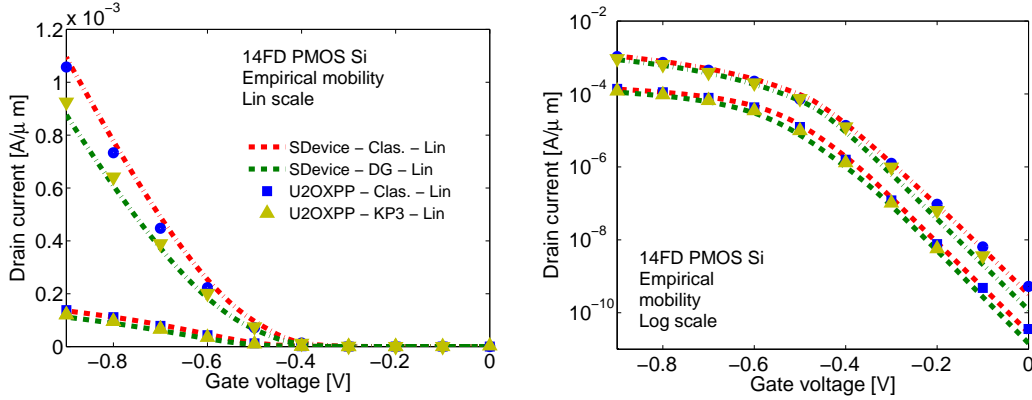


Figure 4.9. Same as Fig. 4.6 but with empirical models to compute the mobility.

The effect of the mobility model (empirical model or KG solver) is shown in Fig. 4.10. PH, LC and SR scattering mechanisms are included in both models, fitted to reproduce the mobility of long-channel bulk MOSFET devices. It is found that the current is increased when KG solver is used to compute the mobility in FDSOI PMOS device, in both the linear and saturation regimes (note that no saturation velocity was used in these simulations).

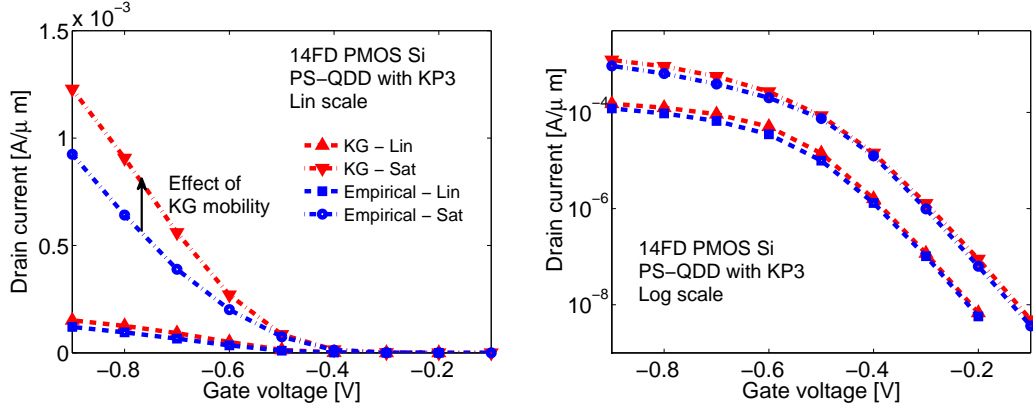


Figure 4.10. Transfer characteristics in linear ( $V_{ds} = -50$  mV) and saturation ( $V_{ds} = -0.9$  V) regime obtained with U2OXPP and using empirical models or KG solver to compute the mobility. Quantum effects are accounted for by the resolution of 3-band KP PS. The left plot is in linear scale and the right plot in logarithmic scale.

To better understand this effect, the mobility maps along the channel are shown in Fig. 4.11. In empirical models, the mobility is local and is a function of  $x$  and  $y$  positions. In KG solver, one value of mobility is resolved in each slice and a function of the transport direction  $x$  alone.

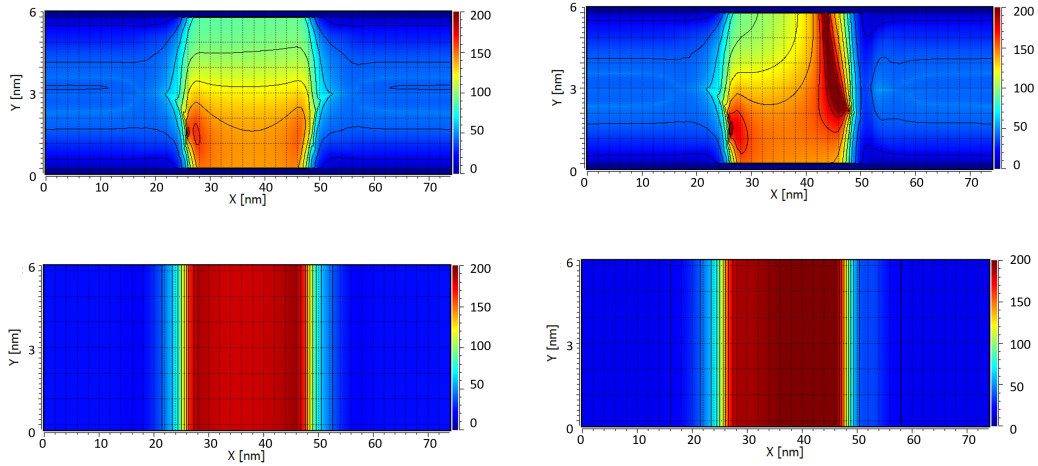


Figure 4.11. Hole effective mobility maps obtained PS-QDD simulations with empirical models (up) and KG solver (down) in the orange rectangular region of Fig. 4.5 at high-inversion ( $V_{gs} = -0.9$  V) in linear (left,  $V_{ds} = -50$  mV) and saturation (right,  $V_{ds} = -0.9$  V) regimes. The same scale is used for each plot in unit of  $[\text{cm}^2(\text{Vs})^{-1}]$ .

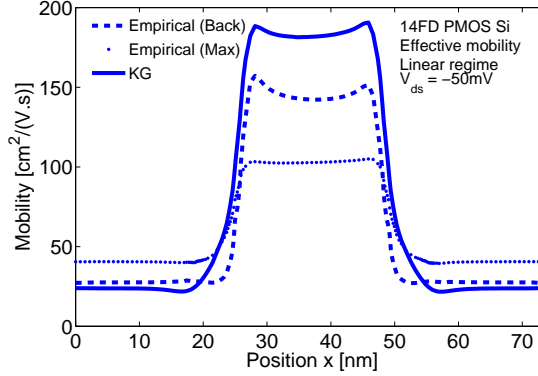


Figure 4.12. Hole effective mobility as a function of the transport  $x$  direction in the FDSOI PMOS device in linear regime, obtained with PS-QDD simulation with empirical models or KG solver. The empirical mobility are horizontally cut at different depths: at the position of the maximum of charge in the channel ( $\sim 2$  nm from the front interface) and close to the back interface ( $\sim 5$  nm from the front interface).

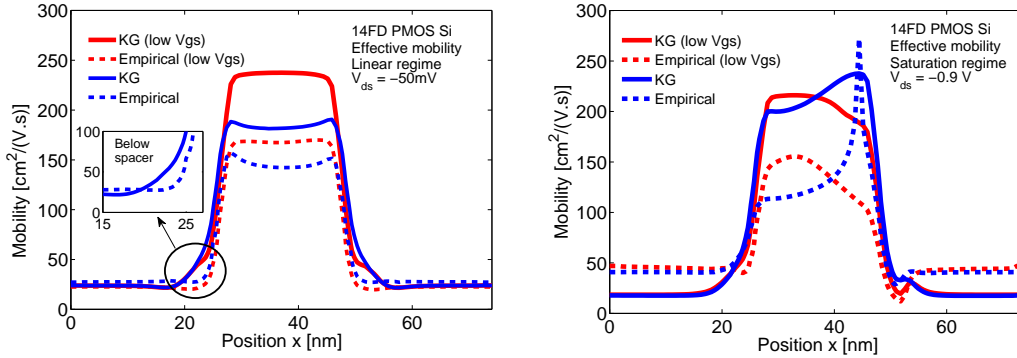


Figure 4.13. Hole effective mobility as a function of the transport  $x$  direction in the FDSOI device, in linear (left) and saturation (right) regimes, obtained with PS-QDD simulation with empirical models or KG solver. The blue lines are below threshold voltage ( $V_{gs} = -0.1$  V) while red lines are at high inversion ( $V_{gs} = -0.9$  V). A significant discrepancy is found in the region below the spacer ( $x \in [19, 25]$  nm and  $x \in [49, 55]$  nm).

The horizontal cuts of these mobility maps are plotted in Fig. 4.12 and 4.13. The different mobility models are first compared in linear regime. As stated earlier, the empirical mobility depends on the depth ( $y$  position of the cut). While the agreement with KG solver is rather good at the back interface, the mobility in the channel significantly decreases close to the interface, due to the stronger electric field (taken into account in the  $E_{normal}$  model). The mobility at the maximum of the charge, that contributes the most to the overall current, is almost half of the one obtained with KG solver. This explains

why the overall current obtained with empirical models is lower than in KG simulation (see Fig. 4.10), and shows the limitation of the empirical models in ultra-thin channels where confinement effects are not treated with physical models.

In Fig. 4.13, one notes that the mobility in the channel decreases when  $V_{gs}$  increases, for both models. However, the mobility decreases less significantly with empirical models than expected with KG calculation. In addition, in the region below the spacer ( $x \in [19,25]$  and  $[49,55]$  nm), the effective mobility variation is sharper with empirical models and closer to the channel. This can be due to an inaccurate treatment of screening by empirical models in this region, where the charge neutrality is not satisfied.

In saturation regime, the local empirical model shows a particular peak of mobility close to the drain side, as shown in Figs. 4.11 and 4.13. This discontinuity is again caused by the dependence of the  $E_{normal}$  model on electric field and is not physical.

### 4.3 NEGF vs QDD: saturation regime

In the previous section, PS-QDD model was used to model FDSOI PMOS device, including KG solver to compute the low-field effective mobility. This model can be used to accurately capture transport properties at low-field (linear regime), thus improving the description of linear current ( $I_{lin}$ ) through a physical-based model. However, to capture the saturation current correctly ( $I_{sat}$ ), the mobility at high-field needs to be modified in TCAD solvers, through the relation (3.25), which accounts for the saturation of the velocity. The saturation velocity parameter  $v_{sat}$  entering this equation needs to be calibrated and becomes an “apparent” effective parameter in nanoscale devices, accounting for both saturation velocity (through optical phonon emission) and injection velocity (ballistic top-of-the-barrier model [205]).

Moreover, the character of transport in nanoscale devices (diffusive or quasi-ballistic) is still under debate and it is not clear whether DD is still applicable in recent nodes FDSOI devices in a physical point of view [221]. In this context, a comparison between NEGF and QDD simulations through local quantities such as quasi-Fermi level, mobility and velocity can bring more direct understanding than just comparing current at terminals.

In this section, we try to answer both questions of whether DD framework can be used to model transport in FDSOI devices and of how to extract the saturation velocity from physical models [236]. For this purpose, we present a careful analysis of quantum simulations in FDSOI NMOS devices and compare results with QDD simulations.

The device architecture is the same as previous section (see Fig. 4.5), except that the doping in the source/drain contact is now of n-type (donor) and that the metal gate workfunction is set to 4.385 eV. In the NEGF simulation, the SR is described geometrically using an rms  $\Delta_{SR} = 0.37$  nm and an exponential autocorrelation function with correlation length  $\Lambda_{SR} = 1.3$  nm. Other parameters and details on the code can be found in Ref. [257]. QDD simulations are performed with our *in-house* QDD module of U2OXPP. Empirical models are used for mobility, including the PhuMob and  $E_{normal}$  models described in Sec. 4.2.3. The Schrödinger equation is solved in the EMA to compute the quantum corrections, including all  $\Delta$  valleys.

### 4.3.1 Extraction of parameters from NEGF

We present here methods used to extract the quasi-Fermi level, the empirical mobility and the velocity profiles from NEGF calculations. As these properties are not explicitly described in NEGF, they have to be deduced from the NEGF density and current.

At low  $V_{ds}$ , electrons are thermalized in the channel and the NEGF occupation factor, defined as the ratio between the occupied density of states and the total density of states (LDOS) [257], follows a Fermi-Dirac distribution along the device, as depicted on Fig. 4.14(left). It demonstrates that for low field, the concept of quasi Fermi level  $\phi_F$  is valid and can be extracted by fitting the occupation factor with a Fermi-Dirac distribution. For high  $V_{ds}$ , this method is not directly applicable, as the electrons do not thermalize within the short channel, but a fraction remain at high energy at the drain side, as shown in Fig. 4.14(right). The distribution function is thus far from an equilibrium Fermi-Dirac function, due to this “hot electrons” tail in the distribution (containing about 10% of the overall carrier density).

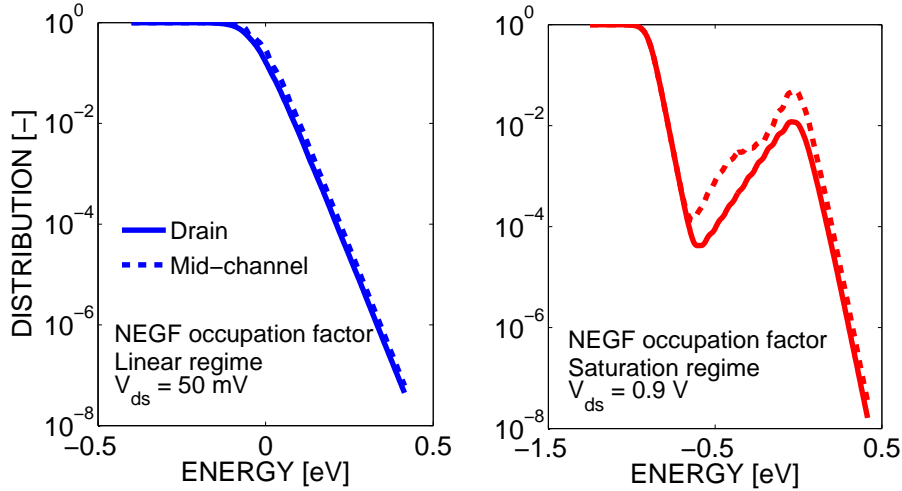


Figure 4.14. Left: NEGF occupation factor at low field ( $V_{ds} = 50$  mV), showing a Fermi-Dirac distribution. Right: NEGF occupation factor at high field ( $V_{ds} = 0.9$  V), showing a non-equilibrium distribution with a high energy tail.

Once the quasi-Fermi level  $\phi_F(x)$  has been extracted, the low-field mobility in the channel can be computed from the relation:

$$J = n\mu\nabla_x\phi_F$$

where  $J$  is the total current in [A/m],  $n$  the carrier density in [ $1/\text{m}^2$ ]. Another way to analyze the mobility consists in using DD equation, as it has been discussed in Sect. 4.1.3. Velocity profiles are finally extracted from NEGF results with the relation:

$$v(x) = \frac{J(x)}{en(x)} \quad (4.20)$$

### Linear regime

The difference in  $\phi_F(x)$  profile between purely ballistic and diffusive transport (with electron-phonon coupling) is shown in Fig. 4.15 in linear regime ( $V_{ds} = 50$  mV).

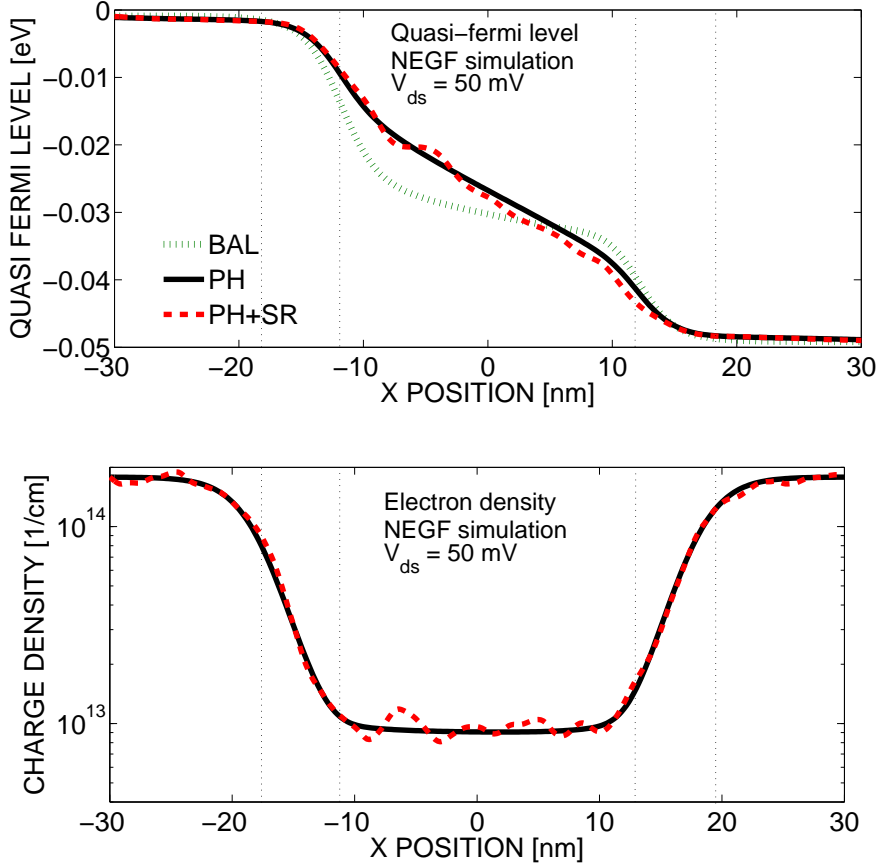


Figure 4.15. Up: NEGF quasi-Fermi level profiles along the channel ( $x$  direction) at low field ( $V_{ds} = 50$  mV) and high inversion ( $V_{gs} = 0.9$  V), without scattering, with PH or with PH+SR scattering. Down: NEGF surface carrier density  $n(x)$  with or without SR scattering. The vertical dotted lines indicate, in order from left to right, the position of: source contact, LDD left spacer, channel, LDD right spacer and drain contact.

The drop of  $\phi_F$  is a good indicator of the main resistive parts of the device. In both cases, a major drop of  $\phi_F$  is found in the near-spacer region, where the quantum resistance plays an important role [307]. In this region, there is a transition from a high carrier density over doped source/drain to a confined inversion layer in the channel. In addition, a constant-slope drop of  $\phi_F(x)$  in the channel is observed in the diffusive case, as the slope  $\phi_F(x)$  is driven there by the mobility:  $\nabla_x \phi_F \sim J/n\mu$ . This relation is not relevant in the ballistic case and  $\phi_F$  is almost flat in the channel in this case. A further investigation has been performed including SR. The corresponding  $\phi_F(x)$  and  $n(x)$  profiles

are also shown in Fig. 4.15. We see that SR does not impact significantly the shape of the  $\phi_F(x)$  profile, even though the density shows strong fluctuations along the device, as expected.

### Saturation regime

In the case of saturation regime ( $V_{ds} = 0.9$  V), the analysis of the quasi-Fermi level is less meaningful, as explained in Section 4.3.1. The  $\phi_F(x)$  and  $n(x)$  profiles in saturation regime are shown in Fig. 4.16.

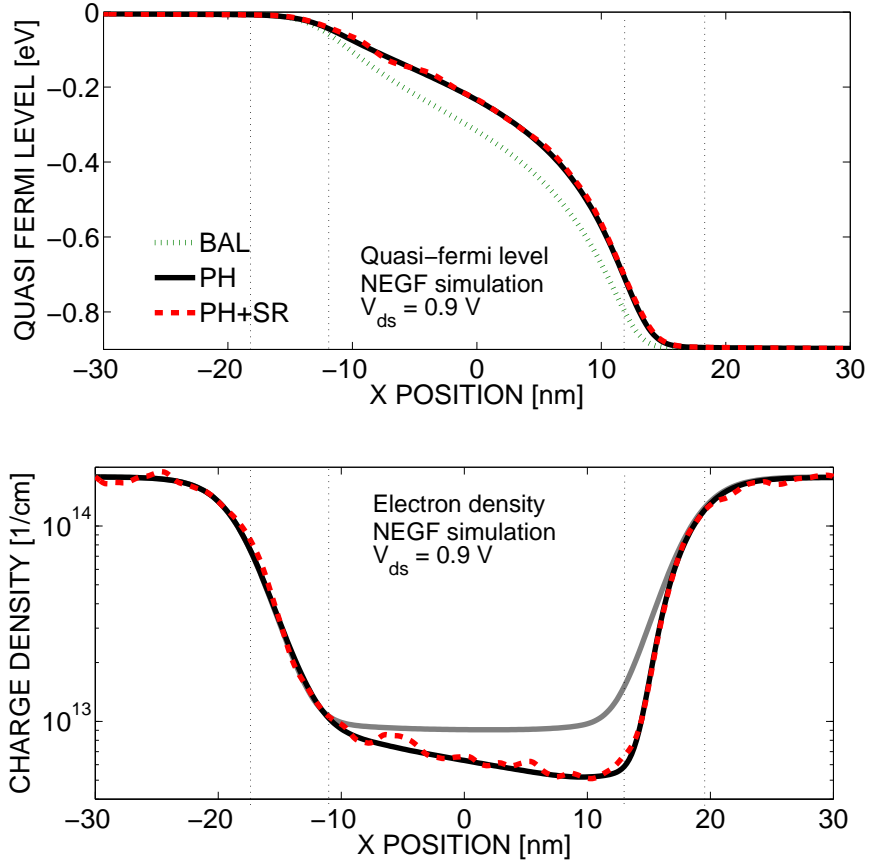


Figure 4.16. Same as Fig. 4.15 but in saturation regime ( $V_{ds} = V_{gs} = 0.9$  V). Down: the grey line also shows the electron density in linear regime with PH scattering, for comparison.

We found that the carrier density drops to low but not negligible value near the drain contact, raising a debate whether the device works in pinch-off regime or not [396] (see the discussion on the saturation mechanisms below, in Sec. 4.3.2). The inclusion of SR induces again strong charge fluctuation, but does not change significantly the behavior of  $\phi_F(x)$  profiles.

### 4.3.2 Saturation mechanisms

The overall drain current obtained with NEGF simulation with the inclusion of the different scattering mechanisms is shown in Fig. 4.17. We see that the saturation current  $I_{sat}$  varies significantly in the different simulations, implying that the different scattering mechanisms all impact  $I_{sat}$ .

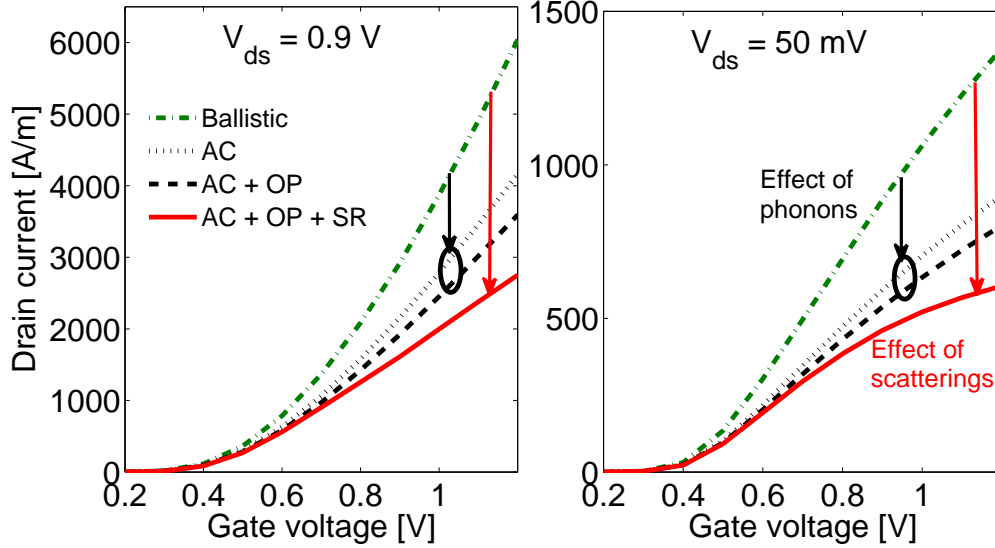


Figure 4.17. Transfer characteristics in FDSOI NMOS devices in saturation (left) and linear (right) regimes obtained with NEGF simulation with different scattering mechanisms included. The effect of elastic and inelastic phonon is shown, as well as the impact of SR.

In a nanoscale device, the current at high  $V_{ds}$  may be impacted by the different saturation mechanisms:

- Pinch-off effect, which is an electrostatic effect also present in long-channel and is due to the loss of the charge inversion close to the drain, which becomes negligible [221].
- Saturation of drift velocity through the emission of optical phonon, which was discussed in Sec. 3.2.1 and is due to the inelastic scattering of carriers. Note that when the transport is driven out of equilibrium (e.g., in regions where high electric field accelerates carriers rapidly), the velocity may locally exceed the theoretical  $v_{sat}$  [16].
- Saturation of the injection velocity close to the source (at the “top-of-the-barrier”), due to the limited number of quantum channels available (see discussion in Sec. 4.3.4). It is a band structure (or multi-subband) effect which limits the velocity in ballistic devices.

It is interesting to note that the saturation current  $I_{sat}$  in Fig. 4.17 is strongly impacted by acoustic phonons, which is an elastic scattering and impacts mainly the electrostatics.

This tends to highlight the role (and existence) of pinch-off regime in this ultra-scaled FDSOI NMOS device. However, these effects are usually not independent. For example, the inclusion of scattering mechanisms in the “top-of-the-barrier” model may also influence the role of injection velocity (see discussion in Sec. 4.3.4).

### Scattering: emission of optical phonon

Below we analyze the description of the saturation velocity by emission of optical phonons (second mechanism in the list) in the NEGF approach in long and short channels.

As it was discussed in Section 3.2.1, the velocity saturates at high field to the so-called saturation velocity (equals to  $1.07 \times 10^5$  m/s for bulk Si). We investigate here this effect with NEGF using a long channel device ( $L_g = 200$  nm) with a frozen electric field set constant along the channel and set to zero in the contacts (calculations performed by Y.M.Niquet [252]). Acoustic and intervalley phonons scatterings are included. The extracted velocities at different longitudinal fields with parabolic EMA and 2-band KP models are shown in Fig. 4.18, together with the saturation velocity extracted from Canali’s formula Eq. (3.23). It is found that the extracted  $v_{sat}$  depends on the band structure model and that the value obtained with 2-band KP ( $1.1 \times 10^5$  m/s) is in agreement with the bulk experimental value ( $1.07 \times 10^5$  m/s).

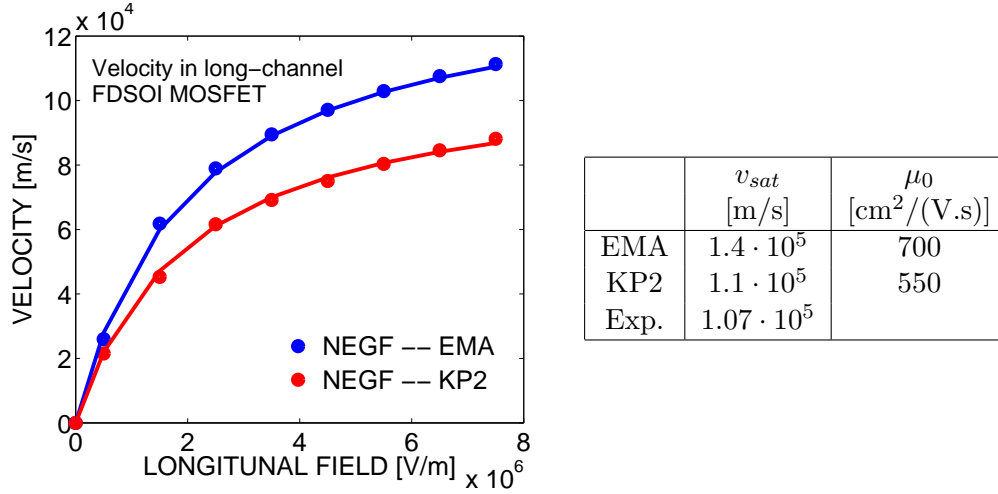


Figure 4.18. Drift velocity versus electric field in FDSOI device extracted from NEGF calculations, with two different band structure models. A long channel ( $L_g = 200$  nm) is considered with constant potential drop in the channel. The velocity in the channel is extracted from Eq. (4.20). The lines are the fits with Canali’s formula Eq. (3.23) and the parameters are given in the Table at the right.

Moreover, in ultra-scaled device at high  $V_{ds}$ , an overshoot phenomenon can be observed that consists in a local velocity  $v > v_{sat}$ . This phenomena can be seen in Fig. 4.19 where the NEGF velocity profile at  $V_{ds} = 0.9$  V extracted with Eq. (4.20) is plotted as a function

of position. One can see that, with PH scattering only, the carrier velocity increases almost linearly in the channel and reaches values two times larger than the  $v_{sat}$  obtained in long-channel. The inclusion of SR lowers the velocity in the channel and the peak value decreases from about 3 to about  $2.5 \times 10^5$  m/s.

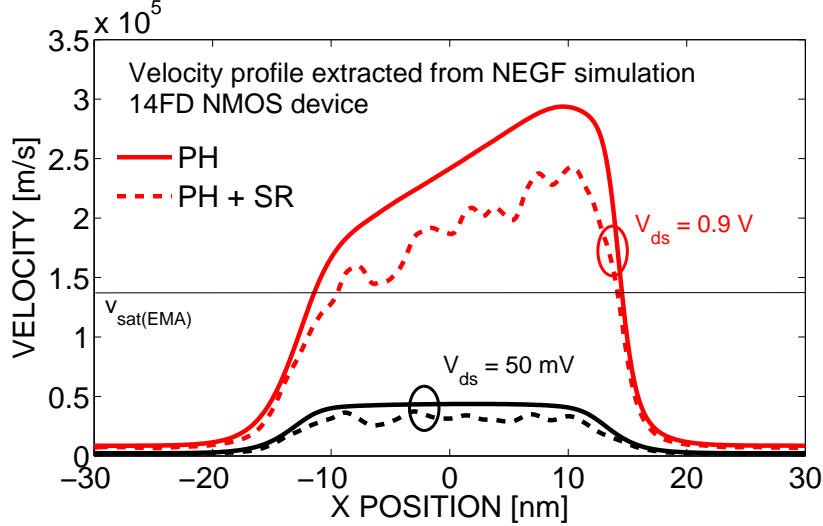


Figure 4.19. Velocity profile as a function of the position in the channel obtained with NEGF simulation in the EMA with or without SR, in linear and saturation regimes. The value of the saturation velocity in long-channel for EMA is shown and overshoot phenomenon in saturation regime is evidenced.

### 4.3.3 QDD model: mobility extraction at high-field

Now comes the question of the relevance of QDD scheme in ultra-scale devices. In this section, we compare NEGF and QDD simulations.

The  $\phi_F(x)$  profile obtained with our QDD solver at low  $V_{ds}$  is shown in Fig. 4.20(up) and compared with NEGF simulations with the same scattering mechanisms included. Despite that in NEGF the transport is treated at a quantum level, the included scattering mechanisms produce a diffusion-like transport, characterized by a nearly linear  $\phi_F$  profile in the channel, comparable to QDD simulations. A small discrepancy between the two models is found in the access region (below the spacer), where the NEGF simulations predict a steeper drop of  $\phi_F$  due to the quantum resistance [307].

A similar study at high  $V_{ds}$ , based on  $\phi_F(x)$  profile extracted from NEGF density, shows that this latter quantity is also comparable to the QDD one (see Fig. 4.20(down)). Although this quantity has not a clear physical signification in the case of out-of-equilibrium transport, it is essential in the application of QDD model. One can argue that QDD model could describe the transport in saturation regime, provided that the quantum and non-equilibrium properties are correctly extracted from more advanced simulations. In

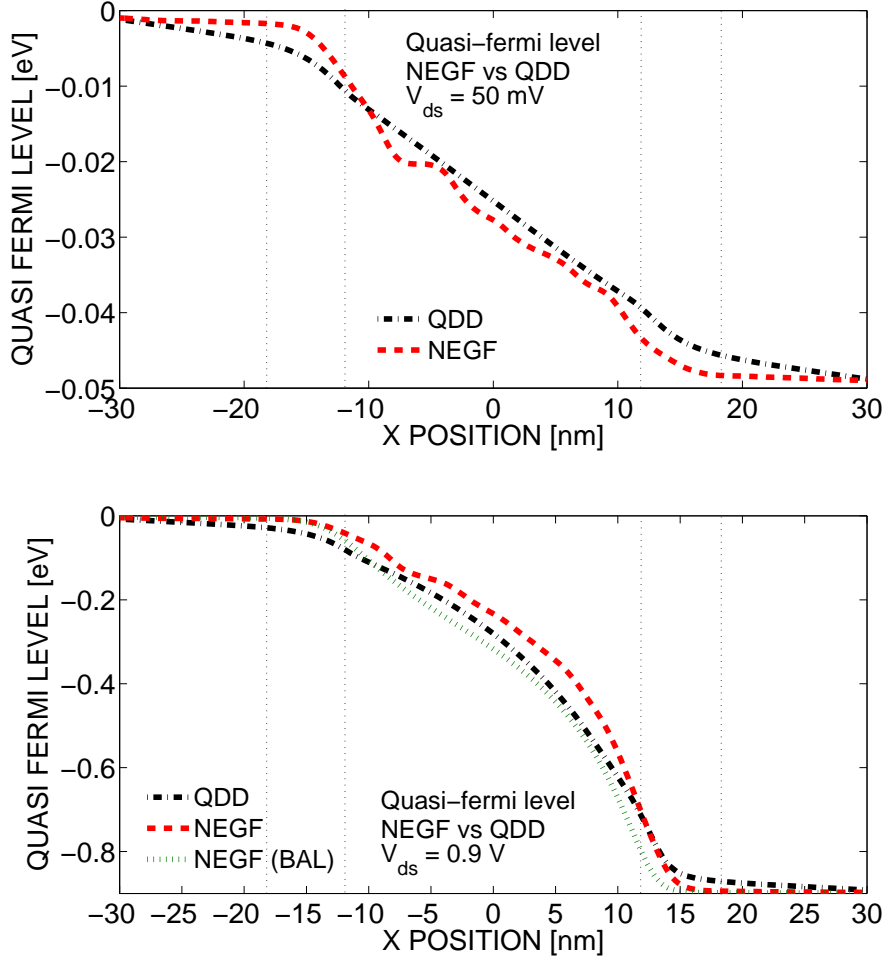


Figure 4.20. Quasi-Fermi level profile obtained with NEGF in linear (Fig. 4.15(up)) and saturation (Fig. 4.16(up)), compared with the ones obtained with QDD approach, including PH, SR and IL scattering mechanisms with empirical models (PhuMob +  $E_{normal}$ ).

Sec. 4.1.2, we proposed a method to go in this direction, by extracting an “apparent” local mobility from simple NEGF simulations. We apply this method below to an FDSOI NMOS device, from uncoupled modespace simulation including scattering with AC and OP phonons in the U2OXPP software.

The mobility extracted from the NEGF current with the method exposed in Sec. 4.1.2 is shown in Fig. 4.21. We note here that this is valid only in the presence of electron-phonon interaction, where the concepts of quasi-Fermi and mobility can be recovered (which do not make sense in a pure ballistic solver). It is stressed here that the concept of “apparent” mobility in this method is a local parameter driven by the DD equations and differs from the empirical mobility computed by scattering rates for example. In Fig. 4.21(right), the

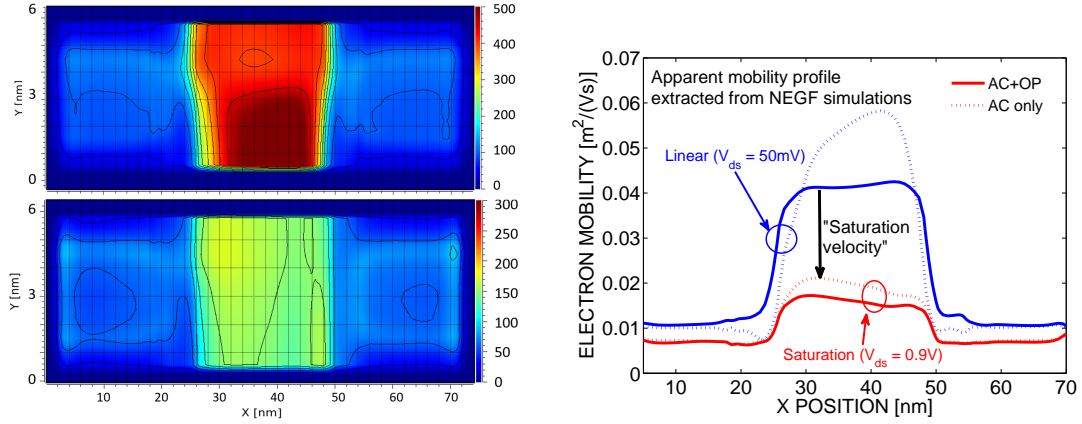


Figure 4.21. Left: “Apparent” position-dependent mobility extracted from NEGF current (uncoupled modespace approach with AC + OP phonon included) at  $V_{ds} = 50$  mV (up) and 0.9 V (down). Values in the colorbar are in unit  $[\text{cm}^2/(\text{V}\cdot\text{s})]$ . Right: horizontal cut in the middle of the channel.

drop of the mobility at high field in the channel is clearly seen, due to the saturation of the velocity which is intrinsically taken into account in NEGF simulations when PH scattering is included.

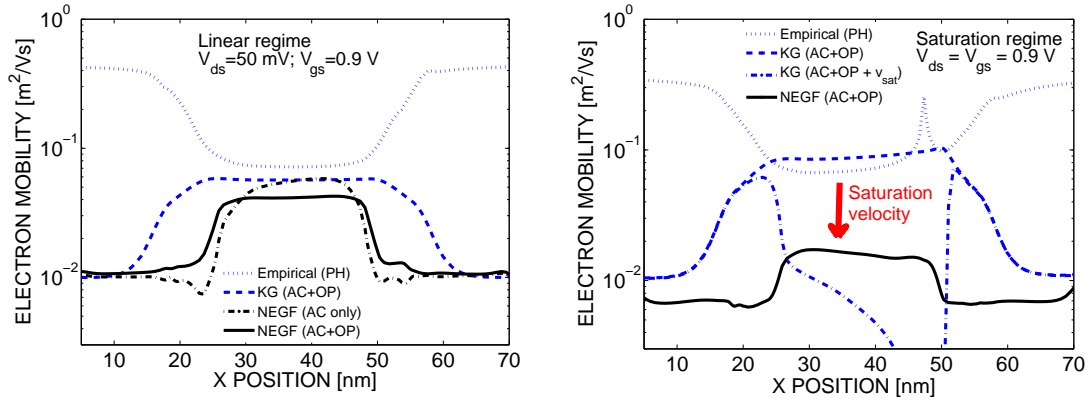


Figure 4.22. “Apparent” position-dependent mobility extracted from NEGF current at  $V_{ds} = 50$  mV (left) and 0.9 V (right).

The PH-limited mobility extracted with this method is compared with the values calculated with KG and empirical methods in Fig. 4.22. While similar results are obtained in the channel at low  $V_{ds}$ , the mobility in the channel is higher with KG and empirical models at high  $V_{ds}$ , due to the lack of saturation of the velocity. In the linear regime

(Fig. 4.22(left)), one notes that the KG and “NEGF” mobilities are also very similar in the source/drain regions. In the region below the spacer, the KG method gives a mobility higher than the extraction from NEGF current, because the quantum resistance of this region is recast in this last one. The mobility obtained with empirical models differs significantly from the two other methods in the source/drain regions, where it increases instead of decreasing. In these regions, the normal effective field induced by the gate is very low, while the carrier density increases of several orders of magnitude due to the doping. As the semiconductor is strongly degenerate but the confinement is lower, the KG mobility decreases due to the occupation factor and the higher density-of-state. This effect is not accounted for in empirical models, that depends only on the normal electric field<sup>1</sup>.

The same effect is observed in saturation regime in Fig. 4.22(right). Moreover, the effect of saturation velocity model (Eq. (3.23)) on the KG mobility is shown. This empirical model induces a decreasing mobility in the channel, dropping to values below  $10^{-2} \text{ cm}^2/(\text{Vs})$  close to the drain. On the other hand, the “apparent” mobility extracted from NEGF simulation saturates uniformly (non-local model).

#### 4.3.4 Ballistic effects: quantum resistance and injection velocity

In short-channel devices, the experimental “effective” mobility extracted from, e.g., split-CV methods, has been found to decrease with the gate length of the device [110]. This effect has been studied in several works and different explanations exist in the literature.

One of the reasons may be the ballistic resistance of the channel. Kim *et al.* (2013) [168] and Kotlyar *et al.* (2015) [174] suggested to use an “apparent” mobility to take into account ballisticity in DD solver, obtained by a simple Matthiessen rule:

$$\frac{1}{\mu} = \frac{1}{\mu_{bal}(L)} + \frac{1}{\mu_{scat}}$$

where  $\mu_{bal}(L)$  is the ballistic mobility in the channel, which is a linear function of the gate length  $L$  and can be computed analytically (see below).

In this section, we present simple analytic models to analyze the ballistic current in the low-field regime (governed by the ballistic mobility or, equivalently, the “quantum” resistance), but also the high-field regime (governed by the injection velocity). While models have been proposed to include the first effect in DD framework [44], we show that the inclusion of the second effect at high-field is more difficult and may require models such as the one of Ref. [336] or the MS-NEGF-based QDD scheme presented above.

In ballistic regime, the drain current can be obtained from the difference between Fermi-Dirac distributions at source and drain:

$$I_{ds} = -\frac{2eW}{(2\pi)^2} \int_{v_x > 0} d^2k (f_S(\mathbf{k}) - f_D(\mathbf{k})) v_x(\mathbf{k}) \quad (4.21)$$

---

<sup>1</sup>Note that LC-limited mobility will be dominant in these regions and that this effect will not affect significantly the results at the end.

where  $W$  and  $L$  are the width and length of the device,  $f_S$  and  $f_D$  are the Fermi-Dirac distribution function evaluated at the source and drain, respectively, and  $v_x$  is the drift velocity of carrier along the transport direction  $x$ .

In the case of low  $V_{ds}$  (linear regime), one can approximate:

$$f_S - f_D \simeq -eV_{ds} \frac{\partial f}{\partial \mathcal{E}}$$

The ballistic resistance of the channel can then be written as:

$$\frac{1}{R_{bal}} = \frac{I_{ds}}{V_{ds}} = \frac{2e^2W}{(2\pi)^2} \int_{v_x > 0} d^2k v_x(\mathbf{k}) \frac{\partial f}{\partial \mathcal{E}} \quad (4.22)$$

In the case of EMA, this expression can be further simplified to:

$$\frac{1}{R_{bal}} = \frac{\sqrt{\pi m_y^* k_B T} e^2 W}{\sqrt{2\pi^2 \hbar^2}} \mathcal{F}_{-1/2}(\eta) \quad (4.23)$$

where  $m_y^*$  is the effective mass along the transverse direction  $y$  and  $\eta = \frac{\mathcal{E}_F - \mathcal{E}_n}{k_B T}$ . From this expression, one can derive the ballistic mobility:

$$\mu_{bal} = \frac{L}{eQ_{inv}WR_{bal}} = \frac{eL}{\sqrt{2\pi k_B T m_x^*}} \frac{F_{-1/2}(\eta)}{F_0(\eta)} \quad (4.24)$$

where  $Q_{inv} = \frac{\sqrt{m_x^* m_y^* k_B T}}{\pi \hbar^2} \mathcal{F}_0(\eta)$ .

The ballistic resistance computed in a Si FDSOI device with different channel thickness obtained with the Eq. (4.22) is plotted in Fig. 4.23, for the case of electrons and holes. It corresponds to the ballistic resistance of a long-channel, without accounting for access region.

It is found that the ballistic “quantum” resistance doesn’t depend strongly on the channel thickness and is well described by a simple formula (derived from Eq. (4.23) in the case of Maxwell-Boltzmann statistics):

$$R_{bal}W = \frac{\sqrt{2\pi k_B T m_x^*}}{e^2 Q_{inv}} \quad (4.25)$$

However, it was found in Rideau *et al.* (2014) [307] that this quantum resistance (or ballistic mobility) of the channel is not enough to explain the decrease of mobility with the gate length observed in measurements. From the NEGF investigation in Sec. 4.3, we found that the near-spacer regions are very resistive and contribute to about 50% of the total resistance in the device considered at low  $V_{ds}$ . Their contributions, as well as the quantum resistance of the channel  $R_{bal}$ , are independent on the length of the device and are both included in the “access” resistance  $R_{acc}$  [34]. Both contributions also depend on the overdrive voltage  $V_{gt} = V_{gs} - V_{th}$  (although the threshold voltage  $V_{th}$  relevant in these two contributions might be different). We may conclude here that the apparent mobility drop in short-channel is mainly due to the near-spacer region, where both quantum resistance

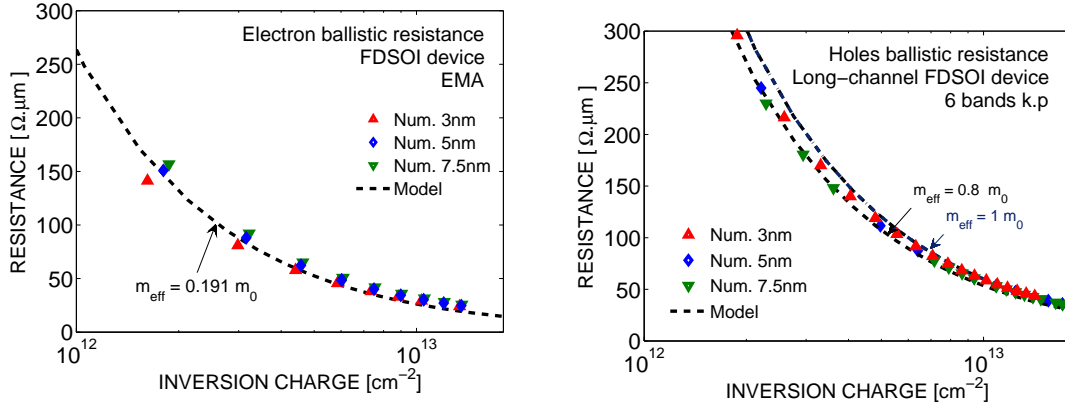


Figure 4.23. Ballistic “quantum” resistance of long-channel for electrons (left) and holes (right) computed with EMA and 6-band KP models, respectively. Symbols are numerical calculations with Eq. (4.22) while lines are plotted with a simple model (Eq. (4.25)). [307]

and scattering with ionized impurity impact the carrier transport. This was also confirmed in the detailed analysis of the role of scattering mechanisms in the near-spacer regions and of the access resistance in Ref. [34].

In our second QDD model, the ballistic mobility is taken into account directly in the quantum MS-NEGF resolution. The extracted “apparent” mobility thus contains both ballistic and phonons contributions and additional empirical models can be added with a Matthiessen rule:

$$\frac{1}{\mu_{\text{tot}}} = \frac{1}{\mu_{\text{app}}} + \frac{1}{\mu_{\text{LC/SR}}}$$

In this way, the resistive part of the near-spacer region may be correctly treated. However, the self-consistent resolution of the MS-NEGF-based QDD scheme with the inclusion of other scattering mechanisms through Matthiessen rule (such as LC and SR) has still to be further investigated and will be discussed in the perspective of this work (see Sec. 5.3).

Now, let’s consider the case of saturation regime (high  $V_{ds}$ ). We can make a similar derivation from the expression of current in Eq. (4.21). In this case, one make the approximation that all carriers flow from the source to the drain (the barrier is too high for the carriers to scatter back from the channel to the source). As a result, the current now becomes:

$$I_{ds} = -\frac{2eW}{(2\pi)^2} \int_{v_x > 0} d^2k f_S(\mathbf{k}) v_x(\mathbf{k}) \quad (4.26)$$

The injection velocity (for one subband) can thus be expressed as:

$$v_{inj} = \frac{I_{ds}}{en_s^+} = \frac{2 \int_{v_x > 0} d^2k f_S(\mathbf{k}) v_x(\mathbf{k})}{\int d^2k f_S(\mathbf{k})} \quad (4.27)$$

where  $n_s^+ = n_s/2$  is the density of forward-directed electrons (with positive velocity). In the case of EMA ( $m^* = m_x^* = m_y^*$ ) and Maxwell-Boltzmann statistics, it can be resumed

to the simple model:

$$v_{inj} = \sqrt{\frac{2k_B T}{m^* \pi}}$$

This formula can be used to have a crude approximation of the injection velocity value in a Si channel:  $v_{inj} \simeq 1.2 \times 10^5$  m/s, with a transport effective mass  $m^* = 0.19m_0$ .

As discussed in Sec. 4.3.2, the injection velocity is a key parameter for the current saturation mechanism in ballistic devices. For short-channel devices, the virtual-source model is very often used [205], where the saturation current in the channel is given as a function of the injection velocity at the top-of-the-barrier, where the potential reaches a maximum (zero transverse electric field):

$$I_{ds,sat} = C_{ox} (V_g - V_t) v_{inj} \frac{1 - r}{1 + r}$$

The last term in this equation accounts for scatterings that may occur in the so-called  $k_B T$ -layer, i.e., the region close to the top-of-the-barrier where the carriers can still scatter back to the source. The back-scattering coefficient  $r$  is usually written as function of the mean-free-path of carriers  $\lambda$  and the length of the  $k_B T$ -layer  $L_{kT}$  [208]:

$$r = \frac{L_{kT}}{L_{kT} + \lambda}$$

This term will have an impact on the quasi-ballistic saturation current in nanoscale devices, showing that the inelastic scattering mechanisms influence the saturation current, not only through the saturation velocity caused by emission of optical phonon, but also through an effective modification of the injection velocity in ballistic devices.

In our second QDD model, the injection velocity is also taken into account in the quantum MS-NEGF resolution and depends on the band structure considered in the calculations. As the value of injection velocity is generally close to the optical-phonon saturation velocity, these two mechanisms are difficult to distinguish.

## 4.4 Conclusion of the Chapter

In this Chapter, the device performances of a template FDSOI MOSFET device were investigated, by mean of QDD and NEGF models. The nature of electron transport in nanoscale device was studied and the assumptions in QDD models were discussed. Physical-based QDD models were presented, in two different approaches:

- “1.5D” PS-QDD approach, including the resolution of the Schrödinger equation in 1D slices and a KG solver for the calculation of the low-field effective mobility;
- MS-QDD approach, including the resolution of uncoupled modespace NEGF equation and accounting for saturation mechanisms such as injection velocity and electron-phonon inelastic interactions.

It was pointed out, that at low  $V_{ds}$ , the transport in the FDSOI device considered remains mainly diffusive, while at high  $V_{ds}$  the transport is driven out-of-equilibrium and about 10% of carriers remain highly energetic at the drain contact.

This study finally showed that the three saturation mechanisms listed in Sec. 4.3.2 are generally dependent on each other and may all contribute to some extent to the overall saturation current in FDSOI devices. This makes it particularly challenging to derive a simple model for high-field transport, that can be used in TCAD model to compute  $I_{ds,sat}$  without empirical and fitting parameters. Our attempt to improve the predictive power of TCAD solvers at high-field implies here the resolution of quantum transport equation through the NEGF framework, in order to extract transport parameters. The 1D resolution of this equation in the uncoupled modespace approach is not significantly more numerically expansive than the resolution of the Schrödinger equation, but limits the study to homogeneous channels without raised source/drain. Moreover, the SR and LC scattering mechanisms cannot easily be included in the NEGF simulation without increasing considerably the numerical cost of the simulation. They need thus to be included via empirical or KG models, in the self-consistent MS-QDD scheme.

## Chapter 5

# General conclusion of the thesis

“I am certain our children or grandchildren will not be using silicon [. . .]  
The world is large; there must be a better material.”  
Chenming Hu, quoted in Ref. [343]

“GaAs material is the material of the future, and will always remain so”  
Old adage, quoted in, e.g., Refs. [212, 32]

### 5.1 Summary

During this PhD, a variety of different numerical tools were used, and sometimes modified when needed, in order to compute the electronic and transport properties in devices made of SiGe and InGaAs channel materials. One purpose of this PhD was to investigate the properties of InGaAs and SiGe materials, such as their band structure, effective mobility and traps density, as presented in the first three Chapters. One other purpose of this PhD was to participate in the development of an industrial simulation framework, in a “light” physical-based approach, allowing the improvements of the predictive power of conventional TCAD solvers. This was done continuously during the PhD, and an example of application is shown in Chapter 4.

Full-zone empirical models were used to compute the band structure (namely EPM, TB and full-band KP models) and related quantities (density-of-states and effective masses). It was found that the parameterizations available in the literature generally reproduce well experimental data and give coherent positions of the band gap and effective masses of these materials. While the positions of satellite valleys in InAs and  $\text{In}_{0.57}\text{Ga}_{0.43}\text{As}$  materials remain controversial, the general trend predicts them about 1 eV higher than the conduction band edge, which means that satellite valleys should not contribute significantly to transport in these materials. The analysis of gate capacitance measurements at low-temperature of  $\text{In}_{0.57}\text{Ga}_{0.43}\text{As} / \text{Al}_2\text{O}_3$  MOSCAPs with an EOT of  $\sim 4$  nm also indicates that only the  $\Gamma$  valley is populated up to an overdrive voltage of 3 V. Two parameterizations for full-zone KP models were also derived for InAs and GaAs.

The effect of the non-parabolicity of the  $\Gamma$  valley of III-As was investigated with atomistic TB and simpler NP-EMA models. In agreement with previous studies, it was found that the non-parabolicity strongly impacts the gate capacitance in both bulk and UTBB

MOSCAPs. The gate capacitance can be doubled compared to parabolic EMA calculations in the case of InAs thin films with ultra-scaled EOT (0.43 nm). However, the gate capacitance value generally remains well below the ones of Si (for the same EOT), due to the low density-of-states of the  $\Gamma$  valley. Higher capacitance values are only achievable when satellite valleys are populated in GaAs thin films. It was also found that the NP coefficient used in NP-EMA models needs to be boosted in III-As thin films in order to reproduce the energy levels obtained with TB.

A small signal analysis model was used to compute the gate capacitance at different frequencies, which was compared to experimental data. The capture and emission rates parameters were computed within a multi-phonon approximation approach and included in a Poisson-Schrödinger solver. Such model could theoretically reproduce the gate capacitance and give insight on the traps distribution, based on a detailed knowledge of the defect properties. However, the defects at the  $\text{In}_{0.57}\text{Ga}_{0.43}\text{As} / \text{Al}_2\text{O}_3$  interface are still under heavy investigation and the knowledge of their properties remains uncertain. It is thus difficult to gain outputs from such an analysis, that uses microscopic properties (such as the lattice relaxation and charge transfer) to compute macroscopic quantities (gate capacitance).

For the transport properties, physical-based models based on the linearization of the Boltzmann transport equation, referred to as the “Kubo-Greenwood” approach, were used to compute the low-field effective mobility. The effective mobility in thin InGaAs and SiGe films was compared with experimental data. These models were also included in a Quantum-corrected Drift-Diffusion (QDD) solver, to compute the current in an FDSOI pMOS device with Si channel. It was found that the empirical and the Kubo-Greenwood approaches differ qualitatively in the region below the spacer, where the doping profile changes significantly, together with the free charge distribution. This also affects the current in both linear and saturation regime.

In the case of SiGe nanowires, the electron mobility in long-channels was investigated in the absence of stress with atomistic models going beyond the deformation potential theory. An abrupt change of mobility was found at the transition point, where the origin of the lowest conduction subbands changes from  $\Delta$  to L valleys. This abrupt change is directly linked with the band structure and the abrupt change of effective mass. It depends on the nanowire orientation and the mobility decreases in  $\langle 001 \rangle$  nanowires, while it increases in  $\langle 110 \rangle$  and  $\langle 111 \rangle$  nanowires.

The high-field transport in Si and SiGe nanowires was also investigated through the resolution of the homogeneous stationary Boltzmann transport equation. It was found that the saturation velocity in small nanowires is close to the bulk value, and that the threshold field and the drift velocity behavior are strongly affected by the confinement. In particular, a peak value is observed in  $\langle 110 \rangle$  nanowires, after which the velocity decreases, due to valley transfer.

Finally, a full-quantum solver and a QDD approach were used to compute the current characteristics in an FDSOI nMOS device and to analyze in detail the saturation mechanisms in current technological node devices. It was found that, while the current remains mainly diffusive in the linear regime, far from equilibrium transport occurs at high  $V_{ds}$ . This makes the saturation current difficult to describe in a drift-diffusion framework. A

model, based on the resolution of a mode-space Green's function approach, was proposed, that could be used in an industrial TCAD framework and improve the predictive power in the saturation regime.

## 5.2 Contributions

All along this PhD, several implementations have been made in STMicroelectronics' solver UTOX, as well as in CEA's solver TB\_Sim. The main implementations were made in order to add models specific to InGaAs and SiGe materials, such as non-parabolic corrections for the EMA model, the 8-band KP model and additional terms in the 30-band KP Hamiltonian and the scattering through Fröhlich interactions and alloy disorder. Some additional features were also added, such as the resolution of the Boltzmann transport equation for the computation of the high-field drift velocity and the inclusion of the mode-space model with phonon interactions in the quantum-corrected drift-diffusion model. Other features were implemented but not used in this work, such as the resolution of the Schrödinger equation in 2D in the multi-band KP models. Finally, the performances of the UTOXPP solver on Windows and Linux machines were tracked and improved through Google regression tests and Valgrind tool, for the improvement of the code efficiency.

The models used in Chap. 2 for capacitance simulation and the influence of traps were implemented in previous work and were only used in this work, without further implementation, except for the inclusion of non-parabolic corrections.

Although some models existed in the literature previously (NP-EMA, 8-band KP, polar-optical phonon scattering), some of these implementations allow to perform innovative simulations and bring additional understanding of physical phenomena present in nanoscale transistors. The inclusion of Kubo-Greenwood model in a QDD solver allows to improve the description of transport at low-field and was also adopted recently by commercial tools, such as GlobalTCAD solutions. The resolution of open-boundary Schrödinger equation within a QDD solver allows to simulate source-drain tunneling effects in thick channels at high drain to source voltage, which was not possible with previous QDD solvers. The resolution of BTE equation in an atomistic approach allows to investigate the effect of full-band phonon scattering on the saturation velocity in long-channel devices. The inclusion of alloy disorder in this approach also allows to simulate SiGe materials and compare the influence of alloy disorder and phonon scattering.

Moreover, the ability to access a variety of different approaches, allowed to compare and to give a status on state-of-the-art solvers, which was given, e.g., in Chap.1 for the band structure of III-As materials.

## 5.3 Perspectives

As stated in the Introduction of this document, SiGe and InGaAs are considered as alternative solutions to Si channels, in order to boost the ON-current and decrease the supply voltage and power consumption. At the time of writing this document, pMOSFET devices with SiGe channel materials are starting to emerge in the market for logic applications.

InGaAs channels are still considered as potential candidates for nMOSFETs and a number of papers are published continuously on the topic.

While the field of research is continuously improving and the performances of InGaAs MOSFETs are close to Si MOSFETs, the gain in performances achievable seems to be yet too low to overcome the cost to introduce them into a production plant. Considering the small window of potential applications, it is likely that InGaAs MOSFETs will not replace the mass production of Si MOSFETs in CMOS fabs. However, these technologies might have some applications for ultra-low-power devices, as well as radio-frequency transistors.

We can think of several future studies that can be performed on the topics addressed during this PhD.

First, the quantum-corrected drift-diffusion tool developed partially during this PhD and used to simulate an FDSOI device with Si channel could be used to simulate devices with other architectures and channel materials. We believe that the physical description included in the quantum-corrected drift-diffusion model would allow simulating the current characteristics in a predictive manner and comparison of the performances of devices made with different materials and architectures.

Considering the bulk band structure, intensive *GW* calculations could be performed on top of Hartree-Fock or Hybrid Functional DFT calculations in order to study in more details the band structure of InAs materials.

With regards to the knowledge of the traps distribution, the Deep-Level Transient Spectroscopy (DLTS) study performed by an experimental team at CEA-LETI could be analyzed in greater detail in order to gain more knowledge about the traps in the semiconductor or close to the interface and their capture cross-sections and positions in energy. Other experimental techniques, such as  $1/f$  and Random Telegraph Noise (RTN) studies, should be explored to analyze the traps in the oxide or at the interface above the conduction band edge of the semiconductor.

Finally, regarding the transport models, the atomistic approach could be extended to include the description of polar-optical phonons and thus the mobility in III-V materials could be modeled. This would allow the study of the effect of confined phonon band structure on this mechanism. The resolution of the Boltzmann transport equation could also be applied to these materials, to model the drift velocity at high field and study the effect of confinement on the saturation velocity.



# Appendix A

## Parameters for band structures models

### A.1 $\mathbf{k} \cdot \mathbf{p}$ models

#### A.1.1 *Low order models*

For many III-V materials, the lowest conduction band lies at the  $\Gamma$  point. For this reason, 8-band KP model is widely used to study III-V materials, which extends the 6-band KP model for the valence band discussed in Chapter 1. However different formulations of the 8-band KP Hamiltonian exist in the literature, based on different renormalization and different set of basis states used (e.g. Kane [156], Bahder [19] and Gershoni [109]). The formulation used in this work is detailed here and preserves the conduction and valence band effective masses, predicted from the Luttinger-Kohn 6-band KP model.

#### 8-band KP theory

Kane exposes for the first time a 4-band (no SO) KP model accounting for 3 degenerated valence bands (heavy holes, light holes and split-off) and 1 degenerated conduction band in  $\Gamma$ . In this work, the 8-band KP matrix (with SO coupling) is written in the set of basis states  $|S\rangle$ ,  $|X\rangle$ ,  $|Y\rangle$  and  $|Z\rangle$  and given by <sup>1</sup>:

$$H^{4 \times 4} = \begin{bmatrix} A'k^2 & iPk_x & iPk_y & iPk_z \\ -iPk_x & L'k_x^2 + M(k_y^2 + k_z^2) & N'k_xk_y & N'k_xk_z \\ -iPk_y & N'k_xk_y & L'k_y^2 + M(k_x^2 + k_z^2) & N'k_yk_z \\ -iPk_z & N'k_xk_z & N'k_yk_z & L'k_z^2 + M(k_x^2 + k_y^2) \end{bmatrix}$$

where the quadratic coupling term have been omitted ( $B = 0$ ). To account for band offset

---

<sup>1</sup>Note that we choose to include the factor  $\hbar^2/(2m_0)$  in the parameters given, so that all parameters here are in units of  $[\hbar^2/(2m_0)]$ .

between valence and conduction band the following matrix has to be added to  $H^{4 \times 4}$ :

$$H_{BO} = \begin{bmatrix} E_c & 0 & 0 & 0 \\ 0 & E_v + \frac{\hbar^2}{2m_0} & 0 & 0 \\ 0 & 0 & E_v + \frac{\hbar^2}{2m_0} & 0 \\ 0 & 0 & 0 & E_v + \frac{\hbar^2}{2m_0} \end{bmatrix}$$

Due to the conduction-valence band coupling, the so-called Dresselhaus [75] parameters L, M, N entering in the Hamiltonian  $H^{4 \times 4}$  are modified as follow:

$$\begin{aligned} L' &= -(\gamma'_1 + 4\gamma'_2 + 1) = L + \frac{E_p}{E_g} \\ M' &= -(\gamma'_1 - 2\gamma'_2 + 1) = M \\ N' &= -6\gamma'_3 = N + \frac{E_p}{E_g} \end{aligned}$$

where the  $\gamma'$ 's are the modified Luttinger parameters <sup>2</sup>:

$$\begin{aligned} \gamma'_1 &= \gamma_1 - \frac{E_p}{3E_g} \\ \gamma'_2 &= \gamma_2 - \frac{E_p}{6E_g} \\ \gamma'_3 &= \gamma_3 - \frac{E_p}{6E_g} \end{aligned}$$

$E_p$  is the optical matrix parameter. The conduction mass  $m_c$  is also changed with:

$$A' = \frac{1}{m_c} - \frac{2E_p}{3E_g} - \frac{1}{3} \frac{E_p}{E_g + \Delta_{SO}} = \frac{1}{m_c} - E_p \frac{E_g + \frac{2}{3}\Delta}{E_g(E_g + \Delta)}$$

For the valence bands, effective masses in different direction are related to Luttinger parameters (or, with the convention used above, the modified parameters) by the relations:

$$\begin{aligned} \frac{1}{m_{100}} &= \gamma_1 \pm 2\gamma_2 \\ \frac{1}{m_{111}} &= \gamma_1 \pm 2\gamma_3 \\ \frac{1}{m_{110}} &= \gamma_1 \pm \sqrt{\gamma_2^2 + 3\gamma_3^2} \end{aligned}$$

---

<sup>2</sup>Note that for example Bahder [19] uses a different convention, in which the spin-orbit parameter is included: replacing  $3E_g \rightarrow (3E_g + \Delta)$  in each denominator in these expressions.

Moreover, the spin-orbit split-off effective mass is given by [109]:

$$\frac{1}{m_{SO}} = \gamma_1 - E_p \frac{\frac{1}{3}\Delta}{E_g(E_g + \Delta)}$$

The set of parameters used in our calculation are given in Tables A.1 and A.2. The band structure obtained in InAs with UTOX and TB\_Sim are compared on Fig. A.1. The same band structure is obtained, validating our numerical implementation.

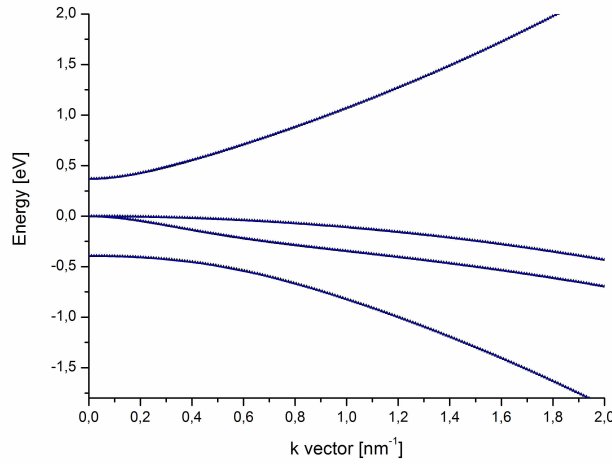


Figure A.1. Bulk band structure of InAs computed with UTOX (blue line) and TBSim (black triangle) with parameters in Table A.1. Perfect match is observed.

Parameters	InAs	GaAs
$m_c [m_0]$	0.023	0.065
$\gamma_1$	20.4	6.85
$\gamma_2$	8.3	2.1
$\gamma_3$	9.1	2.9
$E_g$ [eV]	0.42	1.52
$\Delta_{SO}$ [eV]	0.38	0.34
$E_p$ [eV]	22.2 (18)	25.7 (20)

Table A.1. Parameters for 8-band KP model, fitted on TB. For thin-films, the values in parenthesis are used for  $E_p$  parameters to avoid spurious states in real space.

The stress in the 8-band KP model is taken into account by adding the following strain

matrix to the  $\mathbf{k} \cdot \mathbf{p}$  Hamiltonian [19, 95]:

$$H_{strain} = \begin{bmatrix} a_c[e_{xx} + e_{yy} + e_{zz}] & -iP \sum_j e_{xj}k_j & -iP \sum_j e_{yj}k_j & -iP \sum_j e_{zj}k_j \\ iP \sum_j e_{xj}k_j & le_{xx} + m(e_{yy} + e_{zz}) & ne_{xy} & ne_{xz} \\ iP \sum_j e_{yj}k_j & ne_{xy} & le_{yy} + m(e_{xx} + e_{zz}) & ne_{yz} \\ iP \sum_j e_{zj}k_j & ne_{xz} & ne_{yz} & le_{zz} + m(e_{yy} + e_{xx}) \end{bmatrix}$$

where  $a_c$  is the conduction band hydrostatic deformation potential and the parameters  $l, m$  and  $n$  are related to the valence band deformation potentials  $a_v, b$  and  $d$  by:

$$\begin{aligned} a_v &= \frac{1}{3}(l + 2m) \\ b_v &= \frac{1}{3}(l - m) \\ d_v &= \frac{1}{\sqrt{3}}n \end{aligned}$$

The parameters used for stress in  $\text{In}_x\text{Ga}_{1-x}\text{As}$  are listed in Table A.2. They are extracted from Gershoni *et al.* (1993) [109]. The band structure obtained with UTOX in  $\text{InGaAsP}$  are compared with the ones presented in Gershoni *et al.* (1993) [109] with 2% compressive biaxial strain on Fig. A.2.<sup>3</sup> Band structure obtained with UTOX doesn't take into account the band splitting in  $k \neq 0$  due, according to Gershoni's paper, to tetragonal deformation of the crystalline cell with strain. Note that it was found in the recent work of M.Rau *et al.* (2016) [297] that the standard value of deformation potential used in 8-band KP fail to reproduce stress dependence prediction of DFT and TB models and need to be re-calibrated. Unfortunately, the re-calibration was not provided in their work.

Parameters	InGaAsP
$m_c$ [ $m_0$ ]	0.041
$\gamma_1$	11.01
$\gamma_2$	4.18
$\gamma_3$	4.84
$E_g$ [eV]	0.75
$\Delta_{SO}$ [eV]	0.356
$E_p$ [eV]	25.3
$a_c$ [eV]	-6.2
$a_v$ [eV]	1.56
$b$ [eV]	-1.75
$d$ [eV]	-4.04

Table A.2. Parameters for 8-band KP model used for strain calibration on Gershoni [109].

---

<sup>3</sup>Note that the sign of hydrostatic strain parameter  $a_c$  is here changed compared with the ones given in Gershoni to be consistent with the conduction band shift, lowered in case of compressive (negative) strain.

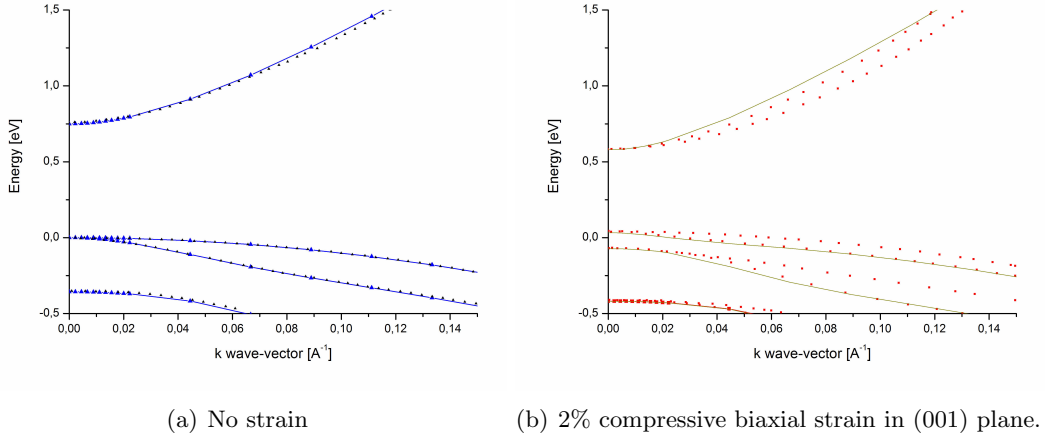


Figure A.2. Bulk band structure of InGaAsP with parameters from Gershoni [109] given in Table A.2 without (a) and with (b) compressive strain. Results of the Fig. 1 of Ref. [109] are reported here with dots symbols and our calculations are shown with lines.

### NP-EMA

One of the first effective mass model to describe non parabolic energy dispersion in bulk semiconductors was proposed by Conwell and Vassel (1968) [59] to describe GaAs band structure. Their derivation comes from the expression of Kane's KP model [156], valid in the approximation of band gap  $E_g$  much larger than spin-orbit splitting energy ( $\Delta_{SO}$ ):<sup>4</sup>

$$\varepsilon(\mathbf{k}) = \frac{\hbar^2 k^2}{2m_0} + \frac{E_g}{2} \left( \sqrt{1 + \frac{4E_p \hbar^2 k^2}{2m_0 E_g^2}} - 1 \right) \quad (\text{A.1})$$

where  $E_p = 2m_0 P^2 / \hbar^2$  is the optical coupling parameters of 8-band KP model. This expression is rearranged and developed for small  $\varepsilon$ :

$$\frac{\hbar^2 k^2}{2m_0} = \varepsilon \left[ \frac{E_g}{E_g + E_p} + \frac{E_g^2 \varepsilon}{(E_g + E_p)^2} - \frac{2E_p^2 \varepsilon^2}{(E_g + E_p)^2} + \dots \right]$$

When  $\varepsilon \rightarrow 0$ , RHS of this equation must be equal to  $\varepsilon m^*/m_0$  to obtain the EMA solution. Thus writing  $E_g/(E_g + E_p) = m^*/m_0$ , one obtains finally the well-known non-parabolic expression of the energy dispersion close to the valley minimum:

$$\frac{\hbar^2 k^2}{2m^*} \equiv \gamma(\mathbf{k}) = \varepsilon [1 + \alpha \varepsilon + \dots] \quad (\text{A.2})$$

---

<sup>4</sup>The expression given here was extracted from Ehrenreich *et al.* (1960) [79] and slightly differs from the original expression.

with the non-parabolic parameter:

$$\alpha = \frac{E_p^2}{E_g(E_g + E_p)^2} = \frac{1}{E_g} \left(1 - \frac{m^*}{m_0}\right)^2 \quad (\text{A.3})$$

Conwell and Vassell (1968) argues that the terms of higher order in the development around  $\varepsilon = 0$  are negligible and Eq.(A.2) is a good approximation for  $\Gamma$  valley until  $\varepsilon \sim 1$  eV above the conduction band minimum. Also, if one takes the first order development only and writes the root of the quadratic expression, one obtains the dispersion relation:

$$\varepsilon(\mathbf{k}) = \frac{1}{2\alpha} \left\{ -1 + \sqrt{1 + 4\alpha\gamma(\mathbf{k})} \right\}$$

which will be useful in the derivation of confined models (see Chapter 1 Sec. 1.2.1). Note that the effective mass in non-parabolic band structure now depends on wavevector  $\mathbf{k}$  and can be written as:

$$m(\mathbf{k}) = m^*(1 + \alpha\varepsilon(\mathbf{k})) \quad (\text{A.4})$$

by equating the classical and quantum momenta  $p = mv = \hbar k$ ;  $m^*$  being the effective mass at the valley minimum energy  $\varepsilon = 0$ .

### A.1.2 High order models

The full-matrix of the 54-band model is given as follows:

$$H_{k,p}^{54} = \begin{bmatrix} H_{\mathbf{k},\mathbf{p}}^{24 \times 24} & H_{\mathbf{k},\mathbf{p}}^{24 \times 30} \\ H_{\mathbf{k},\mathbf{p}}^{30 \times 24} & H_{\mathbf{k},\mathbf{p}}^{30 \times 30} \end{bmatrix}$$

where  $H_{\mathbf{k},\mathbf{p}}^{30 \times 30}$  is the 30-band Hamiltonian (including  $T_d$  group terms in red):

$$H_{k,p}^{30 \times 30} = \begin{bmatrix} H_{\Gamma_{1l}}^{2 \times 2} & UH_k^{2 \times 6} & T'H_k^{2 \times 6} & 0 & 0 & 0 & U'H_k^{2 \times 6} & 0 \\ & H_{\Gamma_{25l}}^{6 \times 6} & QH_k^{6 \times 6} & PH_k^{6 \times 2} & 0 & RH_k^{6 \times 4} & 0 & P''H_k^{6 \times 2} \\ & & H_{\Gamma_{15}}^{6 \times 6} & SH_k^{6 \times 2} & TH_k^{6 \times 2} & 0 & Q'H_k^{6 \times 6} & S'H_k^{6 \times 2} \\ & & & H_{\Gamma_{2l}}^{2 \times 2} & 0 & 0 & P'H_k^{2 \times 6} & 0 \\ & & & & H_{\Gamma_{1u}}^{2 \times 2} & 0 & 0 & 0 \\ & & & & & H_{\Gamma_{12}}^{4 \times 4} & R'H_k^{4 \times 6} & 0 \\ & & & & & & H_{\Gamma_{25u}}^{6 \times 6} & P'''H_k^{6 \times 2} \\ & & & & & & & H_{\Gamma_{2u}}^{2 \times 2} \end{bmatrix}$$

The 24 extra states are coupled through the matrix:

$$H_{k.p}^{24 \times 24} = \begin{bmatrix} H_{\Gamma_{1e}}^{2 \times 2} & 0 & 0 & TeH_k^{2 \times 6} & 0 \\ & H_{\Gamma_{12e}}^{4 \times 4} & YeH_k^{4 \times 6} & ZeH_k^{4 \times 2} & 0 \\ & & H_{\Gamma_{25e}}^{6 \times 6} & 0 & AeH_k^{6 \times 6} \\ & & & H_{\Gamma_{15e}}^{6 \times 6} & QeH_k^{6 \times 6} \\ & & & & H_{\Gamma_{25'u}}^{2 \times 2} \end{bmatrix}$$

And these states are coupled to the 30-band states through the following matrix:

$$H_{k.p}^{30 \times 24} = \begin{bmatrix} 0 & 0 & 0 & Te''H_k^{2 \times 6} & 0 \\ 0 & 0 & Ae''H_k^{6 \times 6} & Qe''H_k^{6 \times 6} & 0 \\ Te'''H_k^{6 \times 2} & Ze'H_k^{6 \times 4} & 0 & 0 & QeH_k^{6 \times 6} \\ 0 & 0 & 0 & 0 & Pe'H_k^{2 \times 6} \\ 0 & 0 & 0 & Te'H_k^{2 \times 6} & 0 \\ 0 & 0 & 0 & 0 & ReH_k^{4 \times 6} \\ 0 & 0 & Ae'H_k^{6 \times 6} & Qe'H_k^{6 \times 6} & 0 \\ 0 & 0 & 0 & 0 & PeH_k^{2 \times 6} \end{bmatrix}$$

The interactions are illustrated on Figure 1.4 and small matrices  $H^{6 \times 2}$ ,  $H^{6 \times 4}$ ,  $H^{6 \times 6}$ ,  $H^{4 \times 4}$  and  $H^{2 \times 2}$  are given in Ref. [304].

Mind that we keep here the state indexes of Diamond structure introduced in Ref. [304]. The notation thus differs from Ref.[298]:

$$\begin{aligned} \Gamma_{2'}^u &\leftrightarrow \Gamma_{6q} \\ \Gamma_{25'}^u &\leftrightarrow \Gamma_{7d-8d} \\ \Gamma_{12'} &\leftrightarrow \Gamma_{8-3} \\ \Gamma_1^u &\leftrightarrow \Gamma_{6u} \\ \Gamma_{15} &\leftrightarrow \Gamma_{7c-8c} \\ \Gamma_{2'}^l &\leftrightarrow \Gamma_6 \\ \Gamma_{25'}^l &\leftrightarrow \Gamma_{7-8} \\ \Gamma_1^l &\leftrightarrow \Gamma_{6v} \end{aligned}$$

where the indexes  $u$  and  $l$  stand for “upper” and “lower” states, and the Zinc-Blende spin-orbit degenerated 7 and 8 states are confounded in one state in the Diamond structure (spin-orbit splitting is taken into account by additional terms).  $\Gamma_1^l$  and  $\Gamma_{25'}^l$  are valence bands while all other states belong to the conduction band.

Table A.3. Energy levels in  $\Gamma$  used for the 54- and 30-band KP models. Letter  $e$  indexes the 12 (220) bands.

Parameter (eV)	GaAs	InAs	Si	GaAs	InAs
	54-band			30-band	
$\Gamma_{1e}$	26.917	22.93	31.275		
$\Gamma_{12e}$	27.655	23.725	25.102		
$\Gamma_{25e}$	25.702	22.657	29.780		
$\Gamma_{15e}$	28.395	25.690	25.204		
$\Delta_{15e}$	0.065	0.077	0.044		
$\Gamma_{25'e}$	27.72	27.067	23.678		
$\Delta_{25'e}$	-0.105	0.070	0		
$\Gamma_{2'u}$	12.752	11.686	15.384	12.752	11.686
$\Gamma_{25'u}$	12.008	10.661	11.684	12.008	10.661
$\Delta_{25'u}$	0.05	0.05	0.012	0.05	0.05
$\Gamma_{12'}$	9.900	9.551	8.707	9.900	9.551
$\Gamma_{1u}$	6.787	6.847	8.736	6.787	6.847
$\Gamma_{15}$	4.751	3.896	3.304	4.751	3.896
$\Gamma_{2'l}$	1.526	0.415	4.096	1.526	0.415
$\Delta_{2'l}$	0.2	0.217	0	0.2	0.217
$\Gamma_{25'l}$	0	0	0	0	0
$\Gamma_{1l}$	-12.446	-12.794	-11.916	-12.446	-12.794
$\Delta_{25'l}$	0.350	0.39	0.044	0.350	0.39
$\Delta_{25'l--25u}$	0	0.388	-0.022	0	0.388

Table A.4. Non-zero matrix terms of the momentum  $\hat{\mathbf{p}}$  and their definitions for 54- and 30-band KP models. Letter  $e$  indexes the 12 (220) bands.

Parameter (a.u.)	GaAs	InAs	Si	GaAs	InAs
	54-band			30-band	
$P = \frac{\hbar}{m} \langle \Gamma_{25'l}   \hat{p}   \Gamma_{2'l} \rangle$	1.2239	1.1170	1.2180	1.1407	1.1284
$Q = \frac{\hbar}{m} \langle \Gamma_{25'l}   \hat{p}   \Gamma_{15} \rangle$	1.1302	1.0340	1.0430	1.1367	1.0803
$R = \frac{\hbar}{m} \langle \Gamma_{25'l}   \hat{p}   \Gamma_{12'l} \rangle$	0.5580	0.5985	0.5380	0.5887	0.5555
$P' = \frac{\hbar}{m} \langle \Gamma_{25'lu}   \hat{p}   \Gamma_{2'lu} \rangle$	0.2207	0.0820	-0.0159	0.1988	0.2718
$P'' = \frac{\hbar}{m} \langle \Gamma_{25'lu}   \hat{p}   \Gamma_{2'l} \rangle$	0.1801	0.1477	0.1535	0.1237	0.2164
$Q' = \frac{\hbar}{m} \langle \Gamma_{25'lu}   \hat{p}   \Gamma_{15} \rangle$	-0.5826	-0.6817	-0.6503	-0.6089	-0.5001
$R' = \frac{\hbar}{m} \langle \Gamma_{25'lu}   \hat{p}   \Gamma_{12'l} \rangle$	0.8852	0.7850	0.8598	0.8042	0.8527
$P''' = \frac{\hbar}{m} \langle \Gamma_{25'lu}   \hat{p}   \Gamma_{2'lu} \rangle$	1.1860	1.0848	1.4852	1.3913	1.3246
$T = \frac{\hbar}{m} \langle \Gamma_{1u}   \hat{p}   \Gamma_{15} \rangle$	1.0250	1.1266	1.1637	1.0320	1.0758
$T' = \frac{\hbar}{m} \langle \Gamma_{1'l}   \hat{p}   \Gamma_{15} \rangle$	0.3702	-0.4449	0.2520	0.1991	0.3536
$S = \frac{\hbar}{m} \langle \Gamma_{15}   \hat{p}   \Gamma_{2'l} \rangle$	-0.0008	-0.0421	–	-0.0013	-0.0408
$S' = \frac{\hbar}{m} \langle \Gamma_{15}   \hat{p}   \Gamma_{2'lu} \rangle$	-0.0031	-0.0679	–	-0.0025	0.1681
$U = \frac{\hbar}{m} \langle \Gamma_{1u}   \hat{p}   \Gamma_{25'l} \rangle$	0.3373	0.3630	–	0.3209	0.3272
$U' = \frac{\hbar}{m} \langle \Gamma_{1u}   \hat{p}   \Gamma_{25'lu} \rangle$	-0.1185	0.0385	–	-0.1112	0.0430
$A_e = \frac{\hbar}{m} \langle \Gamma_{25^e}   \hat{p}   \Gamma_{25^e} \rangle$	2.0852	2.2635	1.4990		
$Y_e = \frac{\hbar}{m} \langle \Gamma_{12^e}   \hat{p}   \Gamma_{25^e} \rangle$	1.0642	1.1634	0.9606		
$Z_e = \frac{\hbar}{m} \langle \Gamma_{12^e}   \hat{p}   \Gamma_{15^e} \rangle$	0.0026	0.0318	0.0025		
$T_e = \frac{\hbar}{m} \langle \Gamma_{1^e}   \hat{p}   \Gamma_{15^e} \rangle$	2.4442	1.0322	2.9834		
$Q_e''' = \frac{\hbar}{m} \langle \Gamma_{15^e}   \hat{p}   \Gamma_{25^e} \rangle$	1.3565	0.2262	1.6829		
$A_e' = \frac{\hbar}{m} \langle \Gamma_{25^e}   \hat{p}   \Gamma_{25^e} \rangle$	-0.1138	-0.0718	-0.1579		
$A_e'' = \frac{\hbar}{m} \langle \Gamma_{25^e}   \hat{p}   \Gamma_{25'l} \rangle$	0.2324	0.0273	0.2896		
$P_e = \frac{\hbar}{m} \langle \Gamma_{25^e}   \hat{p}   \Gamma_{2'lu} \rangle$	0.0005	0.0004	0.0299		
$P_e' = \frac{\hbar}{m} \langle \Gamma_{25^e}   \hat{p}   \Gamma_{2'l} \rangle$	-0.2105	-0.0110	-0.3530		
$Q_e = \frac{\hbar}{m} \langle \Gamma_{25^e}   \hat{p}   \Gamma_{15} \rangle$	0.0100	0.0050	0.1703		
$Q_e' = \frac{\hbar}{m} \langle \Gamma_{15^e}   \hat{p}   \Gamma_{25^e} \rangle$	0.1530	0.0690	0.1258		
$Q_e'' = \frac{\hbar}{m} \langle \Gamma_{15^e}   \hat{p}   \Gamma_{25'l} \rangle$	0.0872	0.0597	0.0066		
$R_e = \frac{\hbar}{m} \langle \Gamma_{12}   \hat{p}   \Gamma_{25^e} \rangle$	-0.0015	-0.0007	-0.0013		
$T_e' = \frac{\hbar}{m} \langle \Gamma_{15^e}   \hat{p}   \Gamma_{1u} \rangle$	-0.0172	-0.1156	-0.0503		
$T_e'' = \frac{\hbar}{m} \langle \Gamma_{15^e}   \hat{p}   \Gamma_{1'l} \rangle$	-0.1808	-0.1045	-0.3486		
$T_e''' = \frac{\hbar}{m} \langle \Gamma_{15}   \hat{p}   \Gamma_{1^e} \rangle$	-0.0007	-0.0234	-0.0267		
$Z_e' = \frac{\hbar}{m} \langle \Gamma_{12^e}   \hat{p}   \Gamma_{15} \rangle$	0.0058	0.0020	0.0054		

## A.2 NL-EPM model

The parameters for non-local EPM calculations in this work have been taken from Kim and Fischetti (2010) [165] for InAs, and Chelikowsky and Cohen (1976) [51] for GaAs. The band structure obtained with these parameters is plotted in Fig. A.3. In order to obtain a good agreement with experimental data for the direct band gap and position of the split-off valence band, the SO parameters were slightly modified in this work. This effect is also shown in Fig. A.3 and the SO parameters used are given in Table A.5.

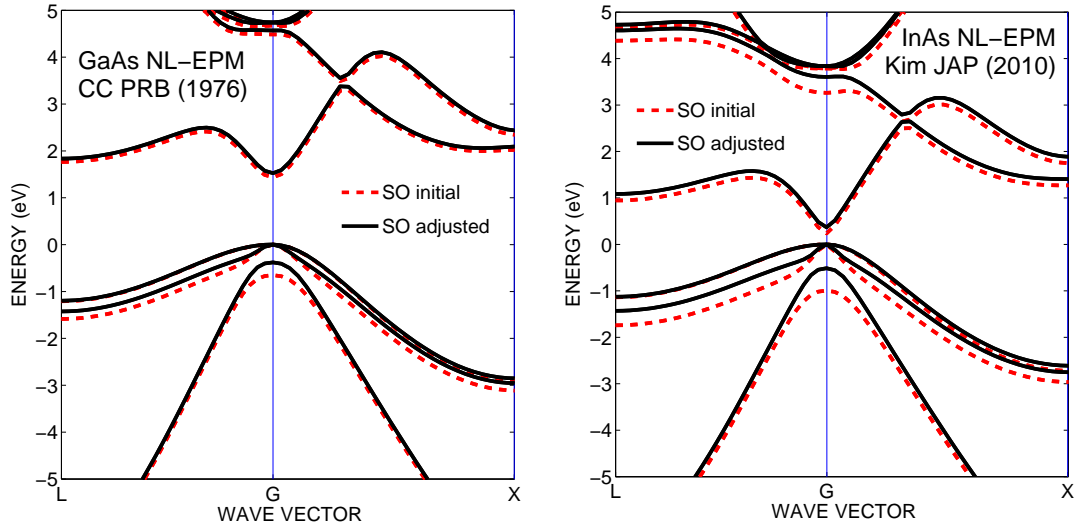


Figure A.3. Band structure of GaAs (left) and InAs (right) obtained with NL-EPM model. The parameters are taken from Ref. [51] for GaAs and Ref. [165] for InAs. SO parameters were slightly modified and are given in Table A.5.

	GaAs	InAs
$\alpha$	1.35	0.74
$\mu$	0.0008	0.00113

Table A.5. SO parameters used in this study to compute the NL-EPM band structures in InAs and GaAs materials. Others NL-EPM parameters are taken from Ref. [165] for InAs and Ref. [51] for GaAs.

### A.3 TB models

The parameters for TB models in Chapter 1 have been taken from Jancu *et al.* (1998) [145] for III-V materials and Niquet *et al.* (2009) [251] for Si and Ge materials. For alloys, two different interpolation procedures were used to simulate SiGe band structure in the VCA approach and compared in Section 1.1.8. In the second model, developed by D.Rideau, two atom types are defined (denoted atoms  $A$  and  $B$ ), whose on-site parameters are interpolated as follows [301]:

- For  $x < 0.5$ :  $A$ 's parameters are the ones of pristine Si, and  $B$ 's parameters are linearly interpolated between Si and Ge;
- For  $x > 0.5$ :  $A$ 's parameters are linearly interpolated between Si and Ge;  $B$ 's parameters are the ones of pristine Ge.

The hopping parameters are interpolated as [273]:

$$V_{A,B}^{hop} = (1-x)V_{Si,Si}^{hop} \left( \frac{d_{Si}}{d_{VCA}} \right)^{\eta_{VCA}} + (x)V_{Ge,Ge}^{hop} \left( \frac{d_{Ge}}{d_{VCA}} \right)^{\eta_{VCA}} - P_{A,B}(1-x)x \quad (\text{A.5})$$

where  $\eta_{VCA}$  are the Harrison parameters of VCA crystal linearly interpolated such as:  $\eta_{VCA} = (1-x)\eta_{Si} + x\eta_{Ge}$  and  $d_{VCA}$  is the nearest neighbor distance, interpolated as:  $d_{VCA} = (1-x)d_{Si} + xd_{Ge} - 0.0117(1-x)x$ .  $P_{A,B}$  are bowing coefficients fitted to reproduce the correct bowing and given in Table A.6. This optimized model improves the agreement with experimental and random supercell calculations, as shown in Fig. 1.10 in Sec. 1.1.8.

Parameters	$P_{A,B}$	$P_{B,A}$
$V_{sp\sigma}$	0.06	-0.06
$V_{sd\sigma}$	0.1	-0.1
$V_{ss^*\sigma}$	-0.19	0.16
$V_{pd\sigma}$	-0.02	0
$V_{pd\pi}$	0.012	0.02
$V_{ps^*\sigma}$	0.05	-0.1
$V_{ds^*\sigma}$	-0.05	-0.05

Table A.6. Bowing coefficient entering Eq. (A.5) for the second VCA model to reproduce the band gap of SiGe bulk material in Fig 1.10 [301].  $P_{A,B}$  denotes the case where first orbital in the parameter's name is on  $A$  atom and second orbital on  $B$  atom, while it is the opposite for  $P_{B,A}$ .

## Appendix B

# Non-radiative multiphonon theory

Multiphonon theory is a complex and broad topic and we will not go into very detailed description here, but rather discuss the different approximation made in the model, leading to the expression of transition probabilities  $W_{c/e}$  given in Eq. (2.17). The derivation written here is taken from the work of D.Rideau [306, 105], based in part on the book of Stoneham [345] and references therein, as well as Goguenheim and Lannoo (1990) [113] and Huang (1981) [137].

The starting point for quantum treatment of the problem is to use the Fermi golden rule to write the transition probability as [113]:

$$W_c = \frac{2\pi}{\hbar} A_{vn} \sum_{n'} |\langle \Psi_{jn'} | \hat{C}_{ij} | \Psi_{in} \rangle|^2 \delta(E_{in} - E_{jn'}) \quad (\text{B.1})$$

where  $A_{vn}$  denotes the thermal average over the initial states,  $\Psi_{in}$  and  $\Psi_{jn'}$  are the total initial and final wavefunctions characterizing the system (electron + lattice) of respective energies  $E_{in}$  and  $E_{jn'}$ , composed of the electronic part wavefunction  $\Phi_i$  and the vibrational one  $\chi_{in}$ .  $C_{ij}$  is a perturbation coupling operator, mixing the two states.

The first approximation made is the so-called Born-Oppenheimer approximation (see discussion in Section B.3), where the total wavefunction is written as:  $|ni\rangle = \Psi_{in} = \Phi_i(\mathbf{r}, Q)\chi_{in}(Q)$ .  $Q$  here represents the ensemble of normal coordinates  $Q_j$  ( $j = 1, \dots, 3N$  where  $N$  is the number of atoms). The electronic and phononic part of the wavefunction are solutions of the equations:

$$\begin{aligned} (H_e + H_{eL}(\mathbf{r}))\Phi_i(\mathbf{r}, Q) &= W_i(Q)\Phi_i(\mathbf{r}, Q) \\ (T_L + V_L + W_i(Q))\chi_{in}(Q) &= E_{in}(Q)\chi_{in}(Q) \end{aligned}$$

where  $H_e$  and  $H_{eL}$  are the electronic and electron-lattice coupling Hamiltonians and  $T_L$  and  $V_L$  are the kinetic energy and potential Hamiltonians of the lattice.

The second approximation is the harmonic approximation, where the electronic energy  $W_i(Q)$  is written as a function of the normal coordinates  $Q$  as [69]:

$$E_{in}(Q) = E_{in}(Q^{(i)}) + \sum_{j=1}^{3N} \frac{\omega_j^2}{2} \left( Q_j - Q_j^{(i)} \right)^2$$

where  $Q_j^i$  is the equilibrium lattice coordinate. In this approximation, the total energy of the system  $E_{in}$  is also harmonic and follows the same dependency over  $Q$  (not demonstrated here). The summation  $j$  runs over all phonons modes, characterized by frequencies  $\omega_j$  and normal vectors  $\mathbf{e}_n^j$  (where  $n$  is the number of atoms and  $\mathbf{e}_n$  is a vector with 3 components  $(x, y, z)$ ). Recall that for a crystal with  $N$  atoms, the number of normal modes associated is  $3N$ . The normal coordinates  $Q_j$  are defined as the coordinate describing the movement of lattice atoms  $S_{in}$  as a function of the normal vectors:

$$\mathbf{S}_n = \frac{1}{M_n} \sum_j Q_j \mathbf{e}_n^j$$

In our model (as well as most models in the literature), a so-called “single-mode” approximation is used. This mode is defined by its phonon energy  $\hbar\omega$  and its single coordinate  $Q$ . This is as if all modes were considered as an average effective mode, which is believed to be a good approximation in the case of optical phonons that all have relatively similar and constant frequencies (flat band structure). This approximation is also valid in the case where the transition occurs in a defect level which is mostly coupled to a single mode of vibration. It greatly simplifies the problem, which is already not easily tractable. The third approximation made is the linear electron-phonon coupling, writing the electron-lattice Hamiltonian as [137]:

$$H_{eL} = \sum_s \omega_s^2 u_s(\mathbf{r}) Q_s \quad (\text{B.2})$$

where  $u_s$  is the displacement of atoms and the sum over the phonon modes  $s$  is reintroduced. This approximation is valid for small distortion of the lattice.

Using these approximations and following the derivation of Huang and Rhys (1950) [138], the matrix element in Eq. (B.1) can be further simplified as (see Section B.3 and Ref. [137] for discussion):

$$\langle \Psi_{jn'} | \hat{C}_{ij} | \Psi_{in} \rangle = \sum_s \langle \Phi_j^0 | u_s(\mathbf{r}) | \Phi_i^0 \rangle \langle \chi_{jn'} | \hat{Q}_s^j - Q_s^i | \chi_{in} \rangle$$

where  $\Phi_{i,j}^0$  are the eigenvectors of electronic Hamiltonian  $H_e$  alone in the equilibrium lattice coordinates  $Q_s^{i,j}$ . Given this expression, the transition matrix (B.1) reads:

$$W_c = \frac{2\pi}{\hbar} A_{vn} \sum_{n'} \left| \sum_s V_s \langle \chi_{in} | \hat{Q}_s^j - Q_s^i | \chi_{jn'} \rangle \right|^2 \delta(E_{in} - E_{jn'}) \quad (\text{B.3})$$

where  $V_s = \langle \Phi_j^0 | u_s(\mathbf{r}) | \Phi_i^0 \rangle$  takes into account the overlap of electronic wavefunctions (which is a temperature independent term) and will be considered later.

## B.1 Vibrational overlap

For the vibrational overlap, one can calculate it using second quantification operators and expanding the vibrational states as  $\chi_{in} = \prod_{l=1}^{3N} |in_l\rangle$  ( $n_l$  being the number of phonons in

the mode  $l = 1, \dots, 3N$ ):

$$\langle \chi_{in} | Q_s^j - Q_s^i | \chi_{jn'} \rangle = A_s \langle n_s | \hat{a}_s + \hat{a}_s^\dagger | n'_s \rangle \prod_{l \neq s} \langle n_l | n'_l \rangle$$

where  $A_s = \sqrt{(\hbar/2M_s\omega_s)}V_s$ . Following Huang-Rhys (1950) [138], it is shown that [67]:

$$\langle n_i | n_j \rangle = 1 - (n_j + 1/2)S_j + O(S_j^2)$$

where  $S_j$  is the Huang-Rhys factor, defined as:

$$S\hbar\omega = \frac{1}{2} \sum_s \omega_s^2 (Q_s^j - Q_s^i)^2 = \frac{1}{2} \sum_s \omega_s^2 (\langle \Phi_j^0 | \hat{u}_s | \Phi_j^0 \rangle - \langle \Phi_i^0 | \hat{u}_s | \Phi_i^0 \rangle)^2$$

As  $S_j$  is of order of  $1/N$  ( $N$  being the number of atoms, supposed big), the terms of higher order  $O(S_j^2)$  can be neglected, and one considers that the electron-phonon coupling is weak between two harmonic oscillators close to each other, thus only terms with  $n_j = n_i - 1$ ,  $n_i$  and  $n_i + 1$  are taken into account.

Taking all approximation together, the transition rate given in Eq. (2.17) is finally found (after some algebra, not demonstrated here):

$$W_c = \frac{2\pi}{\hbar} R(\Delta E) |V|^2 \left[ rS \left( 1 - \frac{E_0}{\hbar\omega S} \right)^2 + (1-r) \sqrt{\left( \frac{\Delta E}{\hbar\omega S} \right)^2 + 4\bar{n}(\bar{n}+1)} \right]$$

where  $S$  is the Huang-Rhys factor,  $\bar{n}$  is the Bose-Einstein distribution of phonons,  $\Delta E = \varepsilon_i - E_0$  is the total energy released in the capture process,  $|V|^2$  is the matrix element of the perturbation due to relaxation of lattice atoms between free-state  $\Phi_i$  and bound state  $\Phi_j$  wavefunction (the free state  $A$  and bound state  $B$  in the Chapter 2 corresponding to the initial  $i$  and final  $j$  states in our derivation):  $|V|^2 = |\langle j^0 | \hat{u} | i^0 \rangle|^2$ , and  $r = |V_\Lambda|^2 / (S|V|^2)$  with  $|V_\Lambda|^2 = |\langle j^0 | \hat{u} | i^0 \rangle|^2 \left( |\langle j^0 | \hat{u} | j^0 \rangle|^2 - |\langle i^0 | \hat{u} | i^0 \rangle|^2 \right)$ . The term  $R(\Delta E)$  is expressed as:

$$R(\Delta E) = \frac{1}{\hbar\omega} \exp \left[ -(2\bar{n}+1)S + \frac{\Delta E}{2kT} \right] \sum_m I_m(\xi) \delta(m\hbar\omega - \Delta E)$$

where  $m$  is the the number of phonons involved in the transition,  $I_m(z)$  is the reduced Bessel function of order  $m$ ,  $\xi = 2S\sqrt{\bar{n}(\bar{n}+1)}$  and  $\delta$  is the Dirac delta function. Note that the summation over the phonons mode  $s$  have been kept in the calculation until the final expression, where the “single-mode” approximation for phonon has been introduced. Note also that in this expression, the electronic overlaps are still unknown and present in the calculation of  $S$ ,  $|V|^2$  and  $|V_\Lambda|^2$  (entering the calculation of  $r$ ).

The cross-section as a function of temperature for defects level in the band gap of GaAs, as characterized and measured by Ref. [128], are compared with results from the current model in Figure B.1. As one can see, the temperature dependence of the process is generally more complex than a simple Arrhenius-like exponential dependence. Figure B.1(a) shows the results obtained with different defects wavefunctions and a relatively similar results is found for all wavefunctions considered (see next subsection for details about the Billard-Ball model).

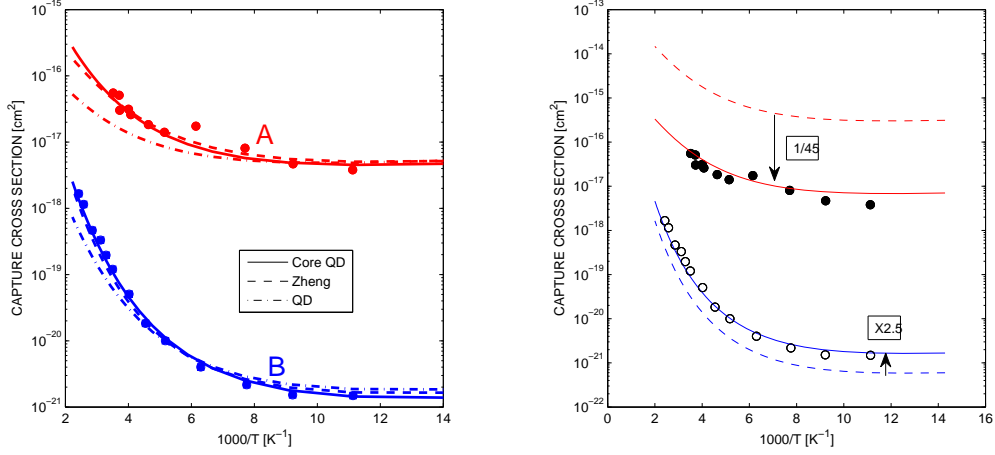


Figure B.1. Left: Capture cross-section extracted from multiphonon theory with different models for traps wavefunction as function of  $1/T$  in GaAs for defects of types A and B (unknown defects in the band gap, extracted from Ref. [128]). Right: Illustration of the constant rigid shift to be applied to fit experimental values.

## B.2 Electronic overlap

In order to calculate the electronic overlaps  $\langle \Phi_{i/j}^0 | \hat{u} | \Phi_{i/j}^0 \rangle$ , the free state electronic wavefunction  $\Phi_i^0$  is taken from the Schrödinger solver in our model (note that in principle it should be modified near the defect due to lattice distortion), while a simple Billiard-Ball model was used for the defect wavefunction  $\Phi_j^0$ , written a function of defect radius  $r_T$  (defining a spherical potential well around the defect):

$$\Phi_j^0 = (1/r_T^{2/3})$$

Using this approximation, the electronic wavefunctions overlap  $|V|^2$  and the Huang-Rhys factor  $S$  can be calculated [105]:

$$|V|^2 = 5\pi S (\hbar\omega)^2 r_T^2 \int_{z-z_T/2}^{z+z_T/2} dz |\phi(z)|^2 \quad (\text{B.4})$$

$$S = \frac{27}{4(\hbar\omega)^2 (q_D z_T)^3} \frac{D_{ph}^2}{M_r \omega / \hbar} \quad (\text{B.5})$$

where  $r_T = \frac{\hbar}{\sqrt{2m_{\sigma_x}^*(E_c - E_T)}}$ ,  $z_T = r_T (\frac{4\pi}{3})^{1/3}$  represents the edge of the cube with the same volume as the defect sphere,  $q_D = (6\pi^2/a_0)^{1/3} = (6\pi^2/4^{2/3})^{1/3}$  is the Debye cutoff wavevector,  $D_{ph}$  is the deformation potential associated to the phonon mode with frequency  $\omega$  and  $\phi(z)$  is the envelope function given by the resolution of the 1D KP Schrödinger equation. In our model, Eq. (B.4) is used to determine the parameter  $|V|^2$  is all cases, while the

Huang-Rhys factor can either be computed with Eq. (B.5) with the physical parameters of the oxide or be given as an input parameter fixed for one specific distribution of defects. This last option is used in our calculation and  $S$  is set for all traps to 15. The influence on the  $C(V)$  when  $S$  is varied from 9 to 15 is shown in Fig 2.20. The parameter  $r$  is used as an adjustable parameter and always set to 1 in our calculations.

For a more detailed study on the derivations of parameters  $S$ ,  $|V|^2$  and  $r$  with more refined defect wavefunctions models and their influence on the capture/emission rates, the reader is referred to the review in Ref. [306].

### B.3 Derivation of MPA model: resolution of electronic overlaps

In order to solve Eq. (B.1), two approximations are found in the literature: the static coupling and the adiabatic approximation.

In the first case, proposed by Helmis (1956) [127] and Pässler (1974) [272] and considered in the studies of Goguenheim and Lannoo (1990) [113] and the recent DFT developments (e.g. Alkauskas *et al.* (2014) [6]), the electronic wavefunctions are calculated for a fixed set of atomic positions  $\mathbf{R}^0$  and supposed to be insensitive to the distortions of the lattice. In this approximation, the transition probability is given by:

$$W_c = \frac{2\pi}{\hbar} A_{vn} \sum_{n'} \left| \langle \chi_{in} | \hat{C}_{ij} | \chi_{jn'} \rangle_Q \right|^2 \delta(E_{in} - E_{jn'}) \quad (\text{B.6})$$

where  $C_{ij}$  is now a coupling operator mixing only lattice vibrational wavefunctions and defined in terms of “static” electronic wavefunctions  $\Phi_i^0$  and  $\Phi_j^0$  as:

$$C_{ij} = \langle \Phi_j^0 | \frac{\partial H_{eL}(r, Q)}{\partial Q} | \Phi_i^0 \rangle_Q$$

where  $\Phi_{i/j}^0$  are the wavefunction at the relaxed atomic position  $\mathbf{R}^0$  and  $H_{eL}$  is the electron-lattice coupling Hamiltonian.

In the second case, the adiabatic approximation takes into account an electronic basis “moving” with respect to the atomic positions. To evaluate the  $Q$ -dependent electronic states used to calculate the matrix element in Eq. (B.1), the so-called Condon approximation was first used [138]. In this approximation, the electronic wavefunctions are calculated using first order perturbation theory, projecting the electron-lattice Hamiltonian on the initial static states  $\Phi_i^0$  and  $\Phi_j^0$ :

$$\Phi_i(\mathbf{r}, Q) \approx \Phi_i^0(\mathbf{r}) + \sum_j \frac{\langle j^0 | \hat{H}_{el} | i^0 \rangle}{W_i^0 - W_j^0} \Phi_j^0(\mathbf{r})$$

However, this approximation leads to  $Q$ -independent  $C_{ij}$  and gives wrong results (as pointed out by Huang (1981) [137]). The solution to this was found in separating first

the Hamiltonian  $H_{eL}$  into a diagonal  $H_{eL}^d$  and non-diagonal  $H_{eL}^{nd}$  term and perform the perturbation only on the non-diagonal term [137]:

$$\Phi_i(\mathbf{r}, Q) \approx \Phi_i^0(\mathbf{r}) + \sum_j \frac{\langle j^0 | \hat{H}_{eL} | i^0 \rangle}{W_i^0 - W_j^0 + (\langle i^0 | \hat{H}_{eL} | i^0 \rangle - \langle j^0 | \hat{H}_{eL} | j^0 \rangle)} \Phi_i^0(\mathbf{r}) \quad (\text{B.7})$$

Note that in this approximation, the wave function  $\Phi_i^0$  are also solutions of:

$$(H_e + H_{eL}^0 + H_{eL}^d) \Phi_i^0(\mathbf{r}) = (W_i^0 + \langle i^0 | \hat{H}_{eL} | i^0 \rangle) \Phi_i^0(\mathbf{r})$$

One notes here that the effect of the lattice distortion is double:

- it applies a shift linear in  $Q$  to the electronic energy:  $W_{elec}(Q) = W_i^0 + \langle i^0 | \hat{H}_{eL} | i^0 \rangle$
- it mixes the  $|i^0\rangle$  states due to the non-diagonal part of the Hamiltonian  $H_{eL}$ .

This latter non-diagonal term will be the one responsible for the non-radiative transition between electronics states (coupled through this term).

Finally, calculating the coupling operator  $C_{ij}$  using this expression for the electronic state gives the expression:

$$\langle \chi_{n'j} | \hat{C}_{ij} | \chi_{ni} \rangle = \int \chi_{n'j}(Q) \langle j^0 | \hat{H}_{eL} | i^0 \rangle \chi_{ni}(Q) dQ$$

Huang (1981) [137] shows that the transition matrix obtained with this non-Condon adiabatic approximation surprisingly ends up to be the same as the one obtained by the static approximation.

## Appendix C

# Derivation of the POP momentum relaxation time expression

In the case of 2D Electron Gas (2DEG), confined in  $z$ -direction, the slowly varying envelope wave function is written as:

$$\Psi_i(\mathbf{K}, \mathbf{r}) = \psi_i(z) \frac{1}{\sqrt{S}} e^{i\mathbf{K} \cdot \mathbf{R}}$$

with

$$\int_0^T dz |\psi_i(z)|^2 = 1$$

where  $\mathbf{R}$  and  $\mathbf{K}$  are 2D vectors along the channel plane in real and reciprocal space and the wavefunction are normalized in a box of surface  $S$  (relaxed dimension) and thickness  $T$  (confined dimension along  $z$  direction). Now consider the transition matrix element defined as (for fixed initial and final states  $(i, \mathbf{K})$  and  $(j, \mathbf{K}')$ ):

$$|M_{ij}(\mathbf{K}, \mathbf{K}')|^2 = \sum_{\mathbf{q}} |M_{ij}^{\mathbf{q}}(\mathbf{K}, \mathbf{K}')|^2$$

where the sum runs over all phonons modes. Inserting Fröhlich potential's expression, one gets:

$$|M_{ij}^{\mathbf{q}}(\mathbf{K}, \mathbf{K}')|^2 = \left( e \left\{ \frac{\hbar\omega_{LO}}{2q^2\Omega} \left[ \frac{1}{\epsilon_{\infty}} - \frac{1}{\epsilon_0} \right] \right\}^{1/2} \right)^2 \left| \langle \chi', \mathbf{K}' | e^{i\mathbf{q} \cdot \mathbf{r}} (a_{-\mathbf{q}}^{\dagger} + a_{\mathbf{q}}) | \mathbf{K}, \chi \rangle \right|^2$$

where  $\chi = \prod_k |in_k\rangle$  is the phonon wavefunction of initial state ( $\chi'$  defined similarly for the final state). The phonon overlap gives the emission:

$$|\langle \chi' | a_{-\mathbf{q}}^{\dagger} | \chi \rangle|^2 = (N_{-\mathbf{q}} + 1)$$

and absorption terms:

$$|\langle \chi' | \hat{a}_{\mathbf{q}} | \chi \rangle|^2 = N_{\mathbf{q}}$$

where  $N_{-\mathbf{q}} = N_{\mathbf{q}} = N_{\text{LO}}$  is the phonons occupation number (given by Bose-Einstein distribution). Keeping only absorption term, the matrix elements read:

$$|M_{ij}^{\mathbf{q}}(\mathbf{K}, \mathbf{K}')|^2 = \frac{e^2}{q^2} \left\{ \frac{\hbar\omega_{\text{LO}}}{2ST} \left[ \frac{1}{\epsilon_{\infty}} - \frac{1}{\epsilon_0} \right] \right\} N_{\text{LO}} \left| \int_{\Omega} d\mathbf{r} \Psi_i^{\dagger}(\mathbf{r}) e^{i\mathbf{q}\cdot\mathbf{r}} \Psi_j(\mathbf{r}) \right|^2$$

Using the fact that:

$$\frac{1}{S} \int_S d^2\mathbf{R} e^{-i(\mathbf{K}' - \mathbf{K} + \mathbf{Q})\cdot\mathbf{R}} = \delta_{\mathbf{K}', \mathbf{K} - \mathbf{Q}}$$

the matrix element can be simplified to:

$$|M_{ij}^{\mathbf{q}}(\mathbf{K}, \mathbf{K}')|^2 = e^2 \{ \dots \} N_{\text{LO}} \frac{F_{i,j}(q_z)}{q^2} \delta_{\mathbf{K}', \mathbf{K} - \mathbf{Q}}$$

where  $F_{i,j}(q_z)$  is the form factor integral:

$$F_{i,j}(q_z) = \int_T \int_T dz_1 dz_2 \psi_i(z_1) \psi_j(z_2) e^{iq_z|z_1 - z_2|} \psi_j^{\dagger}(z_1) \psi_i^{\dagger}(z_2)$$

Now, inserting this expression into the summation over phonon modes reads:

$$|M_{ij}(\mathbf{K}, \mathbf{K}')|^2 = \sum_{\mathbf{q}} |M_{ij}^{\mathbf{q}}(\mathbf{K}, \mathbf{K}')|^2 = \sum_{\mathbf{Q}} \sum_{q_z} e^2 \{ \dots \} N_{\text{LO}} \frac{F_{i,j}(q_z)}{q^2} \delta_{\mathbf{K}', \mathbf{K} - \mathbf{Q}}$$

The discrete summation over phonon modes in  $z$  direction is then converted into a continuous summation over wavevector  $q_z$  (in the approximation of bulk LO phonon) with the relation:

$$\sum_{q_z} \rightarrow \frac{T}{2\pi} \int_{-\infty}^{+\infty} dq_z$$

and the integration over  $q_z$  can be inserted in the form factor and calculated analytically with the residue theorem, giving the following relation [291]:

$$\int dq_z \frac{e^{iq_z|z_1 - z_2|}}{q_z^2 + Q^2} = \int dq_z \frac{e^{iq_z|z_1 - z_2|}}{(q_z + iQ)(q_z - iQ)} = \pi \frac{e^{-Q|z_1 - z_2|}}{Q}$$

The matrix element thus reads:

$$\begin{aligned} |M_{ij}(\mathbf{K}, \mathbf{K}')|^2 &= \sum_{\mathbf{Q}} \frac{T}{2\pi} \int dq_z e^2 \{ \dots \} N_{\text{LO}} \frac{F_{i,j}(q_z)}{q^2} \delta_{\mathbf{K}', \mathbf{K} - \mathbf{Q}} \\ &= \frac{\mathcal{F}}{2\pi} \pi e^2 \left\{ \frac{\hbar\omega_{\text{LO}}}{2S\mathcal{F}} \left[ \frac{1}{\epsilon_{\infty}} - \frac{1}{\epsilon_0} \right] \right\} N_{\text{LO}} \frac{H_{i,j}(Q)}{Q} \\ &= \left\{ \frac{e^2 \hbar\omega_{\text{LO}}}{4S} \left[ \frac{1}{\epsilon_{\infty}} - \frac{1}{\epsilon_0} \right] \right\} N_{\text{LO}} \frac{H_{i,j}(Q)}{Q} \end{aligned}$$

with the new overlap integral:

$$H_{i,j}(Q) = \int_0^T dz_1 \int_0^T dz_2 \psi_i(z_1) \psi_i^*(z_2) \psi_j(z_2) \psi_j^*(z_1) e^{-Q|z_1 - z_2|} \quad (\text{C.1})$$

and where  $Q$  is the norm of the in-plane phonon wavevector  $\mathbf{Q} = \mathbf{K}' - \mathbf{K}$ . Now, inserting this expression in the scattering relaxation rate expression found above (Eq. (3.12)), one obtains:

$$\begin{aligned} \frac{1}{\tau_i^{\text{POP}}} &= \frac{2\pi}{\hbar} \sum_j \frac{S}{(2\pi)^2} \int d^2 K' |M_{ij}(\mathbf{K}, \mathbf{K}')|^2 \delta(\varepsilon_j - \varepsilon_i + \hbar\omega_{LO}) \frac{1-f_j}{1-f_i} \left(1 - \frac{\tau_j v_{u,j}}{\tau_i v_{u,i}}\right) \\ &= \frac{1}{2\pi\hbar} \frac{e^2 \hbar \omega_{LO}}{4} \left[ \frac{1}{\epsilon_\infty} - \frac{1}{\epsilon_0} \right] N_{\text{LO}} \sum_j \int d^2 K' \frac{H_{i,j}(Q)}{Q} \delta(\varepsilon_j - \varepsilon_i + \hbar\omega_{LO}) \frac{1-f_j}{1-f_i} \left(1 - \frac{\tau_j v_{u,j}}{\tau_i v_{u,i}}\right) \end{aligned}$$

This expression can be used to compute directly the scattering rate in KP models. In the case of EMA with an analytic expression linking  $\varepsilon$  and  $\mathbf{K}$ , one can perform the transform:

$$\iint d^2 K' \Rightarrow \int_{\varepsilon_{edge}}^{\infty} d\varepsilon_j \int_0^{2\pi} d\theta \frac{m^*}{\hbar^2}$$

where  $\varepsilon_{edge}$  is the minimum of conduction band in the case of electrons and  $m^*$  is the effective mass of the isotropic valley considered. The scattering rate expression thus becomes:

$$\frac{1}{\tau_{i,j}^{\text{POP}}(\varepsilon_i)} = \frac{e^2 m^* \omega_{LO}}{8\pi\hbar^2} \left[ \frac{1}{\epsilon_\infty} - \frac{1}{\epsilon_0} \right] (N_{\text{LO}} + 1) \delta(\varepsilon_j - \varepsilon_i + \hbar\omega_{LO}) \frac{1-f_j}{1-f_i} \int_0^{2\pi} d\theta \frac{H_{i,j}(Q)}{Q} \left(1 - \frac{\tau_j v_{u,j}}{\tau_i v_{u,i}}\right)$$

This final expression gives the scattering rate due to polar optical phonon, as mostly used in the literature. General expression for absorption and emission (respectively upper and lower signs) reads [285]:

$$\begin{aligned} \frac{1}{\tau_{i,j,\nu}^{\text{POP}}(\varepsilon_i)} &= \frac{g_s e^2 m_\nu^* \omega_{LO}}{8\pi\hbar^2} \left( \frac{1}{\epsilon_\infty} - \frac{1}{\epsilon_0} \right) \left( N_{\text{LO}} + \frac{1}{2} \mp \frac{1}{2} \right) \frac{1-f(\varepsilon_i \pm \hbar\omega_{LO})}{1-f(\varepsilon_i)} \\ &\quad \times [1 + 2\alpha(\varepsilon_i - U_i)] \int_0^{2\pi} d\theta \frac{H_{i,j,\nu}(Q_\pm)}{Q_\pm} \left(1 - \frac{\tau_j v_{u,j}}{\tau_i v_{u,i}}\right) \end{aligned} \tag{C.2}$$

where the spin degeneracy  $g_s$  and the index of the valley  $\nu$  have been added, as well as the term in square parenthesis to account for the NP corrections [263] ( $\alpha$  being the NP coefficient and  $U_i$  the potential as computed in Eq. (1.16)).

## Appendix D

# Intervalley transitions in III-V: deformation potential

As said in Section 3.1.2, two types of interactions between carriers and lattice vibrations can occur in an ionic crystal: deformation-potential interactions and Fröhlich-type interactions. The Fröhlich potential is induced by LO-mode of phonons and goes like the inverse of the phonon wavevector  $1/q$ , making it an intravalley, long-range interaction. On the other side, the deformation potential theory includes intervalley, short-range interactions, which have been found to be important in system with a band structure with multiple valleys, in particular at high field. These interactions scatter electrons between different valleys with different effective masses and can have unexpected effects on the transport properties at high field.

We present below a review of studies on deformation-potential parameters found in the literature for GaAs and InAs for intervalley optical phonon. As said in Chapter 1 Section 1.1.9, the intravalley deformation-potential can be determined experimentally in bulk devices based on the shift of electronic energy with stress, or through first-principle calculations [408, 326, 369]. Intervalley deformation potentials however need more sophisticated methods and cannot be determined easily with first-principle or experimental studies.

To our knowledge, only few experimental studies can be found in the literature, assessing the intervalley deformation potential in GaAs by subpicosecond luminescence spectroscopy [321, 158, 123] or Raman scattering [164, 159]. In most cases however, only scattering rates are deduced from measurements and the deformation potentials are extracted by mean of simulations (Monte Carlo) or models. Considering this uncertainty on the extraction procedure, we turn to theoretical studies.

The first theoretical work on intervalley deformation potentials in GaAs has been performed by Zollner and co-worker in 1990's with an EPM approach. They first pointed out the dependence of these parameters on initial and final electronic wavevector  $k$  [407, 408]. The Tables D.1 and D.2 summarize the value computed. In more recent papers by Wang *et al.* (1992) and Sjakste *et al.* (2007) and (2013), the deformation potentials were computed by mean of first-principle DFT solvers in the LDA approximation [387, 324, 325]. A good agreement between EPM and DFT is found for  $\Gamma - X_1$  transition, while a big

difference is noted for  $\Gamma - X_3$ <sup>1</sup>. The disagreement with EPM values was attributed in both papers to the more accurate treatment of electron redistribution and screening potential in DFT calculations.

Table D.1. Theoretical intervalley deformation potential in GaAs in eV/Å.

References	Transitions (phonon mode involved)							
	$\Gamma \leftrightarrow X_3$	$\Gamma \leftrightarrow X_1$	$\Gamma \leftrightarrow L_1$		$X \leftrightarrow X$		$L \leftrightarrow L$	
	LA	LO	LA	LO	LO	LA	LO	
Zollner <i>et al.</i> (1989) [407] EPM	4.7	4.1	4.1	0.6	7.0	0.1	1.7	
Zollner <i>et al.</i> (1990) [408] EPM	2.9	3.3	3.0	0.4	4.9	1.2 <sup>2</sup>		
Wang <i>et al.</i> (1992) <sup>3</sup> [387] DFT-LDA	4.1	0.6	-	-	-	-	-	
Sjakste <i>et al.</i> (2013) [324] DFT-LDA	4.2	0.5	3.6	2.2	7.5	1.6	0.2	

Table D.2. Theoretical intervalley deformation potential in InAs in eV/Å.

References	Transitions (phonon mode involved)							
	$\Gamma \leftrightarrow X_3$	$\Gamma \leftrightarrow X_1$	$\Gamma \leftrightarrow L_1$		$X \leftrightarrow X$		$L \leftrightarrow L$	
	LO	LA	LA	LO	LA	LA	LO	
Zollner <i>et al.</i> (1989) [407] EPM	2.8	3.2	2.5	1.4	3.6	1.4	0.7	
Zollner <i>et al.</i> (1990) [408] EPM	2.2	2.0	1.7	1.0	2.5	1.1 <sup>4</sup>		
Wang <i>et al.</i> (1992) [387] DFT-LDA	0.5	3.7	-	-	-	-	-	

The analysis of the intervalley deformation potential is also historically linked with Monte Carlo simulations and high field transport. For that reason, in the following we compare the above theoretical data with the deformation potential extracted from Monte Carlo high-field simulations. These parameters are usually extracted by fitting the velocity versus electric field curve, based typically on scattering models exposed in Section 3.1.2 [89, 324]. For III-V materials, Fischetti and Laux (1991) [89] can be considered as a reference paper, as it gives a broad review and range of parameters, that have been widely used in recent KG calculations [263, 216, 215, 336]. The parameters extracted from Fischetti’s paper are given in Table D.3. These parameters for a given transition are “effective” deformation potentials accounting for all phonons modes contributions (LA, LO, TA and

---

<sup>1</sup>Note that the deformation potentials for GaAs presented in the original paper of Wang *et al.* [387] were also reported in Sjakste *et al.* [324], but in an inverse order (transition  $\Gamma - X_1$  and  $\Gamma - X_3$  were inverted). We chose to report them in this latter order here, for coherence in the results.

Table D.3. Effective intervalley deformation potential in the considered III-V materials extracted by Monte Carlo fits in eV/Å at 300K. [89, 86]

References		Transitions			
		$\Gamma \leftrightarrow X$	$\Gamma \leftrightarrow L$	$X \leftrightarrow X$	$L \leftrightarrow L$
GaAs					
Fischetti (1991a) [89]	EPM – MC	5.48	5.25	2.99	5.94
Fischetti (1991b) [86]	EPM NL	4.1	3.5	3.1	3.9
“Experimental” [159]	PL + MC	8.2 [121]	6.5 [321], 7 [164]		
“Effective” DFT [324]	DFT-Conwell		7.9		
InAs					
Fischetti (1991a) [89]	EPM – MC	6.35	5.59	3.36	6.35
Fischetti (1991b) [86]	EPM NL	4.4	3.1	2.8	3.6

TO) with an overall “effective” frequency  $\omega_{\text{eff}}$ , defined in Fischetti’s paper as:

$$(Dq)^2 = (D_{\text{LA}q_{\text{LA}}})^2 + (D_{\text{TA}q_{\text{TA}}})^2 + (D_{\text{OP}})^2 \quad (\text{D.1})$$

where  $D_{\text{LA}}$ ,  $D_{\text{TA}}$  and  $D_{\text{OP}}$  are the fitted acoustical and optical deformation potentials (LO and TO phonons are lumped in a single optical mode), and  $q_m$  is the phonon wavevector of the considered transition with phonon mode ( $m$ ). The paper makes here the approximation of a flat optical phonon mode, characterized by a single frequency  $\omega_{\text{OP}}$  and linear acoustical modes characterized with sound velocity  $v_{\text{AC}}$ . As mentioned in Sjakste *et al.* (2007) [324], the comparison of Monte Carlo “effective” deformation potential with the deformation potentials extracted with DFT is not trivial and should be taken with care. In particular, it depends on the chosen effective phonon frequency, but also the temperature of the measurement. The averaging of the *ab initio* deformation potential over the final wavevector  $k$  can also have a strong impact. In KG simulation, a single intervalley process is often considered and these “effective” deformation potential are often used, as it was done in Section 3.1.3.



# Bibliography

- [1] A. Abramo, L. Baudry, R. Brunetti, R. Castagne, M. Charef, F. Dessenne, P. Dollfus, R. Dutton, W. Engl, R. Fauquembergue, et al. A comparison of numerical solutions of the Boltzmann transport equation for high-energy electron transport silicon. *IEEE Transactions on Electron Devices*, 41(9):1646–1654, 1994.
- [2] S. Adachi. *GaAs and related materials: bulk semiconducting and superlattice properties*. World Scientific, 1994.
- [3] K. C. Akyel, L. Ciampolini, O. Thomas, D. Turgis, and G. Ghibaudo. Impact of random telegraph signals on 6T high-density SRAM in 28nm UTBB FD-SOI. In *Solid State Device Research Conference (ESSDERC), 2014 44th European*, pages 94–97. IEEE, 2014.
- [4] A. Alian, G. Brammertz, R. Degraeve, M. Cho, C. Merckling, D. Lin, W.-E. Wang, M. Caymax, M. Meuris, K. De Meyer, et al. Oxide trapping in the InGaAs–Al<sub>2</sub>O<sub>3</sub> system and the role of sulfur in reducing the trap density. *Electron Device Letters, IEEE*, 33(11):1544–1546, 2012.
- [5] A. Alian, M. A. Pourghaderi, Y. Mols, M. Cantoro, T. Ivanov, N. Collaert, and A. Thean. Impact of the channel thickness on the performance of ultrathin InGaAs channel MOSFET devices. In *Electron Devices Meeting (IEDM), 2013 IEEE International*, pages 16–6. IEEE, 2013.
- [6] A. Alkauskas, Q. Yan, and C. G. Van de Walle. First-principles theory of nonradiative carrier capture via multiphonon emission. *Physical Review B*, 90(7):075202, 2014.
- [7] V. A. Altschul, A. Fraenkel, and E. Finkman. Effects of band nonparabolicity on two-dimensional electron gas. *Journal of applied physics*, 71(9):4382–4384, 1992.
- [8] M. Anantram, M. S. Lundstrom, and D. E. Nikonov. Modeling of nanoscale devices. *Proceedings of the IEEE*, 96(9):1511–1550, 2008.
- [9] M. Ancona and G. Iafrate. Quantum correction to the equation of state of an electron gas in a semiconductor. *Physical Review B*, 39(13):9536, 1989.
- [10] P. W. Anderson. Absence of diffusion in certain random lattices. *Phys. Rev.*, 109(5):1492, 1958.
- [11] F. Andrieu, M. Casse, E. Baylac, P. Perreau, O. Nier, D. Rideau, R. Berthelon, F. Pourchon, A. Pofelski, B. De Salvo, et al. Strain and layout management in dual channel (sSOI substrate, SiGe channel) planar FDSOI MOSFETs. In *Solid State Device Research Conference (ESSDERC), 2014 44th European*, pages 106–109. IEEE, 2014.

- 
- [12] Archimedes. <http://www.gnu.org/software/archimedes/>.
- [13] N. W. Ashcroft and N. D. Mermin. *Solid State Physics*. Holt, Rinehart and Winston, 1976.
- [14] D. Aspnes. GaAs lower conduction-band minima: ordering and properties. *Physical Review B*, 14(12):5331, 1976.
- [15] M. Auslender and S. Hava. On the calculation of alloy scattering relaxation time for ternary III–V and II–VI semiconductors. *Solid state communications*, 87(4):335–339, 1993.
- [16] G. Baccarani, E. Gnani, A. Gnudi, S. Reggiani, and M. Rudan. Theoretical foundations of the quantum drift-diffusion and density-gradient models. *Solid-State Electronics*, 52(4):526–532, 2008.
- [17] O. Badami, E. Caruso, D. Lizzit, P. Osgnach, D. Esseni, P. Palestri, and L. Selmi. An improved surface roughness scattering model for bulk, thin-body, and quantum-well MOSFETs. *IEEE Transactions on Electron Devices*, 63(6):2306–2312, 2016.
- [18] R.-H. Baek, D.-H. Kim, T.-W. Kim, C. Shin, W. Park, T. Michalak, C. Borst, S. Song, G. Yeap, R. Hill, et al. Electrostatics and performance benchmarking using all types of III–V multi-gate FinFETs for sub 7nm technology node logic application. In *VLSI Technology (VLSI-Technology): Digest of Technical Papers, 2014 Symposium on*, pages 1–2. IEEE, 2014.
- [19] T. B. Bahder. Eight-band kp model of strained zinc-blende crystals. *Physical Review B*, 41(17):11992, 1990.
- [20] J. Bardeen and W. Shockley. Deformation potentials and mobilities in non-polar crystals. *Physical Review*, 80(1):72, 1950.
- [21] G. Bastard. Self-consistent variational calculations and alloy scattering in semiconductor heterojunctions. *Surface Science*, 142(1-3):284–289, 1984.
- [22] B. Benbakhti, E. Towie, K. Kalna, G. Hellings, G. Eneman, K. De Meyer, M. Meuris, and A. Asenov. Monte Carlo analysis of In<sub>0.57</sub>Ga<sub>0.43</sub>As implant-free quantum-well device performance. In *Silicon Nanoelectronics Workshop (SNW), 2010*, pages 1–2. IEEE, 2010.
- [23] D. BenDaniel and C. Duke. Space-charge effects on electron tunneling. *Physical Review*, 152(2):683, 1966.
- [24] S. J. Bentley, M. Holland, X. Li, G. W. Paterson, H. Zhou, O. Ignatova, D. Macintyre, S. Thoms, A. Asenov, B. Shin, et al. Electron mobility in surface-and buried-channel flatband In<sub>0.57</sub>Ga<sub>0.43</sub>As MOSFETs with ALD Al<sub>2</sub>O<sub>3</sub> gate dielectric. *IEEE Electron Device Letters*, 32(4):494–496, 2011.
- [25] O. Berolo, J. C. Woolley, and J. Van Vechten. Effect of disorder on the conduction-band effective mass, valence-band spin-orbit splitting, and the direct band gap in III-V alloys. *Physical Review B*, 8(8):3794, 1973.
- [26] R. Berthelon, F. Andrieu, S. Ortolland, R. Nicolas, T. Poiroux, E. Baylac, D. Dutartre, E. Josse, A. Claverie, and M. Haond. Characterization and modelling of layout effects in SiGe channel pMOSFETs from 14nm UTBB FDSOI technology. *Solid-State Electronics*, 128:72–79, 2017.
- [27] R. Berthelon, F. Andrieu, P. Perreau, D. Cooper, F. Roze, O. Gourhant, P. Rivallin, N. Bernier, A. Cros, C. Ndiaye, et al. A novel dual isolation scheme for stress and

- back-bias maximum efficiency in FDSOI technology. In *Electron Devices Meeting (IEDM), 2016 IEEE International*, pages 17–7. IEEE, 2016.
- [28] M. Biercuk, D. Monsma, C. Marcus, J. Becker, and R. Gordon. Low-temperature atomic-layer-deposition lift-off method for microelectronic and nanoelectronic applications. *Applied Physics Letters*, 83(12):2405–2407, 2003.
- [29] M. Billaud, J. Duvernay, H. Grampeix, B. Pelissier, M. Martin, T. Baron, H. Boutry, Z. Chalupa, M. Casse, T. Ernst, et al. Al<sub>2</sub>O<sub>3</sub>/InGaAs interface study on MOS capacitors for a 300nm process integration. In *Ultimate Integration on Silicon (EUROSOI-ULIS), 2015 Joint International EUROSOI Workshop and International Conference on*, pages 113–116. IEEE, 2015.
- [30] M. Billaud, J. Duvernay, H. Grampeix, B. Pelissier, M. Martin, S. David, C. Vallée, Z. Chalupa, H. Boutry, T. Baron, et al. HfO<sub>2</sub>/Al<sub>2</sub>O<sub>3</sub>/InGaAs MOSCAP structures and InGaAs plasma nitridation elaborated in a 300nm pilot line. *ECS Transactions*, 69(5):9–13, 2015.
- [31] G. L. Bir, G. E. Pikus, P. Shelnitz, and D. Louvish. *Symmetry and strain-induced effects in semiconductors*, volume 624. Wiley New York, 1974.
- [32] J. S. Blakemore. *Gallium Arsenide: Edited by John S. Blakemore*. Number 1. Springer Science & Business Media, 1961.
- [33] D. Bohm. A suggested interpretation of the quantum theory in terms of “hidden” variables. I. *Physical Review*, 85(2):166, 1952.
- [34] L. Bourdet, J. Li, J. Pelloux-Prayer, F. Triozon, M. Cassé, S. Barraud, S. Martinie, D. Rideau, and Y.-M. Niquet. Contact resistances in trigate and FinFET devices in a non-equilibrium Green’s functions approach. *Journal of Applied Physics*, 119(8):084503, 2016.
- [35] S. Boyer-Richard, F. Raouafi, A. Bondi, L. Pedesseau, C. Katan, J.-M. Jancu, and J. Even. 30-band k.p method for quantum semiconductor heterostructures. *Applied Physics Letters*, 98:251913, 2011.
- [36] T. B. Boykin, N. Kharche, and G. Klimeck. Brillouin-zone unfolding of perfect supercells having nonequivalent primitive cells illustrated with a Si/ Ge tight-binding parameterization. *Physical Review B*, 76(3):035310, 2007.
- [37] T. B. Boykin, N. Kharche, G. Klimeck, and M. Korkusinski. Approximate band-structures of semiconductor alloys from tight-binding supercell calculations. *Journal of Physics: Condensed Matter*, 19(3):036203, 2007.
- [38] T. B. Boykin, G. Klimeck, R. C. Bowen, and F. Oyafuso. Diagonal parameter shifts due to nearest-neighbor displacements in empirical tight-binding theory. *Physical Review B*, 66(12):125207, 2002.
- [39] T. B. Boykin, G. Klimeck, and F. Oyafuso. Valence band effective-mass expressions in the sp<sup>3</sup> d<sup>5</sup> s\* empirical tight-binding model applied to a Si and Ge parametrization. *Physical Review B*, 69(11):115201, 2004.
- [40] T. Brody and H. Kunig. A high-gain InAs thin-film transistor. *Applied Physics Letters*, 9(7):259–260, 1966.
- [41] S. C. Brugger. *Computation of semiconductor properties using moments of the inverse scattering operator of the Boltzmann equation*. PhD thesis, Swiss Federal Institute of Technology Zurich, 2005.

- 
- [42] M. Burt. The justification for applying the effective-mass approximation to microstructures. *Journal of Physics: Condensed Matter*, 4(32):6651, 1992.
- [43] D. L. Camphausen, G. N. Connell, and W. Paul. Calculation of energy-band pressure coefficients from the dielectric theory of the chemical bond. *Physical Review Letters*, 26(4):184, 1971.
- [44] S. Carapezzi, E. Caruso, A. Gnudi, S. Reggiani, and E. Gnani. TCAD low-field mobility model for InGaAs UTB MOSFETs including quasi-ballistic corrections. In *Solid-State Device Research Conference (ESSDERC), 2016 46th European*, pages 416–419. IEEE, 2016.
- [45] M. Cardona and F. H. Pollak. Energy-band structure of germanium and silicon: The  $k \cdot p$  method. *Physical Review*, 142(2):530, 1966.
- [46] E. Caruso. Modeling approaches for band-structure calculation in III-V FET quantum wells. In *EUROSOI-ULIS 2015-2015 Joint International EUROSOI Workshop and International Conference on Ultimate Integration on Silicon*, pages 101–104. IEEE, 2015.
- [47] E. Caruso, D. Lizzit, P. Osgnach, D. Esseni, P. Palestri, and L. Selmi. Simulation analysis of III–V n-MOSFETs: Channel materials, fermi level pinning and biaxial strain. In *2014 IEEE International Electron Devices Meeting*, pages 7–6. IEEE, 2014.
- [48] C. S. Chang and H. R. Fetterman. Electron drift velocity versus electric field in GaAs. *Solid-state electronics*, 29(12):1295–1296, 1986.
- [49] C. Y.-P. Chao and S. L. Chuang. Spin-orbit-coupling effects on the valence-band structure of strained semiconductor quantum wells. *Physical Review B*, 46(7):4110, 1992.
- [50] J. R. Chelikowsky and M. L. Cohen. Electronic structure of silicon. *Physical Review B*, 10(12):5095, 1974.
- [51] J. R. Chelikowsky and M. L. Cohen. Nonlocal pseudopotential calculations for the electronic structure of eleven diamond and zinc-blende semiconductors. *Physical Review B*, 14:556, 1976.
- [52] K. Cheng, A. Cho, S. Christman, T. Pearsall, and J. Rowe. Measurement of the  $\Gamma$ -L separation in  $\text{Ga}_{0.47}\text{In}_{0.53}\text{As}$  by ultraviolet photoemission. *Applied Physics Letters*, 40(5):423–425, 1982.
- [53] T.-C. Chiang, J. Knapp, M. Aono, and D. Eastman. Angle-resolved photoemission, valence-band dispersions  $e(k)$ , and electron and hole lifetimes for GaAs. *Physical Review B*, 21(8):3513, 1980.
- [54] M. L. Cohen and T. Bergstresser. Band structures and pseudopotential form factors for fourteen semiconductors of the diamond and zinc-blende structures. *Physical Review*, 141(2):789, 1966.
- [55] D. Colleoni, G. Miceli, and A. Pasquarello. Origin of fermi-level pinning at GaAs surfaces and interfaces. *Journal of Physics: Condensed Matter*, 26(49):492202, 2014.
- [56] D. Colleoni, G. Miceli, and A. Pasquarello. Arsenic related defect states resonant with the semiconductor conduction band at the  $\text{In}_{0.53}\text{Ga}_{0.47}\text{As}$ /oxide interface: A density functional study. *Microelectronic Engineering*, 147:260–263, 2015.
- [57] D. Colleoni, G. Miceli, and A. Pasquarello. Band alignment and chemical bonding

- at the GaAs/Al<sub>2</sub>O<sub>3</sub> interface: A hybrid functional study. *Applied Physics Letters*, 107(21):211601, 2015.
- [58] E. Conwell. High field transport in semiconductors. In D. Turnbull and H. Ehrenreich, editors, *Solid State Physics*, volume 9. Academic Press: New York and London, 1967.
- [59] E. M. Conwell and M. O. Vassell. High-field transport in *n*-type GaAs. *Phys. Rev.*, 166:797–821, Feb 1968.
- [60] R. Courtland. Transistors could stop shrinking in 2021. *IEEE Spectrum*, 53(9):9–11, 2016.
- [61] A. Cresti, M. G. Pala, S. Poli, M. Mouis, and G. Ghibaudo. A comparative study of surface-roughness-induced variability in silicon nanowire and double-gate FETs. *IEEE Transactions on Electron Devices*, 58(8):2274–2281, 2011.
- [62] S. Cristoloveanu, N. Rodriguez, and F. Gamiz. Why the universal mobility is not. *IEEE Transactions on Electron Devices*, 57(6):1327–1333, 2010.
- [63] Damocles. <http://gloworm.stanford.edu/tcad/research/damocles.html>.
- [64] C. de Falco. *Quantum-corrected drift-diffusion models and numerical simulation of nanoscale semiconductor devices*. PhD thesis, Ph. D. thesis, Universita degli Studi di Milano, 2006.
- [65] C. De Falco, E. Gatti, A. L. Lacaita, and R. Sacco. Quantum-corrected drift-diffusion models for transport in semiconductor devices. *Journal of Computational Physics*, 204(2):533–561, 2005.
- [66] J. A. Del Alamo, D. A. Antoniadis, J. Lin, W. Lu, A. Vardi, and X. Zhao. Nanometer-scale III-V MOSFETs. *IEEE Journal of the Electron Devices Society*, 4(5):205–214, 2016.
- [67] C. Delerue, G. Allan, and M. Lannoo. Electron-phonon coupling and optical transitions for indirect-gap semiconductor nanocrystals. *Physical Review B*, 64(19):193402, 2001.
- [68] C. Delerue and M. Lannoo. *Nanostructures: theory and modelling*. Springer Science & Business Media, 2004.
- [69] C. Delerue and M. Lannoo. *Nanostructures: theory and modelling*. Springer Science & Business Media, 2004.
- [70] R. Dittich and W. Schroeder. Empirical pseudopotential band structure of In<sub>0.53</sub>Ga<sub>0.47</sub>As and In<sub>0.52</sub>Al<sub>0.48</sub>As. *Solid-State Electronics*, 43(2):403–407, 1999.
- [71] V. Djara, T. O'Regan, K. Cherkaoui, M. Schmidt, S. Monaghan, É. O'Connor, I. Povey, D. O'Connell, M. Pemble, and P. Hurley. Electrically active interface defects in the In<sub>0.53</sub>Ga<sub>0.47</sub>As MOS system. *Microelectronic Engineering*, 109:182–188, 2013.
- [72] V. Djara, M. Sousa, N. Dordevic, L. Czornomaz, V. Deshpande, C. Marchiori, E. Uccelli, D. Caimi, C. Rossel, and J. Fompeyrine. Low Dit HfO<sub>2</sub>/Al<sub>2</sub>O<sub>3</sub>/In<sub>0.53</sub>Ga<sub>0.47</sub>As gate stack achieved with plasma-enhanced atomic layer deposition. *Microelectronic Engineering*, 147:231–234, 2015.
- [73] L. Donetti, F. Gámiz, N. Rodriguez, F. Jimenez, and C. Sampedro. Influence of acoustic phonon confinement on electron mobility in ultrathin silicon on insulator layers. *Applied physics letters*, 88(12):122108, 2006.

- [74] C. Dou, D. Lin, A. Vais, T. Ivanov, H.-P. Chen, K. Martens, K. Kakushima, H. Iwai, Y. Taur, A. Thean, et al. Determination of energy and spatial distribution of oxide border traps in in 0.53 ga 0.47 as mos capacitors from capacitance–voltage characteristics measured at various temperatures. *Microelectronics Reliability*, 54(4):746–754, 2014.
- [75] G. Dresselhaus, A. Kip, and C. Kittel. Cyclotron resonance of electrons and holes in silicon and germanium crystals. *Physical Review*, 98(2):368, 1955.
- [76] W. Drube, D. Straub, and F. Himpsel. Inverse photoemission study of InP, InAs, and InSb. *Physical Review B*, 35(11):5563, 1987.
- [77] R. C. Eden. The development of the first LSI GaAs integrated circuits and the path to the commercial market. *Proceedings of the IEEE*, 76(7):756–777, 1988.
- [78] L. F. Edge, D. G. Schlom, R. Brewer, Y. Chabal, J. R. Williams, S. A. Chambers, C. Hinkle, G. Lucovsky, Y. Yang, S. Stemmer, et al. Suppression of subcutaneous oxidation during the deposition of amorphous lanthanum aluminate on silicon. *Applied physics letters*, 84(23):4629–4631, 2004.
- [79] H. Ehrenreich. Band structure and electron transport of gaas. *Physical Review*, 120(6):1951, 1960.
- [80] R. Engel-Herbert, Y. Hwang, and S. Stemmer. Comparison of methods to quantify interface trap densities at dielectric/III-V semiconductor interfaces. *Journal of Applied Physics*, 108(12):124101, 2010.
- [81] D. Esseni, A. Abramo, L. Selmi, and E. Sangiorgi. Physically based modeling of low field electron mobility in ultrathin single-and double-gate SOI n-MOSFETs. *IEEE Transactions on Electron Devices*, 50(12):2445–2455, 2003.
- [82] D. Esseni and P. Palestri. Linear combination of bulk bands method for investigating the low-dimensional electron gas in nanostructured devices. *Physical Review B*, 72(16):165342, 2005.
- [83] D. Esseni, P. Palestri, and L. Selmi. *Nanoscale MOS transistors: semi-classical transport and applications*. Cambridge University Press, 2011.
- [84] I. Ferain, C. A. Colinge, and J.-P. Colinge. Multigate transistors as the future of classical metal-oxide-semiconductor field-effect transistors. *Nature*, 479(7373):310–316, 2011.
- [85] M. Fischetti. Long-range Coulomb interactions in small Si devices. part II. effective electron mobility in thin-oxide structures. *Journal of Applied Physics*, 89(2):1232–1250, 2001.
- [86] M. Fischetti and J. Higman. Theory and calculation of the deformation potential electron-phonon scattering rates in semiconductors. In *Monte Carlo Device Simulation*, pages 123–160. Springer, 1991.
- [87] M. Fischetti, S. Jin, T.-W. Tang, P. Asbeck, Y. Taur, S. Laux, and N. Sano. Scaling MOSFETs to 10 nm: Coulomb effects, source starvation, and virtual source. In *Computational Electronics, 2009. IWCE'09. 13th International Workshop on*, pages 1–4. IEEE, 2009.
- [88] M. Fischetti and S. Laux. Long-range Coulomb interactions in small Si devices. part I: performance and reliability. *Journal of Applied Physics*, 89(2):1205–1231, 2001.
- [89] M. V. Fischetti. Monte Carlo simulation of transport in technologically significant

- semiconductors of the diamond and zinc-blende structures. I. homogeneous transport. *Electron Devices, IEEE Transactions on*, 38(3):634–649, 1991.
- [90] M. V. Fischetti and S. E. Laux. Monte Carlo analysis of electron transport in small semiconductor devices including band-structure and space-charge effects. *Physical Review B*, 38(14):9721, 1988.
- [91] M. V. Fischetti and S. E. Laux. Monte carlo study of electron transport in silicon inversion layers. *Physical Review B*, 48(4):2244, 1993.
- [92] M. V. Fischetti and S. E. Laux. Band structure, deformation potentials, and carrier mobility in strained Si, Ge, and SiGe alloys. *Journal of Applied Physics*, 80(4):2234–2252, 1996.
- [93] M. V. Fischetti, D. A. Neumayer, and E. A. Cartier. Effective electron mobility in Si inversion layers in metal–oxide–semiconductor systems with a high- $\kappa$  insulator: The role of remote phonon scattering. *Journal of Applied Physics*, 90(9):4587–4608, 2001.
- [94] M. V. Fischetti, T. P. O’Regan, S. Narayanan, C. Sachs, S. Jin, J. Kim, and Y. Zhang. Theoretical study of some physical aspects of electronic transport in nMOSFETs at the 10-nm gate-length. *IEEE Transactions on Electron Devices*, 54(9):2116–2136, 2007.
- [95] G. Fishman. *Semi-conducteurs: les bases de la théorie kp*. Editions Ecole Polytechnique, 2010.
- [96] B. A. Foreman. Effective-mass hamiltonian and boundary conditions for the valence bands of semiconductor microstructures. *Physical Review B*, 48(7):4964, 1993.
- [97] R. H. French. Electronic band structure of Al<sub>2</sub>O<sub>3</sub>, with comparison to Alon and AlN. *Journal of the American Ceramic Society*, 73(3):477–489, 1990.
- [98] W. R. Frensley. Variational formulation of stable discrete k p models. In *Computational Electronics (IWCE), 2015 International Workshop on*, pages 1–4. IEEE, 2015.
- [99] P. Friedel, M. Hybertsen, and M. Schlüter. Local empirical pseudopotential approach to the optical properties of Si/Ge superlattices. *Physical Review B*, 39(11):7974, 1989.
- [100] H. Fröhlich. Theory of electrical breakdown in ionic crystals. *Proceedings of the Royal Society of London. Series A, Mathematical and Physical Sciences*, 160(901):230–241, 1937.
- [101] H. Fröhlich. Theory of electrical breakdown in ionic crystals. ii. *Proceedings of the Royal Society of London. Series A, Mathematical and Physical Sciences*, 172(948):94–106, 1939.
- [102] R. Galatage, D. Zhernokletov, H. Dong, B. Brennan, C. Hinkle, R. Wallace, and E. Vogel. Accumulation capacitance frequency dispersion of III-V metal-insulator-semiconductor devices due to disorder induced gap states. *Journal of Applied Physics*, 116(1):014504, 2014.
- [103] F. Gamiz and J. Roldan. Scattering of electrons in silicon inversion layers by remote surface roughness. *Journal of applied physics*, 94(1):392–399, 2003.
- [104] GARAND. <http://www.goldstandardsimulations.com/products/garand/>.

- [105] D. Garetto. *Numerical and Compact Modeling of Embedded Flash Memory Devices Targeted for IC Design*. PhD thesis, EPFL, 2012.
- [106] D. Garetto, Y. M. Randriamihaja, D. Rideau, A. Schmid, and H. Jaouen. Comparing defect characterization techniques with non-radiative multiphonon charge trapping model. *Journal of Computational Electronics*, 11(3):225–237, 2012.
- [107] D. Garetto, Y. M. Randriamihaja, D. Rideau, A. Zaka, A. Schmid, Y. Leblebici, and H. Jaouen. Modeling stressed MOS oxides using a multiphonon-assisted quantum approach?part II: transient effects. *Electron Devices, IEEE Transactions on*, 59(3):621–630, 2012.
- [108] D. Garetto, Y. M. Randriamihaja, A. Zaka, D. Rideau, A. Schmid, H. Jaouen, and Y. Leblebici. Analysis of defect capture cross sections using non-radiative multiphonon-assisted trapping model. *Solid-State Electronics*, 71:74–79, 2012.
- [109] D. Gershoni, C. Henry, and G. Baraff. Calculating the optical properties of multi-dimensional heterostructures: Application to the modeling of quaternary quantum well lasers. *Quantum Electronics, IEEE Journal of*, 29(9):2433–2450, 1993.
- [110] G. Ghibaudo and T. Boutchacha. Electrical noise and RTS fluctuations in advanced CMOS devices. *Microelectronics Reliability*, 42(4):573–582, 2002.
- [111] G. Gilat and L. Raubenheimer. Accurate numerical method for calculating frequency-distribution functions in solids. *Physical Review*, 144(2):390, 1966.
- [112] GlobalTCAD. <http://www.globaltcad.com/en/home.html>.
- [113] D. Goguenheim and M. Lannoo. Theoretical and experimental aspects of the thermal dependence of electron capture coefficients. *Journal of Applied Physics*, 68(3):1059–1069, 1990.
- [114] J. Goldberger, A. I. Hochbaum, R. Fan, and P. D. Yang. Silicon vertically integrated nanowire field effect transistors. *Nano Lett.*, 6(5):973–977, MAY 2006.
- [115] X. Gonze, J.-M. Beuken, R. Caracas, F. Detraux, M. Fuchs, G.-M. Rignanese, L. Sindic, M. Verstraete, G. Zerah, F. Jollet, et al. First-principles computation of material properties: the ABINIT software project. *Computational Materials Science*, 25(3):478–492, 2002.
- [116] T. Grasser, H. Kosina, M. Gritsch, and S. Selberherr. Using six moments of Boltzmann’s transport equation for device simulation. *Journal of Applied Physics*, 90(5):2389–2396, 2001.
- [117] T. Grasser, T.-W. Tang, H. Kosina, and S. Selberherr. A review of hydrodynamic and energy-transport models for semiconductor device simulation. *Proceedings of the IEEE*, 91(2):251–274, 2003.
- [118] G. Greene-Diniz, M. Fischetti, and J. Greer. Energies of the X-and L-valleys in  $\text{In}_{0.53}\text{Ga}_{0.47}\text{As}$  from electronic structure calculations. *Journal of Applied Physics*, 119(5):055707, 2016.
- [119] G. F. Greene-Diniz. *Computational modeling of defects in nanoscale device materials*. PhD thesis, 2014.
- [120] D. A. Greenwood. The boltzmann equation in the theory of electrical conduction in metals. *Proceedings of the Physical Society*, 71(4):585, 1958.
- [121] S. Guha, Q. Cai, M. Chandrasekhar, H. R. Chandrasekhar, H. Kim, A. Alvarenga, R. Vogelgesang, A. Ramdas, and M. Melloch. Photoluminescence of short-period

- GaAs/AlAs superlattices: A hydrostatic pressure and temperature study. *Physical Review B*, 58(11):7222, 1998.
- [122] D. Guo, G. Karve, G. Tsutsui, K. Lim, R. Robison, T. Hook, R. Vega, D. Liu, S. Bedell, S. Mochizuki, et al. FinFET technology featuring high mobility SiGe channel for 10nm and beyond. In *VLSI Technology, 2016 IEEE Symposium on*, pages 1–2. IEEE, 2016.
- [123] W. Hackenberg and G. Fasol. Polar optic phonon and  $\Gamma$  - L intervalley scattering times in GaAs from steady-state hot-electron luminescence spectroscopy. *Applied Physics Letters*, 57(2):174–176, 1990.
- [124] W. A. Harrison. Tunneling from an independent-particle point of view. *Physical Review*, 123(1):85, 1961.
- [125] W. A. Harrison. *Electronic structure and the properties of solids: the physics of the chemical bond*. Courier Corporation, 2012.
- [126] J. Hauser, M. Littlejohn, and T. Glisson. Velocity-field relationship of InAs-InP alloys including the effects of alloy scattering. *Applied Physics Letters*, 28(8):458–461, 1976.
- [127] G. Helmig. Zur theorie der störstellenelektronen. ii strahlungslose übergänge. *Annalen der Physik*, 454(1-2):41–54, 1956.
- [128] C. Henry and D. V. Lang. Nonradiative capture and recombination by multiphonon emission in GaAs and GaP. *Physical Review B*, 15(2):989, 1977.
- [129] J. Hensel, H. Hasegawa, and M. Nakayama. Cyclotron resonance in uniaxially stressed silicon. II. nature of the covalent bond. *Physical Review*, 138(1A):A225, 1965.
- [130] C. Herring and E. Vogt. Transport and deformation-potential theory for many-valley semiconductors with anisotropic scattering. *Physical Review*, 101(3):944, 1956.
- [131] G. Hiblot. *Modélisation compacte de transistors MOSFETs à canal III-V et films minces pour applications CMOS avancées*. PhD thesis, Grenoble Alpes, 2015.
- [132] G. Hiblot, G. Mugny, Q. Rafhay, F. Boeuf, and G. Ghibaudo. Compact model for inversion charge in III–V bulk MOSFET including non-parabolicity. *IEEE Transactions on Nanotechnology*, 14(4):768–775, 2015.
- [133] G. Hiblot, Q. Rafhay, G. Mugny, F. Boeuf, and G. Ghibaudo. Impact of band-structure effects in III–V nMOSFETS. In *International Conference on Solid State Devices and Materials*. IEEE, 2015.
- [134] G. Hiblot, Q. Rafhay, G. Mugny, G. Ghibaudo, and F. Boeuf. CMOS roadmap analysis from the perspective of III-V technology using MASTAR. In *2015 Silicon Nanoelectronics Workshop (SNW)*, pages 1–2. IEEE, 2015.
- [135] A. Huang, P. K. Chu, H. Yan, and M. Zhu. Dielectric properties enhancement of ZrO<sub>2</sub> thin films induced by substrate biasing. *Journal of Vacuum Science & Technology B: Microelectronics and Nanometer Structures Processing, Measurement, and Phenomena*, 23(2):566–569, 2005.
- [136] J. Z. Huang, K. Wang, W. R. Frensley, and G. Klimeck. Finite difference schemes for kp models: A comparative study. In *Computational Electronics (IWCE), 2015 International Workshop on*, pages 1–2. IEEE, 2015.

- 
- [137] K. Huang. Adiabatic approximation-theory and static coupling theory of nonradiative transition. *Scientia Sinica*, XXIV:27, 1981.
- [138] K. Huang and A. Rhys. Theory of light absorption and non-radiative transitions in F-centres. In *Proceedings of the Royal Society of London A: Mathematical, Physical and Engineering Sciences*, volume 204, pages 406–423. The Royal Society, 1950.
- [139] T. Irisawa, M. Oda, K. Ikeda, Y. Moriyama, E. Mieda, W. Jevasuwan, T. Maeda, O. Ichikawa, T. Osada, M. Hata, et al. High electron mobility triangular InGaAs-OI nMOSFETs with (111) B side surfaces formed by MOVPE growth on narrow fin structures. In *Electron Devices Meeting (IEDM), 2013 IEEE International*, pages 2–2. IEEE, 2013.
- [140] ITRS report. <http://www.itrs2.net/itrs-reports.html>, .
- [141] C. Jacoboni, C. Canali, G. Ottaviani, and A. A. Quaranta. A review of some charge transport properties of silicon. *Solid State Electron.*, 20(2):77 – 89, 1977.
- [142] C. Jacoboni, F. Nava, C. Canali, and G. Ottaviani. Electron drift velocity and diffusivity in germanium. *Physical Review B*, 24(2):1014, 1981.
- [143] C. Jacoboni and L. Reggiani. Bulk hot-electron properties of cubic semiconductors. *Adv. Phys.*, 28(4):493–553, 1979.
- [144] C. Jacoboni and L. Reggiani. The Monte Carlo method for the solution of charge transport in semiconductors with applications to covalent materials. *Rev. Mod. Phys.*, 55:645–705, Jul 1983.
- [145] J.-M. Jancu, R. Scholz, F. Beltram, and F. Bassani. Empirical  $sp^3d^5s^*$  tight-binding calculation for cubic semiconductors: General method and material parameters. *Physical Review B*, 57(11):6493, 1998.
- [146] K. Jansson, E. Lind, and L.-E. Wernersson. Intrinsic performance of InAs nanowire capacitors. *IEEE Transactions on Electron Devices*, 61(2):452–459, 2014.
- [147] W. Jevasuwan, T. Maeda, N. Miyata, M. Oda, T. Irisawa, T. Tezuka, and T. Yasuda. Self-limiting growth of ultrathin  $Ga_2O_3$  for the passivation of  $Al_2O_3/InGaAs$  interfaces. *Applied Physics Express*, 7(1):011201, 2013.
- [148] H. Jiang, S. Shao, W. Cai, and P. Zhang. Boundary treatments in non-equilibrium Green’s function (NEGF) methods for quantum transport in nano-MOSFETs. *Journal of Computational Physics*, 227(13):6553–6573, 2008.
- [149] S. Jin, M. V. Fischetti, and T.-w. Tang. Modeling of electron mobility in gated silicon nanowires at room temperature: Surface roughness scattering, dielectric screening, and band nonparabolicity. *Journal of Applied Physics*, 102(8):083715, 2007.
- [150] S. Jin, A.-T. Pham, W. Choi, Y. Nishizawa, Y.-T. Kim, K.-H. Lee, Y. Park, and E. S. Jung. Performance evaluation of InGaAs, Si, and Ge nFinFETs based on coupled 3d drift-diffusion/multisubband Boltzmann transport equations solver. In *Electron Devices Meeting (IEDM), 2014 IEEE International*, pages 7–5. IEEE, 2014.
- [151] S. Jit. *Advances in microelectronics and photonics*. Nova Science Publishers, Inc, 2011.
- [152] S. Joshi, C. Krug, D. Heh, H. J. Na, H. R. Harris, J. W. Oh, P. D. Kirsch, P. Majhi, B. H. Lee, H.-H. Tseng, et al. Improved Ge surface passivation with ultrathin  $SiO_x$  enabling high-mobility surface channel pMOSFETs featuring a HfSiO/WN gate stack. *IEEE electron device letters*, 28(4):308–311, 2007.

- 
- [153] C. Jungemann, A. Emunds, and W. Engl. Simulation of linear and nonlinear electron transport in homogeneous silicon inversion layers. *Solid-state electronics*, 36(11):1529–1540, 1993.
- [154] C. Jungemann, A. Emunds, and W. Engl. Simulation of linear and nonlinear electron transport in homogeneous silicon inversion layers. *Solid State Electron.*, 36(11):1529 – 1540, 1993.
- [155] C. Jungemann, T. Grasser, B. Neinhuis, and B. Meinerzhagen. Failure of moments-based transport models in nanoscale devices near equilibrium. *IEEE Transactions on Electron Devices*, 52(11):2404–2408, 2005.
- [156] E. O. Kane. Band structure of indium antimonide. *Journal of Physics and Chemistry of Solids*, 1(4):249–261, 1957.
- [157] M. Karner, Z. Stanojevic, F. Mitterbauer, C. Kernstock, and H. Demel. Bringing physics to device design - a fast and predictive device simulation framework. In *Silicon Nanoelectronics Workshop (SNW), 2015*, pages 1–2. IEEE, 2015.
- [158] J. Kash. Hot-electron luminescence: A comparison of GaAs and InP. *Physical Review B*, 47(3):1221, 1993.
- [159] J. Kash and J. Tsang. Light scattering and other secondary emission studies of dynamic processes in semiconductors. In *Light Scattering in Solids VI*, pages 423–518. Springer, 1991.
- [160] L. V. Keldysh et al. Diagram technique for nonequilibrium processes. *Sov. Phys. JETP*, 20(4):1018–1026, 1965.
- [161] F. Khan and P. Allen. Deformation potentials and electron-phonon scattering: Two new theorems. *Physical Review B*, 29(6):3341, 1984.
- [162] N. Kharche, M. Luisier, T. B. Boykin, and G. Klimeck. Electronic structure and transmission characteristics of SiGe nanowires. *Journal of Computational Electronics*, 7(3):350–354, 2008.
- [163] P. A. Khomyakov, M. Luisier, and A. Schenk. Compositional bowing of band energies and their deformation potentials in strained InGaAs ternary alloys: A first-principles study. *Applied Physics Letters*, 107(6):–, 2015.
- [164] D.-s. Kim and Y. Y. Peter. Hot-electron relaxations and hot phonons in GaAs studied by subpicosecond raman scattering. *Physical Review B*, 43(5):4158, 1991.
- [165] J. Kim and M. V. Fischetti. Electronic band structure calculations for biaxially strained Si, Ge, and III–V semiconductors. *Journal of Applied Physics*, 108:013710, 2010.
- [166] K. Kim, P. Kent, A. Zunger, and C. Geller. Atomistic description of the electronic structure of  $\text{In}_x\text{Ga}_{1-x}\text{As}$  alloys and InAs/GaAs superlattices. *Physical Review B*, 66(4):045208, 2002.
- [167] R. Kim, U. E. Avci, and I. A. Young. Comprehensive performance benchmarking of III-V and Si nMOSFETs (gate length= 13 nm) considering supply voltage and OFF-current. *IEEE Transactions on Electron Devices*, 62(3):713–721, 2015.
- [168] S. Kim, M. Salmani-Jelodar, K. Ng, and G. Klimeck. Quantum corrected drift-diffusion simulation for prediction of CMOS scaling. In *Device Research Conference (DRC), 2013 71st Annual*, pages 119–120. IEEE, 2013.
- [169] S. Kim, M. Yokoyama, R. Nakane, O. Ichikawa, T. Osada, M. Hata, M. Takenaka,

- and S. Takagi. High performance sub-20-nm-channel-length extremely-thin body InAs-on-insulator tri-gate MOSFETs with high short channel effect immunity and  $V_{th}$  tunability. In *Electron Devices Meeting (IEDM), 2013 IEEE International*, pages 16–4. IEEE, 2013.
- [170] T.-W. Kim, D.-H. Kim, D. Koh, H. Kwon, R. Baek, D. Veksler, C. Huffman, K. Matthews, S. Oktyabrsky, A. Greene, et al. Sub-100 nm InGaAs quantum-well (QW) tri-gate MOSFETs with  $\text{Al}_2\text{O}_3/\text{HfO}_2$  (EOT; 1 nm) for low-power logic applications. In *Electron Devices Meeting (IEDM), 2013 IEEE International*, pages 16–3. IEEE, 2013.
- [171] Y.-S. Kim, M. Marsman, G. Kresse, F. Tran, and P. Blaha. Towards efficient band structure and effective mass calculations for III-V direct band-gap semiconductors. *Physical Review B*, 82(20):205212, 2010.
- [172] D. Klaassen. A unified mobility model for device simulation - i. model equations and concentration dependence. *Solid-State Electronics*, 35(7):953–959, 1992.
- [173] J. Klimeš, M. Kaltak, and G. Kresse. Predictive G W calculations using plane waves and pseudopotentials. *Physical Review B*, 90(7):075125, 2014.
- [174] R. Kotlyar, R. Rios, C. E. Weber, T. D. Linton, M. Armstrong, and K. Kuhn. Distributive quasi-ballistic drift diffusion model including effects of stress and high driving field. *IEEE Transactions on Electron Devices*, 62(3):743–750, 2015.
- [175] I. Krylov, D. Ritter, and M. Eizenberg. The role of the substrate on the dispersion in accumulation in III-V compound semiconductor based metal-oxide-semiconductor gate stacks. *Applied Physics Letters*, 107(10):103503, 2015.
- [176] R. Kubo. Statistical-mechanical theory of irreversible processes. I. general theory and simple applications to magnetic and conduction problems. *Journal of the Physical Society of Japan*, 12(6):570–586, 1957.
- [177] Y. Lechaux, A. Fadjie-Djomkam, S. Bollaert, and N. Wichmann. Impact of oxygen plasma postoxidation process on  $\text{Al}_2\text{O}_3/\text{n-In}_{0.57}\text{Ga}_{0.43}\text{As}$  metal-oxide-semiconductor capacitors. *Applied Physics Letters*, 109(13):131602, 2016.
- [178] S. Lee, F. Oyafuso, P. von Allmen, and G. Klimeck. Boundary conditions for the electronic structure of finite-extent embedded semiconductor nanostructures. *Physical Review B*, 69:045316, Jan 2004.
- [179] A. Lherbier, M. P. Persson, Y.-M. Niquet, F. Triozon, and S. Roche. Quantum transport length scales in silicon-based semiconducting nanowires: Surface roughness effects. *Physical Review B*, 77(8):085301, 2008.
- [180] J. Li, N. Jomaa, Y.-M. Niquet, M. Said, and C. Delerue. Hole mobility in Ge/Si core/shell nanowires: What could be the optimum? *Applied Physics Letters*, 105(23):233104, 2014.
- [181] J. Li, E. Lampin, C. Delerue, and Y.-M. Niquet. Theoretical investigation of the phonon-limited carrier mobility in (001) Si films. *Journal of Applied Physics*, 120(17):174301, 2016.
- [182] J. Li, G. Mugny, Y.-M. Niquet, and C. Delerue. Drift velocity versus electric field in  $\langle 110 \rangle$  si nanowires: Strong confinement effects. *Applied Physics Letters*, 107(6):063103, 2015.

- 
- [183] J. Lin, D. A. Antoniadis, and J. A. del Alamo. Impact of intrinsic channel scaling on InGaAs quantum-well MOSFETs. *IEEE Transactions on Electron Devices*, 62(11):3470–3476, 2015.
- [184] J. Lin, S. Lee, H.-J. Oh, W. Yang, G. Lo, D. Kwong, and D. Chi. Plasma PH<sub>3</sub>-passivated high mobility inversion InGaAs MOSFET fabricated with self-aligned gate-first process and HfO<sub>2</sub>/TaN gate stack. In *Electron Devices Meeting, 2008. IEDM 2008. IEEE International*, pages 1–4. IEEE, 2008.
- [185] J. Lin, X. Zhao, T. Yu, D. A. Antoniadis, and J. A. Del Alamo. A new self-aligned quantum-well MOSFET architecture fabricated by a scalable tight-pitch process. In *Electron Devices Meeting (IEDM), 2013 IEEE International*, pages 16–2. IEEE, 2013.
- [186] L. Lin and J. Robertson. Defect states at III-V semiconductor oxide interfaces. *Applied Physics Letters*, 98(8):2903, 2011.
- [187] L. Lin and J. Robertson. Passivation of interfacial defects at III-V oxide interfaces. *Journal of Vacuum Science & Technology B*, 30(4):04E101, 2012.
- [188] E. Lind, Y.-M. Niquet, H. Mera, and L.-E. Wernersson. Accumulation capacitance of narrow band gap metal-oxide-semiconductor capacitors. *Applied Physics Letters*, 96(23):233507–233507, 2010.
- [189] M. Littlejohn, J. Hauser, T. Glisson, D. Ferry, and J. Harrison. Alloy scattering and high field transport in ternary and quaternary III–V semiconductors. *Solid-State Electronics*, 21(1):107–114, 1978.
- [190] Y. Liu, N. Neophytou, G. Klimeck, and M. S. Lundstrom. Band-structure effects on the performance of III–V ultrathin-body SOI MOSFETs. *Electron Devices, IEEE Transactions on*, 55(5):1116–1122, 2008.
- [191] D. Lizzit, D. Esseni, P. Palestri, P. Osgnach, and L. Selmi. Performance benchmarking and effective channel length for nanoscale InAs, In<sub>0.57</sub>Ga<sub>0.43</sub>As, and sSi n-MOSFETs. *IEEE transactions on Electron Devices*, 61(6):2027–2034, 2014.
- [192] D. Lizzit, D. Esseni, P. Palestri, and L. Selmi. A new formulation for surface roughness limited mobility in bulk and ultra-thin-body metal–oxide–semiconductor transistors. *Journal of Applied Physics*, 116(22):223702, 2014.
- [193] D. Lizzit, P. Palestri, D. Esseni, A. Revelant, and L. Selmi. Analysis of the performance of n-type FinFETs with strained SiGe channel. *IEEE Transactions on Electron Devices*, 60(6):1884–1891, 2013.
- [194] K. L. Low, Y.-C. Yeo, and G. Liang. Ultimate performance projection of ultrathin body transistor based on group IV, III-V, and 2-D-materials. *IEEE Transactions on Electron Devices*, 63(2):773–780, 2016.
- [195] P.-O. Löwdin. A note on the quantum-mechanical perturbation theory. *The Journal of Chemical Physics*, 19:1396, 1951.
- [196] L. Lucci. *Modeling of advanced nanometer scale MOSFETs devices with the multi-subband Monte Carlo approach*. PhD thesis, Grenoble, INPG, 2007.
- [197] L. Lucci, P. Palestri, D. Esseni, and L. Selmi. Modeling the uniform transport in thin film {SOI} {MOSFETs} with a Monte-Carlo simulator for the 2D electron gas. *Solid State Electron.*, 49(9):1529 – 1535, 2005. Special Issue: Papers Selected from the {EUROSIOI} Workshop Granada, 19-21 January 2005.

- 
- [198] M. Luisier. *Quantum Transport Beyond the Effective Mass*. PhD thesis, Swiss Federal Institute of Technology Zurich, 2007.
- [199] M. Luisier. Performance comparison of GaSb, strained-Si, and InGaAs double-gate ultrathin-body n-FETs. *IEEE electron device letters*, 32(12):1686–1688, 2011.
- [200] M. Luisier. Phonon-limited and effective low-field mobility in *n*- and *p*-type [100]-, [110]-, and [111]-oriented Si nanowire transistors. *Appl. Phys. Lett.*, 98(3):032111, 2011.
- [201] M. Luisier and G. Klimeck. Atomistic full-band simulations of silicon nanowire transistors: Effects of electron-phonon scattering. *Phys. Rev. B*, 80:155430, Oct 2009.
- [202] M. Luisier and G. Klimeck. Investigation of  $\text{In}_x\text{Ga}_{1-x}\text{As}$  ultra-thin-body tunneling FETs using a full-band and atomistic approach. In *2009 International Conference on Simulation of Semiconductor Processes and Devices*, pages 1–4. IEEE, 2009.
- [203] M. Luisier, M. Lundstrom, D. A. Antoniadis, and J. Bokor. Ultimate device scaling: Intrinsic performance comparisons of carbon-based, InGaAs, and Si field-effect transistors for 5 nm gate length. In *Electron Devices Meeting (IEDM), 2011 IEEE International*, pages 11–2. IEEE, 2011.
- [204] M. Luisier, A. Schenk, and W. Fichtner. Quantum transport in two- and three-dimensional nanoscale transistors: coupled mode effects in the nonequilibrium green’s function formalism. *Journal of Applied physics*, 100(4):043713, 2006.
- [205] M. Lundstrom. Elementary scattering theory of the Si MOSFET. *IEEE Electron Device Letters*, 18(7):361–363, 1997.
- [206] M. Lundstrom. *Fundamentals of carrier transport*. Cambridge University Press, 2009.
- [207] M. Lundstrom. Drift-diffusion and computational electronics—still going strong after 40 years! In *Simulation of Semiconductor Processes and Devices (SISPAD), 2015 International Conference on*, pages 1–3. IEEE, 2015.
- [208] M. Lundstrom and Z. Ren. Essential physics of carrier transport in nanoscale MOSFETs. *IEEE Transactions on Electron Devices*, 49(1):133–141, 2002.
- [209] J. M. Luttinger and W. Kohn. Motion of electrons and holes in perturbed periodic fields. *Physical Review*, 97(4):869, 1955.
- [210] D. D. D. Ma, C. S. Lee, F. C. K. Au, S. Y. Tong, and S. T. Lee. Small-diameter silicon nanowire surfaces. *Science*, 299(5614):1874–1877, MAR 21 2003.
- [211] G. D. Mahan. *Many-particle physics*. Springer Science & Business Media, 4th edition, 2013.
- [212] R. J. Malik. *III-V Semiconductor Materials and devices*, volume 7. Elsevier, 2012.
- [213] T. S. D. Manual. Ver. C-2010.03, Synopsys, 2010.
- [214] E. Marin, F. Ruiz, A. Godoy, I. Tienda-Luna, and F. Gámiz. Implicit versus explicit momentum relaxation time solution for semiconductor nanowires. *Journal of Applied Physics*, 118(2):024504, 2015.
- [215] E. Marin, F. Ruiz, A. Godoy, I. Tienda-Luna, and F. Gámiz. The unexpected beneficial effect of the L-valley population on the electron mobility of GaAs nanowires. *Applied Physics Letters*, 106(2):022113, 2015.

- 
- [216] E. Marin, F. Ruiz, A. Godoy, I. Tienda-Luna, C. Martínez-Blanque, and F. Gámiz. Theoretical interpretation of the electron mobility behavior in InAs nanowires. *Journal of Applied Physics*, 116(17):174505, 2014.
- [217] E. G. Marin, F. G. Ruiz, A. Godoy, I. M. Tienda-Luna, and F. Gamiz. Size-dependent electron mobility in InAs nanowires. In *Solid State Device Research Conference (ESSDERC), 2014 44th European*, pages 317–320. IEEE, 2014.
- [218] E. G. Marin, F. G. Ruiz, A. Godoy, I. M. Tienda-Luna, and F. Gámiz. Mobility and capacitance comparison in scaled InGaAs versus Si trigate MOSFETs. *IEEE Electron Device Letters*, 36(2):114–116, 2015.
- [219] R. M. Martin. *Electronic structure: basic theory and practical methods*. Cambridge university press, 2004.
- [220] C. Martinez-Blanque, F. G. Ruiz, A. Godoy, E. G. Marin, L. Donetti, and F. Gámiz. Influence of alloy disorder scattering on the hole mobility of SiGe nanowires. *Journal of Applied Physics*, 116(24):244502, 2014.
- [221] S. Martinie. *Modélisation du transport quasi-balistique pour la simulation de circuits à base de nano-transistor multigrilles*. PhD thesis, Université de Provence-Aix-Marseille I, 2009.
- [222] L. Masoero. *Etude d’architectures et d’empilements innovants de mémoires Split-Gate (grille séparée) à couche de piégeage discret*. PhD thesis, Citeseer, 2012.
- [223] P. V. Medeiros, S. S. Tsirkin, S. Stafström, and J. Björk. Unfolding spinor wave functions and expectation values of general operators: Introducing the unfolding-density operator. *Physical Review B*, 91(4):041116, 2015.
- [224] S. Mehrotra, P. Long, M. Povolotskyi, and G. Klimeck. Atomistic simulation of phonon and alloy limited hole mobility in  $\text{Si}_{1-x}\text{Ge}_x$  nanowires. *physica status solidi (RRL)-Rapid Research Letters*, 7(10):903–906, 2013.
- [225] S. R. Mehrotra, A. Paul, and G. Klimeck. Atomistic approach to alloy scattering in  $\text{Si}_{1-x}\text{Ge}_x$ . *Applied Physics Letters*, 98(17):173503, 2011.
- [226] G. Miceli and A. Pasquarello. Defect energy levels of the As–As dimer at InGaAs/oxide interfaces: A first principles study. *Microelectronic Engineering*, 109:60–63, 2013.
- [227] G. Miceli and A. Pasquarello. Defect levels at GaAs/ $\text{Al}_2\text{O}_3$  interfaces: As–As dimer vs. Ga dangling bond. *Applied Surface Science*, 291:16–19, 2014.
- [228] M. Michailat. *Paramètres matériau pour la simulation de transistors bipolaires à hétérojonctions Si/SiGe et Si/SiGeC*. PhD thesis, Université Paris Sud-Paris XI, 2010.
- [229] F. Michelini, N. Cavassilas, R. Hayn, and M. Szczap. Multiband kp models for strained zincblende crystals: Application to the fine structure of ZnO. *Physical Review B*, 80(24):245210, 2009.
- [230] MONACO. <http://www.nanosimgraphene.org/nav2/partners/ief.html>.
- [231] K. Moors, B. Sorée, and W. Magnus. Modeling surface roughness scattering in metallic nanowires. *Journal of Applied Physics*, 118(12):124307, 2015.
- [232] J. J. Moré, B. S. Garbow, and K. E. Hillstrom. User guide for MINPACK-1. Technical report, CM-P00068642, 1980.

- 
- [233] M. Moreau. *Modélisation et simulation numérique des nano-transistors multi-grilles à matériaux innovants*. PhD thesis, Université de Provence-Aix-Marseille I, 2010.
- [234] G. Mugny, J. Li, F. , Y.-M. Niquet, D. Rideau, and C. Delerue. Electronic structure and electron mobility in  $\text{Si}_{1-x}\text{Ge}_x$  nanowires. *Applied Physics Letters*, 110(5):052102, 2017.
- [235] G. Mugny, F. G. Pereira, O. Nier, D. Rideau, Y.-M. Niquet, F. c. Triozon, M.-A. Jaud, D. Garetto, and C. Delerue. Investigation of 14nm PMOS FDSOI devices with quantum-corrected drift diffusion. In *EMRS 2016, Symposium K*, 2016.
- [236] G. Mugny, F. G. Pereira, D. Rideau, F. c. Triozon, Y.-M. Niquet, M. Pala, D. Garetto, and C. Delerue. A study of diffusive-transport in 14nm FDSOI MOS-FET: NEGF versus QDD. In *ESSDERC 2016*, 2016.
- [237] G. Mugny, D. Rideau, F. Triozon, Y.-M. Niquet, C. Kriso, F. Pereira, D. Garetto, C. Tavernier, and C. Delerue. Full-zone  $k \cdot p$  parametrization for III-As materials. In *2015 International Conference on Simulation of Semiconductor Processes and Devices (SISPAD)*, pages 28–31. IEEE, 2015.
- [238] G. Mugny, F. Triozon, J. Li, Y.-M. Niquet, G. Hiblot, D. Rideau, and C. Delerue. Band structure of III-V thin films: An atomistic study of non-parabolic effects in confinement direction. In *Ultimate Integration on Silicon (EUROSIO-ULIS), 2015 Joint International EUROSIO Workshop and International Conference on*, pages 301–304. IEEE, 2015.
- [239] D. Munteanu and J. Autran. Two-dimensional modeling of quantum ballistic transport in ultimate double-gate SOI devices. *Solid-State Electronics*, 47(7):1219–1225, 2003.
- [240] F. Murphy-Armando and S. Fahy. First-principles calculation of carrier-phonon scattering in n-type  $\text{Si}_{1-x}\text{Ge}_x$  alloys. *Phys. Rev. B*, 78(3):035202, 2008.
- [241] NanoMOS. <https://nanohub.org/resources/nanomos>.
- [242] R. Neffati, I. Saïdi, and K. Boujdaria. Full-zone  $kp$  model for the electronic structure of unstrained  $\text{GaAs}_{1-x}\text{P}_x$  and strained  $\text{Al}_x\text{In}_{1-x}\text{As}$  alloys. *Journal of Applied Physics*, 112(5):053716, 2012.
- [243] NEMO5. <https://engineering.purdue.edu/gekcogrp/software-projects/nemo5/>.
- [244] T. Nguyen, G. Mahieu, M. Berthe, B. Grandidier, C. Delerue, D. Stiévenard, and P. Ebert. Coulomb energy determination of a single Si dangling bond. *Physical review letters*, 105(22):226404, 2010.
- [245] O. Nier. *Development of TCAD modeling for low field electronics transport and strain engineering in advanced Fully Depleted Silicon On Insulator (FDSOI) CMOS transistors*. PhD thesis, Université Grenoble Alpes, 2015.
- [246] D. Nikonov, H. Pal, and G. Bourianoff. Electron-phonon and spin scattering in NEGF: Made simple, 2009.
- [247] Y. Niquet, C. Delerue, G. Allan, and M. Lannoo. Method for tight-binding parametrization: Application to silicon nanostructures. *Physical Review B*, 62(8):5109, 2000.
- [248] Y. Niquet, C. Delerue, G. Allan, and M. Lannoo. Interpretation and theory of tunneling experiments on single nanostructures. *Physical Review B*, 65(16):165334, 2002.

- 
- [249] Y. Niquet, I. Duchemin, V.-H. Nguyen, F. Triozon, and D. Rideau. Remote surface roughness scattering in fully depleted silicon-on-insulator devices with high- $\kappa$ /SiO<sub>2</sub> gate stacks. *Applied Physics Letters*, 106(2):023508, 2015.
- [250] Y. Niquet, A. Lherbier, N. Quang, M. Fernández-Serra, X. Blase, and C. Delerue. Electronic structure of semiconductor nanowires. *Physical Review B*, 73(16):165319, 2006.
- [251] Y. Niquet, D. Rideau, C. Tavernier, H. Jaouen, and X. Blase. Onsite matrix elements of the tight-binding hamiltonian of a strained crystal: Application to silicon, germanium, and their alloys. *Physical Review B*, 79(24):245201, 2009.
- [252] Y.-M. Niquet. Private communication.
- [253] Y. M. Niquet. *Etude des propriétés de transport de nanostructures de semiconducteurs*. PhD thesis, Lille 1, 2001.
- [254] Y.-M. Niquet and C. Delerue. Band offsets, wells, and barriers at nanoscale semiconductor heterojunctions. *Physical Review B*, 84(7):075478, 2011.
- [255] Y.-M. Niquet and C. Delerue. Carrier mobility in strained Ge nanowires. *Journal of Applied Physics*, 112(8):084301, 2012.
- [256] Y.-M. Niquet, C. Delerue, D. Rideau, and B. Videau. Fully atomistic simulations of phonon-limited mobility of electrons and holes in  $\langle 001 \rangle$ -,  $\langle 110 \rangle$ -, and  $\langle 111 \rangle$ -oriented si nanowires. *IEEE T. Electron. Dev.*, 59:1480, 2012.
- [257] Y.-M. Niquet, V.-H. Nguyen, F. Triozon, I. Duchemin, O. Nier, and D. Rideau. Quantum calculations of the carrier mobility: Methodology, Matthiessen’s rule, and comparison with semi-classical approaches. *Journal of Applied Physics*, 115(5):054512, 2014.
- [258] L. Nordheim. The electron theory of metals. *Ann. Phys*, 9:607, 1931.
- [259] H. Oh, J. Lin, S. Suleiman, G. Lo, D. Kwong, D. Chi, and S. Lee. Thermally robust phosphorous nitride interface passivation for InGaAs self-aligned gate-first n-MOSFET integrated with high-k dielectric. In *Electron Devices Meeting (IEDM), 2009 IEEE International*, pages 1–4. IEEE, 2009.
- [260] T. Ohashi, T. Tanaka, T. Takahashi, S. Oda, and K. Uchida. Experimental study on deformation potential ( $D_{ac}$ ) in MOSFETs: Demonstration of increased  $D_{ac}$  at MOS interfaces and its impact on electron mobility. *IEEE Journal of the Electron Devices Society*, 4(5):278–285, 2016.
- [261] OMEN. <https://engineering.purdue.edu/gekcogrp/software-projects/omen/>.
- [262] Z. Or-Bach. 28nm: The last node of Moore’s law. *EE Times*, 2014.
- [263] T. O’Regan, M. Fischetti, B. Soré, S. Jin, W. Magnus, and M. Meuris. Calculation of the electron mobility in III-V inversion layers with high- $\kappa$  dielectrics. *Journal of Applied Physics*, 108(103705):1–11, Nov. 2010.
- [264] T. O’Regan, P. Hurley, B. Sorée, and M. Fischetti. Modeling the capacitance-voltage response of In<sub>x</sub>Ga<sub>1-x</sub>As 57 metal-oxide-semiconductor structures: Charge quantization and nonparabolic corrections. *Applied Physics Letters*, 96(21):213514, 2010.
- [265] N. Orlova. Variation of phonon dispersion curves with temperature in indium arsenide measured by X-ray thermal diffuse scattering. *physica status solidi (b)*, 119(2):541–546, 1983.

- 
- [266] G. Ottaviani, L. Reggiani, C. Canali, F. Nava, and A. Alberigi-Quaranta. Hole drift velocity in silicon. *Phys. Rev. B*, 12:3318–3329, Oct 1975.
- [267] G. Paasch and H. Übensee. A modified local density approximation. electron density in inversion layers. *Physica status solidi (b)*, 113(1):165–178, 1982.
- [268] P. Palestri, C. Alexander, A. Asenov, V. Aubry-Fortuna, G. Baccarani, A. Bournel, M. Braccioli, B. Cheng, P. Dollfus, A. Esposito, et al. A comparison of advanced transport models for the computation of the drain current in nanoscale nMOSFETs. *Solid-State Electronics*, 53(12):1293–1302, 2009.
- [269] H.-H. Park, C. Jeong, S. Jin, W. Choi, Y.-T. Kim, U.-H. Kwon, K.-H. Lee, and Y. Park. Calculation of alloy scattering mobility in SiGe FETs based on atomistic tight-binding approach. In *Computational Electronics (IWCE), 2013 International Workshop on*, pages 156–157, 2013.
- [270] H.-H. Park, Y. Lu, W. Choi, Y.-T. Kim, K.-H. Lee, and Y. Park. Atomistic simulations of phonon-and alloy-scattering-limited mobility in SiGe nFinFETs. In *Simulation of Semiconductor Processes and Devices (SISPAD), 2014 International Conference on*, pages 257–260. IEEE, 2014.
- [271] S. H. Park, Y. Liu, N. Kharche, M. S. Jelodar, G. Klimeck, M. S. Lundstrom, and M. Luisier. Performance comparisons of III–V and strained-Si in planar FETs and nonplanar FinFETs at ultrashort gate length (12 nm). *IEEE Transactions on Electron Devices*, 59(8):2107–2114, 2012.
- [272] R. Pässler. Description of nonradiative multiphonon transitions in the static coupling scheme. *Czechoslovak Journal of Physics B*, 24(3):322–339, 1974.
- [273] A. Paul, S. Mehrotra, M. Luisier, and G. Klimeck. Performance prediction of ultrascaled SiGe/Si core/shell electron and hole nanowire mosfets. *Electron Device Letters, IEEE*, 31(4):278–280, 2010.
- [274] V. Peikert. A new hybrid method for the current-based one-particle Monte Carlo approach. Master’s thesis, ETHZ, 2008.
- [275] V. Peikert. *Utilizing wavelets to solve high-dimensional transport equations in nano-devices*. PhD thesis, ETH ZURICH, 2013.
- [276] S. J. Penn, N. M. Alford, A. Templeton, X. Wang, M. Xu, M. Reece, and K. Schrapel. Effect of porosity and grain size on the microwave dielectric properties of sintered alumina. *Journal of the American Ceramic Society*, 80(7):1885–1888, 1997.
- [277] O. Penzin, L. Smith, A. Erlebach, and K.-H. Lee. Layer thickness and stress-dependent correction for InGaAs low-field mobility in TCAD applications. 2015.
- [278] R. People, A. Jayaraman, K. Wecht, D. Sivco, and A. Cho. Measurement of the pressure dependence of the direct band gap of  $\text{In}_{0.57}\text{Ga}_{0.43}\text{As}$  using stimulated emission. *Applied physics letters*, 52(25):2124–2126, 1988.
- [279] F. Pereira, D. Rideau, O. Nier, C. Tavernier, F. Triozon, D. Garetto, G. Mugny, B. Sklenard, G. Hiblot, and M. Pala. Modeling study of the mobility in FD-SOI devices with a focus on near-spacer-region. In *Ultimate Integration on Silicon (EUROSUI-ULIS), 2015 Joint International EUROSUI Workshop and International Conference on*, pages 49–52. IEEE, 2015.
- [280] F. G. Pereira. *Advanced numerical modeling applied to current prediction in ultimate CMOS devices*. PhD thesis, Université Grenoble Alpes, 2016.

- 
- [281] M. P. Persson, A. Lherbier, Y.-M. Niquet, F. Triozon, and S. Roche. Orientational dependence of charge transport in disordered silicon nanowires. *Nano Lett.*, 8(12):4146–4150, 2008.
- [282] M. P. Persson, H. Mera, Y.-M. Niquet, C. Delerue, and M. Diarra. Charged impurity scattering and mobility in gated silicon nanowires. *Physical Review B*, 82(11):115318, 2010.
- [283] P. Pfeffer, I. Gorczyca, and W. Zawadzki. Theory of free-electron optical absorption in n-GaAs. *Solid state communications*, 51(3):179–183, 1984.
- [284] G. Pikus and G. Bir. Effect of deformation on the energy spectrum and the electrical properties of imperfect germanium and silicon, 1959.
- [285] M. Poljak, V. Jovanovic, D. Grgec, and T. Suligoj. Assessment of electron mobility in ultrathin-body InGaAs-on-Insulator MOSFETs using physics-based modeling. *Electron Devices, IEEE Transactions on*, 59(6):1636–1643, June 2012.
- [286] F. H. Pollak and M. Cardona. Piezo-electroreflectance in Ge, GaAs, and Si. *Physical Review*, 172:816, 1968.
- [287] N. Pons, F. Triozon, M.-A. Jaud, R. Coquand, S. Martinie, O. Rozeau, Y.-M. Niquet, V.-H. Nguyen, A. Idrissi-El Oudrhiri, and S. Barraud. Density gradient calibration for 2D quantum confinement: Tri-Gate SOI transistor application. In *Simulation of Semiconductor Processes and Devices (SISPAD), 2013 International Conference on*, pages 184–187. IEEE, 2013.
- [288] E. Pop, R. W. Dutton, and K. E. Goodson. Analytic band Monte Carlo model for electron transport in Si including acoustic and optical phonon dispersion. *Journal of Applied Physics*, 96(9):4998–5005, 2004.
- [289] W. Pötz and P. Vogl. Theory of optical-phonon deformation potentials in tetrahedral semiconductors. *Physical Review B*, 24(4):2025, 1981.
- [290] R. Prange and T.-W. Nee. Quantum spectroscopy of the low-field oscillations in the surface impedance. *Physical Review*, 168(3):779, 1968.
- [291] P. J. Price. Polar-optical-mode scattering for an ideal quantum-well heterostructure. *Physical Review B*, 30(4):2234, 1984.
- [292] S. B. Radhia, N. Fraj, I. Saidi, and K. Boujdaria. The eight-level kp model for the conduction and valence bands of InAs, InP, InSb. *Semiconductor Science and Technology*, 22(4):427, 2007.
- [293] M. Radosavljevic, B. Chu-Kung, S. Corcoran, G. Dewey, M. Hudait, J. Fastenau, J. Kavalieros, W. Liu, D. Lubyshev, M. Metz, et al. Advanced high-k gate dielectric for high-performance short-channel In<sub>0.57</sub>Ga<sub>0.43</sub>As quantum well field effect transistors on silicon substrate for low power logic applications. In *Electron Devices Meeting (IEDM), 2009 IEEE International*, pages 1–4. IEEE, 2009.
- [294] M. Radosavljevic, G. Dewey, D. Basu, J. Boardman, B. Chu-Kung, J. Fastenau, S. Kabehie, J. Kavalieros, V. Le, W. K. Liu, D. Lubyshev, M. Metz, K. Millard, N. Mukherjee, L. Pan, R. Pillarisetty, W. Rachmady, U. Shah, H. W. Then, and R. Chau. Electrostatics improvement in 3-D tri-gate over ultra-thin body planar InGaAs quantum well field effect transistors with high-k gate dielectric and scaled gate-to-drain/gate-to-source separation. In *Electron Devices Meeting (IEDM), 2011 IEEE International*, pages 33.1.1–33.1.4, Dec 2011.

- 
- [295] M. Radosavljevic, G. Dewey, J. Fastenau, J. Kavalieros, R. Kotlyar, B. Chu-Kung, W. Liu, D. Lubyshev, M. Metz, K. Millard, et al. Non-planar, multi-gate InGaAs quantum well field effect transistors with high-k gate dielectric and ultra-scaled gate-to-drain/gate-to-source separation for low power logic applications. In *Electron Devices Meeting (IEDM), 2010 IEEE International*, pages 6–1. IEEE, 2010.
- [296] A. Rahman, M. S. Lundstrom, and A. W. Ghosh. Generalized effective-mass approach for n-type metal-oxide-semiconductor field-effect transistors on arbitrarily oriented wafers. *Journal of applied physics*, 97(5):053702, 2005.
- [297] M. Rau, T. Markussen, E. Caruso, D. Esseni, E. Gnani, A. Gnudi, P. A. Khomyakov, M. Luisier, P. Osgnach, P. Palestri, et al. Performance study of strained III–V materials for ultra-thin body transistor applications. In *Solid-State Device Research Conference (ESSDERC), 2016 46th European*, pages 184–187. IEEE, 2016.
- [298] S. Richard. *Modélisation Physique de la structure électronique, du transport et de l'ionisation par choc dans les matériaux IV-IV massifs, contraints et dans les puits quantiques*. PhD thesis, Université Paris Sud-Paris XI, 2004.
- [299] S. Richard, F. Aniel, and G. Fishman. Energy-band structure of ge, si, and gaas: A thirty-band k p method. *Physical Review B*, 70:235204, 2004.
- [300] C. Riddet, J. Watling, K. Chan, A. Asenov, B. De Jaeger, J. Mitard, and M. Meuris. Monte Carlo simulation study of hole mobility in germanium MOS inversion layers. In *Computational Electronics (IWCE), 2010 14th International Workshop on*, pages 1–4. IEEE, 2010.
- [301] D. Rideau. Private communication.
- [302] D. Rideau. Full band models for strained Silicon and Germanium devices. In S. Jit, editor, *Advances in microelectronics and photonics*. Nova Science Publishers Inc, New York, 2011.
- [303] D. Rideau, E. Batail, S. Monfray, C. Tavernier, and H. Jaouen. Modeling study of ultra-thin Ge layers using tight-binding, LCBB and kp methods. In *Simulation of Semiconductor Processes and Devices 2007*, pages 145–148. Springer, 2007.
- [304] D. Rideau, M. Feraille, L. Ciampolini, M. Minondo, C. Tavernier, H. Jaouen, and A. Ghetti. Strained Si, Ge, and  $\text{Si}_{1-x}\text{Ge}_x$  alloys modeled with a first-principles-optimized full-zone kp method. *Physical Review B*, 74(19):195208, 2006.
- [305] D. Rideau, M. Feraille, M. Michailat, C. Tavernier, and H. Jaouen. Transport masses in strained silicon MOSFETs with different channel orientations. *ENERGY*, 1:1–245, 2008.
- [306] D. Rideau, D. Garetto, and G. Mugny. Critical understanding of traps dynamics models in oxide layers, 2015.
- [307] D. Rideau, F. Monsieur, O. Nier, Y. Niquet, J. Lacord, V. Quenette, G. Mugny, G. Hiblot, G. Gouget, M. Quoirin, et al. Experimental and theoretical investigation of the ‘apparent’ mobility degradation in bulk and UTBB-FDSOI devices: a focus on the near-spacer-region resistance. In *2014 International Conference on Simulation of Semiconductor Processes and Devices (SISPAD)*, pages 101–104. IEEE, 2014.
- [308] M. M. Rieger and P. Vogl. Electronic-band parameters in strained  $\text{Si}_{1-x}\text{Ge}_x$  alloys on  $\text{Si}_{1-y}\text{Ge}_y$  substrates. *Physical Review B*, 48(19):14276, 1993.
- [309] J. Robertson. High dielectric constant gate oxides for metal oxide Si transistors.

- Reports on Progress in Physics*, 69(2):327, 2005.
- [310] U. Rössler. Nonparabolicity and warping in the conduction band of GaAs. *Solid state communications*, 49(10):943–947, 1984.
- [311] K. Rupp, C. Jungemann, S.-M. Hong, M. Bina, T. Grassler, and A. Jüngel. A review of recent advances in the spherical harmonics expansion method for semiconductor device simulation. *Journal of Computational Electronics*, 15(3):939–958, 2016.
- [312] M. Salmani-Jelodar, A. Paul, T. Boykin, and G. Klimeck. Calculation of phonon spectrum and thermal properties in suspended  $\langle 100 \rangle$   $\text{In}_{0.57}\text{Ga}_{0.43}\text{As}$  nanowires. *Journal of Computational Electronics*, 11(1):22–28, 2012.
- [313] M. L. Sancho, J. L. Sancho, J. L. Sancho, and J. Rubio. Highly convergent schemes for the calculation of bulk and surface Green functions. *Journal of Physics F: Metal Physics*, 15(4):851, 1985.
- [314] M. Scarpino, S. Gupta, D. Lin, A. Alian, F. Crupi, N. Collaert, A. Thean, and E. Simoen. Border traps in InGaAs nMOSFETs assessed by low-frequency noise. *Electron Device Letters, IEEE*, 35(7):720–722, 2014.
- [315] D. L. Scharfetter and H. K. Gummel. Large-signal analysis of a silicon read diode oscillator. *IEEE Transactions on electron devices*, 16(1):64–77, 1969.
- [316] S. Selberherr. *Analysis and simulation of semiconductor devices*. Springer Science & Business Media, 2012.
- [317] N. Seoane, G. Indalecio, M. Aldegunde, D. Nagy, M. A. Elmessary, A. J. Garcia-Loureiro, and K. Kalna. Comparison of fin-edge roughness and metal grain work function variability in InGaAs and Si FinFETs. *IEEE Transactions on Electron Devices*, 63(3):1209–1216, 2016.
- [318] G. Sereni, L. Larcher, L. Vandelli, D. Veksler, T. Kim, D. Koh, and G. Bersuker. A novel technique exploiting C–V, G–V and I–V simulations to investigate defect distribution and native oxide in high- $\kappa$  dielectrics for III–V MOSFETs. *Microelectronic Engineering*, 147:281–284, 2015.
- [319] G. Sereni, L. Vandelli, R. Cavicchioli, L. Larcher, D. Veksler, and G. Bersuker. Substrate and temperature influence on the trap density distribution in high-k III-V mosfets. In *Reliability Physics Symposium (IRPS), 2015 IEEE International*, pages 2E–6. IEEE, 2015.
- [320] G. Sereni, L. Vandelli, D. Veksler, and L. Larcher. A new physical method based on-simulations for the characterization of the interfacial and bulk defect density in high-k/III-V MOSFETs. *Electron Devices, IEEE Transactions on*, 62(3):705–712, 2015.
- [321] J. Shah, B. Deveaud, T. Damen, W. Tsang, A. Gossard, and P. Lugli. Determination of intervalley scattering rates in GaAs by subpicosecond luminescence spectroscopy. *Physical review letters*, 59(19):2222, 1987.
- [322] W. Shockley and W. Read Jr. Statistics of the recombinations of holes and electrons. *Physical review*, 87(5):835, 1952.
- [323] Silvaco. <http://www.silvaco.com/products/tcad.html>.
- [324] J. Sjakste, V. Tyuterev, and N. Vast. Intervalley scattering in GaAs: ab initio calculation of the effective parameters for Monte Carlo simulations. *Applied Physics A*, 86(3):301–307, 2007.

- 
- [325] J. Sjakste, N. Vast, H. Jani, S. Obukhov, and V. Tyuterev. Ab initio study of the effects of pressure and strain on electron-phonon coupling in IV and III-V semiconductors. *physica status solidi (b)*, 250(4):716–720, 2013.
- [326] J. Sjakste, N. Vast, and V. Tyuterev. Ab initio method for calculating electron-phonon scattering times in semiconductors: Application to GaAs and GaP. *Physical review letters*, 99(23):236405, 2007.
- [327] J. C. Slater and G. F. Koster. Simplified LCAO method for the periodic potential problem. *Physical Review*, 94(6):1498, 1954.
- [328] J. Slotboom. The pn – product in silicon. *Solid-State Electronics*, 20(4):279–283, 1977.
- [329] A. Sonnet, R. Galatage, P. Hurley, E. Pelucchi, K. Thomas, A. Gocalinska, J. Huang, N. Goel, G. Bersuker, W. Kirk, et al. On the calculation of effective electric field in In<sub>0.57</sub>Ga<sub>0.43</sub>As surface channel metal-oxide-semiconductor field-effect-transistors. *Applied Physics Letters*, 98(19):193501, 2011.
- [330] A. Sonnet, R. Galatage, P. Hurley, E. Pelucchi, K. Thomas, A. Gocalinska, J. Huang, N. Goel, G. Bersuker, W. Kirk, et al. Remote phonon and surface roughness limited universal electron mobility of In<sub>0.57</sub>Ga<sub>0.43</sub>As surface channel MOSFETs. *Microelectronic Engineering*, 88(7):1083–1086, 2011.
- [331] A. Sonnet, R. Galatage, M. Jivani, M. Milojevic, P. Kirsch, J. Huang, R. Chapman, C. Hinkle, R. Wallace, and E. Vogel. Impact of surface preparations on the transport characteristics of In<sub>x</sub>Ga<sub>1-x</sub>As metal-oxide-semiconductor field effect transistors MOSFETs. In *Semiconductor Device Research Symposium, 2009. ISDRS'09. International*, pages 1–2. IEEE, 2009.
- [332] A. Soussou. *Modeling and characterization of electrical effects of Ge integration in Metal/High-k/SiGe MOS structures*. PhD thesis, Université Grenoble Alpes, 2014.
- [333] Sparta. <https://iis-people.ee.ethz.ch/~bufler/professional/sparta.html>.
- [334] Z. Stanojević, O. Baumgartner, M. Karner, L. Filipović, C. Kernstock, and H. Kosina. On the validity of momentum relaxation time in low-dimensional carrier gases. In *2014 International Conference on Simulation of Semiconductor Processes and Devices (SISPAD)*, pages 181–184. IEEE, 2014.
- [335] Z. Stanojevic, O. Baumgartner, M. Karner, F. Mitterbauer, H. Demel, and C. Kernstock. Simulation study on the feasibility of Si as material for ultra-scaled nanowire field-effect transistors. In *Ultimate Integration on Silicon (EUROSOI-ULIS), 2016 Joint International EUROSOI Workshop and International Conference on*, pages 147–150. IEEE, 2016.
- [336] Z. Stanojevic, O. Baumgartner, F. Mitterbauer, H. Demel, C. Kernstock, M. Karner, V. Eyert, A. France-Lanord, P. Saxe, C. Freeman, et al. Physical modeling-a new paradigm in device simulation. In *Electron Devices Meeting (IEDM), 2015 IEEE International*, pages 5–1. IEEE, 2015.
- [337] Z. Stanojevic, M. Karner, M. Aichhorn, F. Mitterbauer, V. Eyert, C. Kernstock, and H. Kosina. Predictive physical simulation of III/V quantum-well MISFETs for logic applications. In *Solid State Device Research Conference (ESSDERC), 2015 45th European*, pages 310–313. IEEE, 2015.
- [338] Z. Stanojevic, M. Karner, F. Mitterbauer, and C. Kernstock. New computational

- perspectives on scattering and transport in III/V channel materials. In *Computational Electronics (IWCE), 2015 International Workshop on*, pages 1–3. IEEE, 2015.
- [339] Z. Stanojević and H. Kosina. Surface-roughness-scattering in non-planar channels - the role of band anisotropy. In *Simulation of Semiconductor Processes and Devices (SISPAD), 2013 International Conference on*, pages 352–355. IEEE, 2013.
- [340] Z. Stanojević, V. Sverdlov, O. Baumgartner, and H. Kosina. Subband engineering in n-type silicon nanowires using strain and confinement. *Solid-state electronics*, 70:73–80, 2012.
- [341] S. Steiger, M. Salmani-Jelodar, D. Areshkin, A. Paul, T. Kubis, M. Povolotskyi, H.-H. Park, and G. Klimeck. Enhanced valence force field model for the lattice properties of gallium arsenide. *Physical Review B*, 84(15):155204, 2011.
- [342] S. Stemmer, V. Chobpattana, and S. Rajan. Frequency dispersion in III-V metal-oxide-semiconductor capacitors. *Applied Physics Letters*, 100(23):233510, 2012.
- [343] R. Stevenson. Changing the channel. *IEEE Spectrum*, 50(7):34–39, 2013.
- [344] G. Stillman, C. Wolfe, and J. Dimmock. Hall coefficient factor for polar mode scattering in n-type GaAs. *Journal of Physics and Chemistry of Solids*, 31(6):1199 – 1204, 1970.
- [345] A. M. Stoneham. *Theory of defects in solids: electronic structure of defects in insulators and semiconductors*. Oxford University Press, 2001.
- [346] D. Strauch and B. Dorner. Phonon dispersion in GaAs. *Journal of Physics: Condensed Matter*, 2(6):1457, 1990.
- [347] S. A. B. Suleiman, H.-J. Oh, and S. Lee. Effects of plasma PH<sub>3</sub> passivation on mobility degradation mechanisms of In<sub>0.57</sub>Ga<sub>0.43</sub>As nmosfets. *IEEE Transactions on Electron Devices*, 59(5):1377–1384, 2012.
- [348] Synopsys. Sentaurus band structure user guide, 2013.
- [349] S. Takagi, T. Tezuka, T. Irisawa, S. Nakaharai, T. Maeda, T. Numata, K. Ikeda, and N. Sugiyama. Hole mobility enhancement of p-MOSFETs using global and local Ge-channel technologies. *Materials Science and Engineering: B*, 135(3):250–255, 2006.
- [350] S.-i. Takagi, A. Toriumi, M. Iwase, and H. Tango. On the universality of inversion layer mobility in Si MOSFET's: Part I-effects of substrate impurity concentration. *IEEE Transactions on Electron Devices*, 41(12):2357–2362, 1994.
- [351] Y. Tan, M. Povolotskyi, T. Kubis, Y. He, Z. Jiang, G. Klimeck, and T. B. Boykin. Empirical tight binding parameters for GaAs and MgO with explicit basis through DFT mapping. *Journal of Computational Electronics*, 12(1):56–60, 2013.
- [352] Y. P. Tan, M. Povolotskyi, T. Kubis, T. B. Boykin, and G. Klimeck. Tight-binding analysis of Si and GaAs ultrathin bodies with subatomic wave-function resolution. *Physical Review B*, 92(8):085301, 2015.
- [353] N. Taoka, M. Yokoyama, S. Kim, R. Suzuki, R. Iida, S. Lee, T. Hoshii, W. Jevasuwan, T. Maeda, T. Yasuda, et al. Impact of fermi level pinning inside conduction band on electron mobility of In<sub>x</sub>Ga<sub>1-x</sub>As mosfets and mobility enhancement by pinning modulation. In *Electron Devices Meeting (IEDM), 2011 IEEE International*, pages 27–2. IEEE, 2011.

- [354] N. Taoka, M. Yokoyama, S. H. Kim, R. Suzuki, S. Lee, R. Iida, T. Hoshii, W. Jevasuwan, T. Maeda, T. Yasuda, et al. Impact of fermi level pinning inside conduction band on electron mobility in InGaAs metal-oxide-semiconductor field-effect transistors. *Applied Physics Letters*, 103(14):143509, 2013.
- [355] K. Tomioka, M. Yoshimura, E. Nakai, F. Ishizaka, and T. Fukui. Integration of III-V nanowires on Si: From high-performance vertical FET to steep-slope switch. In *Electron Devices Meeting (IEDM), 2013 IEEE International*, pages 4–1. IEEE, 2013.
- [356] P. Toniutti. *Impact of the technology boosters on the MOSFET performance*. PhD thesis, Università degli Studi di Udine, 2012.
- [357] P. Toniutti, D. Esseni, and P. Palestri. Failure of the scalar dielectric function approach for the screening modeling in double-gate SOI MOSFETs and in FinFETs. *IEEE Transactions on Electron Devices*, 57(11):3074–3083, 2010.
- [358] P. Toniutti, P. Palestri, D. Esseni, F. Driussi, M. De Michielis, and L. Selmi. On the origin of the mobility reduction in n-and p-metal-oxide-semiconductor field effect transistors with hafnium-based/metal gate stacks. *Journal of Applied Physics*, 112(3):034502, 2012.
- [359] A. Trellakis, A. Galick, A. Pacelli, and U. Ravaioli. Iteration scheme for the solution of the two-dimensional schrödinger-poisson equations in quantum structures. *Journal of Applied Physics*, 81(12):7880–7884, 1997.
- [360] F. Triozon and P. Dollfus. *Simulation of Transport in Nanodevices*. John Wiley & Sons, 2016.
- [361] F. Triozon, S. Roche, and Y.-M. Niquet. Introduction to quantum transport. In F. Triozon and P. Dollfus, editors, *Simulation of Transport in Nanodevices*. Wiley Online Library, 2016.
- [362] R. Tubino, L. Piseri, and G. Zerbi. Lattice dynamics and spectroscopic properties by a valence force potential of diamondlike crystals: C, Si, Ge, and Sn. *J. Chem. Phys.*, 56(3):1022–1039, 1972.
- [363] K. Uchida, H. Watanabe, A. Kinoshita, J. Koga, T. Numata, and S. Takagi. Experimental study on carrier transport mechanism in ultrathin-body SOI nand p-MOSFETs with SOI thickness less than 5 nm. In *Electron Devices Meeting, 2002. IEDM'02. International*, pages 47–50. IEEE, 2002.
- [364] UGR. <http://www.ugr.es/>.
- [365] UNIUD. <http://www2.diegm.uniud.it/diegm/>.
- [366] Y. Urabe, N. Miyata, H. Ishii, T. Itatani, T. Maeda, T. Yasuda, H. Yamada, N. Fukuhara, M. Hata, M. Yokoyama, et al. Correlation between channel mobility improvements and negative  $V_{th}$  shifts in III-V MISFETs: Dipole fluctuation as new scattering mechanism. In *Electron Devices Meeting (IEDM), 2010 IEEE International*, pages 6–5. IEEE, 2010.
- [367] A. Vais, H.-C. Lin, C. Dou, K. Martens, T. Ivanov, Q. Xie, F. Tang, M. Givens, J. Maes, N. Collaert, et al. Temperature dependence of frequency dispersion in III-V metal-oxide-semiconductor CV and the capture/emission process of border traps. *Applied Physics Letters*, 107(5):053504, 2015.
- [368] A. Vais, K. Martens, J. Franco, D. Lin, A. Alian, P. Roussel, S. Sioncke, N. Collaert,

- A. Thean, M. Heyns, et al. The relationship between border traps characterized by ac admittance and bti in iii-v mos devices. In *Reliability Physics Symposium (IRPS), 2015 IEEE International*, pages 5A–7. IEEE, 2015.
- [369] C. G. Van de Walle. Band lineups and deformation potentials in the model-solid theory. *Physical Review B*, 39(3):1871, 1989.
- [370] W. Van Den Daele, C. Le Royer, E. Augendre, J. Mitard, G. Ghibaudo, and S. Cristoloveanu. Detailed investigation of effective field, hole mobility and scattering mechanisms in GeOI and Ge pMOSFETs. *Solid-State Electronics*, 59(1):25–33, 2011.
- [371] D. Vanderbilt, S. H. Taole, and S. Narasimhan. Anharmonic elastic and phonon properties of Si. *Phys. Rev. B*, 40:5657–5668, Sep 1989.
- [372] M. Vasicek, J. Cervenka, D. Esseni, P. Palestri, and T. Grassler. Applicability of macroscopic transport models to decananometer MOSFETs. *IEEE Transactions on Electron Devices*, 59(3):639–646, 2012.
- [373] R. Venugopal, Z. Ren, S. Datta, M. Lundstrom, and D. Jovanovic. Simulating quantum transport in nanoscale transistors: Real versus mode-space approaches. *Journal of Applied Physics*, 92(7):3730–3739, 2002.
- [374] R. G. Veprek. *Computational modeling of semiconductor nanostructures for optoelectronics*. Hartung-Gorre, 2009.
- [375] R. G. Veprek, S. Steiger, and B. Witzigmann. Ellipticity and the spurious solution problem of kp envelope equations. *Physical Review B*, 76(16):165320, 2007.
- [376] [http://electroiq.com/blog/2010/03/iii-v\\_mosfets/](http://electroiq.com/blog/2010/03/iii-v_mosfets/). . .
- [377] [https://www.globalfoundries.com/technology\\_solutions/cmos/fox/22fox/](https://www.globalfoundries.com/technology_solutions/cmos/fox/22fox/). . .
- [378] <https://zhidao.baidu.com/question/48856179.html>. . .
- [379] [http://translation-dictionary.net/chinese\\_english/](http://translation-dictionary.net/chinese_english/). . .
- [380] [http://www.eetimes.com/document.asp?doc\\_id=1323892](http://www.eetimes.com/document.asp?doc_id=1323892). . .
- [381] TB\_Sim. [http://inac.cea.fr/l\\_sim/tb\\_sim/](http://inac.cea.fr/l_sim/tb_sim/). . .
- [382] A. Verma, A. K. Buin, and M. P. Anantram. High-field hole transport in silicon nanowires. *J. Appl. Phys.*, 106(11):–, 2009.
- [383] D. Verreck, M. Van De Put, A. Verhulst, B. Sorée, W. Magnus, A. Dabral, A. Thean, and G. Groeseneken. 15-band spectral envelope function formalism applied to broken gap tunnel field-effect transistors. In *Computational Electronics (IWCE), 2015 International Workshop on*, pages 1–4. IEEE, 2015.
- [384] D. Verreck, A. S. Verhulst, M. L. Van de Put, B. Sorée, N. Collaert, A. Mocuta, A. Thean, and G. Groeseneken. Uniform strain in heterostructure tunnel field-effect transistors. *IEEE Electron Device Letters*, 37(3):337–340, 2016.
- [385] I. Vurgaftman, J. Meyer, and L. Ram-Mohan. Band parameters for III–V compound semiconductors and their alloys. *Journal of applied physics*, 89(11):5815–5875, 2001.
- [386] J. Wang, A. Rahman, A. Ghosh, G. Klimeck, and M. Lundstrom. On the validity of the parabolic effective-mass approximation for the IV calculation of silicon nanowire transistors. *IEEE Transactions on Electron Devices*, 52(7):1589–1595, 2005.
- [387] J.-Q. Wang, Z.-Q. Gu, M.-F. Li, and W.-Y. Lai. Intervalley  $\gamma$ -x deformation potentials in III-V zinc-blende semiconductors by ab initio pseudopotential calculations.

- Physical Review B*, 46(19):12358, 1992.
- [388] L. Wang, P. M. Asbeck, and Y. Taur. Self-consistent 1-D Schrödinger–Poisson solver for III–V heterostructures accounting for conduction band non-parabolicity. *Solid-State Electronics*, 54(11):1257–1262, 2010.
- [389] J. Weber and M. I. Alonso. Near-band-gap photoluminescence of Si-Ge alloys. *Physical Review B*, 40:5683–5693, Sep 1989.
- [390] J. Weber, A. Janotti, and C. Van de Walle. Native defects in Al<sub>2</sub>O<sub>3</sub> and their impact on III-V/Al<sub>2</sub>O<sub>3</sub> metal-oxide-semiconductor-based devices. *Journal of Applied Physics*, 109(3):033715, 2011.
- [391] V. Wilkinson, A. Prins, J. Lambkin, E. OReilly, D. Dunstan, L. Howard, and M. Emeny. Hydrostatic pressure coefficients of the photoluminescence of In<sub>x</sub>Ga<sub>1-x</sub>As /gaas strained-layer quantum wells. *Physical Review B*, 42(5):3113, 1990.
- [392] G. P. Williams, F. Cerrina, G. Lapeyre, J. Anderson, R. Smith, and J. Hermanson. Experimental study of the band structure of GaP, GaAs, GaSb, InP, InAs, and InSb. *Physical Review B*, 34(8):5548, 1986.
- [393] Y. Wu, Y. Cui, L. Huynh, C. J. Barrelet, D. C. Bell, and C. M. Lieber. Controlled growth and structures of molecular-scale silicon nanowires. *Nano Lett.*, 4(3):433–436, MAR 2004.
- [394] Y. Xuan, Y. Wu, and P. Ye. High-performance inversion-type enhancement-mode InGaAs MOSFET with maximum drain current exceeding 1 A/mm. *Electron Device Letters, IEEE*, 29(4):294–296, April 2008.
- [395] M. Yahyaoui, K. Sellami, K. Boujdaria, M. Chamarro, and C. Testelin. Band parameters of InGaAs/GaAs quantum dots: electronic properties study. *Semiconductor Science and Technology*, 28(12):125018, 2013.
- [396] P. Yang, L. Chan, S. Siah, S. W. Lai, V. Lo, and W. Lau. *The Evolution of Theory on Drain Current Saturation Mechanism of MOSFETs from the Early Days to the Present Day*. INTECH Open Access Publisher, 2010.
- [397] J. Yota, H. Shen, and R. Ramanathan. Characterization of atomic layer deposition HfO<sub>2</sub>, Al<sub>2</sub>O<sub>3</sub>, and plasma-enhanced chemical vapor deposition Si<sub>3</sub>N<sub>4</sub> as metal–insulator–metal capacitor dielectric for GaAs HBT technology. *Journal of Vacuum Science & Technology A*, 31(1):01A134, 2013.
- [398] P. Yu and M. Cardona. *Fundamentals of semiconductors: physics and materials properties*. Springer-Verlag Berlin Heidelberg, fourth edition edition, 2010.
- [399] D. H. Zadeh, H. Oomine, K. Kakushima, Y. Kataoka, A. Nishiyama, N. Sugii, H. Wakabayashi, K. Tsutsui, K. Natori, and H. Iwai. Low Dit high-k/ In<sub>0.57</sub>Ga<sub>0.43</sub>As gate stack, with CET down to 0.73 nm and thermally stable silicide contact by suppression of interfacial reaction. In *2013 IEEE International Electron Devices Meeting*, pages 2–4. IEEE, 2013.
- [400] Z. Zeng, F. Triozon, and Y.-M. Niquet. Carrier scattering by workfunction fluctuations and interface dipoles in high-k/metal gate stacks. In *Simulation of Semiconductor Processes and Devices (SISPAD), 2016 International Conference on*, pages 369–372. IEEE, 2016.
- [401] G. Zerveas, E. Caruso, G. Baccarani, L. Czornomaz, N. Daix, D. Esseni, E. Gnani,

- A. Gnudi, R. Grassi, M. Luisier, et al. Comprehensive comparison and experimental validation of band-structure calculation methods in III–V semiconductor quantum wells. *Solid-State Electronics*, 115:92–102, 2016.
- [402] W. Zhang, C. Delerue, Y.-M. Niquet, G. Allan, and E. Wang. Atomistic modeling of electron-phonon coupling and transport properties in n-type [110] silicon nanowires. *Physical Review B*, 82(11):115319, 2010.
- [403] H. Zhao, Y.-T. Chen, J. H. Yum, Y. Wang, N. Goel, and J. C. Lee. High performance In<sub>0.7</sub>Ga<sub>0.3</sub>As metal-oxide-semiconductor transistors with mobility > 4400 cm<sup>2</sup>/v s using InP barrier layer. *Applied Physics Letters*, 94(19):193502, 2009.
- [404] H. Zhao, J. H. Yum, Y.-T. Chen, J. C. Lee, et al. In<sub>0.57</sub>Ga<sub>0.43</sub>As n-metal-oxide-semiconductor field effect transistors with atomic layer deposited Al<sub>2</sub>O<sub>3</sub>, HfO<sub>2</sub>, and LaAlO<sub>3</sub> gate dielectrics. *Journal of Vacuum Science & Technology B*, 27(4):2024–2027, 2009.
- [405] X. Zhao, J. Lin, C. Heidelberger, E. A. Fitzgerald, and J. A. del Alamo. Vertical nanowire InGaAs MOSFETs fabricated by a top-down approach. In *Electron Devices Meeting (IEDM), 2013 IEEE International*, pages 28–4. IEEE, 2013.
- [406] X. Zhu and S. G. Louie. Quasiparticle band structure of thirteen semiconductors and insulators. *Physical Review B*, 43(17):14142, 1991.
- [407] S. Zollner, S. Gopalan, and M. Cardona. Intervalley deformation potentials and scattering rates in zinc blende semiconductors. *Applied physics letters*, 54(7):614–616, 1989.
- [408] S. Zollner, S. Gopalan, and M. Cardona. Microscopic theory of intervalley scattering in GaAs: k dependence of deformation potentials and scattering rates. *Journal of Applied Physics*, 68(4):1682–1693, 1990.
- [409] A. Zunger, S.-H. Wei, L. Ferreira, and J. E. Bernard. Special quasirandom structures. *Physical Review Letters*, 65(3):353, 1990.